

KATHOLIEKE UNIVERSITEIT LEUVEN
FACULTEIT INGENIEURSWETENSCHAPPEN
DEPARTEMENT ELEKTROTECHNIEK
Kasteelpark Arenberg 10, 3001 Leuven (Heverlee)

QUANTIFICATION AND CLASSIFICATION OF MAGNETIC RESONANCE SPECTROSCOPIC DATA FOR BRAIN TUMOR DIAGNOSIS

Promotor:
Prof. dr. ir. S. Van Huffel

Proefschrift voorgedragen tot
het behalen van het doctoraat
in de ingenieurswetenschappen

door

Jean-Baptiste Poullet

November 2008

KATHOLIEKE UNIVERSITEIT LEUVEN
FACULTEIT INGENIEURSWETENSCHAPPEN
DEPARTEMENT ELEKTROTECHNIEK
Kasteelpark Arenberg 10, 3001 Leuven (Heverlee)

QUANTIFICATION AND CLASSIFICATION OF MAGNETIC RESONANCE SPECTROSCOPIC DATA FOR BRAIN TUMOR DIAGNOSIS

Jury:
Prof. dr. ir. L. Froyen, voorzitter
Prof. dr. ir. S. Van Huffel, promotor
Prof. dr. U. Himmelreich
Prof. dr. ir. J.A.K. Suykens
Prof. dr. ir. R. Pintelon (VUB)
Prof. dr. B. Celda (UVEG Valencia)
Dr. ir. D. Graveron-Demilly (INSA Lyon)

Proefschrift voorgedragen tot
het behalen van het doctoraat
in de ingenieurswetenschappen

door

Jean-Baptiste Poullet

U.D.C. 681.3*J3 November 2008

© Katholieke Universiteit Leuven – Faculteit Ingenieurswetenschappen

Arenbergkasteel, B-3001 Leuven (Belgium)

Alle rechten voorbehouden. Niets uit deze uitgave mag vermenigvuldigd en/of openbaar gemaakt worden door middel van druk, fotocopie, microfilm, elektronisch of op welke andere wijze ook zonder voorafgaande schriftelijke toestemming van de uitgever.

All rights reserved. No part of the publication may be reproduced in any form by print, photoprint, microfilm or any other means without written permission from the publisher.

D/2008/7515/104

ISBN 978-90-5682-994-0

Foreword

Research is rarely a one-man's work. There are a number of people that directly or indirectly have contributed to the completion of this dissertation.

First of all, I would like to express my sincere gratitude to my promotor, Sabine Van Huffel, who has made this work possible. In spite of her very busy schedule, she has always found time for me. My deep thanks also go to Professor Rik Pintelon for his availability and his precious help and guidance. I also would like to thank the members of the exam committee, Professors Johan Suykens, Uwe Himmelreich, Bernardo Celda and Danielle Graveron-Demilly, for their constant good mood and their valuable comments and suggestions. Thank you all for serving as members of this committee. More generally, thanks to all the members of the EU projects ETUMOUR (FP6-2002-LIFESCIHEALTH 503094), FAST Project (FP6-MC-RTN-035801) and BIOPATTERN (FP6-2002-IST 508803) for the nice discussions, as well during the scientific meetings as during the more informal occasions. The financial support of these 3 sponsors is greatly appreciated.

I also would like to thank all my colleagues from the Biomed group. They provided a very good working environment and a friendly atmosphere.

I cannot forget my parents and family who have always been there to bring me their support and their encouragement. I thank them!

Last but not least, I particularly thank Véronique, my wife, for her love and her support through all these years.

Abstract

Magnetic Resonance Spectroscopy has been successfully used in brain tumor diagnosis and represents a complementary aid to the well-known technique, Magnetic Resonance Imaging, by providing metabolic information that is not available with the latter. Both Imaging and Spectroscopy can be used for the grading and typing of brain tumors.

Classifying brain tumors from spectroscopic data is not trivial and requires several steps. The common main steps are preprocessing, feature extraction and, finally, classification of the data. The preprocessing step aims to clean up the data and to normalize them in order to facilitate the extraction of the relevant features. These features, once selected and extracted, are used in a classifier, whose output is a brain tumor class. The challenge is to improve brain tumor diagnosis based on spectroscopic data. In this thesis, we analyzed methods used in each of the steps of the procedure in order to extract their advantages and limitations. Due to the complexity and diversity of the data and the still limited amount of available data, there is no gold standard procedure which would provide the best classification results. However, this thesis aims to identify the problems that can be encountered during the whole procedure (preprocessing, feature extraction and classification) and to provide the reader with possible solutions. In particular, a large part of this thesis is devoted to the quantification of MRS data, which remains very complicated, especially when dealing with *in vivo* MRS(I) data.

Notation

Acronyms and abbreviations

AA	anaplastic astrocytoma
Ala	alanine
AMARES	advanced method for accurate, robust and efficient spectral fitting [299]
ANN	artificial neural network
AQSES	automated quantification of short echo time MRS [213]
AQSES GUI	AQSES graphical user interface
ARMA	autoregressive moving average
CFIT	circle fitting [89]
Cr	creatine
CRB	Cramér-Rao bounds
CSA	chemical shift anisotropy
CSI	chemical shift imaging
CT	Computed Tomography
DFT	discrete Fourier transform
DSS	decision support system
ECC	eddy current correction [138]
EM	expectation-maximization
ER-filter	extraction and reduction filter [37]
ESPRIT	estimation of signal parameters via rotational invariance techniques [233]
FDM	filter diagonalization method [175]
FID	free induction decay
FIDO	filtering and downsampling [239]
FIR	finite impulse response filter
FWHM	full width at half maximum
GAMMA	a general approach to magnetic resonance mathematical analysis [256]
GBM	glioblastoma multiforme
Glc	glucose
Gln	glutamine
Glu	glutamate
Glx	glutamine + glutamate
Gly	Glycine

GP	gaussian processes
GPCh	glycerphosphocholine
GPLS	generalized partial least squares
GSH	glutathione
HLSVD	Hankel Lanczos singular value decomposition [210]
HLSVD-IRL	HLSVD with implicitly restarted Lanczos algorithm [30]
HLSVD-PRO	HLSVD with partial reorthogonalization [152]
HR-MAS	high resolution magic angle spinning
HSVD	Hankel singular value decomposition [12]
HTLS	Hankel total least squares [295]
HTLS-PK	Hankel total least squares using prior knowledge [42]
ICA	independent component analysis
IQML	iterative quadratic maximum likelihood [314]
KLR	kernel logistic regression [315]
KNOB-TLS	knowledge based total least squares [154]
Lac	lactate
LCModel	linear combination of model spectra [220]
LDA	linear discriminant analysis
LE	long echo time
LF	lineshape fitting [3]
LGA	low grade astrocytoma
Lip1	lipids at 1.3 ppm
Lip2	lipids at 0.9 ppm
LP	linear prediction
LS	least-squares
LS-SVM	least-squares support vector machines
MeFreS	Metropolis frequency-selective [230]
MEN	meningioma
MET	metastasis
MM	macromolecule
MODE	method of direction estimation [38]
MP	matrix pencil [224]
MP-FIR	maximum-phase FIR [273]
MR	magnetic resonance
MRS	magnetic resonance spectroscopy
MRSI	magnetic resonance spectroscopic imaging
Myo	myo-inositol
NAA	N-acetyl-aspartate
NLLS	nonlinear least-squares
NMR	nuclear magnetic resonance
NMR-SCOPE	NMR spectra calculation using operators [99]
PCA	principal component analysis
PCh	phosphocholine
PET	Positron Emission Tomography
PLS	partial least squares
PM	performance measure

PR	pattern recognition
PSR	P-spline signal regression
QUALITY	quantification improvement by converting lineshapes to the Lorentzian type [58]
QUECC	QU from QUALITY and ECC [13]
QUEST	quantitation based on quantum estimation [225]
RBF	radial basis function
RF	random forest
RRMSE	relative root mean squared error
SB-HOYWSVD	sub-band high-order Yule-Walker singular value decomposition [283]
SE	short echo time
SELF-MODE	selective-frequency MODE [239]
SELF-SVD	selective-frequency singular value decomposition [267]
SNR	signal-to-noise ratio
SVD	singular value decomposition
SVM	support vector machines
Tau	taurine
tCho	total choline
tCr	total creatine
TDFD	time-domain frequency-domain
TLS	total least squares
VARPRO	variable projection [292]
VOI	volume of interest

Contents

1 Introduction **1**

1.1 Basics of Magnetic Resonance 1
1.1.1 Magnetic Resonance Spectroscopy 1
1.1.2 Magnetic Resonance Imaging 4
1.1.3 Magnetic Resonance Spectroscopic Imaging 6
1.1.4 High Resolution Magic Angle Spinning Data 7
1.2 Magnetic Resonance Spectroscopy for brain tumor diagnosis 8
1.2.1 About brain tumors 9
1.2.2 Metabolites characterizing brain tumors 15
1.3 Goal and outline of the thesis 23
1.4 Conclusions 24

2 From FIDs to classification results **25**

2.1 The model for short echo time MR data 25
2.2 Preprocessing methods 26
2.2.1 Typical preprocessing steps 27
2.2.2 Water filtering techniques 29
2.3 Feature extraction methods 34
2.3.1 Extraction of features with physical meaning 34
2.3.2 Extraction of features based on mathematical criteria . . . 40
2.4 Classification methods 43
2.4.1 Linear Discriminant Analysis 43
2.4.2 (Least Squares) Support Vector Machines 43
2.4.3 Performance measure 46
2.5 Conclusion 49

3 Review of quantification methods in ^{1}H MRS **51**

3.1 Introduction 51
3.2 Absolute or relative concentrations 52
3.3 Effects of acquisition conditions and MRS spectra quality assessment . 53
3.3.1 Effects of relaxation times on metabolite signals 53
3.3.2 Effects of physiological motion 54
3.3.3 Effects of shape and location of the volume of interest . . 54
3.3.4 MRS spectra quality assessment 54

3.3.5 Quantification accuracy . . . 55
3.4 Time-domain quantification methods . . . 55
3.4.1 Interactive methods . . . 55
3.4.2 Black -box methods . . . 57
3.5 Frequency-domain quantification methods . . . 59
3.5.1 Non-iterative methods . . . 59
3.5.2 Iterative methods . . . 59
3.5.3 Other techniques . . . 60
3.6 Preprocessing techniques . . . 61
3.6.1 Correction for lineshape or model imperfections . . . 61
3.6.2 Water peak removal . . . 62
3.6.3 The effect of errors in the initial FID data points and macromolecular signals . . . 65
3.7 Discussion . . . 67
3.8 Conclusions . . . 70

4 Review of pattern recognition methods in MRS 71
4.1 Introduction . . . 71
4.2 MRS data classification . . . 72
4.2.1 Feature reduction . . . 73
4.2.2 Classification methods . . . 74
4.3 Tissue segmentation and nosologic images based on MRSI . . . 76
4.4 Conclusion . . . 76

5 The quantification method AQSES 79
5.1 Introduction . . . 79
5.2 Simulated examples and *in vivo* quantification . . . 80
5.3 Results . . . 83
5.3.1 Performances of AQSES . . . 83
5.3.2 AQSES versus QUEST . . . 87
5.4 Discussion . . . 88
5.5 Conclusion . . . 90

6 Solvent suppression methods: MP-FIR vs HLSVD-PRO 91
6.1 Introduction . . . 91
6.2 MP-FIR and HLSVD-PRO in quantification methods . . . 93
6.2.1 FIR filter inside AQSES . . . 93
6.2.2 FIR filter outside AQSES . . . 94
6.2.3 HLSVD-PRO in quantification methods . . . 95
6.3 Materials and Methods . . . 97
6.3.1 Database and simulated signals . . . 97
6.3.2 Methodology . . . 99
6.4 Results . . . 100
6.5 Discussion . . . 103
6.6 Conclusions . . . 107

7 A new FIR filter technique for solvent suppression MRS signals 109
7.1 Introduction . . . 109
7.2 The proposed filter . . . 110
7.3 Experimental results using simulations and real-life examples . . . 114
7.3.1 Material . . . 114
7.3.2 Description of the experiments . . . 118
7.3.3 Results . . . 121
7.3.4 Discussion . . . 123
7.4 Conclusions . . . 127

8 Effect of feature extraction on short echo time MR data classification 129
8.1 Introduction . . . 129
8.2 Methods . . . 131
8.2.1 Data . . . 132
8.2.2 Peak integration . . . 135
8.2.3 Peak regions - binning . . . 135
8.2.4 Bagging with Fisher criterion, Kruskal-Wallis test and Relief-F . . . 135
8.2.5 ICA . . . 137
8.2.6 Linear PCA . . . 137
8.2.7 Stepwise selection . . . 137
8.2.8 AQSES . . . 137
8.2.9 QUEST . . . 137
8.2.10 Experimental setup and evaluation . . . 137
8.3 Results . . . 138
8.4 Discussion . . . 139
8.5 Conclusions . . . 143

9 Quantification and classification of HR-MAS signals 145
9.1 Introduction . . . 145
9.2 Materials and methods . . . 146
9.3 Results . . . 147
9.4 Discussion . . . 148

10 Conclusions and open problems 151
10.1 General conclusions of the thesis . . . 151
10.2 Future work and open problems . . . 153

A AQSES GUI 157

B Least squares cost function in MPFIR0, Eq. (7.8) 161

C SPID: Simulation Package based on *In vitro* Databases 163

Bibliography 167

Chapter 1
Introduction

The purpose of this chapter is to introduce the main aspects of Magnetic Resonance (MR) and its relevance for brain tumor diagnosis is illustrated. Section 1.1 explains the principles of MR and how the technique is used in MR Spectroscopy (MRS) and Magnetic Resonance Imaging (MRI). The specificities of High Resolution Magic Angle Spinning (HR-MAS) are also outlined in this section. Section 1.2 is composed of two parts. The first one provides the medical background about brain tumors. The second explains the links or correlations existing between brain tumors and MRS features. The goal of the thesis is formulated at the end of this chapter as well as the description of the different chapters.

1.1 Basics of Magnetic Resonance

Magnetic Resonance (MR) or Nuclear Magnetic Resonance (NMR) has been widely used in hospital since the 80's. MR consists of two main fields: Magnetic Resonance Imaging (MRI) and Magnetic Resonance Spectroscopy (MRS). In this section, the main principles of these techniques are reviewed, and the particularities of high resolution magic angle spinning (HR-MAS) data are outlined.

1.1.1 Magnetic Resonance Spectroscopy

MRS is based on two main observations:

- nuclei with a magnetic spin can be excited by an external electromagnetic field, and
- nuclei of the same isotope that are not chemically equivalent are separable in frequency due to the effect of shielding.

Different atomic nuclei, like ^{1}H (proton)[1], ^{13}C (carbon), ^{19}F (Fluor) and ^{31}P (phosphorus), can be used in MR as long as they have an inherent angular momentum or spin, and thereby behave like little magnets. In its simplest form, an MRS experiment consists of immersing the sample into a static external field B_0 to align the angular momentum of

[1] Proton MRS(I) will be used all along the thesis.

the nuclei, applying a radio frequency (RF) pulse with a bandwidth chosen to excite all the nuclei within the required frequency range and acquiring the emitted signal as the response. The amount of energy emitted by the nuclei, and thus the signal intensity, depends on the population difference between the two energy states. The higher the energy, the higher the number of nuclei in a less stable state. In thermal equilibrium, the relative amounts $n-$ and $n+$ of nuclei in the highest (spin $-\frac{1}{2}$) and the lowest (spin $+\frac{1}{2}$) energy states are given by

$$n-/n+ = e^{-\Delta E/kT}, \tag{1.1}$$

where k is the Boltzman constant (1.381×10^{-23} J/K), T the temperature in Kelvin and ΔE the energy difference between both states is defined by

$$\Delta E = \gamma \hbar B_0,\ \hbar = h/(2\pi), \tag{1.2}$$

where γ is the gyromagnetic ratio, characteristic of the isotope (*e.g.*, γ=42.58, 10.71, 40.08 and 17.25 MHz/T, for ^{1}H, ^{13}C, ^{19}F and ^{31}P, respectively) and h the Planck constant ($6.626 \times 10 - 34$ J s).

The ratio $n-/n+$ is very close to unity in normal circumstances, resulting in a low absorption of energy. This explains the inherently low signal-to-noise ratio (SNR) of the signal emitted when the spin system returns to equilibrium after excitation. The emitted signal is called a free induction decay (FID) signal and corresponds to an exponentially decaying sinusoid in the time domain.

The intensity of the signal is proportional to the number of nuclei that contribute to it. In order to increase the SNR, several data acquisitions are performed consecutively and the final signal is the average of all measured signals. As shown in Eq. (1.1) and Eq. (1.2), a higher intensity is obtained for higher B_0 and smaller temperature. For *in vivo* experiments, the temperature is fixed (body temperature) and one can only vary B_0 within a secure range to prevent tissue heating.

The RF pulse is meant to excite all the nuclei of an isotope, for example all protons (^{1}H). This would not be useful if the effect of shielding was not present. When an atom is placed in a magnetic field, its electrons circulate about the direction of the applied magnetic field. This circulation causes a small magnetic field at the nucleus which opposes the externally applied field. The amount of shielding, experienced by a nucleus, determines the effective magnetic field,

$$B_{eff} = B_0(1 - \sigma') \tag{1.3}$$

where σ' is the shielding constant, a dimensionless unit that depends on the electrical environment of a nucleus. The electron density around each nucleus in a molecule varies according to the types of nuclei and bonds in the molecule. The opposing field and therefore the effective field at each nucleus will vary. This is also called the chemical shift phenomenon. This explains for example why metabolites such as lactate (Lac) and choline (Cho) are distinguishable in the MR spectrum (signal in the frequency domain).

Nuclei which are close to each other exert an influence on each other's effective magnetic field. This effect shows up in the NMR spectrum when the nuclei are nonequivalent, i.e., experiencing different environment (= having different chemical shifts). If the distance between nonequivalent nuclei is less than or equal to three bond lengths, this effect is observable. This effect is called spin-spin coupling or J-coupling. This explains for example

why the contribution of Lac at +/- 1.33 ppm exhibits a doublet (two close peaks of same intensity) in the MR spectrum.

In MRS, the frequency axis is given in part per million (ppm) in order to be independent from the spectrometer frequency in the sense that, if a metabolite resonates at a certain ppm-value for a spectrometer frequency of 63.8 MHz, it will resonate at the same ppm-value for a spectrometer frequency of 500 MHz. The ppm-value of a resonance is defined by

$$ppm_M = \frac{f_{Hz}10^6}{f_S} + ppm_{Ref} \tag{1.4}$$

where f_{Hz} is the resonance frequency in Hz, f_S the spectrometer frequency in Hz and ppm_{Ref} the ppm-value of the reference resonance (4.7 ppm is often chosen in proton spectroscopy).

Important parameters in MRS

In addition to the external field B_0 and the temperature of the sample, other important parameters influences the acquired FID signal.

The timing of the different pulses is determined by the echo time (TE) and the repetition time (TR). The echo time represents the time in milliseconds between the application of the 90°pulse and the peak of the echo signal in spin echo and inversion recovery pulse sequences. The repetition time is the amount of time that exists between successive pulse sequences applied to the same slice. Short TEs (*e.g.*, 30 ms) provide more metabolic information than long TEs (*e.g.*,135 ms) since less signal intensity of the metabolites will have decayed. On the other hand, long TEs allow an easier extraction of the metabolic information of the slowly decaying components, like Cho, N-acetyl-aspartate (NAA) or creatine (Cr) in proton spectroscopy. To improve the SNR, repeated measurements are consecutively performed. The choice of TR results from a compromise between the SNR and the total measurement time.

Other important parameters are the relaxation times T_1 and T_2. These parameters are not chosen by the user of the scanner like TE or TR, but are important since they have a direct impact on the absolute concentration estimates of the metabolites. T_1, also called the spin-lattice relaxation time, is the time to reduce the difference between the longitudinal magnetization after the RF pulse (see Fig. 1.1) and its equilibrium value by a factor of e^1,

$$M_z(t) = M_0(1 - e^{\frac{-t}{T_1}}) \tag{1.5}$$

where $M_z(t)$ is the longitudinal net magnetization at time t, M_0 is the initial net magnetization, which is aligned with the external field B_0.

The net magnetization starts to dephase because each of the spin packets making it up is experiencing a slightly different magnetic field and rotates at its own Larmor frequency. The longer the elapsed time, the greater the phase difference. The time constant which describes the return to equilibrium of the transverse magnetization, M_{xy}, is called the spin-spin relaxation time, T_2 and is defined such that

$$M_{xy}(t) = M_{xy_0}e^{\frac{-t}{T_2}} \tag{1.6}$$

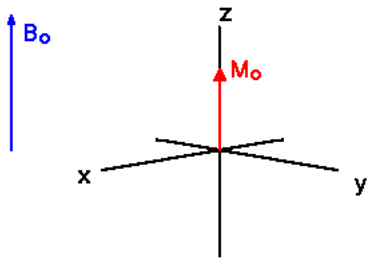


Figure 1.1. *At equilibrium, the net magnetization M_0 is aligned with the external field B_0. The RF pulse tilts the net magnetization into the xy-plane, the radio frequency field B_1 is applied perpendicularly to B_0. The extra energy acquired by the nuclei is then emitted and the net magnetization turns back along the z-axis.*

where M_{xy_0} is the net transversal magnetization at time 0. T_2 is always less than or equal to T_1. The net magnetization in the xy-plane goes to zero and then the longitudinal magnetization grows until we have the net magnetization along the z-axis. Note that the coils which acquire the signal are located along the x- and y-axis. This explains why T_2 is more important than T_1 in MRS. T_1 and T_2 depend on the metabolites. Typical T_1 relaxation times at 1.5 T are 1430 $\pm$ 165 ms for NAA, 1330 $\pm$ 199 ms for choline, 1460 $\pm$ 270 ms for total creatine and 1140 $\pm$ 308 ms for myo-inositol [146, 79, 235]. Typical T_2 relaxation times at 1.5 T are 422 $\pm$ 48 ms for NAA, 356 $\pm$ 35 ms for choline, 214 $\pm$ 23 ms for total creatine and 200 $\pm$ 20 ms for myo-inositol [146, 25, 235]. Macromolecules often have $T_2 < 50$ ms, explaining why the macromolecules are mostly absent in long echo time signals ($TE = 135$ ms $\gg T_2 = 50$ ms). In an idealized nuclear magnetic resonance experiment, the FID decays approximately exponentially with a time constant T_2, but, in practice, small differences in the static magnetic field at different spatial locations, also called inhomogeneities, cause the Larmor frequency to vary across the body creating destructive interference which shortens the FID. The time constant for the observed decay of the FID is called T_2* ("T 2 star") relaxation time, and is always shorter than T_2. T_2 values of the metabolites are known to vary according to the location of the analyzed voxel [87, 10, 205] and according to the pathology [129]. The parameters TE, TR, T_1 and T_2 are further discussed in Chapter 2.

1.1.2 Magnetic Resonance Imaging

Magnetic resonance imaging (MRI) is primarily a medical imaging technique most commonly used in Radiology to visualize the structure and function of the body. It allows to visualize the spatial distribution of protons, providing detailed images of the body in any plane. The principles are similar to the ones of MRS (see Section 1.1.1). However, gradients in the magnetic field are necessary to localize in the space the contribution of the different metabolites. The idea is to generate a different strength of the magnetic field for each point inside the magnet.

MRI provides much greater contrast between the different soft tissues of the body than does computed tomography (CT), making it especially useful in neurological (brain),

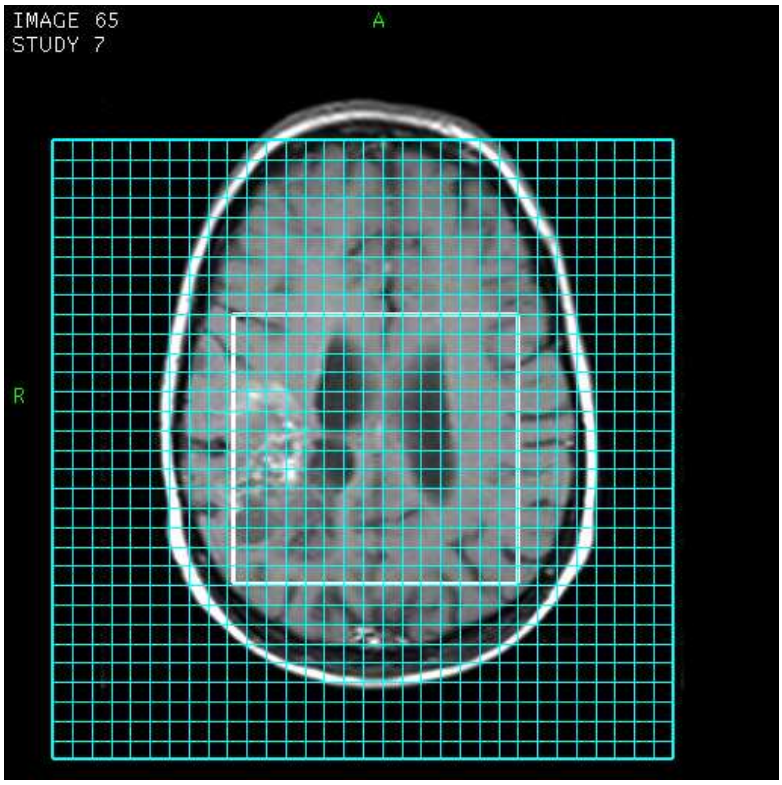


Figure 1.2. *Illustration of MRI data: T1 weighted (TE/TR=15/644ms) acquired with a 1.5 T Siemens Vision using a CP-head coil. The data were acquired using a 2D STEAM pulse sequence with the STEAM box positioned in a transversal plane through the brain. Patient with astrocytoma grade III.*

musculoskeletal, cardiovascular, and oncological (cancer) imaging. Contrast agents may be injected intravenously to enhance the appearance of blood vessels, tumors or inflammation. An illustration of MRI image is given in Fig. 1.2.

Image contrast is created by differences in the strength of the NMR signal at different locations within the sample. This depends upon the relative density of excited nuclei (usually protons) and on differences in relaxation times (T_1, T_2 and T_2*) of those nuclei after excitation. Contrast in most MR images is actually a mixture of all these effects, but careful design of the imaging sequence, including parameters, allows one contrast mechanism to be emphasized while the others are minimized. The ability to choose different contrast mechanisms gives MRI tremendous flexibility. In the brain, T1-weighting causes the nerve connections of white matter to appear white, and the congregations of neurons of gray matter to appear gray, while cerebrospinal fluid (CSF) appears dark. The contrast of white matter, gray matter and cerebrospinal fluid is reversed using T_2 or T_2* imaging, whereas proton-weighted imaging provides little contrast in healthy subjects. Other more modern MRI methods like diffusion-weighted imaging and functional MRI can also be used, but

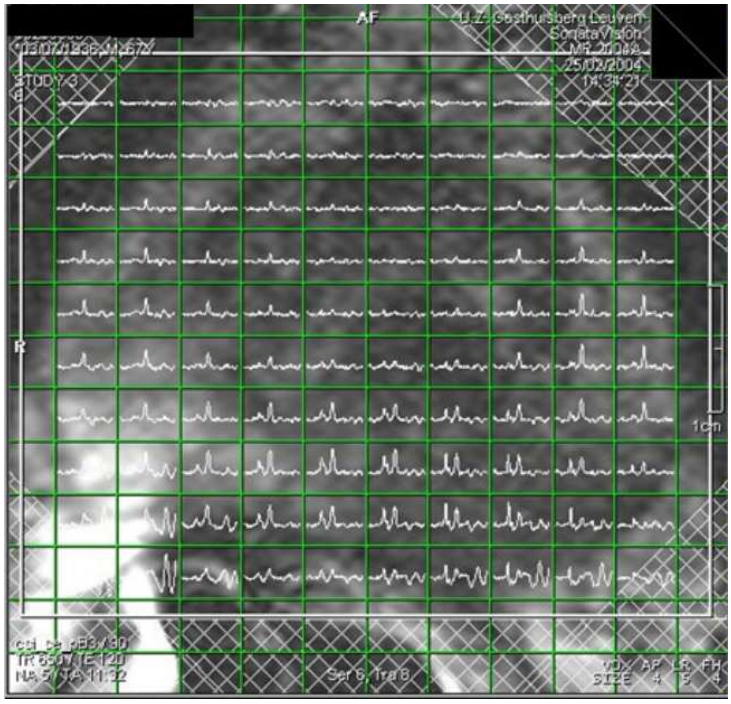


Figure 1.3. *Screenshot from the 1.5 T Siemens scanner for in vivo prostate MRSI data acquired at 63.6 MHz, using a 3D PRESS CSI sequence (TR = 600 ms, TE = 100 ms). The image is provided by Paul Van Hecke, Biomedical NMR Unit, Gasthuisberg, Katholieke Universiteit Leuven, Leuven, Belgium.*

are beyond the scope of this thesis.

1.1.3 Magnetic Resonance Spectroscopic Imaging

Magnetic resonance spectroscopic imaging (MRSI), also called Chemical Shift Imaging (CSI) or multi voxel spectroscopy, combines both spectroscopic and imaging methods to produce spatially localized spectra from within the sample or patient. MRSI acquires simultaneously signals from a two-dimensional grid of volume elements (voxels), while MRS acquires one signal from one voxel. The resolution is lower in MRSI (limited by the available SNR) than in MRS, but MRSI provides extra information for identifying the heterogeneity and the borders of a tumorous region. The spatial resolution is also lower in MRSI than in MRI, but MRSI provides spectroscopic information that MRI does not. An example of MRSI data is illustrated in Fig. 1.3.

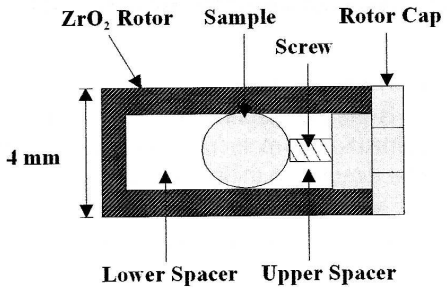


Figure 1.4. *Schematic of the rotor used for HR-MAS experiments.*

1.1.4 High Resolution Magic Angle Spinning Data

High Resolution Magic Angle Spinning (HR-MAS) is a technique used to perform solid-state Nuclear Magnetic Resonance and which improves considerably the resolution of the classical Magnetic Resonance Spectroscopy (MRS) acquisition methods. However, it requires the use of a biopsy and is therefore invasive. The biopsy is placed in a small rotor filled in with a solvent, *e.g.*, D_2O (see Fig. 1.4). The rotor is spinned at a few kHz during the acquisition.

The principles in Section 1.1.1 are still valid when performing HR-MAS experiments. However, the linewidth in HR-MAS data is much smaller, yielding well-resolved spectra with many peaks. In MRS, several factors can contribute to the linewidth: B_0 inhomogeneities (imperfect shimming, magnetic susceptibility), the relaxation times (see Section 1.1.1), dipolar interaction, chemical shift anisotropy (CSA), quadrupolar interaction, chemical exchange. The last two effects are less important for the linewidth and will not be discussed here. In solution, when a sample is placed in a homogeneous magnetic field H_0, it acquires a magnetization M given by

$$M = \chi H_0 \tag{1.7}$$

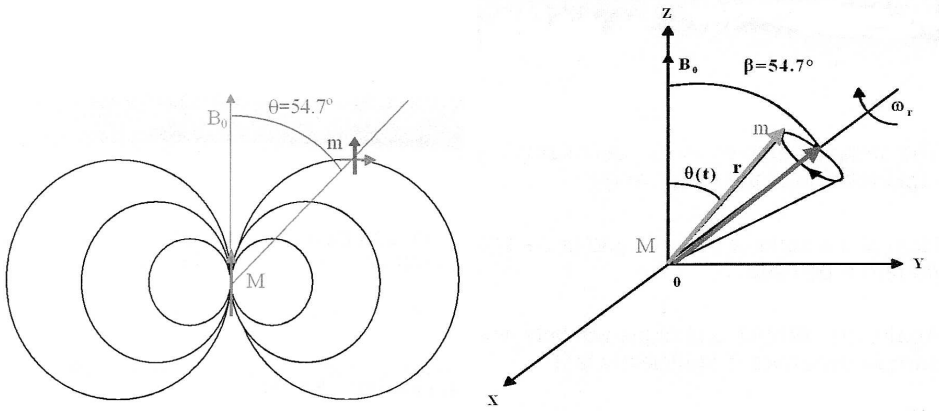
where χ is the magnetic susceptibility which may not be homogeneous across the sample. Large differences of magnetic susceptibilities can not be corrected using the shim system of the spectrometer. The magnetic field B_0 felt within the sample is therefore modified by the sample magnetization:

$$B_0' = \mu_0 H_0 + \mu_0 M = \mu_0(1+\chi)H_0 \tag{1.8}$$

where μ_0 is the permeability of free space. The line broadening due to magnetic susceptibility effects can be treated as a dipolar interaction between a sphere of magnetization M and the magnetic moment m of the spins in its surrounding (see Fig. 1.5(a)). This dipolar interaction can be represented by (see Fig. 1.5(b)):

$$E(r) = \frac{\mu_0}{4\pi}\frac{Mm}{r^3}(1 - 3\cos^2\theta). \tag{1.9}$$

where r is the distance between the anchor point of M and the one of the dipole. At the magic angle $\theta = 54.7°$, the dipolar field is cancelled out, the interaction vanishes. Conse-



(a) *Magnetization of a volume element M and a spin m.*

(b) *The rotor is spinned at a certain frequency ω_r such that all spins of the sample will be on average at the magic angle with respect to the external field B_0, the rotation axis of the rotor being itself at the magic angle.*

Figure 1.5. *Illustration of the magic angle: the dipolar interaction between a volume element of magnetization M and a spin of magnetization m is cancelled out at the magic angle $\theta = 54.7°$.*

quently, the effect of B_0 inhomogeneities disappear. An interaction oriented at 54.7°with respect to B_0 will show no linebroadening. However, a real sample usually contains a distribution of θ and a slight linebroadening remains present. Spinning the sample allows that the vector joining M and m behaves on average as if it were along the magic angle to remove the effect of magnetic susceptibility inhomogeneities. The chemical shift anisotropy is due to the asymmetry of the electron density around the kernel and is also proportional to $(1 - 3\cos^2\theta)$. Consequently, the residual linewidth is mainly determined by the quality of the shim system and the dynamics of the system (relaxation).

HR-MAS data are comparable to *in vivo* MRS data since they are supposed to measure the same thing [15]. For example, Tzika *et al.* [287] showed some high linear correlation between NMR *in vivo* and *ex vivo* for PCho/tCr, (PCho+Cho)/tCr with Cho/tCr *in vivo*, and the same for PCho/NAA, (PCho+Cho)/NAA (see Section 1.2.2 for the notations). An example of HR-MAS spectrum is illustrated in Fig. 1.6.

1.2 Magnetic Resonance Spectroscopy for brain tumor diagnosis

This thesis mainly focuses on the use of MRS in brain tumor diagnosis. This section aims to show the potential of MRS in brain diagnosis by correlating biological MRS features and brain tumors. First, an overview of brain tumors is given (statistics, diagnosis, treatment, types of tumors). Then, links between brain tumors and MRS features are described.

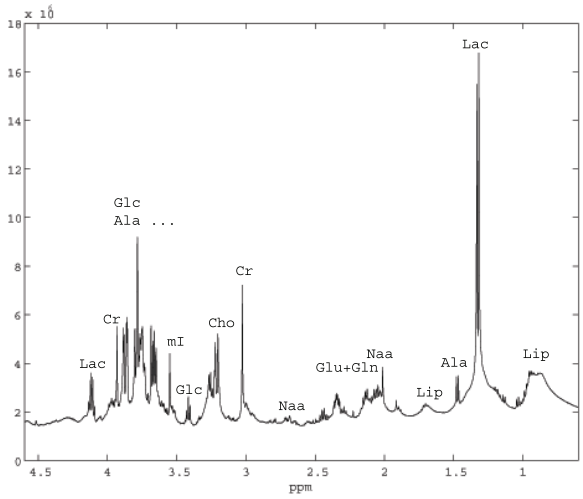


Figure 1.6. *Example of 1D PRESAT (pulse-and-acquire) HR-MAS data acquired at 11.7 T (500 MHz for ^1H) at 0-4°C and 4,000 Hz spinnning rate using BRUKER Analytik GmbH spectrometers. Patient with metastasis.*

1.2.1 About brain tumors

A brain tumor is any intracranial tumor created by abnormal and uncontrolled cell division, normally either in the brain itself (neurons, glial cells (astrocytes, oligodendrocytes, ependymal cells), lymphatic tissue, blood vessels), in the cranial nerves (myelin-producing Schwann cells), in the brain envelopes (meninges), skull, pituitary and pineal gland, or spread from cancers primarily located in other organs (metastatic tumors)[2].

Some statistics

Primary (true) brain tumors are commonly located in the posterior cranial fossa in children and in the anterior two-thirds of the cerebral hemispheres in adults, although they can affect any part of the brain. In the United States, in 2005, it was estimated by the Central Brain Tumor Registry of the United States (CBTRUS) that there were 43,800 new cases of brain tumors (Primary Brain Tumors in the United States, Statistical Report, 2005–2006) [101], which accounted for 1.4 percent of all cancers, 2.4 percent of all cancer deaths, and 20–25 percent of pediatric cancers (American Cancer Society, http://www.cancer.org) [39]. It is estimated that there are 13,000 deaths/year in United States as a result of brain tumors [101]. In total, each year, more than 200,000 people in the United States are diagnosed with a primary or metastatic brain tumor. CBTRUS has calculated a preliminary worldwide estimate of 186,835 newly diagnosed primary nonmalignant brain and central nervous system tumors per annum for 2002 (males: 80,769; females: 106,066). The preliminary worldwide incidence rate of primary nonmalignant brain and central nervous system tumors is estimated to be 2.9 per 100,000 (males: 2.5 per 100,000; females: 3.3 per

[2]Definition from http://en.wikipedia.org/wiki/Brain_tumor, accessed on August 1, 2008.

100,000). CBTRUS also reports that males-females have a 0.67%-0.53% lifetime risk of being diagnosed with a primary malignant brain/central nervous system tumor and 0.48%-0.39% chance of dying from a brain/central nervous system tumor (excluding lymphomas, leukemias, tumors of pituitary and pineal glands, and olfactory tumors of the nasal cavity). Additional statistics can be found from the Statistics from Accelerate Brain Cancer Cure (ABC^2) (http://www.abc2.org), the American Cancer Society (http://www.cancer.org/) or the Brain Tumor Society and National Brain Tumor Foundation (http://www.tbts.org/).

A distribution of all primary brain and CNS Tumors by histology is shown in Fig. 1.7. The following information was gathered by the CBTRUS (http://www.cbtrus.org/), from 2000 to 2004 with a subject pool (n) of 73,583. A distribution of the most common primary tumors, the gliomas, is given in Fig. 1.7(b) and a distribution of their location in the brain is given in Fig. 1.7(c).

According to the Brain Tumor Society and National Brain Tumor Foundation, there are currently no known causes of brain tumors, however, epidemiological studies are ongoing. Complete and accurate data on all primary brain tumors is needed for investigations, possibly leading to improved diagnosis and treatment.

Diagnosis of brain tumors

Diagnosis of brain cancer currently mainly depends on histological examination of a brain biopsy. However, extracting biopsy has significant risks with an estimated morbidity of 2.4–3.5% [81, 107] and a death rate of 0.2–0.8% [81, 83]. Normally, the biopsy will be available since most patients will undergo surgery, but in some cases surgery will not be considered, for example, in very ederly and infirm patients with obviously malignant lesions, or patients with tumors growing very slowly. Moreover, surgery will be avoided for certain pathologies such as lymphomas and brain abcesses [279] and non-invasive diagnosis are certainly useful in those cases. ^{1}H MRS is a very promising non-invasive method for brain tumor diagnosis, which can be used as a complement to MRI. It becomes commonly used in clinical practice but still requires a high expertise to be correctly dealt with. Consequently, the so-called computer-based decision support systems (DSS), aimed to provide automatic decision support for brain tumor diagnosis, would particularly be helpful. The diagnosis should not be limited to the recognition of the tumor but also of its grade since the prognosis can be completely different. For example, 65% of patients with low-grade astrocytoma who have combined tumor therapies can expect a survival time of about 5 years, while the latter is limited to 17 months for patients with malignant astrocytoma and similar treatment [100].

A. Brain Tumor Symptoms

The principal symptoms of brain cancer are headaches, seizures, nausea and vomiting. The Brain Tumor Society and National Brain Tumor Foundation lists the following tumor symptoms (http://www.tbts.org/):

- A new seizure in an adult.
- Gradual loss of movement or sensation in an arm or leg.
- Unsteadiness or imbalance, especially if it is associated with headache.

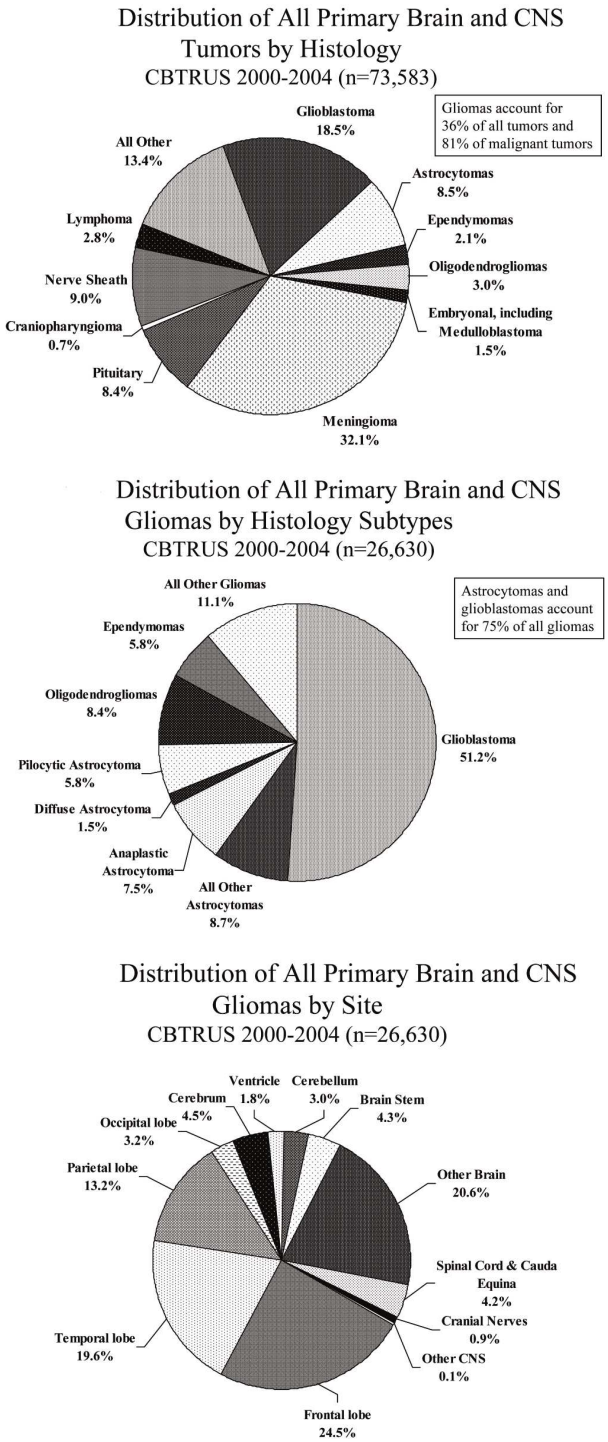


Figure 1.7. *Plots taken from the 2007-2008 report of CBTRUS on Primary Brain Tumors in the United States, Statistical report. The data were collected between 2000 and 2004.*

- Loss of vision in one or both eyes, especially if it is more peripheral vision loss.
- An eating disorder as a child.
- Double vision, especially if it is associated with headache.
- Hearing loss with or without dizziness.
- Speech difficulty of gradual onset.

B. Diagnostic tools

When a brain tumor is suspected, the first test a doctor gives is a traditional neurological examination. This exam is divided into several components each focusing on a different part of the nervous system. It evaluates eye movement, eye reflexes, and pupillary reactions, reflexes, hearing, sensation, movement, balance, and coordination. The neurological exam also includes a mental status exam, a series of questions designed to test cognitive ability, memory, and abstract thinking. In addition, the physician often orders additional specialized tests to come to a diagnosis. These techniques (see below) have dramatically improved the diagnosis of brain tumors in recent years and have replaced older tests, such as conventional X-rays, which do not show tumors located inside the skull or spine, and cerebral angiography. Note that many low-grade (benign) tumors can remain asymptomatic (symptom-free) for years and they may accidentally be discovered by imaging exams for unrelated reasons (such as a minor trauma).

CT Scan (Computed Tomography Imaging)
Computed Tomography, often called a "CT" or "CAT" scan, uses special X-ray equipment, which obtains images from different angles, and a computer that assembles them to create a detailed cross-sectional picture of the body tissues. These pictures are called "slices". These slices provide more detailed information on brain tumors than conventional X-ray films. In some cases, a special dye is injected into a vein before the scan. The dye or contrast agent helps to show differences in the tissues of the brain.

MRI Scan (Magnetic Resonance Imaging)
Unlike conventional X-rays and CT scans, MRI does not use radiation. Instead, radio waves and a strong magnetic field are used to produce clear and detailed pictures of internal organs. In the setting of a strong magnetic field, the protons become excited and then relaxed, emitting radio signals, which are then computer-processed to form an image. Since protons are most abundant in the hydrogen atoms of water and lipids, an MRI image shows differences in the water content or lipid content in various body tissues. For example, different types of tissue within the same organ, such as the white and gray matter of the brain, can be distinguished. Small tumors, tumors next to bone, brain stem tumors, and low grade or metastatic tumors are often best imaged by MRI.

PET Scan (Positron Emission Tomography)
A PET scan provides a picture of brain activity, rather than structure, by measuring levels of injected glucose (sugar) labeled with a radioactive tracer. After a low-dose of radioactive

glucose is injected, a scanner rotates around the patient's head and detects the amount of radioactivity in different parts of the brain. Different degrees of brightness and color represent different types of tissue or organ function. For example, cancerous tissue uses more glucose than healthy tissue, and consequently, appears brighter when scanned. A PET scan is not regularly used for diagnosing tumors, but is used with other scans to determine the grade of the tumor or distinguish between necrosis and scar tissue.

Angiogram
An angiogram, or arteriogram, is a series of X-rays taken after a special dye is injected into an artery (usually in the area where the abdomen joins the top of the leg). The dye, which flows through the blood vessels of the brain, can be seen on the X-rays. These X-rays can show the tumor and blood vessels that lead to it.

Myelogram
A myelogram is an X-ray of the spine. A special dye is injected into the cerebrospinal fluid in the spine, and the patient is tilted to allow the dye to mix with the fluid. This test may be done when the doctor suspects a tumor in the spinal cord.

Biopsy
A biopsy is an invasive medical test involving the removal of cells or tissues for examination. A hole of about 1cm-diameter is carried out in the skull and a sample is taken out of the tumor with a needle passing through the hole. The type and grade of the tumor are obtained by hispathology, that is the microscopic examination of tissue.

In spite of the quality of the above mentioned noninvasive radiological tools, a biopsy is often required before a treatment plan can be developed. Biopsy has a significant risk of mortality and does not always lead to the correct diagnosis, since it is difficult to collect the tissue sample from the exact location of the tumor. The tissue sample is often heterogeneous, which complicates the identification of the tumor type by the pathologist. Moreover, a biopsy only provides local information from the tumor, while tumors are known to be heterogeneous and infiltrative. Therefore it is crucial to develop new noninvasive radiological tools that can aid in the diagnosis of tumor type and grade.

Treatment of brain tumors

At present, the standard treatments for brain tumors include surgery, radiation therapy, and chemotherapy. These may be used either individually or in combination. Factors such as age, performance status, and tumor grades have been linked with differences in survival and are used in determining the most appropriate forms of therapy, the location of the tumor and its spatial extent are critical in deciding between alternative strategies [199].

Surgery
Surgery is the usual treatment for most brain tumors. To remove a brain tumor, a neurosurgeon makes an opening in the skull. This operation is called a craniotomy. Whenever possible, the surgeon attempts to remove the entire tumor. If the tumor cannot be completely removed without damaging vital brain tissue, the doctor may remove as much of

the tumor as possible. Partial removal helps to relieve symptoms by reducing pressure on the brain and reduces the amount of tumor to be treated by radiation therapy or chemotherapy. Some tumors cannot be removed. In such cases, only a biopsy is carried out for diagnosis.

Radiotherapy

Radiation therapy, also called radiotherapy, is the use of high-powered rays to damage cancer cells and stop them from growing. It is often used to destroy tumor tissue that cannot be removed with surgery or to kill cancer cells that may remain after surgery. Radiation therapy also is used when surgery is not possible.

Radiation therapy may be given in two ways: external or internal radiation. External radiation comes from a large machine. Generally, external radiation treatments are given five days a week for several weeks. The treatment schedule depends on the type and size of the tumor and the age. Giving the total dose of radiation over an extended period helps to protect healthy tissue in the area of the tumor. External radiation may be directed just to the tumor, the surrounding tissue or the entire brain. When the whole brain is treated, the patient often receives an extra dose of radiation to the area of the tumor. This boost can come from external radiation or from an implant. Radiation can also come from radioactive material placed directly in the tumor, or implant radiation therapy. Depending on the material used, the implant may be left in the brain for a short time or permanently. Implants lose a little radioactivity each day. The patient stays in the hospital for several days while the radiation is most active.

The Gamma Knife, or stereotactic radiosurgery, is another way to treat brain tumors. The Gamma Knife isn't actually a knife, but a radiation therapy technique that delivers a single, finely focused, high dose of radiation precisely to its target. Treatment is given in just one session. High-energy rays are aimed at the tumor from many angles. In this way, a high dose of radiation reaches the tumor without damaging other brain tissue.

Chemotherapy

Chemotherapy is the use of drugs to kill cancer cells. The doctor may use just one drug or a combination, usually giving the drugs orally or by injection into a blood vessel or muscle. Intrathecal chemotherapy involves injecting the drugs into the cerebrospinal fluid. Advances in chemotherapy include direct placement into the tumor cavity using a new technique called convection enhanced delivery.

Chemotherapy is usually given in cycles. A treatment period is followed by a recovery period, then another treatment period and so on. Patients often don't need to stay in the hospital for treatment and most drugs can be given in the doctor's office or clinic. However, depending on the drugs used, the way they are given and the patient's general health, a short hospital stay may be necessary.

Brain tumors

A detailed histological classification is done based on the World Health Organization (WHO) classification on nervous system tumors [161]. We give below a brief description of the main brain tumors.

Meningioma
Meningioma is a type of tumor, generally benign, that is formed in the meninges (thin layers of tissue that cover and protect the brain and spinal cord). Meningiomas usually occur in adults and most of them grow slowly and can do it for years without producing any symptoms. When they do produce symptoms, it is due to irritation of compressed brain tissue (seizures), damage to brain tissue (neurological deficit such as paralysis) or elevation of intracranial pressure from the mass of the tumor itself.

Metastasis
The most common tumor type is secondary or metastatic brain tumors, which is cancer that spreads from other parts of the body (such as the lung, kidney or liver) to the brain. These individual tumor cells usually migrate from their primary site to the brain via the blood stream. Upon reaching the capillary blood vessels of the brain, the tumor cells take root and they continue growing as another tumor. They can be as malignant as the cancerous primary tumor from which they came, sometimes multiple metastatic tumors are formed and can be found in different areas of the brain.

Glioma
Gliomas represent about half of all primary brain tumors and are formed in glial cells. Typing of brain tumors is based on the supposed cell of origin. For example, astrocytomas are derived from astrocytes, oligodendrogliomas derived from oligodendroglial cells and mixed gliomas (or oligoastrocytomas) are derived from both astrocytes and oligodendroglial elements. These cells are the supporting cells of our nervous system. Patients with benign gliomas may survive for many years [124, 209], while survival in most cases of glioblastoma multiforme is limited to a few months after diagnosis if treatment is ignored. In general, all glial tumors, including oligodendrogliomas, will become malignant.

1.2.2 Metabolites characterizing brain tumors

MRS spectra are different between healthy brain tissue and tumor tissue and consistent patterns have been found in a variety of tumor types [117]. The metabolite information obtained by ^{1}H-MRS has proven to be important in the investigation of brain tumors [217, 200] and can provide a noninvasive tool for determining histology [217, 218]. There is also evidence that MRS can facilitate selection of the optimal biopsy site [27, 218], detect tumor that is not discernable on MRI [27]. Several metabolite concentrations have been found to be lowered or increased in tumors compared with normal tissue.

From metabolites to tumors

Examples of *in vitro* metabolite spectra are given in Fig. 1.8.

N-acetyl-aspartate (NAA), singlet at 2.03 ppm
NAA is a marker of normal neuronal function, and its reduction in tumors has been attributed to a low density of neuronal cells within tumor tissue [199], the neuronal cells being replaced by tumor cells [88]. Previous *in vitro* studies demonstrated that NAA exists

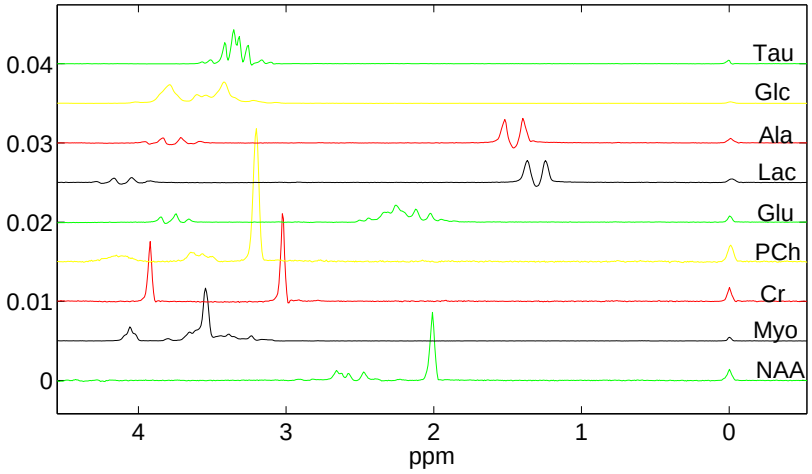


Figure 1.8. *Examples of in vitro metabolite spectra (NAA, Myo, Cr, Pch, Glu, Lac, Ala, Glc, Tau). These spectra were acquired on a 1.5 T Philips NT Gyroscan using a PRESS sequence (more details can be found in Appendix A, Database 1).*

only in the neuron and not in the glial cells or in the tumor cells [88]. The concentration of NAA in the gray matter has been found to be approximately equal or greater than that in the white matter [231]. The typical concentration and *in vivo* relaxation rates of the cerebral N-acetyl containing metabolites in humans have been reported in several studies (reviewed by Kreis [143], see also Pouwels and Frahm [215]). Reported concentrations in human brain are in the range of 7–16 mmol/kg of wet weight. NAA can be used to distinguish gliomas from normal brains ($p<0.001$), and low-grade gliomas from the high grade gliomas ($p<0.001$) [284].

Total Choline (tCho), peak at about 3.22 ppm

The tCho peak include the contributions from free choline (Cho), glycerophosphocholine (GPCh), and phosphorylcholine (PCh) and may be as much as three or four times larger in tumor than in normal voxels [199]. Although those peaks are not distinguishable in *in vivo* MR spectra, they are in HR-MAS data. PCho is involved in the synthesis of the insoluble membrane phospholipids, while GPCho is a product of membrane degradation, and free choline is involved in synthesis of the neurotransmitter, acetylcholine, as well as membrane synthesis [231, 199]. An increase in the tCho peak is associated with an increase in membrane breakdown or turnover, myelination or inflammation and has been observed in demyelinating diseases and in brain tumors [231]. The tCho peak is also thought to reflect cellular density (as opposed to NAA reflecting only neuronal density) [231]. The total choline concentration in human brain is approximately 1–2 mmol/kg of wet weight, and known to be nonuniformly distributed [303, 215]. Choline-containing compounds were present in all tumors except craniopharyngioma, and their concentrations were particularly high in a metastatic brain tumor from hepatocellular carcinoma [135]. tCho can help to dis-

tinguish between meningioma and glioblastoma or metastasis, but also between anaplastic astrocytoma and glioblastoma or metastasis. Certain ratios, such as tCho/tCr, may also aid for some classification problems (see Table 1.1 for more details) [172]. The increase of Cho could not be used to differentiate gliomas from normal brains ($p<0.13$), and low-grade gliomas from high-grade gliomas ($p<0.75$) [284]. Meningiomas can have choline concentrations comparable to grade III astrocytomas [117, 176] and as high PCh/GPCh ratios as glioblastoma cells [85].

Total Creatine (tCr), singlets at 3.03 and 3.9 ppm
tCr refers to the sum of creatine (Cr) and phosphocreatine (PCr). tCr resonances reflect the energetic status of the tissue and may be both reduced in some regions of the lesion and increased in other regions [199]. tCr is often used as an internal reference, however the accuracy of tCr is controversial because tCr may vary under pathological conditions [231]. Concentrations in the human brain are approximately 4.0–5.5 mmol/kg of wet weight for phosphocreatine, and 4.8–5.6 mmol/kg of wet weight for creatine, with the total creatine signal reported to be higher in gray matter [231], at 6.4–9.7 mM, than in white matter, at 5.2–5.7 mM. The concentration of tCr could be used to distinguish gliomas from normal brains ($p<0.001$), and low-grade gliomas from high-grade gliomas ($p<0.01$) [284]. tCr is also almost absent in meningiomas, schwannomas [196] and metastasis [122].

Myo-inositol (Myo), multiplets appearing at $\sim$ 3.56 ppm
Myo is located within astrocytes [232], and its concentrations is normally elevated in the newborn brain, but rapidly decreases thereafter [284]. Myo is a precursor for inositol lipid synthesis and is constituent of membrane lipids [231]. Normal concentrations range from 4 to 8 mmol/kg of wet weight [143, 215]. Myo is high in low-grade gliomas [117, 32] but are low or absent in non-glial tumors such as schwannomas [196] or meningiomas [117]. A relative elevation of Myo is found in low-grade astrocytomas when compared with high-grade astrocytomas because this portion of Myo is converted into phosphatidylinositol [284]. The (Myo + Gly)/H_2O ratio could be used to distinguish gliomas from normal brains ($p<0.05$), and low-grade gliomas from high-grade gliomas ($p<0.05$) [284].

Glycine (Gly), singlet at $\sim$ 3.56 ppm
Gly, which is the simplest amino acid and involved in many metabolic pathways, was observed in gliomas [284, 135]. Its concentration is well regulated in the brain, being primarily synthesized from glucose through serine, with a concentration of approximately 1 mmol/kg of wet weight in humans [136]. Results of *in vitro* experiments showed a trend toward increased Gly concentration in astrocytomas compared with peritumoral brain [284]. This is confirmed by HR-MAS studies of tumor biopsies which also indicate that Gly and Myo show a decrease with grade and are absent in meningiomas. Gly increased remarkably in glioblastoma, regardless of the necrotic fraction [284, 137].

Glutamine and Glutamate (Glx), between 2 and 2.4 ppm and $\sim$ 3.8 ppm
Glutamine and glutamate are the amino acids which are the most abundant amino acid in the brain and are released by 90 % of excitatory neurons [231] (most important exciter neurotransmitter). Glu and Gln concentrations are in the range of approximately 12 mmol/kg of wet weight [306] and 24 mM [215], respectively. Glx resonances were detected in all

highly malignant tumors [287, 80]. Glx is high in meningiomas [176]. Glx can be used to distinguish between meningioma and low grade astrocytoma oranaplastic astrocytoma [172].

Lactate (Lac), doublet at 1.33 ppm
Lactate is the end product of anaerobic glycolysis. In *in vivo* MRS , Lac is usually detected only under pathologic conditions, when energy metabolism is affected severely (*e.g.*, anaerobic metabolism). A greater amount of lactate was detected in the higher grade tumors [88] but not always detectable even in glioblastomas or metastasis [80]. Lac levels do not correlate well with tumor grade [149]. In addition Lac can be elevated in peritumoral region due to hypoxia caused by vasogenic oedema [80]. According to [80, 122, 128] the lactate is of no use in the differentiation of gliomas and metastasis. Healthy tissue does not have sufficient lactate to be detectable with *in vivo* MRS, but cerebrospinal fluid (CSF) contains lactate which may then be visible if the voxel overlap with a ventricle. Lac is also found in cysts and abscesses [40].

Lipids (Lip), at 1.3 and 0.9 ppm
The presence of mobile Lip is thought to correspond to cellular and membrane breakdown corresponding to necrosis [199]. Spectra with peaks corresponding to Lac/Lip are typically elevated in the necrotic core of the tumor. Increase lipid peaks were found in the tumoral region of both metastasis and glioblastomas [80, 122]. Lipids are characteristics of high-grade tumors at short TE [7, 117], but are only observed in 41% of high-grades at long TE [198], due to the T_2 relaxation times of lipids that is much shorter than those of the main metabolites (see Section 1.1.1). In healthy tissue of *in vivo* MRS data, there should be very little lipid in the spectrum unless the area includes subcutaneous fat from the skull.

Taurine (Tau), multiplets at about 3.42 ppm
Tau is a β-amino acid found in all tissues of most animal species except for the pituitary gland and pineal gland, the Tau level in the retina is the highest of all organs [284]. Tau is reported to have a number of biological functions, including osmoregulation and modulation of the action of neurotransitters [108]. It is found at high concentration at the time of birth and decreases with age, to a concentration of approximately 1.5 mM [97]. Taurine is high in medulloblastoma compared with gliomas [284].

Alanine (Ala), doublet at 1.47 ppm
Alanine, a nonessential amino acid that contains a methyl group, and is present in the human brain at approximately 0.5 mmol/kg of wet weight [97]. Alanine is elevated in meningioma [176, 211], glioma, pituitary adenoma and medulloblastomas [284].

From tumors to metabolites

Typical spectra of common brain tumors are illustrated in Fig. 1.9.

Normal brains
MR spectra of normal brains demonstrate a high NAA peak, high tCr peak and low peaks of tCho, Glx, Gly and Myo [284] compared to abnormal spectra. The concentration of wa-

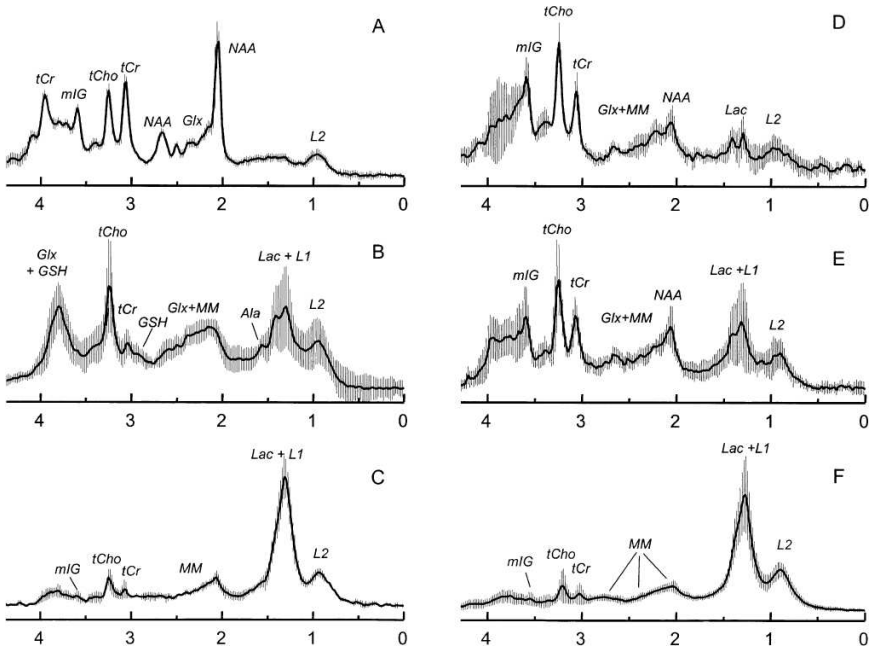


Figure 1.9. *Mean and standard deviation (vertical lines) based on n normalized STEAM TE 30 ms spectra. (A) Normal parietal white matter (n = 6). (B) Meningioma (n = 8). (C) Metastases (n = 6). (D) Astrocytoma grade II (n = 5). (E) Anaplastic astrocytoma (n = 7). (F) Glioblastoma (n = 13). Abbreviations: GSH, glutathione; MM, macromolecules; mIG, myo-inositol + glycine; L1, lipid at 1.3 ppm; L2, lipid at 0.9 ppm. The figure has been taken from [117].*

ter in the hemispheric gray matter is higher than in the hemispheric white matter ($p<0.05$), thus attention must be paid to the location of the lesions in analyzing the MR spectra. The NAA/tCr ratio may not be a reliable marker when differentiating between normal and abnormal brain tissue samples, at least for nonglioma tumors, since both (NAA and tCr) decrease [183].

Gliomas

Gliomas are characterized by decreased NAA, decreased tCr and increased lactate compared to healthy tissue [284, 28, 232]. tCho is also increased, reflecting a relative increase in glial cellular density as contrasted with normal neuronal tissue [281, 198]. The concentration of water in gliomas (52290.45 mM) is larger than the concentration in normal brains (47280.96 mM) [284]. It is therefore necessary to calculate the concentration of water in the volume of interest (VOI) before using the fully relaxed water signal as an internal standard [284]. Tong *et al.* [284] studied several ratios to compare glioma and normal brain spectra. In gliomas the ratio of NAA/tCr, NAA/tCho, tCr/tCho, NAA/H_2O and tCr/H_2O were significantly decreased compared to those in normal brain ($p<0.01$), H_2O being the concentration of the water. All gliomas demonstrate a high tCho/(tCho+NAA+tCr) ratio

and a low NAA/(tCho+NAA+tCr), and the ratio between tCho from tumor and normal tissue does not change with the grading of the tumor [88].

Grading gliomas is not always obvious due to the tissue heterogeneity [88]. Tong *et al.* [284] showed that the NAA/H_2O, NAA/tCho and tCr/H_2O ratios were significantly decreased in high-grade gliomas as compared with those in low-grade gliomas. (Myo+Gly)/H_2O was different among the low grades, the high grades, and the normal brain ($p<0.05$), in gliomas less than in normal brains and in high-grade gliomas 50% less than in low-grade gliomas. tCho/tCr peak area ratio is a reliable marker for tumor grade identification [86, 117, 92]. The tCho/(tCho+NAA+tCr) ratio decreases with the malignancy of the tumor due to the low cellularity of high-grade gliomas, which contain a large amount of necrosis [88]. Short TE data have shown a decrease in Myo/tCr or Myo/tCho peak areas with grade [32, 117]. However, there is significant overlap of these indices between grades, most likely due to the general heterogeneity of tumors. Lipid concentrations measured in short TE studies increase with grade [117, 7].

The ratio between tCr or NAA from glioma grade IV or glioblastoma (GBM) and normal tissue are also smaller than glioma grade II or III. The tCr concentrations decreases according to the malignancy, the concentration of tCr is relatively preserved in neuroectodermal or glioma tumors but is low in nonneuroectodermal tumors [137]. Majos *et al.* [172] found that Gly-Myo at short TE provided some separation between low grade astrocytomas (LGA) and anaplastic astrocytomas (AA, grade III glioma) and provided also significant differences between GBM-Metastasis and AA or LGA. The most difficult differentiation (= largest number of misclassifications) was between AA and LGA.

Astrocytic cells do not have any measurable amount of NAA [232]. Thus, measured NAA in such tumor spectra represents either normal neuronal tissue inside the tumor or infiltration of tumor cells within the normal brain. The degree of infiltration is much higher in grades III and IV than in grades I and II astrocytomas [86]. Consequently a glioblastoma multiforme would have a largely decreased NAA. Glx can be used to differentiate between low grade astrocytoma and low grade oligodendroglioma, while lipids+lactate can be used for separating high and low grade oligodendrogliomas [228]. Tugnoli *et al.* described intense multiplets assigned to Glx as one of the main spectroscopic features in ^{1}H MR spectra of low-grade oligodendrogliomas [286].

Fan *et al.* [80] found high tCho concentration in tumoral regions of metastasis and GBM, suggesting that high tCho peaks in the tumoral regions is characteristic of rapidly growing tumors rather than unique for gliomas. However, [80] found high tCho peak and elevated tCho/tCr ratio in the peritumoral regions of high grade gliomas but not in metastasis. This suggests that the infiltration of adjacent brain tissue by tumor is a unique feature of high-grade gliomas. They also found an elevated Myo/tCr ratio within the enhancing foci of gliomas but not in metastasis and believe that the increased Myo levels in the tumoral region are more likely to be present in glioma. Statistically significant differences were found in tCho/tCr and Glx/tCr ratio in peritumoral regions between GBM (larger values) and anaplastic astrocytomas [80]. Peritumoral tCho/tCr ratios were significantly higher in glioblastomas compared with solitary metastases, suggesting that metabolite maps can be used to classify these two tumor types, which are not easily distinguished by other means [27].

It has been proposed that GBM can be differentiated in two groups : primary and secondary GBMs, with short and long survival, respectively [180]. Primary GBMs are

more frequent in patients older than 60 years, and show a rapid clinical development and more aggressive evolution. Secondary GBMs appear in younger patients (30-50 years old) with a slower clinical development and a better prognosis [180]. The concentrations of Cho-containing compounds, inositol, alanine, glycine, and phosphorylethanolamine (PEA) increase according to the degree of malignancy [137]. In particular the glycine concentration is very high in glioblastomas [137]. When quantifying, one has to pay attention when dealing with tumor tissue possibly containing necrosis. For example, high-grade tumors can have apparently less tCho than normal brain tissue, an effect of dilution of absolute cellular density by the presence of necrosis [117].

Meningiomas
Meningiomas often grow quite largely before they cause symptoms. They occur most often in women between 30 and 50. Fountas *et al.* [86] noted that in meningiomas there was a high concentration of tCho, decreased tCr, decreased NAA and presence of lipids for 76% of the patients with meningiomas. Kinoshita *et al.* [137] have demonstrated that the concentration of Cho-containing compound was not increased but there were an increased alanine content. Meningiomas do not include neurons but NAA can be detected by contamination of surrounding brain tissue because the measurement volume was larger than the pure meningioma [88]. A characteristic is the high level of tCho and extremely low content of tCr and NAA [88, 86]. High tCho/tCr ratio and elevated lipid levels are also a characteristic of malignant meningiomas.

Secondary brain tumors or Metastasis
In the experience carried out by Fountas *et al.* [86], there was a high concentration of tCho but total absence of tCr, NAA and lactate for LE data. In almost 75% of the patients, a significant amount of lipids was detected [86]. High tCho/tCr ratio and elevated lipid levels are also a characteristic of malignant metastasis.

Table 1.1 reports potentially interesting MRS features for different pairwise comparison problems.

Table 1.1. *Comparison of tumor groups: metabolite potential of differentiation. Lip1 = lipid at 1.3 ppm, Lip2 = lipid at 0.9 ppm. Gly-Myo = Gly and/or Myo. (LE) or (SE) indicates whether the feature can be used for differentiation at long or short echo time, respectively. (Peri) indicates that the measure is done in the peritumoral region.*

Pairwise comparisons	Metabolites for distinction between tumors
MEN vs LGA	Ala [172],Glx [172], tCho(LE) [172], Gly-Myo(SE) [172]
MEN vs AA	Ala [172], Glx(LE) [172], tCr(SE) [172]
MEN vs GBM	Lip2 [172], Lip1 [172],Ala [172], Glx [172], tCho [172], Lac(LE) [172], NAA(LE) [172], tCr(SE) [172], Gly-Myo(SE) [172]
MEN vs MET	Lip2 [172], Lip1 [172], Ala [172], Glx[172], tCho [172], Lac(LE) [172], NAA(LE) [172], tCr(SE) [172], Gly-Myo(SE) [172]
LGA vs AA	Gly-Myo(SE) [172], NAA/H_2O [284], NAA/tCho [284], tCr/H_2O [284], (Myo+Gly)/H_2O [284], tCho/tCr [86, 117, 92], tCho/(tCho+NAA+tCr) [88]
LGA vs GBM	Lip2 [172], Lip1 [172], tCr [172], Gly-Myo(SE) [172], Lac(LE) [172], NAA/H_2O [284], NAA/tCho[284], tCr/H_2O [284], (Myo+Gly)/H_2O [284], tCho/tCr [86, 117, 92]
LGA vs MET	Lip2 [172], Lip1 [172], tCr [172], Gly-Myo(SE) [172], Lac(LE) [172]
AA vs GBM	Lip13 [172], tCr [172], tCho [172] , Lip09 [172], tCho/tCr(Peri) [80], Glu-n/tCr(Peri) [80], Gly-Myo(SE) [172], NAA(LE) [172], tCho/tCr(LE) [86]
AA vs MET	Lip1 [172], tCr [172], tCho [172] , Lip2 [172], Gly-Myo(SE) [172], NAA(LE) [172]
GBM vs MET	tCho (Peri) [80], tCho/tCr(Peri) [80], Myo/tCr [80]

1.3 Goal and outline of the thesis

This thesis deals with brain tumor MRS(I) data (*in vivo* and *ex vivo*). The challenge is to improve brain tumor diagnosis by using spectroscopic data. As mentioned before, 3 main steps are necessary for obtaining a diagnosis from the raw data. The first step consists of different types of preprocessings on the data. This usually involves 1) eddy current correction, 2) residual water filtering, 3) Fourier transformation, 4) phase correction and 5) normalization. Preprocessing of the MRS data is a crucial step due to the low SNR of *in vivo* MRS signals. If an error is generated at this step, it will be propagated all along the process (from preprocessing to classification). The second step involves feature reduction of the highly dimensional spectroscopic data. This step aims to find the best set of variables that are diagnostically relevant for the classification. Feature reduction should be performed in such a way that the information that optimally discriminates the tumor classes is kept. The third step consists of the classification itself. The features selected or extracted in the previous step are used as input in the classifier. In this thesis, preprocessing, processing or feature extraction and classification methods are analyzed.

Chapter 1 introduces the main principles of different MR modalities (MRS, MRI, MRSI and HR-MAS) which are used in the studies of this thesis. The characteristics of these modalities are outlined by emphasizing on the differences, giving their advantages and limitations. Several concepts (TE, TR, T_1, T_2, etc) explained in this chapter are used all along the thesis. A minimal medical background familiarizes the reader with the main characteristics of brain tumor diagnostics (statistics, diagnosis tools, treatments, main types of brain tumors). The second section links metabolite concentrations to brain tumors and shows in that way that MRS features are relevant for brain tumor diagnosis.
Chapter 2 gives the theoretical aspects of the preprocessing, feature extraction and classification methods used in this thesis. In particular, it introduces the methods used in Chapters 5 to 9, but also introduces basis concepts in order to understand Chapters 3 and 4.
Chapter 3 reviews the quantification methods used in MRS. The main aspects of MRS quantification are described: the principles, the obstacles but also the pitfalls are explained. Most recent extensive reviews on quantification methods go back to 2001 [190, 297]. Since then, many new quantification methods have been published, especially devoted to short echo time *in vivo* MR data. These reviews were generally limited to a certain type of domain (time-domain method [297], frequency-domain method [190]), or a type of model (parametric [239], nonparametric [269]). The review proposed in this chapter is much more extensive, including time- and frequency-domain methods, discussing the different types of possible models and including the recently published quantification algorithms. It also gives a more detailed analysis of the different so-called nuisance component correction or modeling methods. In addition, it emphasizes the main characteristics of MRS quantification and helps the reader to choose the most appropriate quantification method, which is not a trivial process. This choice should emerged from the comparison of all existing quantification methods, which was not possible in previous publications. Chapter 3 is the result of two papers, one accepted in Journal of Magnetic Resonance and the other submitted for publication to the Encyclopedia of Magnetic Resonance.
Chapter 4 reviews briefly the pattern recognition methods. An overview of the features extraction methods and the classification methods is given. As far as we know, the last paper

on the topic (pattern recognition methods applied for brain tumor diagnosis) was published in 1998 [106]. This chapter largely extends this list of pattern recognition methods and also overviews those based on MRSI data, contrarily to [106], which was only focused on MRS data. This work was submitted for publication to the Encyclopedia of Magnetic Resonance.

Chapter 5 analyzes the performances of the quantification method AQSES (processing method) developed for short echo time MR spectra. After reviewing the different quantification methods in Chapter 3, we focus on a particular method, AQSES, which presents numerous advantages over other existing methods. This chapter reveals how such a method deals with the so-called nuisance components, *i.e.* the components of no interest, which complicate quantification. The maximum-phase finite impulse response (MP-FIR) filter used in AQSES is introduced. More details on the filter are given in Chapter 6. This work has been published in NMR in Biomedicine [213].

Chapter 6 compares two solvent suppression methods which were proven to be the most successful methods for long echo time MR spectra. It shows that both methods are successful for short echo time MR spectra and shows the advantages and limitations of both methods, in particular it shows the interest of using MP-FIR inside a quantification method such as AQSES. Although the suppression of solvents precedes quantification, the results of this study are mainly based on the parameter estimates obtained with AQSES, which explains why the chapter on AQSES shows up before. This work has been published in Journal of Magnetic Resonance [214].

Chapter 7 presents a new FIR filter technique that improves the performances of MP-FIR in terms of attenuation of the wide peaks, which can particularly be interesting if one does not want to filter out the macromolecular components. The design of the new filter is based on the use of more prior knowledge and is therefore more appropriate for MRS data. This work has been submitted for publication to the Journal of Magnetic Resonance.

Chapter 8 studies the importance of feature selection methods. Quantification is just one way to extract features. However, there exist many other feature selection techniques that can be exploited, as explained in Chapter 4. We investigate a few of them and discuss their performance on short echo time MR data. This work has been published in Magnetic Resonance in Medicine [167].

Chapter 9 studies the relevance of HR-MAS data for classifying brain tumors. A complete procedure (preprocessing, processing and classification) is proposed for brain tumor diagnosis using only HR-MAS data. This work has been published in Conference Proceedings of IEEE Engineering Medicine and Biology Society [212].

1.4 Conclusions

The basics concepts of Magnetic Resonance have been introduced. This chapter also shows the potential of MRS for brain tumor diagnosis in clinical practice. This thesis studies each of the main steps leading to diagnosis: preprocessing, processing and classification steps.

Chapter 2

From FIDs to classification results

This chapter reviews the methods used in this thesis to convert the FIDs into classification results (tumor class). Section 2.1 describes the model used in this thesis for short echo time MR data. Preprocessing methods are outlined in Section 2.2. First, the typical preprocessing methods are briefly reviewed. Next, we focus on the water filtering methods MP-FIR and HLSVD-PRO. Section 2.3 gives the theoretical background of the feature extraction methods used all along the thesis. Section 2.4 focuses on the classification methods.

2.1 The model for short echo time MR data

During an *in vivo* MRS experiment, the measured time-domain signal consists of responses from all metabolites (including macromolecules), noise and partially suppressed water. Spectra of metabolites that are visible during *in vivo* spectroscopy can also be measured *in vitro* or they can be simulated using quantum mechanical knowledge, and these signals can be grouped in a database of metabolite profiles. An *in vivo* time-domain signal has, in theory, the shape of a sum of complex damped exponentials. Instead of modeling these individual lineshapes, the *in vivo* short echo time MRS signal can be modeled using (a selection of) the profiles in the database, such that the prior knowledge that relates individual peaks in the *in vivo* spectrum is implicitely imposed. The quantities of interest, the metabolite *concentrations*, can be estimated from the weighting coefficients (amplitudes) of the linearly combined *in vitro* profiles. The linear combination should allow small corrections in spectral parameters like frequency shifts, damping corrections and phase shifts, as well, since these parameters may vary from measurement to measurement [226]. Any quantification method should also take into account the presence of a partially suppressed water resonance and the presence of the macromolecular baseline. The frequency region where the water is located is known, while the macromolecular baseline overlaps with the metabolites of interest.

We consider that we are given a "metabolite database" as a set $\{v_k, \text{ for } k = 1, \ldots, K\}$

of complex-valued time series of length N, representing *in vitro* measured NMR responses. An *in vivo* measured MR signal y, which is another complex-valued time series of length N, satisfies the model

$$y(t) = \widehat{y}(t) + \varepsilon_t, \quad t = t_0, \ldots, t_{m-1}, \qquad \text{with} \tag{2.1}$$

$$\widehat{y}(t) = \sum_{k=1}^{K} \alpha_k \left(\zeta_k\right)^t \left(\eta_k\right)^{t^2} v_k(t) + b(t) + w(t), \tag{2.2}$$

where $\alpha_k, \zeta_k \in \mathbb{C}$ are unknown parameters that account for amplitudes of the metabolites in the database and for the necessary corrections of the database signals. The complex amplitudes α_k and the complex values ζ_k can be written as (with $j = \sqrt{-1}$):

$$\begin{aligned} \alpha_k &= a_k \exp(j\phi_k), \\ \zeta_k &= \begin{cases} \exp(-d_k + jf_k), & \text{for Lorentzian and Voigt lineshapes;} \\ \exp(jf_k), & \text{for Gaussian lineshapes;} \end{cases} \\ \eta_k &= \begin{cases} \exp(je_k), & \text{for Lorentzian lineshapes;} \\ \exp(-g_k + jf_k), & \text{for Gaussian and Voigt lineshapes;} \end{cases} \end{aligned} \tag{2.3}$$

where a_k are the real amplitudes, ϕ_k are the phase shifts, d_k are damping corrections, f_k are frequency shifts, g_k are Gaussian damping corrections, and e_k are eddy current correction terms. For ease of exposition, the following of this thesis will be restricted to the classical Lorentzian line shapes. In (2.1), the term ε_t denotes an unknown noise perturbation with zero mean, and in (2.2), $b(t)$ denotes the "baseline", and $w(t)$ denotes the water component. For illustration, an example of metabolite database is given in Fig. 1.8, a water signal extracted from the NAA metabolite profile in Fig. 2.1, and macromolecule components (constituting the so-called macromolecular baseline) in Fig. 2.2.

Note that for long echo time MR data, the commonly used model is a linear combination of K exponentially damped sinusoids

$$y(t) = \sum_{k=1}^{K} \alpha_k \left(\zeta_k\right)^t + w(t) + \varepsilon_t, \tag{2.4}$$

with similar notations as in Eq. (2.1)-Eq. (2.3) except that these parameters are not corrections of the metabolite profiles and suffice to characterize the signal (no need of a metabolite database).

2.2 Preprocessing methods

The aim of the preprocessing step is to remove the irrelevant information, while enhancing the key features in order to extract them. MRS signals are affected by the presence of artifacts, instrumental errors, noise and other unwanted components. The spectral quality can be considerably improved by appropriate manipulation of the data. The sequence of preprocessing methods should be chosen carefully since one step may influence the other. For example, frequency alignement should precede water filtering, which requires the definition of the water peak region. Signal normalization should also be applied after water

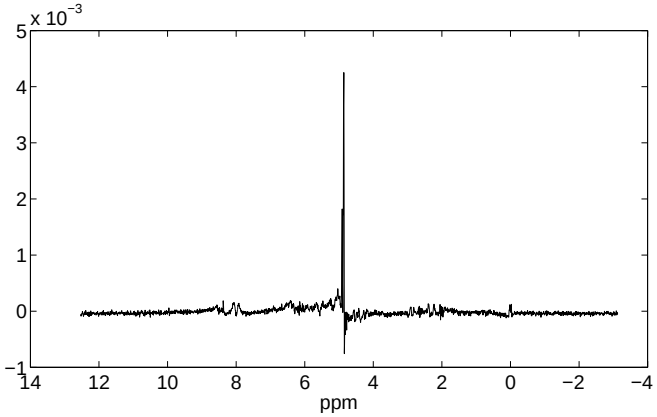


Figure 2.1. *Example of water signal in the frequency domain (real part). This signal has been extracted from the NAA metabolite profile of Database 1 in Annexe A using HLSVD-PRO (see Section 2.2.2) with a model order of 30 and a frequency passband equal to [4.4,5.3] ppm.*

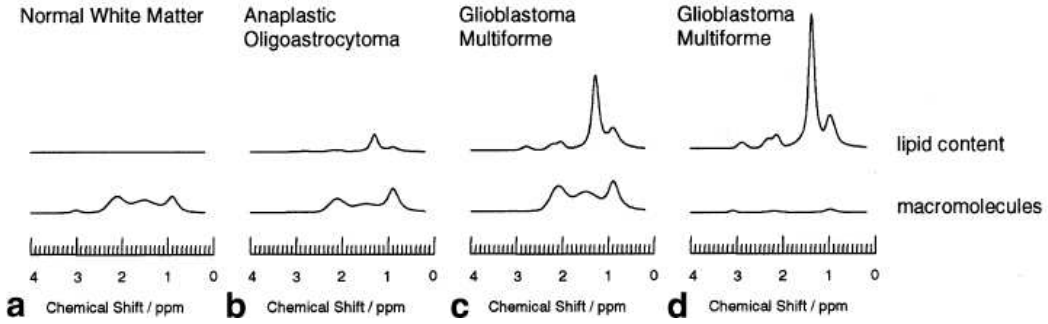


Figure 2.2. *Example of macromolecule spectra for different tissue types. One can notice the typical smoothness of macromolecular baseline spectra in in vivo MRS (1.5 T). Lipid spectra have also been added to the plots to show the complexity of disentangling both lipids and macromolecule components. This figure has been taken and adapted from Fig. 5 in [242].*

normalization since the water contribution of the water suppressed signal should not be taken into account in the normalization process. The preprocessing methods are presented in Section 2.2.1 in their common and logical sequential order.

2.2.1 Typical preprocessing steps

Frequency alignment. The frequency alignment is performed first since most of the methods require correctly aligned spectra. In *in vivo* MR data at 1.5T, large peaks

such as NAA, Cho or Cr are generally used as reference for alignment, while doublets are preferred for *ex vivo* HR-MAS data (*e.g.*, Ala or Lac doublet). The spectra are shifted in the frequency domain and transformed back into the time domain by the inverse Fourier transformation.

Phase/lineshape correction. In case a water-unsuppressed signal is available together with the water suppressed signal, Klose's method [138] can be carried out for phase correction. This corrects for eddy currents (caused by instrumental imperfections) by dividing the water suppressed signal by the phase term of the water unsuppressed signal. Lineshape correction methods like QUALITY [58] and QUECC [13] can also correct for distortions in the magnitude of the signal. The goal of these methods is to transform the original signal such that it follows a Lorentzian model, which is often used in quantification methods. This is particularly interesting indeed prior to a quantification method, but will be less critical for methods such as peak integration, for which a phase correction method, such as Klose's, already provides good results.

Water filtering. Residual water removal can be performed by a subspace-based modeling approach such as HSVD [12] or HLSVD-PRO [152] or by filtering such as MP-FIR [298] (more details in Section 2.2.2).

Signal normalization. Two main normalization approaches can be applied to MRS signals; normalization with respect to a particular mathematical norm and normalization by division by an intensity of a particular molecule. Normalizing MR signals is especially complicated when the data have been acquired by several clinical centers, several scanners or with several acquisition protocols.

- Mathematical normalization: if the spectrum is considered as a vector v, then the L1-norm is defined as the sum of the absolute form of the elements in that vector, which corresponds to the integral of the spectrum. Each spectral value is then divided by the L1-norm of the spectrum, in order to obtain an L1-normalized spectrum. The spectral vector can also be divided by its L2-norm $||v||_2$, which is defined as the square root of the sum of the squares of the elements in that vector [278, 288]. After division, the spectrum has unity norm with respect to the L2-norm.
- Normalization by an intensity of a molecule: a common normalization approach is to normalize the signal with respect to the amplitude of Cr [217] which is assumed to be constant in normal tissue of the complete brain as well as in many pathologies. Nevertheless, Li *et al.* [157] found that this normalization method increases variability. An alternative method divides the spectrum by the intensity of water, estimated from a spectrum without water suppression [288]. This requires an additional measurement of a corresponding water unsuppressed signal, acquired with the same acquisition parameters and originating from the same voxel. The intensity of the water peak can be estimated for example by taking the highest value in the time domain signal, by peak integration in the frequency domain [189], by modeling the water unsuppressed signal using HSVD [12], HLSVD-PRO [152] or other modeling approaches.

Baseline correction. There exist many baseline correction methods (see Chapter 3). In this thesis, we tested the following approaches:

- Non parametric modeling of the baseline in AQSES (see Section 2.3.1).
- Multiplication of the FID by an exponentially decaying function. The baseline is fitted as the product of the original FID and an exponentially decreasing apodization function ([249]), which requires only the decay as parameter to be selected. As the baseline consists of broad fast decaying components, their main contribution is in the first part of the FID. After multiplication with a decaying function, the resulting function will mainly contain the broad baseline components.
- Truncation of the initial points in the FID proposed by Ratiney *et al.* [225] in the method QUEST. The baseline, being a broad component in the spectrum, decays very rapidly (T_2-value of the macromolecules is small as seen in Chapter 1). Hence, removing the initial part of the FID should suppress the baseline components. However, this operation also suppresses part of the metabolite contributions and might reduce the accuracy of the estimates since the SNR is decreased. Note that the metabolite profiles in the database are also truncated to avoid large estimation error.

2.2.2 Water filtering techniques

SVD-based techniques

Typically, the quantification methods assume that the water resonance is removed in a *preprocessing step*, using a frequency selective method. For instance, the HSVD (Hankel singular value decomposition) method is based on the idea of first fitting the whole signal as a sum of complex damped exponentials and then subtracting all the components whose frequencies were estimated in the frequency region of the water resonance.

HSVD is a subspace–based parameter estimation method in which the noisy signal is arranged in a Hankel matrix $\mathbf{H}$. Its Singular Value Decomposition (SVD) allows to compute a "signal" subspace and a "noise" subspace. In fact, if $\mathbf{H}$ is constructed from a noiseless time–domain signal, the data matrix $\mathbf{H}$ has rank exactly equal to K, the number of exponentials that model the underlying signal. Due to the presence of the noise, $\mathbf{H}$ becomes a full–rank matrix. However, as long as the SNR of the signal is not too low, one can still define the "numerical" rank being approximately equal to K. Then, the "signal" subspace is found by truncating the SVD of the matrix $\mathbf{H}$ to rank K. We derive the method for noiseless and noisy data.

HSVD - noiseless data

Arrange the N noiseless data points $\hat{y}_n$ defined in Eq. (2.4) in a Hankel matrix $\hat{\mathbf{H}}$ of di-

mensions $L \times M$, with L and M greater than K and $N = L + M - 1$

$$\hat{\mathbf{H}} = \begin{bmatrix} \hat{y}_0 & \hat{y}_1 & \cdots & \hat{y}_{M-1} \\ \hat{y}_1 & \hat{y}_2 & \cdots & \hat{y}_M \\ \vdots & \vdots & \vdots & \vdots \\ \hat{y}_{L-1} & \hat{y}_L & \cdots & \hat{y}_{N-1} \end{bmatrix}. \tag{2.5}$$

The model of Eq. (2.4) can be rewritten in the discrete case in terms of complex amplitudes c_k and signal poles ζ_k as follows

$$\hat{y}(n) = \sum_{k=1}^{K} a_k e^{j\phi_k} e^{(-d_k + j2\pi f_k)n\Delta t} = \sum_{k=1}^{K} \alpha_k \zeta_k^n, n = 0, \ldots, N-1., \tag{2.6}$$

where $\alpha_k = a_k e^{j\phi_k}$ and $\zeta_k = e^{(-d_k + j2\pi f_k)\Delta t}$. Using this model function, the Hankel matrix $\hat{\mathbf{H}}$ can be factorized as follows

$$\begin{aligned} \hat{\mathbf{H}} &= \begin{bmatrix} 1 & 1 & \cdots & 1 \\ \zeta_1 & \zeta_2 & \cdots & \zeta_k \\ \vdots & \vdots & \ddots & \vdots \\ \zeta_1^{L-1} & \zeta_2^{L-1} & \cdots & \zeta_k^{L-1} \end{bmatrix} \begin{bmatrix} \alpha_1 & 0 & \cdots & 0 \\ 0 & \alpha_2 & \cdots & 0 \\ \vdots & \vdots & \ddots & \vdots \\ 0 & 0 & \cdots & \alpha_k \end{bmatrix} \begin{bmatrix} 1 & 1 & \cdots & 1 \\ \zeta_1 & \zeta_2 & \cdots & \zeta_k \\ \vdots & \vdots & \ddots & \vdots \\ \zeta_1^{M-1} & \zeta_2^{M-1} & \cdots & \zeta_k^{M-1} \end{bmatrix}^T \\ &= \hat{\mathbf{S}}\hat{\mathbf{C}}\hat{\mathbf{T}}^T \end{aligned} \tag{2.7}$$

This factorization is called the Vandermonde decomposition and from it the signal parameters can immediately be derived. Unfortunately, there is no algorithm that computes such a decomposition directly and, therefore, the parameters need to be computed indirectly.
From Eq. (2.7) it can be easily proved that the matrix $\hat{\mathbf{S}}$ satisfies the so–called shift–invariance property, *i.e.*

$$\hat{\mathbf{S}}^{\uparrow} = \hat{\mathbf{S}}_{\downarrow}\hat{\mathbf{Z}} \tag{2.8}$$

where $\hat{\mathbf{S}}^{\uparrow}$ and $\hat{\mathbf{S}}_{\downarrow}$ are derived from $\hat{\mathbf{S}}$ by deleting its first and last row respectively, and $\hat{\mathbf{Z}}$ is a $K \times K$ complex diagonal matrix with entries equal to the K signal poles ζ_k, $k = 1, \ldots, K$. The rank of the matrix $\hat{\mathbf{H}}$ is equal to K and, thus, its SVD has the following form

$$\hat{\mathbf{H}} = \hat{\mathbf{U}}\hat{\mathbf{\Sigma}}\hat{\mathbf{V}}^H = \begin{bmatrix} \hat{\mathbf{U}}_K & \hat{\mathbf{U}}_2 \end{bmatrix} \begin{bmatrix} \hat{\mathbf{\Sigma}}_K & \mathbf{0} \\ \mathbf{0} & \mathbf{0} \end{bmatrix} \begin{bmatrix} \hat{\mathbf{V}}_K & \hat{\mathbf{V}}_2 \end{bmatrix}^H = \hat{\mathbf{U}}_K \hat{\mathbf{\Sigma}}_K \hat{\mathbf{V}}_K^H, \tag{2.9}$$

where $\hat{\mathbf{U}}_K \in \mathbb{C}^{L \times K}$, $\hat{\mathbf{U}}_2 \in \mathbb{C}^{L \times (L-K)}$, $\hat{\mathbf{\Sigma}}_K \in \mathbb{C}^{K \times K}$, $\hat{\mathbf{V}}_K \in \mathbb{C}^{M \times K}$, $\hat{\mathbf{V}}_2 \in \mathbb{C}^{M \times (M-K)}$. From the comparison of Eq. (2.7) and Eq. (2.9), it follows that $\hat{\mathbf{S}}$ and $\hat{\mathbf{U}}_K$ span the same column space and hence are equal up to a multiplication by a non singular matrix $\hat{\mathbf{Q}} \in \mathbb{C}^{K \times K}$, *i.e.*

$$\hat{\mathbf{U}}_K = \hat{\mathbf{S}}\hat{\mathbf{Q}}. \tag{2.10}$$

Using Eq. (2.10), the shift–invariance property of Eq. (2.8) becomes

$$\hat{\mathbf{U}}_K^{\uparrow} = \hat{\mathbf{U}}_{K\downarrow}\hat{\mathbf{Q}}^{-1}\hat{\mathbf{Z}}\hat{\mathbf{Q}}. \tag{2.11}$$

From Eq. (2.11) the matrix $\hat{\mathbf{Q}}^{-1}\hat{\mathbf{Z}}\hat{\mathbf{Q}}$ can be determined and since the eigenvalues of $\hat{\mathbf{Q}}^{-1}\hat{\mathbf{Z}}\hat{\mathbf{Q}}$ and $\hat{\mathbf{Z}}$ are equal, the signal poles are easily derived as

$$\{\zeta_k\}_{k=1}^{K} = eig(\hat{\mathbf{Q}}^{-1}\hat{\mathbf{Z}}\hat{\mathbf{Q}}) = eig(\hat{\mathbf{Z}}), \tag{2.12}$$

where the function $eig(.)$ determines the eigenvalues of the matrix between brackets.
From the signal poles, frequency and damping factors are estimated. By filling in these estimates into the model function Eq. (2.6), a new system of linear equations is obtained with unknowns equal to the complex amplitudes α_k. Its solution provides estimates for the amplitudes and the phases.
Note that, once the signal poles have been estimated, the amplitudes and phases can be obtained by using other estimation methods. One example is the so–called APES method, where the acronym stands for Amplitude and Phase EStimation, which provides accurate estimates at a reasonable computational cost as shown in [269].

HSVD - noisy data

When noise affects the data, as in real MRS signals, the noisy Hankel matrix $\mathbf{H}$ replaces $\hat{\mathbf{H}}$ and the relation (2.9) no longer holds. Although no exact solution of the shift–invariance property exists, the matrices $\mathbf{H}$ and $\hat{\mathbf{H}}$ have the same structure and, if the noise is small compared to the signal, $\mathbf{H}$ can be approximated by the truncated SVD, *i.e.*

$$\mathbf{H} = \mathbf{U}\mathbf{\Sigma}\mathbf{V}^H \approx \mathbf{U}_K\mathbf{\Sigma}_K\mathbf{V}_K^H = \mathbf{H}_K, \tag{2.13}$$

where $\mathbf{U}_K$ and $\mathbf{V}_K$ are the first K columns of $\mathbf{U}$ and $\mathbf{V}$, respectively, and $\mathbf{\Sigma}_K$ is the $K \times K$ upper-left sub-matrix of $\mathbf{\Sigma}$.
The matrix $\mathbf{H}_K$ has rank K but its Hankel structure has been destroyed by the truncation of the SVD. Therefore, the system in Eq. (2.11) has no longer an exact solution. However, estimates of the signal poles can still be obtained by solving the aforementioned system in a LS sense and the signal parameters can be derived from such estimates as in the noiseless case. Further details about the derivation of HSVD can be found in [12].

The Hankel-Lanczos SVD decomposition with partial reorthogonalization (HLSVD-PRO) benefits from the efficiency of the Lanczos algorithm, which is made robust thanks to the partial reorthogonalization. More details can be found in [152] and references therein, in particular [248].

MP-FIR

MP-FIR is a maximum-phase FIR filter based on the constrained least squares design of FIR filters proposed by Selesnick *et al.* [243], who does not specifically consider the case

of complex damped exponentials. Nevertheless, the use of a maximum-phase FIR filter instead of a general FIR filter is motivated by the assumption of such a model (sum of complex damped exponentials) as detailed below. Moreover, the filter length is optimized with respect to the noise and the water resonances of the signal under processing. All components in the frequency region of no interest are attenuated such that the largest magnitude in that region is smaller than twice the standard deviation of the noise. Although the filter coefficients are optimized before starting the iterative optimization for quantification, MP-FIR is applied to the MRS signal and each **corrected** metabolite profile $\{y_k\}_{k=1,\ldots,K}$ in each iteration of the optimization procedure. In order to avoid signal distortion, the first $M-1$ points are discarded from the filtered signal [273], $M-1$ being the filter order. The filter design is given in Alg. (2.2.1).

Algorithm 2.2.1 MP-FIR

Input: data samples $y(n)$, $n = 0, \ldots, N-1$, the filter cut-off frequencies fl_r and fh_r corresponding to the user-selected frequency region(s) containing the nuisance peaks $[fl_r, fh_r]$, $r = 1, \ldots, R$, where R is the number of regions.

1: An estimate $\hat{\sigma}$ of the noise standard deviation is calculated as the standard deviation of the last samples of the signal. The peak value, s_0, is computed as the value of the strongest nuisance peak

$$s_0 = \max_l |\frac{Y(f_l)}{\sqrt{N}}|, \tag{2.14}$$

where $f_l \in [fl_r, fh_r]$.

2: The initial filter suppression sup is taken equal to

$$sup = \frac{2.5\hat{\sigma}}{s_0} \tag{2.15}$$

and starting values for the filter order (*e.g.*, $M = 30$) and the passband ripple (*e.g.*, $r = 5\%$) are chosen.

3: The linear-phase filter is designed by the constrained least squares algorithm of [243] and transformed into a maximum-phase filter.

4: The signal is filtered and the maximum value s_m in the frequency regions of the nuisance peaks is calculated

$$s_m = \max_l |\frac{Y(f_l)}{\sqrt{N}}|, \tag{2.16}$$

If

$$s_m > 2.5\hat{\sigma}, \tag{2.17}$$

the filter suppression is increased (*e.g.*, $sup = sup/5$) and the process is restarted from *Step 3*. If s_m does not decrease in the next iteration, the filter order is increased (*e.g.*, $M = M + 10$).

Output: the filter coefficient h

Analytical validation of MP-FIR for short echo time MRS quantification

MP-FIR was initially designed for long echo time MRS quantification [273]. This section shows that this filter can be applied to short echo time MR spectra as well.

The result of applying a FIR filter to a time-domain signal y is defined in the time domain by the convolution

$$y_{fil}(n) = \sum_{m=0}^{M-1} h_m y(n-m), \tag{2.18}$$

where $\{h_m\}_{m=0,...,M-1}$ are the constant (possibly complex) filter coefficients. By truncating the distorted first $M-1$ data points [1] of this filtered signal, with $n = 0, ..., N-M$, $\hat{y}_{fil}(n)$ can be expressed as

$$\begin{aligned}
\hat{y}_{fil}(n) &= \sum_{m=0}^{M-1} h_m \sum_{k=1}^{K} \hat{y}_k(n-m+M-1) \\
&= \sum_{m=0}^{M-1} h_m \sum_{k=1}^{K} \alpha_k \zeta_k^{n-m+M-1} \sum_{p=1}^{P_k} \alpha_{k,p} \zeta_{k,p}^{n-m+M-1} \\
&= \sum_{k=1}^{K} \alpha_k \zeta_k^n \sum_{p=1}^{P_k} \alpha_{k,p} \zeta_{k,p}^n \sum_{m=0}^{M-1} h_m \zeta_k^{-m+M-1} \zeta_{k,p}^{-m+M-1} \\
&\simeq \sum_{k=1}^{K} \alpha_k \zeta_k^n \sum_{p=1}^{P_k} \alpha_{k,p} \zeta_{k,p}^n \sum_{m=0}^{M-1} h_m \zeta_{k,p}^{-m+M-1},
\end{aligned} \tag{2.19}$$

where we assume that $\zeta_k^{-m+M-1} \zeta_{k,p}^{-m+M-1} \simeq \zeta_{k,p}^{-m+M-1}$ and that each metabolite profile $v_k(n)$ can be modeled by a sum of Lorentzians, *i.e.* $v_k(n) = \sum_{p=1}^{P_k} \alpha_{k,p} \zeta_{k,p}^n$, P_k being the number of Lorentzians used to model the metabolite profile k. The linear part, $\alpha_{k,p}$, and the nonlinear part, $\zeta_{k,p}$ are defined similarly as in Eq. (2.3). Sundin *et al.* [273] showed that each individual Lorentzian (or by extension each corrected Lorentzian) lying in the frequency region of interest is not distorted by the filter if the condition of no distortion of Lorentzian (p,k) is written as

$$|\bar{h}\bar{\zeta}_{k,p}| = 1 \tag{2.20}$$

where

$$\bar{h} = (h_{M-1} \ \dots \ h_0) \tag{2.21}$$

and

$$\bar{\zeta}_{k,p} = (1 \ \ e^{(-d_{k,p}+j2\pi f_{k,p})\Delta t} \ \dots \ e^{(M-1)(-d_{k,p}+j2\pi f_{k,p})\Delta t})^T \tag{2.22}$$

Selesnick *et al.* [243] provided tools for calculating the coefficients h_m, which ensure that the magnitude response of $\hat{h}$ (*i.e.*, $|\bar{h} \ (1 \ \ e^{j2\pi f_{k,p}\Delta t} \ \dots \ e^{(M-1)(j2\pi f_{k,p})\Delta t})^T|$) is approximately equal to 1 in the frequency region of interest and equal to zero elsewhere. If we use the linear FIR filter by Selesnick, the components with higher damping factors $d_{k,p}$

[1] they are distorted since they assume zero values for the unknown $y(-1), ..., y(-M+1)$

will undergo a smaller gain (*i.e.*, smaller $|\bar{h}\bar{\zeta}_{k,p}|$) than the other ones resulting in signal distortion as described in [273]. In order to reduce the effect of this distortion vector, Sundin *et al.* [273] proposed to transform Selesnick's FIR filter into a maximum-phase FIR filter, moving most of the energy towards the first coefficients of $\bar{h}$ (*i.e.*, $h_{M-1}, h_{M-2}, ...$). The same principle is applicable for short echo time MR spectra.

2.3 Feature extraction methods

2.3.1 Extraction of features with physical meaning

In this section, classical MRS feature extraction methods (whole spectrum, peak integration, binning) are first discussed, then the quantification methods AQSES [213] and QUEST [225] are explained. Both methods are based on the model given in Eq. (2.2). However, they differ on several points:

- QUEST models the baseline using heuristic methods, where several steps are involved: truncation, partial fitting, subtraction, and final fitting. AQSES uses only one common optimization problem for the fitting of both the model and the baseline. As for the water removal, we conjecture that AQSES is thus less prone to accumulated errors, since its method is direct, and not a sequence of operations;
- AQSES uses the FIR filtering technique during quantification, while QUEST performs water suppression as a preprocessing step, generally using an SVD-based method such as HLSVD;
- In reference [226], an augmented Fisher information matrix (inspired by [262]) is used for the computation of confidence bounds for the variables of interest, but it is not clear how to choose the value for the number of effective parameters involved. In this respect, the semiparametric framework discussed in [246], based on asymptotic nonlinear regression theory, clarifies the way the confidence bounds can be automatically estimated for the procedure in AQSES.

Whole spectrum

Every point of the real or magnitude spectrum in the frequency region of interest is considered as an individual feature. In this thesis, magnitude spectra have been used to avoid phasing problems.

Peak integration

The oldest and still widely used quantification method in the frequency domain is based on the integration of the area under the peaks of interest [189]. The advantage is that no assumptions have to be made concerning the lineshape of the signal. Unfortunately, this method is not able to disentangle overlapping peaks and therefore to extract information from individual peaks or metabolite contributions. Residual baseline signals and low SNRs will also hamper good quantification. Furthermore, an appropriate phasing is necessary when dealing with the real part of the frequency-domain MRS signal, which is far from

trivial. Peak integration depends widely on the defined bounds. The tail of the peaks is also neglected by peak integration and the area under the peaks will be therefore underestimated (possibly by up to 40% [189]).

Binning

Instead of integrating over frequency regions, it is possible to aggregate the entire frequency ranges, described in the previous section, of the magnitude spectrum in a single pattern and use it as input for the classifier. Theoretically, compared to the full spectra, redundancy generated by spectral noise and artifacts is reduced in this manner. Also, these regions are assumed to contain most of the information, necessary to discriminate among tissue types.

AQSES

AQSES [213] is a time domain quantification method designed for short echo time MR spectra. The quantities of interest, *i.e.* the metabolite amplitudes, are the weighting coefficients of a linear combination of corrected *in vitro* metabolite profiles. The macromolecular baseline is incorporated into the fit via nonparametric modeling.

About the nuisance components
In AQSES, the baseline $b(t)$ is characterized by a smooth function. For the nonparametric modeling of the baseline, we construct a basis of splines [74, 57] and put the discretized splines as columns in a matrix A. An arbitrary nonlinear function can be approximated as a linear combination of spline functions. The coefficients in this linear combination are unknowns that must be identified. We denote these linear coefficients by $c_1, \ldots, c_n$ (or by $\mathbf{c} \in \mathbb{C}^n$, when stacked in a column vector). Thus, the discretization of a nonlinear function approximated with splines (in our case, the Fourier transform of the baseline b) can be written in matrix notation as the matrix-vector product $A \cdot \mathbf{c}$. Since the goal is to reconstruct a smooth baseline in the frequency-domain, while still fitting in the time domain, we transform the spline basis matrix A to the time domain, using the discrete inverse Fourier transform.

In order to fit the model and the smooth baseline at the same time, we consider the regularized nonlinear least squares criterion

$$\min \frac{1}{N} \sum_{t=t_0}^{t_{N-1}} |y(t) - \widehat{y}(t)|^2 + \lambda^2 \|D\mathbf{c}\|^2, \tag{2.23}$$

where $\widehat{y}$ is given in (2.2), but with the baseline b replaced by the formula $b = \mathcal{A} \cdot \mathbf{c}$, which is the inverse Fourier transformation of the frequency-domain baseline $A \cdot \mathbf{c}$. In Eq. (2.23), the whole term $\lambda^2 \|D\mathbf{c}\|^2$ is responsible for ensuring a certain degree of smoothness to the baseline b. The regularization matrix D is needed to measure the smoothness of the baseline in the frequency domain. We can take D as a (combination of) discrete derivative operator(s) [74]. λ is a fixed *regularization (penalty) parameter*; the value that we give to λ controls the degree of smoothness; this value can be automatically selected using a generalized cross validation criterion (see [246] for more details).

In AQSES, the water term $w(t)$ in Eq. (2.2) is *filtered out* using the maximum-phase pass-band FIR filter from [273], which is explained in Section 2.2.2. However, the region(s)

that should be filtered out of the *in vivo* signal should be specified by the user. Ideally, this filter will suppress all the components in the specified frequency region(s) so that the spectrum becomes there smaller than an estimated noise level, while keeping the frequency region(s) of interest undistorted. The design of the filter is performed outside the actual fitting method of AQSES (see Chapter 6). A FIR filter is a linear operator that commutes with the sum; however, it does not commute with the *modified* sum of metabolites, since the shifts and corrections on the spectral parameters involve nonlinear operations. When such an operation is applied to the measured signal, it must also be taken into account by the fitting model. In other words, a filtered measured signal will be fitted with a filtered model plus a filtered baseline. Thus, the filter is used explicitly during the iterative minimization in AQSES.

The quantification method

Assuming that we neglect the filter for sake of simplicity, the nonlinear least squares problem (2.23) becomes

$$\min_{\alpha_k,\zeta_k,\mathbf{c}} \frac{1}{N} \sum_{i=0}^{N-1} \left| y(t_i) - \sum_{k=1}^{K} \alpha_k \left(\zeta_k\right)^{t_i} v_k(t_i) - \left(\mathcal{A}\mathbf{c}\right)_i \right|^2 + \lambda^2 \|D\mathbf{c}\|^2 =$$
$$\min_{\boldsymbol{\alpha},\boldsymbol{\zeta},\mathbf{c}} \frac{1}{N} \left\|\mathbf{y} - \Phi(\boldsymbol{\zeta})\boldsymbol{\alpha} - \mathcal{A}\mathbf{c}\right\|^2 + \lambda^2 \|D\mathbf{c}\|^2, \tag{2.24}$$

where $\mathbf{y}$ is a column vector containing $y(t_0), \ldots, y(t_{N-1})$, $\boldsymbol{\alpha}$ and $\boldsymbol{\zeta}$ are defined as K-dimensional column vectors from the respective variables α_k, ζ_k, and the $N \times K$ matrix $\Phi(\boldsymbol{\zeta})$ has elements of the form:

$$\Phi_{ik} = \left(\zeta_k\right)^{t_i} v_k(t_i) = \exp\left((-d_k + j2\pi f_k)t_i\right) \cdot v_k(t_i), \tag{2.25}$$

Problem (2.24) is a *separable* problem, where linear parameters $\boldsymbol{\alpha}$ and $\mathbf{c}$ can be projected out of the least squares problem, and only a smaller sized nonlinear least squares problem remains to be solved for the nonlinear variables $\boldsymbol{\zeta}$, via an iterative minimization algorithm of the Levenberg-Marquardt type [193]. This technique is called *variable projection* (VARPRO [96, 95]). The VARPRO method was already used in MRS problems [292, 297]; a historical note on the application of VARPRO to MRS data quantification is given in Section 17 of the review work [96]. The previous use of VARPRO in the above mentioned works was restricted to long echo time MRS signals and models of the type "sum of complex damped exponentials."

In the AQSES framework, the classical VARPRO method is modified [247] such that it is possible to impose *prior knowledge* in the form of upper and lower bounds on the nonlinear parameters, linear equalities between some variables of the same sort among d_k or f_k, or even some constraints on the linear parameters (non-negative amplitudes and equal phases). Normally, VARPRO allows the complex amplitudes α_k to take any complex value such that the residual fit is minimized. In terms of the real parameters, this means that the real amplitudes a_k could take any non-negative value, while the phase corrections ϕ_k would be unconstrained between $-\pi$ and π. AQSES allows an option of *equal phase corrections*

for each metabolite, since it assumes that the database of metabolites is already constructed to have metabolites in phase. In terms of the VARPRO implementation, the equal phase constraint is a difficult constraint, since it involves part of the linear variables. Sima and Van Huffel [247] deal with this problem by adding one common phase correction variable to the nonlinear set of variables, and effectively imposing a *non-negativity* condition on the real-valued amplitudes a_k. The solution is numerically computed thanks to a nonnegative least squares method instead of closed-form least squares.

The VARPRO method implemented in AQSES is much more efficient than optimizing the nonlinear least squares problem (2.23) directly, over all linear and nonlinear parameters without separation. This improvement in computation efficiency is more important than in the previous use of VARPRO for long echo time MRS [292], since there are many more linear parameters than nonlinear ones, as many as there are spline coefficients. The number of spline coefficients is typically one tenth of the number of data points. Another advantage of VARPRO is that it does not encounter numerical problems when some amplitudes a_k are nearly zero. Moreover, the Levenberg-Marquardt algorithm needs good initial values for its variables; we found that good initial values for all the nonlinear parameters – frequency and damping corrections – are zeros, which means that we start the optimization with no spectral corrections to the signals in the database. In the equal phase case, an initial guess for the common phase corrections is estimated from a preliminary optimization round of the free phase algorithm.

Cramer-Rao bounds, specially adapted for semiparametric nonlinear regression [246], can also be computed as a by-product of the quantification procedure. They correspond to all the spectral parameters for the metabolites of interest (linear and nonlinear parameters, as well) and give an indication about the uncertainty of the final quantified parameters. If the given bounds are small enough relative to the corresponding parameter value, then it means that the computed value is reliable. If a large bound is found for a certain component, then the computed parameters might be unreliable. This is not due to a faulty minimization process; instead, it is due to poor signal-to-noise ratio, incomplete database of metabolites, or the inclusion of metabolites having similar spectra resulting in convergence problems. The risk of converging to local minima instead of global minima is indeed higher with a poor signal-to-noise ratio. The Cramer-Rao bounds estimated in AQSES are proportional to the variance of the residue plotted in AQSES GUI (see Appendix A). Therefore, it might also be helpful to inspect the residue to detect convergence problems. An example of result obtained with AQSES GUI is illustrated in Fig. 2.3. The parameter estimates and the Cramer-Rao bounds are given on the left hand side of the window.

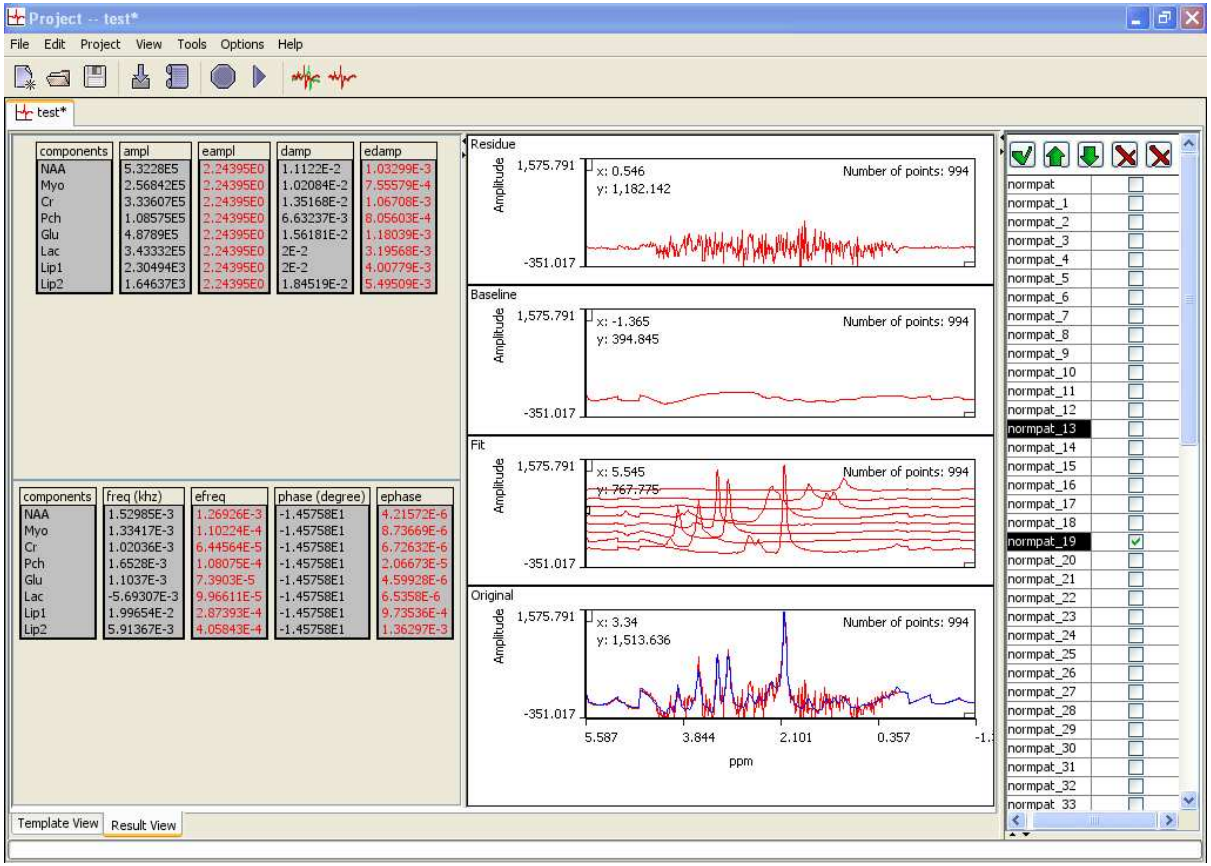


Figure 2.3. *The AQSES GUI results window. Plots from top to bottom: residue, baseline, corrected individual metabolite profiles and filtered original versus filtered reconstructed spectra (real part).*

QUEST

QUEST [225] is a time domain quantification method primarily designed for short echo time MR spectra and is implemented in the software package jMRUI-3.0[2]. Based on the fast decay of the background signal in the time domain, the background can be subtracted from the raw data after automatic estimation [225]. The nonlinear least squares problem in QUEST can be formulated as

$$\min_{\boldsymbol{\alpha},\boldsymbol{\zeta},\mathbf{c}} \frac{1}{N} \left\| \mathbf{y} - \Phi(\boldsymbol{\zeta})\boldsymbol{\alpha} \right\|^2 , \tag{2.26}$$

with the same notation as in Eq. (2.24). The NLLS fit method used in QUEST is described in [56]. In brief, it amounts to deriving a first-order Taylor expansion of Eq. (2.2), where the terms $b(t)$ and $w(t)$ have been removed, with respect to the parameters a_k, d_k, f_k and ϕ_k and iteratively solving for the unknown increments of these parameters by invoking the LAPACK subroutine DGELSS.

As mentioned, water filtering is not integrated in QUEST. Nevertheless, QUEST is able to deal with baseline via the heuristic below called the "subtract" method (see Alg. (2.3.1)).

Algorithm 2.3.1 *Subtract* method in QUEST

Input: filtered signal $y_{fil}(n)$, $n = 0, \ldots, N-1$, the number of points to be truncated

1: Truncate the initial data-points in which the macromolecule signal decays to below or near the noise level.
2: Estimate the metabolite parameters in Eq. (2.26) with a nonlinear least-squares (NLLS) fit. The fit should be perturbed by the macromolecules due to the truncation in *Step 1*. However, the truncation causes some loss of metabolite information, resulting in reduced precision of the estimates.
3: From the estimated parameters, compute the metabolite signal for $n = 0, \ldots, N-1$, and subtract the result from the measured MRS signal. The remainder is a metabolite-free estimate of the macromolecule signal including the measurement noise.
4: Model the macromolecule signal by a sum of K exponentially damped sinusoids with a state space method (*e.g.*, HLSVD-PRO).
5: Subtract the state space modeling result from the measured MRS signal. The remainder should be a "macromolecule-free" estimate of the metabolite signal including the measurement noise.
6: Estimate the metabolite parameters in Eq. (2.26) from the signal resulting in the previous step with an NLLS fit.

Output: the parameter estimates

Note that this algorithm can be repeated from *Step 3*, which may improve the accuracy of the parameter estimates as shown in [226]. However, the use of QUEST in this thesis is limited to the noniterative case.

[2] http://www.mrui.uab.es/mrui/ (Accessed: August 1, 2008)

2.3.2 Extraction of features based on mathematical criteria

Linear PCA

Principal component analysis (PCA) is a vector space transform often used to reduce multidimensional data sets to lower dimensions for analysis. PCA involves the calculation of the eigenvalue decomposition of a data covariance matrix or singular value decomposition of a data matrix, usually after mean centering the data for each attribute. For a data matrix, X^T, with zero empirical mean (the empirical mean of the distribution has been subtracted from the data set), where each row represents a different repetition of the experiment, and each column gives the results from a particular probe, the PCA transformation is given by:

$$Y^T = X^T W = V\Sigma \tag{2.27}$$

where $V\Sigma W^T$ is the singular value decomposition (SVD) of X^T. PCA has the property of being the optimal linear transformation for extracting the subspace that has largest variance. The applicability of PCA is limited by the assumptions made in its derivation:

- **Linearity.** The observed data set is assumed to be linear combinations of certain basis. Note that nonlinear methods such as kernel PCA have been developed wich do not assume linearity.
- **Statistical importance of mean and covariance.** PCA only finds the independent axes of the data under the Gaussian assumption. For non-Gaussian or multi-modal Gaussian data, PCA simply de-correlates the axes.
- **Large variances have important dynamics.** PCA simply performs a coordinate rotation that aligns the transformed axes with the directions of maximum variance. It is only when we believe that the observed data has a high signal-to-noise ratio that the principal components (PCs) with larger variance correspond to interesting dynamics and lower ones correspond to noise. In the case of low signal-to-noise ratio, the noise may contribute to the first PCs, and reducing the set of features may not be appropriate.

ICA

ICA is a technique that extracts statistically independent components from a set of measured signals [31]. The method is used for blind sources separation and can extract a pure signal from a set of mixtures. As there are partial volume effects present in MRS, a signal from a specific voxel can contain components of different tissue types. This is the main motivation to apply ICA to a set of MRS or MRSI spectra. With linear ICA, the components x_i of the observed random vector $x = (x_1, \ldots, x_m)^T$ are generated as a sum of the independent components s_k, $k = 1, \ldots, l$ weighted by the mixing weights $a_{i,k}$. With the added assumption of zero-mean and uncorrelated Gaussian noise $n \sim N(0, \mathrm{diag}(\Sigma))$, the ICA model takes the form $x = As + n$. Using a nonlinear mixing function $f(\cdot|\theta)$ with parameters θ the nonlinear ICA model is $x = f(s|\theta) + n$. The identifiability of independent component analysis requires that: 1) at most one of the sources s_k can be Gaussian, 2) the number of observed mixtures, m, must be at least as large as the number of estimated

components l: $m \geq l$. In other words, the mixing matrix A must be of full rank, such that an inverse exists.

Typical algorithms for ICA use centering, whitening, and dimensionality reduction as preprocessing steps in order to simplify and reduce the complexity of the problem for the actual iterative algorithm. Whitening and dimension reduction can be achieved with principal component analysis or singular value decomposition. Whitening ensures that all dimensions are treated equally a priori before the algorithm is run.

Fisher discriminant criterion

Fisher's criterion is a simple measure to compare the correlation between variables and the class label [84]. The idea is to project the D-dimensional input vector **x** onto a line

$$y = \mathbf{w}^T \mathbf{x} \tag{2.28}$$

where y is a scalar and **w** is a weight vector. Considering a treshold y_{th}, we classify $y \geq y_{th}$ as class $\mathcal{C}_1$, and otherwise as class $\mathcal{C}_2$. In general, the projection onto one dimension leads to a considerable loss of information, and classes that are well separated in the original D-dimensional space may become strongly overlapping in one dimension. In a two-class problem, the means of classes $\mathcal{C}_1$ and $\mathcal{C}_2$ are given by

$$\tilde{\mu}_1 = \frac{1}{N_1} \sum_{n \in \mathcal{C}_1} \mathbf{x}_n, \;\; \tilde{\mu}_2 = \frac{1}{N_2} \sum_{n \in \mathcal{C}_2} \mathbf{x}_n. \tag{2.29}$$

where N_1 and N_2 are the numbers of data of class $\mathcal{C}_1$ and $\mathcal{C}_2$, respectively; $\mathbf{x}_n$ is the nth observation (D-dimensional vector). We could define the distance between the projected means as our objective function, trying to find the best **w** such that $J(\mathbf{w})$ is maximum, with

$$J(\mathbf{w}) = \mathbf{w}^T |\tilde{\mu}_2 - \tilde{\mu}_1|. \tag{2.30}$$

However, this criterion does not take into account the standard deviation within the class. If the distance between the means is small compared to the spread of the data within the groups, it is logical to conclude that the discrimination power is also small. The criterion proposed by Fisher takes the standard deviation into account:

$$J(\mathbf{w}) = \frac{\mathbf{w}^T S_B \mathbf{w}}{\mathbf{w}^T S_W \mathbf{w}}. \tag{2.31}$$

where S_B is the between-class covariance matrix, given by

$$S_B = (\tilde{\mu}_2 - \tilde{\mu}_1)(\tilde{\mu}_2 - \tilde{\mu}_1)^T \tag{2.32}$$

and S_W is the total within-class covariance matrix, given by

$$S_W = \sum_{n \in \mathcal{C}_1} (\mathbf{x}_n - \tilde{\mu}_1)(\mathbf{x}_n - \tilde{\mu}_1)^T + \sum_{n \in \mathcal{C}_2} (\mathbf{x}_n - \tilde{\mu}_2)(\mathbf{x}_n - \tilde{\mu}_2)^T \tag{2.33}$$

Since the goal here is to establish the discrimative power of particular features, we project the samples onto the dimension of each of these features, and **w** is not optimized for maximizing $J(\mathbf{w})$ as defined in Eq. (2.31). For all variables in the training/validation set, a score is obtained and the features are ranked according to these scores. The goal is to trace the variables that best discriminate between the groups.

Kruskal-Wallis test

The Kruskal-Wallis test is a nonparametric alternative to the well-known one-way independent samples ANalysis Of VAriance (ANOVA). In contrast with ANOVA, this test makes no assumptions about the distribution of the data, so it can be used when normality of the data is not guaranteed. The main disadvantage is that the test is less powerful than ANOVA. The null hypothesis of the test is that the samples come from populations with equal medians. The Kruskal-Wallis test statistic is

$$H = \frac{12}{N(N+1)} \sum_{i=1}^{n_C} n_i (\overline{R_i} - \overline{\overline{R}})^2 \tag{2.34}$$

or alternatively

$$H = \frac{12}{N(N+1)} (\sum_{i=1}^{n_C} n_i \overline{R_i}^2) - 3(N+1), \tag{2.35}$$

where

$$\overline{R_i} = \frac{1}{n_i} \sum_{j=1}^{n_i} R_{ij}, \quad \overline{\overline{R}} = \frac{1}{n_C} \sum_{i=1}^{n_C} \overline{R_i}, \tag{2.36}$$

n_i denotes the number of samples in group i, n_C is the number of groups, R_{ij} is the rank of case j in group i after ranking all the cases of all groups and N is the total number of samples. When two values are equal, the average of the two ranks for which they tie is assigned. The value for the Kruskal-Wallis test can be compared with the chi-square statistic with $n_C - 1$ degrees of freedom if the sample size within each group is large enough (*e.g.*, > 5). This score is derived for all the features so that they can be ranked according to their chi-square value.

Relief-F

Relief-F is an extended and more robust version of the original Relief algorithm [229]. In contrast to many heuristic measures for feature selection, Relief-F does not assume conditional independence of the variables. The main idea of the Relief-F is to estimate the quality of features based on how good their values discriminate between samples that are close. Consecutively random samples are drawn from the data set. Each time the k (*e.g.* 10) nearest neighbors of the same class and the opposite class are determined. Based on these neighboring cases the weights of the attributes are adjusted. The simplified Relief-F algorithm for two classes is structured as explained below (see Alg. (2.3.2)).

If the selected case has different values for an attribute compared to the neighbors of the same class, the weight of that attribute decreases. On the other hand when the attribute value for the specific case is different from the ones of the opposite class neighbors, the weight of the attribute increases. The contribution of all the hit and missing neighbors is averaged in the weight computation rule. The difference measure is defined as

$$\text{diff}(a, x_1, x_2) = \frac{|x_{1a} - x_{2a}|}{\text{range}(a)}, \tag{2.37}$$

Algorithm 2.3.2 Relief-F

Input: r = number of random examples to draw, f = number of features, k = number of nearest neighbors, x = training data, y = labels of the training data.

1: **for** $a = 1, \ldots, f$ **do**
2: W_a = 0
3: **end for**
4: **for** $i = 1, \ldots, r$ **do**
5: randomly select an instance (x_t,y_t)
6: compute the k nearest h_j with similar y_t value
7: compute the k nearest m_j with different y_t value
8: **for** $a = 1, \ldots, f$ **do**
9: $W_a := W_a - \sum_{j=1}^{k} \frac{\text{diff}(a,x_t,h_j)}{rk} + \sum_{j=1}^{k} \frac{\text{diff}(a,x_t,m_j)}{rk}$
10: **end for**
11: **end for**

Output: W = weights indicating quality of the features

where x_{1a} and x_{2a} are the values for feature a for instance x_1 and instance x_2, respectively. The range of a feature is defined as the difference between its maximum and minimum value over all training data. As within the two previous algorithms the variables are ranked and different models are built by dropping the variable with the smallest weight. The other part of the selection procedure is completely analogous to the one followed in the two previous methods. Although the Relief-F algorithm is computationally more expensive and complex than the previous techniques, the cost of an exhaustive search is still much higher.

2.4 Classification methods

2.4.1 Linear Discriminant Analysis

Linear discriminant analysis (LDA) and the related Fisher's linear discriminant are methods used in statistics and machine learning to find the linear combination of features which best separate two or more classes of objects or events. Starting from the Fisher criterion in Eq. (2.28), the data are classified in class $\mathcal{C}_1$ if $y \geq y_{th}$, and $\mathcal{C}_2$ otherwise. In this case, $\mathbf{w}$ is chosen to maximize the criterion $J(\mathbf{w})$ in Eq. (2.31). Choosing a nonoptimal $\mathbf{w}$ would lead to a classifier with less discrimant abilities as shown in Fig. 2.4.

2.4.2 (Least Squares) Support Vector Machines

Support vector machines (SVMs) are very flexible sparse models for regression and classification [300]. SVMs are developed for binary classification, even though multi-class extensions exist [301, 308]. SVM maps the input vector $\mathbf{x}$ into a high dimensional feature space $\mathcal{H}$ through a (non)linear mapping $\varphi : D \rightarrow \mathcal{H}$, with D and $\mathcal{H}$ are p and q dimensional (see Fig. 2.5). The feature space can be infinite dimensional. A class of hyperplanes in the

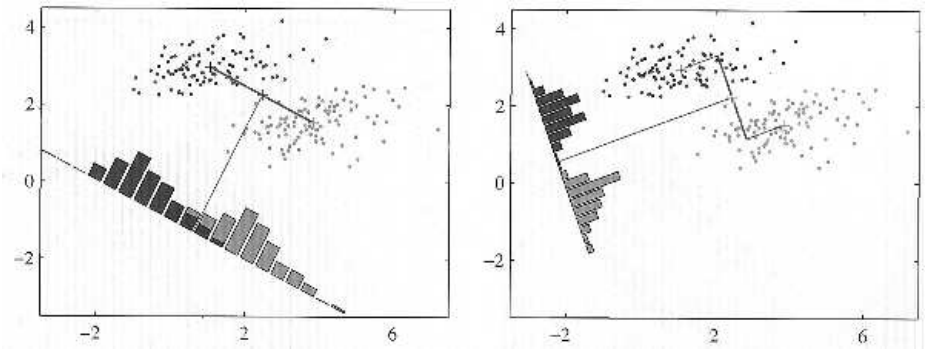


Figure 2.4. *These plots illustrate that a nonoptimal choice of* $\mathbf{w}$ *leads to a classifier with poor discriminant abilities. Left: nonoptimal* $\mathbf{w}$*. Right: optimal* $\mathbf{w}$*. Figure taken from [19].*

feature space is then given by $\mathbf{w}^T\phi(\mathbf{x}) + b$ with $b \in \Re$ and $\mathbf{w}$ a weighting vector with the same dimension as $\varphi(\mathbf{x})$. The goal is to find the hyperplane which separates the best both classes, by finding a trade-off between maximization of the margin between both classes and minimization of the number of misclassifications. In this thesis, a variant of SVM, the least squares support vector machines (LS-SVM), is used. LS-SVM can be solved by a linear system, while SVM requires to solve a quadratic programming problem. On the other hand, LS-SVM loses the property of sparseness, which also reduces the complexity of the problem by reducing the number of support vectors (data that actually contribute to the classification). The LS-SVM classifier in the primal space is

$$y(\mathbf{x}) = \text{sign}\Big[\mathbf{w}^T\varphi(\mathbf{x}) + b\Big], \tag{2.38}$$

where $y(\mathbf{x})$, the class prediction, is obtained by minimizing the objective function

$$\begin{aligned} \min_{\mathbf{w},b,\mathbf{e}} \mathcal{J}_P(\mathbf{w},\mathbf{e}) &= \frac{1}{2}\mathbf{w}^T\mathbf{w} + \gamma\sum_{n=1}^{N} e_n^2 \\ \text{such that} \quad & y_n\Big[\mathbf{w}^T\varphi(\mathbf{x}_n) + b\Big] = 1 - e_n,\ n = 1, ..., N \end{aligned} \tag{2.39}$$

where the first term in Eq. (2.39) is responsible for margin maximization, the second term is responsible for minimization of misclassifications, $\mathbf{w}$ is the weight vector of length q, b is the bias term, e_n is the error variable, and γ is a hyperparameter to control the amount of regularization. Some tolerance of misclassification is allowed by e_n. The Lagrangian can be constructed from Eq. (2.39).

$$\mathcal{L}(\mathbf{w}, b, e, \alpha) = \mathcal{J}_P(\mathbf{w}, e) - \sum_{n=1}^{N}\alpha_n\Big(y_n\Big[\mathbf{w}^T\varphi(\mathbf{x}_n) + b\Big] - 1 + e_n\Big), \tag{2.40}$$

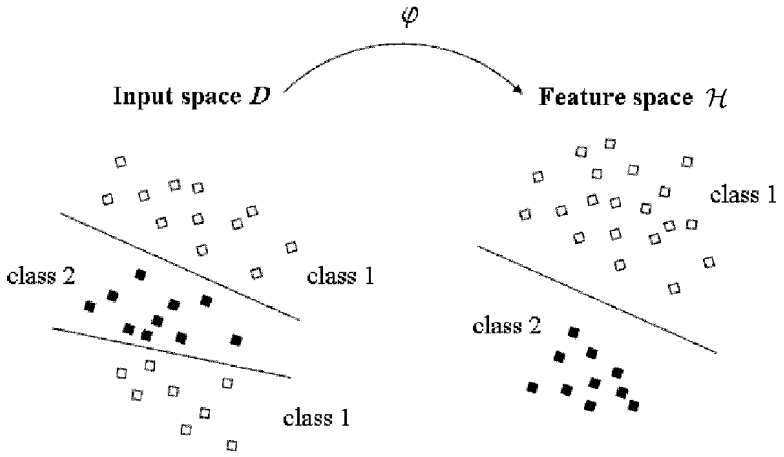


Figure 2.5. *In the input space classes 1 and 2 are nonlinearly separable. By mapping the input space to a high-dimensional feature space a linear separation can be made.*

where α_n are the Lagrange multipliers ($n = 1, ..., N$) or the support values.

$$\begin{cases} \frac{\partial \mathcal{L}}{\partial \mathbf{w}} & = & 0 \rightarrow \mathbf{w} = \sum_{n=1}^{N} \alpha_n y_n \varphi(\mathbf{w}_n) \\ \frac{\partial \mathcal{L}}{\partial b} & = & 0 \rightarrow \sum_{n=1}^{N} \alpha_n y_n = 0 \\ \frac{\partial \mathcal{L}}{\partial e_n} & = & 0 \rightarrow \alpha_n = \gamma e_n, \ n = 1, ..., N \\ \frac{\partial \mathcal{L}}{\partial \alpha_n} & = & 0 \rightarrow y_n \Big[\mathbf{w}^T \varphi(\mathbf{x}_n) + b \Big] - 1 + e_n = 0, \ n = 1, ..., N. \end{cases} \tag{2.41}$$

This results in the following linear optimization problem in the dual space, to be solved in

$$\left[\begin{array}{c|c} 0 & \mathbf{y}^T \\ \hline \mathbf{y} & \Omega + I/\gamma \end{array} \right] \left[\begin{array}{c} b \\ \hline \alpha \end{array} \right] = \left[\begin{array}{c} 0 \\ \hline 1_N \end{array} \right], \tag{2.42}$$

where $\mathbf{y} = [y_1 ... y_n]^T$, $1_N = [1...1]^T$, and $\Omega \in \mathbb{R}^{N \times N}$ is a matrix with elements $\Omega_{nm} = y_n y_m \varphi(\mathbf{x}_n)^T \varphi(\mathbf{x}_m)$ with $n, m = 1, ..., N$.

Given an input vector $\mathbf{x}$, the classifier in the dual space takes the form

$$y(\mathbf{x}) = \text{sign} \left[\sum_{n=1}^{N} \alpha_n y_n K(\mathbf{x}, \mathbf{x}_n) + b \right], \tag{2.43}$$

where $K(\cdot, \cdot)$ is a kernel function. This reformulation allows us to work in the high-dimensional feature space without explicitly constructing it by using a positive definite

kernel satisfying the Mercer's condition

$$K(\mathbf{x}, \mathbf{z}) = \varphi(\mathbf{x})^T \varphi(\mathbf{z}). \tag{2.44}$$

This relation is often called the kernel trick. The feature space is determined by the specific kernel function used. The linear kernel, $K(\mathbf{x}, \mathbf{z}) = \mathbf{x}^T\mathbf{z}$, results in a linear separation between the two classes in the original input space. On the other hand, nonlinear kernels such as the radial basis function (RBF) kernel, $K(\mathbf{x}, \mathbf{z}) = \exp\big(-\|\mathbf{x} - \mathbf{z}\|^2\big)/\sigma^2$, create a nonlinear decision boundary in the input space.

Some properties and remarks on LS-SVM

- **Global and unique solution.** The optimization problem in LS-SVM is convex, which means that a unique and global solution exists (at least if we consider that the matrix in Eq. (2.42) has full rank).
- **Lack of sparseness.** Typically, no support value α_n will be zero and all training cases are support vectors. The training cases with large $|\alpha_n|$ are not necessarily close to the decision boundary, but they have a high contribution on the latter.
- **Primal or dual space.** Depending on the problem it may be more interesting to solve the problem in the primal space, when the number of training data is large compared to the number of features, or the dual space, when the number of features is large compared to the number of training data.
- **Choice of γ and σ.** The choice of the regularization parameter γ and the kernel width σ (used in case of RBF kernel) is often done by cross-validation methods. A bayesian framework is also possible [274].
- **From continuous latent output to binary class prediction.** In Eq. (2.38), the prediction is based on the sign of the latent output. However, this may not be the best way to obtain the best predictions. Another threshold may be preferred, especially if one class is more common than the other. This can also be obtained by adjusting the value of the bias term b.

2.4.3 Performance measure

The basic measures of accuracy of a diagnostic test are the sensitivity, the specificity and the accuracy:

- the **sensitivity** is the proportion of cases of the class of interest (often called class 1) that are correctly predicted as class 1 members,
- the **specificity** is the proportion of cases from the other class (class 0) that are correctly predicted,
- the **accuracy** is the proportion of cases correctly predicted

The sensitivity, specificity and accuracy can be also be expressed in terms of true positive (TP), true negative (TN), false positive (FP) and false negative (FN):

$$\text{sensitivity} = \frac{\text{TP}}{\text{TP}+\text{FN}}, \text{specificity} = \frac{\text{TN}}{\text{FP}+\text{TN}}, \text{accuracy} = \frac{\text{TN}+\text{TP}}{\text{total}}.$$

A test sample is assigned to one of the two groups or classes depending on the output value (latent output) of the diagnostic test relative to a certain cut-off point. The choice of this cut-off point is arbitrary. Hence it is important to choose a performance criterion that is independent from the cut-off point: the area under the curve (**AUC**) of the receiver operating characteristic (ROC). The ROC curve is a graphical representation of sensitivity versus 1-specificity as the cut-off is varying, each point of the graph being generated with a different cut-off point (see Fig. 2.6). Tests with an AUC of 0.5 have no discrimination ability since there is 50% chance of predicting the wrong class, which could be reached without classifier. The closer the AUC is from 1, the better the diagnostic test, a perfect test passing through the upper left corner in Fig. 2.6 (100% sensitivity and 100% specificity). When the number of data in, at least, one of the classes is limited, the ROC takes a bumpy shape and smoothing methods might be useful to obtain better estimates of the AUC. These methods can be parametric [187], nonparametric [317] or based on bootstrap [202].

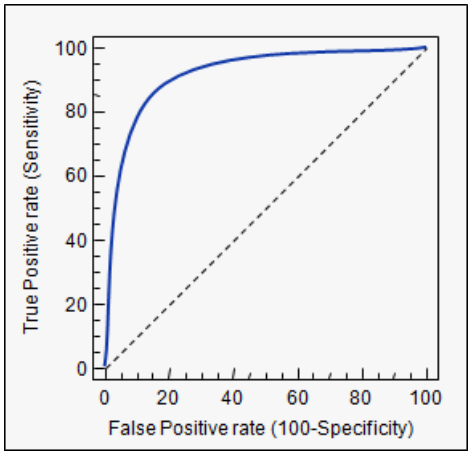


Figure 2.6. *Example of ROC curve.*

In chapter 8, we also perform multiple comparison procedures such as the Tukey test and the Friedman test. These tests are briefly explained below.

Tukey multiple comparison procedure

In the Tukey test, the family of interest is the set of all pairwise comparisons of factor level means:

$$H_0 : \mu_i - \mu_{i'} = 0$$

$$H_1 : \mu_i - \mu_{i'} \neq 0$$

When all sample sizes are equal, the family confidence coefficient is exactly $1 - \alpha$ and the family significance level is α. When the sample sizes are not equal the family confidence coefficient is greater than $1 - \alpha$ and the family significance level is less than α, which means that this test is conservative when the sample sizes are not equal.

A tool commonly used when all samples sizes are equal, *i.e.*, when $n_i \equiv n$, is the "paired comparison plot". Around each estimated treatment mean $\hat{Y}_{i.} = \sum_j \frac{Y_{ij}}{n_i}$ is plotted an interval whose limits are

$$\hat{Y}_{i.} \pm \frac{1}{2} T s\{\hat{D}\} \tag{2.45}$$

where $\hat{D} = \hat{Y}_{i.} - \hat{Y}_{i'.}$, $s\{\hat{D}\} = MSE(\frac{1}{n_i} + \frac{1}{n_{i'}})$, $MSE = \frac{\sum_i \sum_j (\hat{Y}_{i.} - Y_{ij})^2}{n_T - r}$ is the mean squared error, n_T is the number of data in total, *i.e.*, $n_T = \sum_{i=1}^{r} n_i$, r the number of treatments, $T = \frac{1}{\sqrt{2}} q(1 - \alpha; r, n_T - r)$, q follows a studentized range distribution (see, *e.g.*, [201]).

Friedman test

1. Given data $\{x_{ij}\}_{n \times k}$, that is, a array with n rows (the blocks), k columns (the treatments) and a single observation at the intersection of each block and treatment, calculate the ranks within each block. If there are tied values, assign to each tied value the average of the ranks that would have been assigned without ties. Replace the data with a new array $\{r_{ij}\}_{n \times k}$ where the entry r_{ij} is the rank of x_{ij} within block i.
2. Find the values:

- $\bar{r}_{\cdot j} = \frac{1}{n} \sum_{i=1}^{n} r_{ij}$
- $\bar{r} = \frac{1}{nk} \sum_{i=1}^{n} \sum_{j=1}^{k} r_{ij}$
- $SS_t = n \sum_{j=1}^{k} (\bar{r}_{\cdot j} - \bar{r})^2$,
- $SS_e = \frac{1}{n(k-1)} \sum_{i=1}^{n} \sum_{j=1}^{k} (r_{ij} - \bar{r})^2$

3. The test statistic is given by $Q = \frac{SS_t}{SS_e}$. Note that the value of Q as computed above does not need to be adjusted for tied values in the data.
4. Finally, when n or k is large (*i.e.* $n > 15$ or $k > 4$), the probability distribution of Q can be approximated by that of a chi-square distribution. In this case the p-value is given by $\mathbf{P}(\chi^2_{k-1} \geq Q)$. A p-value inferior to the significance level α indicates that the treatment means differ. If n or k is small, the approximation to chi-square becomes poor and the p-value should be obtained from tables of Q specially prepared for the Friedman test. If the p-value is significant, appropriate post-hoc multiple comparisons tests would be performed.

2.5 Conclusion

In this chapter, the different methods used in this thesis have been described. We defined how we model *in vivo* MRS data and how we preprocess them. The preprocessing methods should be applied in a specific sequential order. A special attention is paid to water filtering methods, namely HLSVD-PRO and MP-FIR, that are further analyzed in Chapters 6 and 7. Although these methods have the same purpose, *i.e.*, filtering out the water components, they are based on totally different approaches and exhibit different properties. In the second part of this chapter, we detailed the feature extraction methods. We distinguished between the methods that extract features with physical meaning and the ones that extract features based on mathematical considerations. The former ones provide biologically interpretable features, which may be interesting for developing new medical treatments, while the mathematical methods may extract information from the data that allows a better separation of the tumor classes, but may be hard to interprete in biological terms. In the last part of this chapter, a linear classification method, LDA, and a nonlinear one, LS-SVM, are outlined. The dimensionality of MRS data when taking all the spectral points may be very high. In that case, LDA needs to be preceded by a feature reduction method like PCA. On the contrary, LS-SVM is particularly well designed for high dimensional data in terms of computation complexity. Moreover, nonlinear boundaries (separating the classes) can be determined with LS-SVM, but not with LDA. Performance measures are finally defined together with multiple comparison procedures, which allow to determine whether a treatment is significantly different from another.

Chapter 3

Review of quantification methods in ^{1}H MRS

This chapter[1] *reviews the existing quantification methods in Magnetic Resonance Spectroscopy. The goal of this chapter is multifold: to introduce the problematic of quantification, to explain the main principles of the quantification methods and to help anyone involved in* ^{1}*H MRS to choose the most appropriate quantification method. Quantification of* ^{1}*H MRS is not a trivial problem due to a nonperfect acquisition (instrumental effects, imperfect shimming, body motion), but also due to the large amount of information that is often contained in such spectra. The quantification strategy and, consequently, the quantification method, depends on the data but also on the pursued objectives: are we working on long or short echo time data, on in vivo or ex vivo data; are we interested in macromecules or just in metabolites (or even in only one or two metabolites), etc. This chapter deals with these different aspects of quantification.*

3.1 Introduction

Magnetic resonance spectroscopy (MRS), able to reflect the concentration of metabolites, complements magnetic resonance imaging (MRI) as a noninvasive means for the characterization of tissue. Although the use of MRS in clinical practice remains relatively limited, especially due to time constraints and the lack of expertise in MRS, it has been increasingly used in hospitals. Information that can be extracted from in vivo MRS is continuously increasing thanks to, among others, shorter echo times and higher external magnetic fields (up to 7T for human beings). From one voxel, the information has been extended to a grid of voxels using magnetic resonance spectroscopic imaging (MRSI), allowing the use of spatial information. Encouraging results have shown the potential of MRS and MRSI

[1] J. Poullet, D.M. Sima, S. Van Huffel, MRS signal quantification: a review of time- and frequency-domain methods, J. Magn. Reson. 195(2) (2008) 134-144, and
J. Poullet, D.M. Sima, S. Van Huffel, Metabolite quantification in MRS and pattern recognition, Internal Report 08-84, ESAT-SISTA, K.U.Leuven (Leuven, Belgium), 2008, submitted for publication to the Encyclopedia of Magnetic Resonance.

and the interest to develop automated diagnosis tools based on these techniques. The great success of MRS and MRSI is mainly due to their noninvasiveness. Indeed, a noninvasive and accurate prediction of lesion type may reduce unnecessary surgical biopsy procedures for noncancerous lesions and for less accessible tumors that would be treated by radio- or chemotherapy rather than surgical resection [117]. A biopsy is not without risk of morbidity and mortality and cannot be performed in some cases (for example, brain stem tumors, paediatric tumors). Quantification can be useful for clinical diagnosis to characterize pathological tissue. It has been successfully applied to the diagnosis of cancer [65], epilepsy [302], dementia [119], leukemia [47], multiple sclerosis [234].

One of the major goals in MRS is to quantify metabolite concentrations. However, despite tremendous efforts and numerous publications on the subject, it remains difficult to obtain accurate estimates of these concentrations, due to, *inter alia*, field inhomogeneities, relatively low signal-to-noise ratios (SNR), physiologic motion.

The goal of this chapter is to give an overview of the existing MRS quantification methods. Preprocessing methods, as part of the quantification strategy, are also addressed. This includes macromolecule and solvent (or water) suppression and lineshape correction. MRS quantification methods are usually divided into two principal categories: methods in the time domain [289, 297] and methods in the frequency domain [190]. In theory, there are no differences between the two domains [2]. However, we will see that this is not totally true in practice due to some practical limitations. An introduction of the common processing methods in *in vivo* MR spectra is given in [121]. For sake of space, the scope of this thesis is limited to post-acquisition methods, *i.e.* methods that are applied after signal acquisition. Time-domain methods are known to give more flexibility for the model function and specific time-domain preprocessing [297], whereas frequency-domain methods are intuitively suited for visual interpretation and frequency selective analysis [190]. This section is organized as follows. First, we introduce the concept of absolute and relative concentrations, their advantages and limitations (Section 3.2). Then, the effects of acquisition conditions are outlined and general rules for assessing the quality of a spectrum are given (Section 3.3). Finally, the main principles of quantification methods are reviewed (methods in the time domain in Section 3.4 and in the frequency domain in Section 3.5), nuisance component effects and methods to correct or remove them are reported, and tools to study the quantification error estimates are given (Section 3.6). Tips for choosing the most appropriate quantification method are also proposed (Section 3.7).

3.2 Absolute or relative concentrations

An MR spectrum is made of components (peaks) corresponding to several metabolites. The molecular structure of a particular metabolite is reflected by a typical peak pattern. The separation between peaks is due to the differences in the chemical environment of the different nuclei (see Section 1.1.1). The area under a peak is directly proportional to the number of nuclei and to the metabolite concentration to which the nuclei belong. The linewidth is related to the mobility of the metabolite in its environment, large molecules (or macromolecules) having less mobility and thus larger linewidths. The lineshape of the metabolite resonances is, in theory, Lorentzian, but, due to diverse artefacts, may deviate

from this ideal shape in experimental conditions. The problem of quantification is to disentangle the contributions of each component: the metabolites, the macromolecule (also possibly divided into several components), the water resonances, the noise, etc. Due to the imperfections and the large amount of information in the signal, prior knowledge is often required to obtain accurate concentration estimates.

Quantification can provide absolute metabolite concentrations or ratios relative to a certain resonance (for example, the water resonance [284] or a metabolite resonance like the one of Creatine at 3.03 ppm [80]) or other signal features (for example, the so-called L2-norm, which is the norm of the metabolite signal in the region of interest [65], see Section 2.2.1). Absolute concentrations are expressed in biochemical units such as molarity (number of moles of metabolite per litter of tissue water) and molality (number of moles of metabolite per kilogram of tissue water), whereas ratios are expressed in arbitrary units. Absolute quantification involves corrections for T_1- and T_2-relaxation behaviour. As T_1- and T_2-values differ between different brain regions [192] and water T_2-values are elevated in several brain tumour tissues compared to normal white matter [117], assessment of good estimates of T_1- and T_2-values for all relevant types of pathological tissues is very difficult. Advantages and drawbacks of both absolute concentrations and ratios can be summarized here:

- Ratios are less sensitive to abnormalities than absolute concentrations.
- The reference peak used in the ratios is not quantifiable, reducing by 1 the number of features. Furthermore, it is impossible to assess which metabolite concentrations have actually changed (reference peak or the numerator). The assumption that the concentration of a reference metabolite remains constant may be incorrect.
- Ratios may cause larger errors than absolute concentrations, with higher coefficients of variations for ratios in single voxel MRS [240] and chemical shift imaging (CSI) [157].
- Absolute concentrations are only useful when all reference steps are done correctly (for example, T_1 and T_2 should be correctly estimated), otherwise unwanted additional errors may be introduced.

3.3 Effects of acquisition conditions and MRS spectra quality assessment

3.3.1 Effects of relaxation times on metabolite signals

Peak areas are influenced by the T_1 and T_2 relaxation times. T_1 values are not the same for most metabolites and a too small repetition time (TR) will result in a decrease of the metabolite signals. For example, a TR of 2000 ms will cause a reduction of the NAA signal of approximately 25%, whereas a TR of 7000 ms will cause a reduction of only 0.7% [125]. Increasing the TR means increasing the duration of the MR acquisition.

T_2 values also influence the metabolite signals. For example, a TE of 100 ms will lead to a decrease of approximately 21% of the NAA signal, while the signal loss will be reduced to 5% if a TE of 20 ms is used [125]. Macromolecules (compounds with a high

relative molecular weight) have a very short T_2 relaxation time (<50 ms at 2.1 T [17]). This explains why these components are absent in long echo time MRS spectra, where almost only uncoupled spins remain visible such as NAA, choline or total creatine. An echo time of 20 ms will lead to a loss of approximately 30% of the macromolecule signal.

An accurate estimation of T_2 is therefore required to obtain correct absolute metabolite concentrations. Relaxation times may be influenced by pathological conditions. For example, for diseases such as low-grade glioma and high-grade glioma, the T_2 relaxation times can be reduced up to 38% and 43%, respectively [123]. Metabolite T_1 and T_2 may also be age-dependent [147] or body-region-dependent [197].

3.3.2 Effects of physiological motion

Physiologic motion can have a large effect on MRS quantification [82]. Even small repeated body motions or pulsatile motion due to cardiac activity can substantially affect the characteristics of the MR signal.

3.3.3 Effects of shape and location of the volume of interest

When a section-selective gradient is applied to a volume containing metabolites with different chemical shifts, the sensitive volume for each resonance will be shifted according to the bandwidth of the radio frequency (RF) pulse [60] and the voxel size. For example, consider two resonances spaced by 100 Hz in the frequency domain, a RF bandwidth of 1000 Hz and a voxel size of $2\times2\times2$ cm^3. The displacement of each of the voxel will be of 100/1000=0.1 cm in the three directions, resulting in an 85.7% overlap of the two voxels. This should be taken into account, especially when quantifying metabolites in voxels located at border regions (for example, in the neighborhood of the skull or of a tumor region). There are two ways to reduce this displacement effect, either we increase the RF bandwidth or we increase the voxel size. Increasing the RF bandwidth is limited by safety conditions, since the RF energy will induce electrical currents within conductive human tissue, which might lead to tissue heating if they are excessive. Increasing the voxel size will result in less homogeneous voxels, which might hamper tumor typing for instance.

3.3.4 MRS spectra quality assessment

The quality of an MR signal can be based on several criteria: the linewidth, the signal-to-noise ratio (SNR), the Cramér-Rao bounds (see Section 3.3.5), the signal features. From a statistical point of view, discarding data should only be performed when the data are abnormal. The boundaries of abnormality are difficult to define. However, criteria exist to reject MR spectra. First, one can estimate the linewidth of the peaks and their expected values. If the peaks are too wide, the spectrum is rejected. Smaller VOI, better shimming, and VOI further from tissue interfaces may improve the linewidth. Kreis [144] proposed the following rejection criteria for MRS spectra and their fitting results:

1. full width at half maximum of the metabolites larger than 0.07-0.1 ppm;

2. Cramér-Rao bound larger than 50% for the estimated concentrations;

3. unexplained features in the residuals of the model fitting;

4. peaks doubled or patient moved;

5. presence of artefact or strongly asymmetric lineshapes after eddy current correction.

In [291], van der Graaf *et al.* describe a practical approach to spectral quality assessment and quality control in a multicentre MRS study on brain tumors.

3.3.5 Quantification accuracy

A perfect fit does not mean that the parameter estimates are equal to the true parameter values. A common tool to study the error estimates in fitting algorithms is the Cramér-Rao bound (CRB) which expresses a lower bound on the variance of estimators of a deterministic parameter. Systematic errors due, for example, to incorrect prior knowledge may result in underestimation errors. Constraints on the fitting model reduce the CRBs of the spectral parameters [36]. The values of the CRBs give an indication of the precision of the parameter estimates. Nevertheless, one should be careful when drawing conclusions from the CRBs since small CRBs do not necessarily ensure that the parameter estimates are close to the true values. Ratiney *et al.* [226] and Sima and Van Huffel [246] proposed different approaches to extend the classical CRB to semiparametric modeling problems in order to take into account the baseline in the calculation of the covariance matrix.

3.4 Time-domain quantification methods

Recently, more attention has been paid to time-domain fitting methods [213, 226, 78]. Quantification is carried out in the same domain as the domain where the signals are measured, giving more flexibility to the model function and allowing specific time-domain preprocessing. Time-domain fitting methods are usually divided into two main classes: black-box or non interactive methods (see, *e.g.*, [230, 11, 277, 210, 42, 152]) and methods based on iterative model function fitting or interactive methods (see, *e.g.*, [213, 226, 78, 292, 299]), referring to the degree of interaction required by the method from the user.

3.4.1 Interactive methods

Global or local optimization

The objective of the interactive methods is usually to minimize the difference between the data and the model function, resulting in a typical nonlinear least-squares (NLLS) problem. This problem can be solved using local or global optimization theory. The main disadvantage of optimization procedures finding global optima, such as simulated annealing or genetic algorithms (used in MRS in [305, 188, 69]), is their poor computational efficiency. However, these methods decrease the risk of converging to a local minimum, which often occurs when the search space is of high dimension and when the starting values for the parameters are far from the global optimum. Most of the quantification methods in MRS are based on local optimization techniques (see, *e.g.*, [292, 299, 213]).

Use of a basis set of metabolite profiles in the model function or not

Another important feature of the interactive methods is whether they use a basis set of metabolite profiles or not. VARPRO [292], the local optimization procedure based on Osborne's Levenberg-Marquardt algorithm [206], was the first widely used method for quantifying MRS data. It has been replaced later by AMARES, which proved to be better than VARPRO in terms of robustness and flexibility [299]. AMARES allows more prior knowledge and can also fit echo signals. These methods do not use a metabolite basis set even if the prior knowledge in AMARES can be derived from phantom data as suggested in [236]. In the presence of water components, the frequency-selective versions of VARPRO [140] and AMARES (AMARES$_W$ [298]) are preferred and are expected to give good results for relatively well-separated peaks. However, these methods break down if nuisance peaks (*i.e.*, peaks that are in the same frequency region but are unwanted) have large amplitudes or are close, in frequency, to the peaks of interest [230, 298]. Although methods such as AMARES have been applied quite successfully to short echo time MR spectra [130], the nuisance peaks and the more intensive user interaction tend to encourage methods based on the use of metabolite profiles since more prior knowledge is implicitly included in the model, especially information related to experimental conditions of acquisition.

On the other hand, methods such as AQSES [213] or QUEST [226] make use of a metabolite basis set, which can be built up from simulated spectra (*e.g.*, via programs based on quantum mechanics such as NMR-SCOPE [99] or GAMMA [256]) or from *in vitro* spectra. In [311], a spectral simulation method using GAMMA for generating *a priori* information to be used in parametric spectral analysis is described. The use of a metabolite basis set facilitates the disentangling of overlapping resonances when the corresponding metabolite profiles also contain at least one non-overlapping resonance. Incorporating prior knowledge has been shown to provide better accuracy [35]. When adding prior knowledge one should take into account the acquisition specifications such as the type of external field B_0, temperature, echo time, repetition time, pH, pulse sequence, etc. If the metabolite profiles are *in vitro* signals, the protocol used to acquire the *in vitro* signals should be similar to the one used to acquire the *in vivo* data. The influence of measured and simulated basis sets on metabolite concentration estimates, using QUEST as quantification method, has been studied in [54]. In [78], Elster *et al.* proposed a semi-parametric model with an uncertainty analysis based on a Bayesian framework. They showed that this analysis yields a more appropriate characterization of the errors on the parameter estimates than the commonly used Cramér-Rao error bounds, which tend to overestimate accuracy.

How to choose the lineshape and the number of components in the model?

Even though individual metabolite signals can theoretically be represented by one or several complex damped exponentials (*i.e.*, Lorentzians), in real-world situations, a perfect homogeneous magnetic field cannot be obtained throughout the sample. Therefore, Gaussian and/or Voigt lineshapes are sometimes preferred when substantial deviations from the ideal Lorentzian lineshape occur. In [244], the continuous wavelet transform is proposed to extract iteratively each resonance from the raw signal starting with the water peak, and is able to accomodate to both the Lorentzian and the Gaussian models. The model giving the best fit is selected. The problem with this approach is that if an error occurs in the first step it will be propagated all along the extracting process. The choice of the lineshape, which also determines the number of parameters per component in the model is a nontrivial

problem, which is hardly solvable by a simple glance at the spectra.

Another nontrivial choice is how many components should be used in the model, *i.e.*, how many Lorentzians (or other lineshapes) in VARPRO or AMARES or which metabolite profiles in AQSES or QUEST. Knijn *et al.* [140] showed that the use of a variable projection method (used in VARPRO and AQSES and not in AMARES or QUEST) reduces the sensitivity to the absence of features in the model. A variable projection method does not encounter numerical problems either when some amplitudes are nearly zero [213]. It is therefore reasonable to prefer methods based on the variable projection algorithm when there is an uncertainty about the components present in the signal. Therefore, iterative time-domain quantification methods such as AMARES, which are not based on the variable projection algorithm, are less appropriate for complex signals such as short echo time *in vivo* MRS data. A method like peak picking to identify starting values for the parameters and the number of peaks can fail when several peaks are overlapping. In [227], more flexibility on the metabolite basis set is obtained by dividing each metabolite signal into groups of magnetically equivalent spins to form a new basis. This can be useful, for example, when temperature or pH variations are expected between the *in vitro* basis set and the signal undergoing analysis, resulting in different chemical shifts for the same group of spins. This method is particularly interesting in high resolution MR data such as magic angle spinning data, where the influence of pH and temperature on the chemical shifts is higher.

Intuitively, the number of components has an influence on the efficiency of the method. Some methods are particularly sensitive in terms of efficiency to the number of components. For example, in [45, 48, 191], the expectation-maximization (EM) algorithm is proposed to be applied to NMR. This algorithm divides the problem into K independent optimizations, K being the number of components in the signal, and allows computations on parallel computers to reduce its characteristic high computation load. In [23], Bayesian probability theory is used to estimate the exponential parameters of a known model. Probability density estimation requires the computation of integrals for which no analytical solution exists and numerical estimation is needed. Due to its intrinsic high computation load, this method is only suitable for simple signals where only a few exponentials are present. A companion paper [24] extends [23] for determining the functional form of the model (*i.e.*, the number of exponentials).

3.4.2 Black -box methods

The black-box methods, either based on the linear prediction (LP) principle or based on state-space theory like HSVD (both initially introduced in MRS applications by Barkhuijsen *et al.* [11, 12]), allow less inclusion of prior knowledge than interactive methods, being thus less suitable for more complicated signals such as short echo time MRS signals. Furthermore, these methods are limited to Lorentzian spectra. To overcome this limitation, Belkic *et al.* [18] proposed a method based on the Padé transform and capable to extract unequivocally the exact number of resonances directly from the time signal, but presenting the same limitations in terms of prior knowledge as the SVD-based methods. Indeed, if a single component identified by the Padé approximant has contributions from more than

one biochemical source, there is no mechanism to separate these contributions. In addition, the Padé approximant is not able to extract components with amplitudes at the same level as the noise [309]. To improve the LP and total least squares (TLS) based methods [295], Zhu *et al.* [314] proposed the use of an iterative quadratic maximum likelihood (IQML) method and proved the superiority of IQML over LP or TLS based methods in terms of accuracy. One drawback of this method is that, similarly to LP, it needs to calculate the roots of a polynomial which may generate numerical problems when the order becomes too large. By representing non-Lorentzian lineshapes as superpositions of Lorentzian lineshapes, these methods are not able to provide physical information. These limitations are inherent to this type of methods, constituting a serious drawback, since imposing prior knowledge related to specific physical parameters may be crucial for obtaining reliable and consistent results (see *e.g.*, [34]). Furthermore, these limitations make these techniques not appropriate for further classification problems since the extracted features will likely vary from one signal to another.

Although imposing prior knowledge is limited, some can however be incorporated into the model [42, 43, 154, 268]. Chen *et al.* [42, 43] derived an algorithm HTLS-PK able to include prior knowledge of known signal poles. This method has been outperformed by KNOB-TLS, a method proposed in [154], especially in terms of robustness. KNOB-TLS provides parameter estimates which are comparable to those obtained with AMARES, and which could be used as starting values in AMARES as suggested in [154]. In [230], Romano *et al.* proposed a frequency-selective method referred to as MeFreS (Metropolis Frequency-Selective), based on rank minimization of a Hankel matrix. The minimization procedure uses the down-hill simplex method implemented with simulated annealing. MeFreS does not use any preprocessing steps or filter to suppress nuisance peaks, but the signal model function is directly fitted. This method is compared to AMARES$_W$ and VARPRO in [230]. Simulations show that MeFreS is able to correctly identify spectral parameters also in those cases where AMARES$_W$ and VARPRO are expected to fail. The fitting process is also different since MeFreS fits only one spectral component/peak at a time by first selecting its single frequency, while AMARES$_W$ and VARPRO need to fit all peaks that fall in the specified frequency range.

Another important limitation of SVD-based methods is their unsuitability for dealing with data that contain significant signal intensity from rapidly decaying resonances of macromolecules. SVD-based methods require manipulating the original data to make them compatible with the method. This is always inferior to a method that models the data as they were collected. Disentangling the signal of interest from the baseline requires prior knowledge often lacking (or not includable into the model) when using SVD-based methods. Moreover, these methods assume a Lorentzian-type model, which might be too limited for baseline signals, Gaussian lineshapes being often preferred to model the broad resonance signals from macromolecules (see, *e.g.*, [242]).

A more detailed overview of the black-box methods is given in Section 3.6 since these methods are nowadays mainly used as solvent suppression methods.

3.5 Frequency-domain quantification methods

The frequency domain is naturally suited for frequency selective analysis with the advantage of decreasing the number of model parameters. Visual interpretation of the measured MRS signals and of the fitting results is best done in the frequency domain.

3.5.1 Non-iterative methods

Peak integration - binning - whole spectrum
These methods have been detailed in Section 2.3.1.

SVD-based techniques
The frequency domain allows a straightforward selection of a frequency interval. SVD-based techniques are based on this observation and are therefore frequency selective methods. Only the points in the frequency region of interest are considered for quantification, resulting in faster algorithms. In [239], five methods are compared: the filter diagonalization method (FDM) [175, 174], a modified version of MODE [38] to be usable in a SELected Frequency band (SELF-MODE), a data filtering and decimation approach FIDO (FIltering and DOwnsampling) [239], the ARMA-modeling based filtering and decimation technique called SB-HOYWSVD [283], and the frequency-selective implementation of ESPRIT [233] (see, *e.g.*, [266]) called SELF-SVD [267]. For moderately high SNRs, FDM seems to give better estimates than the 4 other methods. SELF-MODE and SELF-SVD have a stable parameter accuracy with relative root mean squared errors (RRMSEs) lying between FDM and the two filtering and decimation methods. SELF-SVD is the fastest method. SB-HOYWSVD has the largest number of user parameters (*i.e.*, the most interactive method). Djermoune *et al.* proposed an adapted version of SB-HOYWSVD [70], which is intended to reduce the computational burden and to avoid the choice of the decimation factor (or the width of the spectral windows) which, in the case of a uniform decomposition, strongly conditions the estimation results. In [173], FDM has been shown to outperform LP-ZOOM [277]. The computational speed of these methods is generally superior to that of the time-domain SVD-based method HSVD, depending on the size of the frequency interval of interest, the number of components and the total number of data samples. As it is possible to decrease the computational load for time-domain SVD-based methods by using the fast Lanczos algorithm, it is equally possible to use the latter for these frequency-selective methods. The limitations regarding prior knowledge of time-domain SVD-based methods remain true for these frequency-domain methods.

3.5.2 Iterative methods

In parallel, methods based on model functions have been proposed (see *e.g.*, [2, 110, 59, 220, 312]). Although these methods are equivalent to time-domain fitting methods from a theoretical point of view, a simple exact analytical expression of the discrete Fourier transform (DFT) of the model function is often not available for the Voigt and/or Gaussian lineshapes, even if numerical approximations exist [102, 179, 126]. For example, in [179, 93], approximated Voigt lineshapes have been proposed, and the spectra were fit with the Levenberg-Marquardt algorithm. In any case, the model functions in the frequency domain

are, in general, more complicated than in the time domain and necessitate thereby more computation time. Marshall *et al.* [178] show that the choice of the lineshape affects the metabolite peak areas and suggest the use of Gaussian lineshapes instead of Lorentzian lineshapes. The frequency-domain methods which only use the real part of the spectrum in their model, such as LCModel [220], require a very good phasing to get the spectrum in its absorption mode.

As for time-domain methods, many frequency-domain methods solve the NLLS problem by local optimization techniques, in particular using the Levenberg-Marquardt algorithm (see, *e.g.*, [312, 220]).

3.5.3 Other techniques

A real-time automated way of quantifying metabolites in long echo time *in vivo* NMR spectra using an artificial neural network (ANN) analysis is presented in [127, 111]. The performance of the ANN was compared with an established lineshape fitting (LF) analysis [3] using both simulated and experimental spectral data as inputs. The ANN quantified these spectra with an accuracy similar to LF analysis but was more easily automated.

Principal component analysis (PCA) has also been proposed as quantification method in MRS [272]. PCA has the advantage of being model independent, making it well suited for the analysis of spectra with complicated or unknown lineshapes. It is not suitable if several overlapping peaks have to be quantified but might be useful when dealing with isolated peaks. PCA considers an entire data set at once, improving its precision in the presence of noise over methods that analyze one spectrum at a time. However, standard PCA will never give parameter information such as chemical shifts or linewidth and it will be accurate for low SNR only if the number of available spectra is large enough. A severe drawback of standard PCA was that all spectra in the data had to be in phase, which is often far from being trivial. To circumvent this issue, a modified PCA, which utilizes complex SVD to analyze spectral data sets with any amount of variation in spectral phase, has been developed [76]. More recent developments have extended this method to quantify all peak characteristics, including the linewidths [310]. In [270], a review of NMR spectra quantification by PCA is given. Stoyanova *et al.* [271] proposed a superior method to the one in [310] in terms of stability, convergence and the range of variations it can determine. In [151], Ladroue *et al.* combined PCA and independent component analysis (ICA) and showed that signals with low occurrence and low SNR can be identified.

In [89], a quantification algorithm for *in vivo* MR spectra based on the analysis of circles (CFIT) is described. The circular trajectories resulting from the projection of the peaks onto the complex plane, are fitted with active circle models. The use of active contour strategies allows incorporation of prior knowledge as constraint energy terms. The problem of phasing spectra is eliminated, and baseline artefacts are dealt with using active contours-snakes. A wide range of prior knowledge, including non-linear constraints, can be incorporated in CFIT. Slightly less good relative root mean squares errors (RRMSEs) have been reported for CFIT compared to AMARES. On the other hand, CFIT presents a better success rate for resolving the peaks of interest within specific intervals lying symmetrically around the true frequencies than AMARES, especially in the presence of baseline distortions.

Another quantification method which aims to circumvent the disadvantages of both

time- and frequency-domain fitting has been proposed in [253], and referred to as time-domain frequency-domain (TDFD) fitting. The model is expressed in the time domain to keep flexibility for the lineshapes and for possible truncation or other typical time-domain processing. However, the fitting itself occurs in the frequency domain after Fourier transforming the discrete time-domain signals, which are the model and the signal under investigation. Due to the additional Fourier transform needed at each optimization iteration, TDFD fitting is approximately 20% slower than a pure time domain fitting method such as VARPRO. This difference is reduced when considering frequency-selective fitting for which time-domain methods require an additional method while frequency selection is straightforward in the frequency domain. TDFD fitting also allows non-analytical lineshapes.

3.6 Preprocessing techniques

Acquired MRS signals are rarely purely exponentially decaying due to experimental conditions (shimming imperfections, physiologic motion, etc) and need to be preprocessed to be suitable for analysis, *i.e.*, such that the modified signals match the model. The influence of nuisance peaks in NLLS parameter estimation techniques such as VARPRO and AMARES has been studied in [140].

3.6.1 Correction for lineshape or model imperfections

Lineshape deviations from an exponentially decaying signal due to residual eddy currents and magnetic field inhomogeneities are often present in ^{1}H spectroscopic data. The rapid switch of the gradient pulses can generate Eddy currents (EC) in the surrounding conducting surfaces around the gradient coils. In spite of the shielded gradients coils which strongly reduce the generation of EC, they remain present. Several effects can be observed in the acquired spectrum: phase changes, gradient-induced broadening of the linewidth, time-dependent but spatially invariant B_0 shift effects (which appears as ringing in the spectrum).

One of the oldest and still widely used techniques was proposed by Klose *et al.* [138], inspired by [204], to correct pointwise the time-domain signal using, as reference, the water unsupressed signal (no hardware suppression of the water signal). In [9], wavelets have been used to remove the phase distortion induced by Eddy currents.

Other methods aim to correct for arbitrary lineshape imperfections (i.e, not following a perfect exponentially decaying signal). In [194], a reference peak is chosen as one of the peaks in the experimental data. The time-domain reference signal is obtained by setting the spectral values outside the reference peak frequency region to zero and using the Fourier transform. A potential drawback is that the reference signal might be equal or close to zero in certain time points, resulting in spikes in the frequency domain. Moreover, setting points to zero boils down to multiplying the frequency signal by a rectangular window, generating the well-known ringing effect in the time domain. An algorithm based on the same principle as in [194] was proposed in [58]. The idea of this method, the so-called QUALITY method, is to pointwise divide the signal under investigation by an estimated lineshape deviation (from a pure decaying exponential) using either separated data or an

isolated peak in the data to be quantitated. A further development for automating this method has been proposed in [182, 304]. The problem of the above methods including QUALITY is the potential risk of dividing by zero (spike effect described above). In [13], a method inspired by [58] and [138], from which it takes its name QUECC (concatenation of "QU" for QUALITY and "ECC" for Klose's eddy Current Correction method), is meant to benefit from the advantages of both methods, QUALITY for a complete correction of the lineshape such that it matches a decaying exponential and ECC for avoiding the spike effect. The signal is separated in two parts defined by a crossover point in the time domain which depends on the slope and the SNR of points in the time domain reference data. The first part of the signal is corrected using QUALITY deconvolution, while the second part is corrected using ECC. To avoid discontinuity in the signal, an exponential damping constant is evaluated to equalize the magnitude of the last point that was QUALITY deconvolved with the magnitude of the first ECC point.

Instead of deconvolving the experimental signal, the lineshape can be incorporated into the fit by multiplying the model lineshapes or the metabolite profiles in the time domain with the reference lineshape (see, *e.g.*, [253]). In the case where no information is available for the lineshape, the latter can be incorporated into the fit as an unknown vector which is convolved with the metabolite profiles in the frequency domain (see [220] for more details), modeled in the time domain (see, *e.g.*, [253]), or estimated from the convolution of the raw data with a undamped spectrum (*i.e.*, a simulated spectrum with zero linewidth) followed by measurement of the full width at half maximum (FWHM) value [312]. In [181], Maudsley proposed another method which does not require the use of a reference peak. The method is iterative and based on an initial estimate of the parameters of the spectral components.

3.6.2 Water peak removal

Biological or biochemical samples are generally recorded in aqueous solution. Due to the large proportion of water, the signal intensity of water is often several orders of magnitude larger than the signal intensities of the other metabolite components. Suppressing the water signal has been a key issue for designing spectrometers, acquisition sequences and post-acquisition methods (called preprocessing methods in this thesis). An overview of these preprocessing methods for solvent suppression is given in this section. This section considers both cases: water-suppressed and water-unsuppressed signals. Note also that several pulse sequences achieve water suppression (see, *e.g.*, [255, 219, 252]).

Water-suppressed signals

Using water-suppressed signals for quantification is still the standard procedure, although recent publications (see, *e.g.*, [72, 49]) have shown that quantification of water unsuppressed signals could also be carried out successfully. Most of the water suppression techniques have been developed based on water-suppressed signals and have been widely tested. With water-unsuppressed signals, gradients-induced artifacts, which originate from the switching of gradient pulses, cannot be totally removed, thereby reducing the accuracy of the parameter estimates. We can distinguish between methods based on the use of a finite impulse response filter and those based on a model function.

FIR filter techniques

In [150] Kuroda *et al.* used first and second order differentiation to suppress the water peak. In order to improve this filter, Marion *et al.* [177] proposed a low pass FIR filter. The drawback of these filters is that they are linear phase filters which generate signal distortion due to the fact that the signals are composed of exponentially damped sinusoids and not pure sinusoids as shown in [273]. In order to reduce this distortion, Sundin *et al.* [273] proposed a maximum-phase FIR filter (MP-FIR). Although, these distortions are strongly reduced, they cannot be neglected when the stopband region is large or when the damping factor is high, as noticed by Poullet *et al.* [214]. Entire tails of frequency domain water signals can be removed by this method. A generalization of the method and advices to use it are given in [298]. Wavelets have also been used for water removal (see, *e.g.*, [5, 6, 52, 103]) and, in [6], the Gabor transform is proposed as a good alternative to the wavelets. In a review of filtering approaches to solvent suppression in MRS [52], 5 filtering methods are compared: a Gabor transform based method [6], the method of Marion *et al.* [177], the method of Sodano and Delepierre [258], the Cross method [53], the maximum-phase Finite Impulse Response (MP-FIR) filter method [273]. MP-FIR filter by Sundin *et al.* [273] has been shown to be the most accurate and efficient technique among them for quantifying long echo time MRS spectra. In addition, MP-FIR allows the inclusion of prior knowledge that may be taken into account during quantification (see [52] for more details). MP-FIR have also been successful in quantifying short echo time *in vivo* MRS [213].

In [37], the ER-filter method is proposed. The idea is to select the frequency region of interest by filtering with a rectangular window in the frequency domain, and to get back to the time domain, reducing substantially the number of points in the signal. Although this technique inherently distorts the signal (ringing effect of the reduced FID due to rectangular filtering), it can be used when the wanted spectral region is small compared to the width of the full spectrum and the number of data points is large [298]. Its use might also be interesting for speeding up the quantification process [222]. The estimation results are largely influenced by the choice of the filter type and filter order, for which only limited guidelines have been provided.

Based on a model function

Another approach is to model the water signal and subtract it from the original signal. The water signal is rarely a pure exponentially decaying signal due to field inhomogeneities and/or partial water suppression and is thereby not easily parameterized. However, the so-called blackbox methods have been successful in reconstructing the water signal usually modeled as a sum of Lorentzians. The most common method is HLSVD developed by Pijnappel *et al.* [210] which reduces the computational load of the original HSVD method by computing only part of the SVD by using the Lanczos algorithm. An improved variant of HSVD is HTLS [295] which computes the TLS solution instead of the LS solution. In [71], HTLS is improved to deal with spectra which contain closely spaced sinusoids. From HLSVD, several variants have been developed (see, *e.g.*, [30, 152]). The main advantage of these methods compared to linear prediction methods [257] is that polynomial rooting and root selection are avoided. This is also the case for Matrix Pencil (MP) methods (see, *e.g.*, [158]), since these methods also find (like state-space methods) the estimates of the signal poles as eigenvalues of a matrix. In [224], Rao reported no difference between estimates obtained by MP and state-space methods. The Cadzow method or minimum variance

technique can also be used to preprocess the data to improve the basic HSVD and HTLS algorithm [41]. In [152], Laudadio *et al.* compare HLSVD with two other proposed variants: the method based on the Lanczos algorithm with Partial ReOrthogonalization (HLSVD-PRO) and the method based on the Implicitly Restarted Lanczos Algorithm (HLSVD-IRL [30]). HLSVD-PRO and HLSVD-IRL outperform HLSVD in terms of computational efficiency and numerical reliability. Moreover, HLSVD-PRO is faster than HLSVD-IRL [296]. The user has to specify the model order and the frequency region of the water peak. These choices may influence the accuracy of the estimated parameters as shown in [298, 29]. A drawback of these methods is their large computational complexity. Even fast methods such as HLSVD or HLSVD-PRO are much less efficient than FIR filter based methods (see *e.g.*, [298, 214]). After subtracting the water signal from the original signal, most of the water tails are removed and the influence on the peaks of interest is small. However, as shown in [214], this influence exists and can reduce the quality of the parameter estimates.

HSVD and MP-FIR used with AMARES [299] are compared in [298] (so-called AMARES$_H$ and AMARES$_f$ for HSVD and MP-FIR, respectively). Combined with AMARES, HSVD is proved to be less accurate and efficient than MP-FIR for long echo time MR data. Similar observations have been done in [214] for short echo time MR data with HLSVD-PRO and MP-FIR combined with AQSES [213] (see Chapter 6), where MP-FIR outperformed HLSVD-PRO in terms of accuracy and efficiency.

In frequency-domain quantification methods, the residual water peak tails are often dealt with by considering them as an additional baseline (*e.g.*, [110, 253, 164]).

Water-unsuppressed signals

Water-unsuppressed signals have become competitive thanks to high-resolution analog-to-digital converters (ADCs), which avoid digitizer overload (due to the high dynamic range, *i.e.*, the high amplitude of the water compared to the metabolite amplitude) that results in severe digital noise. Dong *et al.* [72] report the following disadvantages of water-suppressed signals: 1) signals with small chemical shift differences to water are also partially suppressed, 2) magnetization transfer effects to metabolites [155, 61, 185] may cause systematic quantification errors, and 3) RF pulses used for water suppression increase the total RF power deposition and may require additional adjustments. Furthermore, water-suppressed signals also present the following advantages: the water signal can be used as a reference for lineshape transformation and as an internal reference for absolute metabolite quantification, both without additional measurements [72], but also for phase correction accounting for motion induced phase fluctuation between individual scans [264]. Note that additional preprocessing steps may be needed when using water-suppressed signals, for example to avoid nuisance peaks due to sideband artefacts (see, *e.g.*, [49, 72]). Although most of the methods used for water-suppressed signals should be applicable to water-unsuppressed signals, one should be careful when using FIR filtering techniques since these techniques may have limited performance in terms of attenuation of the water peak. Indeed, a water peak amplitude of 3 to 5 orders higher than the metabolite peak amplitudes requires an attenuation of -60 to -100 dB, which may be difficult to achieve due to the constraints imposed on the FIR filter (*e.g.*, length of the filter or transition band width). SVD-based methods or MP method (used in [72]) are not affected by this problem.

3.6.3 The effect of errors in the initial FID data points and macromolecular signals

In MRS, when the initial time points in the FID are incompatible with the model for the data, this incompatibility is often referred to as the baseline. The incompatibility arises from two different phenomena: 1) the amplitude of the initial FID data points are distorted due to instrumental imperfections (baseline distortion), 2) signal amplitude from macromolecules. However, these phenomena arise from totally different sources. The reasons of baseline distortions are diverse [276]: nonlinearity of the filter-phase response, discrete nature of the Fourier transform, instrumental instabilities, and other reasons. Macromolecular signals, coming from the macromolecules present in the tissue under investigation, are characterized by broad spectral lines (short T_2), which often overlap in the frequency domain with metabolite components. Their dominant appearance in short echo time ^{1}H-MR spectra of human brain complicates drastically the quantification process.

Baseline distortions

As previously mentioned, the hardware/software solutions to baseline distortions will not be discussed in this thesis. With the use of modern spectrometers with 16-bit analog-to-digital converters, digital signal processing and oversampling techniques [195], most of the problems related to baseline distortions are overcome, but post-processing techniques may still be needed to remove some unwanted broad lines. A classical case is the distortion of the first points in an FID, coming from probe acoustical ringing or, more commonly, filter distortion. This basically introduces a rolling baseline in the frequency domain (after Fourier transformation of the time domain signal). Different techniques to obtain a flat baseline have been proposed in the literature. Popular approaches include reconstruction of the first points of the FID [276] and approximation of the baseline in the frequency domain using linear functions [110] for narrower frequency regions or sophisticated analytical functions such as Fourier series [265] or polynomials [67, 26] for wider regions. Most recent techniques are composed of 2 steps, a baseline recognition step in which the signal-free regions of the spectrum are detected using some threshold values (see, *e.g.*, [94, 50] for more details), and a baseline modeling step where a smoothing algorithm estimates the baseline spectrum given the signal-free (or baseline) points.

Macromolecular signals

Macromolecular signals are often considered as nuisance components in MRS since they usually overlap with the metabolite contributions in the frequency domain. However, recent studies [113, 169, 184] show that strong correlation between the macromolecular concentration/composition and the location of the voxel in the brain have been found. Hoffmann *et al.* [113] also found significant correlation with age but not with gender, while no significant correlation with age could be detected by Mader *et al.* [169] (the correlation with gender was not studied in the latter reference). Similarly, several conditions such as stroke [98], brain tumors [242] and multiple sclerosis [170] show an altered macromolecule profile. Therefore, the macromolecular signal can provide relevant clinical information. The goal is thus to disentangle the macromolecule contributions from the metabolite signals in

order to obtain accurate parameter estimates from quantification while keeping the information provided by the extracted macromolecular signal.

In spite of our better knowledge of the macromolecular signal, it remains difficult to predict it in *in vivo* MRS signals, and most of the classical methods just assume its smoothness in the frequency domain. The macromolecular signal can be removed in a preprocessing step (see, *e.g.*, [226, 312, 260]) or can be modeled in the quantification step (see, *e.g.*, [213, 78, 220]).

In the preprocessing step

Different preprocessing approaches have been developed. The simplest one, based on the fact that the macromolecular components decay more rapidly than the metabolites, is to truncate some of the initial points in the time domain [263] (also called the 'Trunc' method by Ratiney *et al.* [226]). However, the useful information is partially lost and selecting the number of points to be truncated is difficult. More advanced techniques consist of subtracting a modeled macromolecular signal in the frequency domain from the original spectrum. Models may be generated with wavelets [312, 259, 245, 72, 93] or splines [316]. A comparison between wavelets and splines has been done in [260] but no significant differences have been found. The macromolecular baseline can also be measured in the time [131] or the frequency domain [17], then modeled as a sum of Gaussian peaks [14] or Voigt lines [113], and finally subtracted from the original signal. Ratiney *et al.* [226] proposed a three-step method (called 'Subtract') for subtracting the macromolecular baseline (see Alg. (2.3.1)): (1) truncate the initial points and quantitate with QUEST [225] the metabolites, (2) estimate the baseline from the metabolite-free signal by an SVD-based method or AMARES, and (3) subtract the parameterized baseline from the raw signal. The so-called time-domain frequency-domain (TDFD) methods follow the same principle [253, 312, 77] even if the wavelets or splines are usually preferred to the SVD-based methods for modeling the baseline. Other techniques such as SVD-based methods [51] have also been proposed. Although these methods have been shown to be rather successful for removing the baseline, they require an additional step prior to the quantification, thereby increasing the risk of larger errors in the amplitude estimates.

In the quantification step

On the other hand, the baseline can be modeled in the quantification step. In parametric models, the profiles of the baseline components, obtained from measurements [169, 242, 148, 114, 7, 168, 208] or from theoretical considerations [117], are added to the database of metabolites. The authors of these papers conclude that including the baseline components in the basis set of metabolite profiles provides more accurate results. The baseline can be measured using specific sequences based on T_1 relaxation such as the inversion-recovery [17, 139] or the saturation-recovery sequences [113]. Baseline removal can also be based on T_2 relaxation by increasing the echo time [146]. However, the *in vivo* determination of the exact relaxation times for both macromolecules and metabolites is complicated and time consuming. Furthermore, neither metabolites nor macromolecules necessarily present a narrow distribution of relation times. Williamson *et al.* used the Padé Transform to separate the baseline from the metabolite signals [309].

In semi-parametric models, the baseline signal is supposed to be smoother than the spectral components of interest. Different functions have been used to approximate the baseline: linear combination of splines (see, *e.g.*, LCModel [220] or AQSES [213]), linear combination of reproducing kernels associated with a reproducing kernel Hilbert space (see, *e.g.*, [78]). Incorporating the baseline into the fit via non parametric modeling allows a one-step procedure which reduces the risk of accumulated error.

3.7 Discussion

A beginner in the field of MRS quantification who needs to choose an appropriate quantification method may face a big challenge. The choice is often made based on the availability (free or commercial, accessible via internet or not) of the method and its user-friendliness. In this chapter and, in particular, in this section, we enlighten the general features of quantification methods to help the reader to choose an appropriate method for his/her data. A better quantification often results from better prior knowledge, and quantification methods should be chosen in order to include as much prior knowledge as possible in the model. However, one should remember that incorporating prior knowledge is only beneficial when it is sufficiently close to the reality. There are indeed two reasons for ending up in an unwanted local minimum when using local optimization algorithms: bad initial estimates of the parameters, and wrongly implemented prior knowledge. Here is a list of key points for choosing a quantification method. The features of the main quantification methods are reported in Table 3.1, each column corresponding to one of the following features:

1. **Using an *in vitro* or simulated database of metabolite profiles**
   A first step is to identify the data to be analyzed, their complexity (*i.e.*, high number of peaks?, overlapping peaks?). As a rule of thumb, spectra with a large number of overlapping peaks are more easily modeled by a linear combination of metabolite profiles rather than a linear combination of Lorentzian, Gaussian or Voigt components. On the other hand, signals with a low number of resonances are easily handled by methods like AMARES or VARPRO. AMARES should be preferred to VARPRO particularly when constraints on the linear parameters (metabolite amplitudes, phases) have to be imposed. For example, complex signals such as short echo time MRS data will be quantified by AQSES, LCModel, QUEST, TDFDFit or Elster's while VARPRO or AMARES should be applied to long echo time MRS data. When there is no prior knowledge, or at least, no reliable prior knowledge is available, nonparametric approaches [269] such as HLSVD can be used to quantify MRS data.

2. **Incorporating an unknown nonparametric lineshape into the fitting model**
   Taking the lineshape into account is necessary in MRS quantification. Marshall *et al.* gives a simple example in [178] where modeling a Gaussian peak with a Lorentzian peak results in a 26% error. This error decreases for 2 overlapping peaks with a minimum of 17% for a distance between the peaks of about twice their FWHM. Peaks or apparent signals in the fitting residuals are usually an indication of an inappropriate model. In general, the best way to correct for non-exponential decay is to use a reference signal (such as the water-unsuppressed signal) which has undergone

the same distortions (see, *e.g.*, [13, 58, 138]). Instead of deconvolving the original signal, one should, if possible, add the distortions to the profiles of the metabolite database to avoid any division by zero (see Section 3.6.1). If no reference signal is available, one can still include the lineshape estimation into the fitting process (see, *e.g.*, [220, 253]).

3. **Incorporating water filtering into the fitting process**
   Frequency-domain methods usually consider the water tails overlapping with the metabolites of interest as part of the baseline and do not consider water filtering. On the contrary, time-domain methods need to remove the water components. As shown in [214], including water filtering inside the optimization process may improve the parameter estimates. When dealing with unsuppressed water signals, it is preferable to use SVD-based methods instead of FIR filtering techniques to avoid problems due to a too weak attenuation of the water signal (see Section 3.6.2).

4. **Modeling the macromolecular signal and baseline distortions**
   The macromolecular signal should be included in the model (*i.e.*, used in the quantification step, see Section 3.6.3) when macromolecular contributions are present in the signals, either as a smooth function (see, *e.g.*, [78, 213, 220]) or as additional "metabolite" profiles in the database. The latter is often preferred in recent publications (see, *e.g.*, [169, 242, 148, 114]). This can be explained by the fact that adding macromolecular profiles adds more prior knowledge than the assumption of smoothness of the macromolecular signal. Disentangling the baseline from the rest of the signals before the quantification process increases the risk of errors since any error due to disentangling will affect the parameter estimates and be superimposed to the fitting errors. The methods with an 'X' in the last column of Table 3.1 assume the smoothness of the baseline without distinguishing between baseline distortions and macromolecular signal. Moreover, frequency-domain methods such as LCModel [220] considers the tails of the water resonance as part of the baseline distortions.

Other important considerations:

- **Time- or frequency-domain method?**
  Time- and frequency-domain methods are theoretically similar in performance even if the time-domain methods allow more flexibility in terms of model lineshapes. Only a few took the risk of comparing time- and frequency-domain methods and no strong conclusions could be drawn. In [290], 4 methods have been compared on *in vivo* ^{31}P MR data of tumors: VARPRO and HLSVD as time-domain quantification methods, and peak integration and Lorentzian fitting as frequency-domain quantification methods. The results suggest that VARPRO is the method of choice for quantitative analysis of tumour ^{31}P MR spectra, giving the most reliable results at low SNR. Kanowski *et al.* [130], for instance, reported comparable results for AMARES and LCModel. It is also important to notice that the fast Fourier transform (FFT) is suboptimal if 1) the noise is not Gaussian, 2) the sampling time is not constant (different time steps), 3) samples are missing. In these cases, it might be preferable to avoid the FFT and to do the analysis in the measurement or time domain.

Table 3.1. *Features of some quantification methods. An 'X' indicates that the method (i) uses an in vitro or simulated database of metabolite profiles, (ii) incorporates an unknown nonparametric lineshape into the fitting model, (iii) incorporates water filtering into the fitting process, (iv) models the macromolecular signal and baseline distortions*

Methods	(i)profiles	(ii)lineshape	(iii)water	(iv)baseline
HLSVD [210]				
VARPRO [292]				
AMARES [299, 298]			X	
AQSES [213]	X		X	X
QUEST [225]	X			X
Elster *et al.*'s [78]	X			X
TDFD Fit [253]	X	X		X
CFIT [89]				X
LCModel [220]	X	X		X
Young/Soher *et al.*'s [259, 311, 312]		X		X

- **Lorentzian, Gaussian or Voigt model?**
  The choice of the model is a nontrivial question. One should first correct for lineshape imperfections as mentioned above. These corrections may not be sufficient to obtain pure Lorentzian signals and other lineshape models such as Gaussian or Voigt may be preferable. It is often complicated to judge whether the peaks in the signal are Lorentzian, Gaussian or Voigt. However, one can test different lineshape models and choose the one which gives the best residuals (small residuals with no peak or signal in it) and the best success rate in the sense of Gabr *et al.* [89] (see Section 3.5.3). As Marshall *et al.* showed numerically [178], choosing a wrong model is less important when modeling two Gaussians than one unique Gaussian. This is explained by the fact that the large Lorentzian tails compensate the natural overestimation of the amplitudes when modeling Gaussians by Lorentzians. One can also intuitively imagine that adding noise (smaller SNR) or baseline distortions will also reduce the effect of a wrong model (which does not mean that the error will be smaller). However, it would be very challenging to fix a threshold value for the SNR at which we can consider the choice of the lineshape as important since this value depends on the signal under investigation (number/shape of peaks, artefacts in the signal, macromolecular signal, etc).

- **Is my method robust?**
  Most of the quantification methods claim to be robust, but are not necessarily robust against the same type of disturbances (noise, baseline, water peak, etc.). Moreover, they usually base their conclusions on simulated spectra that do not reflect all the artefacts or distortions present in a measured signal. In order to analyze the robustness of a method on *in vivo* signals, Gabr *et al.* [89] proposed to study the success rate (or failure rate) to resolve the peaks of interest within specific intervals lying symmetrically around the true frequencies. They show that CFIT is less sensitive than AMARES to baseline distortions. When considering only non failure cases, AMARES presents lower RRMSE than CFIT. That is why it is important to identify

the components in the signal, known and unknown: the rolling baseline is visible and is not part of the metabolite signal, therefore it should be removed before using AMARES. Gabr *et al.* confirm that much better success rates are obtained when using AMARES after filtering the rolling baseline. High failure rates may be an indication of a wrong model, or remaining artefacts (in this case the rolling baseline) that should be removed prior to quantification. Signals with non Gaussian noise can also lead to non optimal parameter estimation. Indeed, the least squares problem yields the smallest estimation errors when the distribution is Gaussian and is suboptimal otherwise. MR scanner noise is supposed to be Gaussian, but perturbations or deviations from Gaussian distribution may occur due, for example, to body motion [254]. These perturbations may be considered as acquisition artefacts which are beyond the scope of the thesis. In [254], Slotboom *et al.* proposed a method to detect and discard signals with non Gaussian noise.

- **Variable projection or not in the optimization algorithm?**
  When no prior knowledge about the linear parameters (amplitudes, phases) of the model is available, an optimization method using variable projection (like in [213, 292]) is preferable because all linear parameters are projected out thereby reducing the number of parameters to be optimized by one half or more. If equal phases are assumed, variable projection can still be used in a modified form [247]. In other cases, a more general optimization algorithm (like the one used in AMARES [299]), which optimizes all parameters (linear and nonlinear) is recommended.

- **Weighting and normalization**
  If one wants to give more importance to particular frequency regions, a weighting matrix can be used in the minimization function, which multiplies the vector of squared errors (see, *e.g.*, Eq. [11] in [253]). The largest weights are assigned to the frequency points of interest.

  One may also want to give the same importance or the same weight to all the peaks. In that case the least squares error can be normalized in order to balance the peak contributions with respect to this error (see, *e.g.*, Eq. [12] in [253]). This might however be dangerous since quantification methods like LCModel or TDFD Fit tend to overestimate the amplitude of low concentration metabolites [145].

3.8 Conclusions

In spite of numerous publications on the topic, quantification of MRS data remains an important issue. No satisfactory systematic study of the accuracy of the methods has been performed. One of the obstacles is the lack of gold standard simulated signals which would mimic real-world signals and permit fair comparisons between the methods. In this chapter, advantages and drawbacks of the different methods have been depicted and it appears clearly that none of the methods outperforms the others in all cases. However, the choice of the quantification method should result from the objectives that the analyst pursues (*e.g.*, which data he/she wants to analyze, etc) and tips are given in that respect (see Section 3.7).

Chapter 4

Review of pattern recognition methods in MRS

This chapter[1] *reviews the main principles of pattern recognition methods used in MRS. The family of feature reduction methods is briefly outlined, either based on physical meanings or based on mathematical criteria. Classification methods are also reviewed and their behavior in MRS is briefly discussed. Finally, tissue segmentation and nosologic images based on MRSI are introduced.*

4.1 Introduction

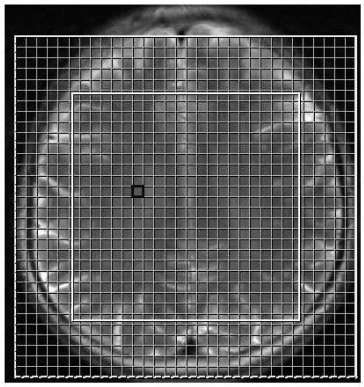
MRS and MRSI data are important diagnosis tools (*e.g.*, for brain tumor diagnosis). Although based on the same principles, these data yield different properties. MRS signals show better SNRs compared to MRSI signals, but spatial information is also limited to the location of the voxel under investigation. In MRSI, correlations between adjacent voxels can be exploited, for example, to improve tumor typing, starting from the assumption that similar tissue types are expected in adjacent voxels. Allocating a color to a specific tissue type is called "nosologic imaging" [73]. It has also been shown that using MRSI improved significantly the classification results obtained with MRI data [250, 66].

An atlas of body sections can also be used along with MRI images as a tool for tissue segmentation (see, *e.g.*, [132, 216]), allowing, for example, to distinguish between abnormal tissue and other brain tissue such as cerebrospinal fluid (CSF), white matter and grey matter tissue. More recently, MRSI has been used in the segmentation process [153, 63]. Note that tissue segmentation can be strictly based on MRI images [237].

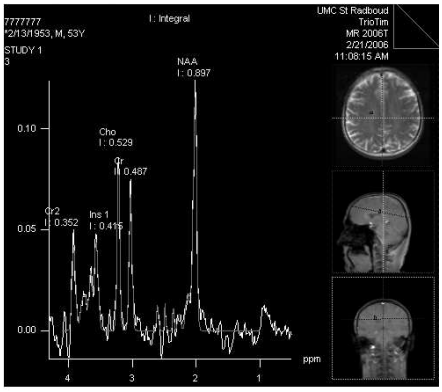
The two main operations of a pattern recognition (PR) process are feature reduction from the MRS(I) signals and data classification relying on the extracted features. PR features are based on mathematical or statistical concepts and do not usually have physical meanings, contrary to features extracted from a metabolite quantification method. In the

[1] J. Poullet, D.M. Sima, S. Van Huffel, Metabolite quantification in MRS and pattern recognition, Internal Report 08-84, ESAT-SISTA, K.U.Leuven (Leuven, Belgium), 2008, submitted for publication to the Encyclopedia of Magnetic Resonance.

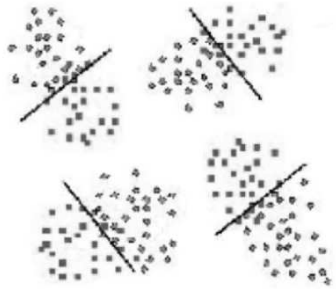




1. Acquisition and preprocessing



2. Feature extraction



3. Feature mapping and classification

Figure 4.1. *Pattern recognition scheme. First, the MR data are acquired and preprocessed. Then, the features are extracted from the preprocessed data. Finally, classifiers are constructed and tested based on the extracted features. The classification result is evaluated using performance measures. Images provided by UMC St Radboud of Nijmegen.*

following, the main principles of PR for MRS(I) data are summarized. In Section 4.2, a review of the PR methods applied to MRS classification is given. Note that these methods can also be used for MRSI data if the voxels of the grid are considered independently from each other. Methods exploiting spatial information are presented in Section 4.3.

4.2 MRS data classification

A typical scheme representing the different steps of the PR process based on MRS data is given in Fig. 4.1. In this section, a brief review of the feature reduction and classification methods applied to MRS data is given in Section 4.2.1 and Section 4.2.2, respectively.

4.2.1 Feature reduction

One can consider two types of features: features with a physical meaning and mathematically extracted features. The goal of a feature reduction method is to improve the prediction performance of the predictors (accuracy), to provide more efficient predictors (computation time) and to provide a better understanding of the underlying process that generated the data. The reader interested in feature reduction techniques is referred to [104, 160].

Methods able to extract features with **physical meanings** are, for instance, peak integration or peak fitting methods (see Section 2.3.1). Other simple methods are: the whole spectrum in the frequency region of interest, peak bucketing which considers as features the points of the spectra in several particular disjoint frequency regions (corresponding to the regions of interest), or binning (*i.e.*, gathering adjacent spectral points) which is less sensitive to small deviations in pH or temperature. Special attention must be paid to correct alignment of MR spectra, especially if the spectral points are directly used as features. Note that the chemical shift is dependent on pH and temperature which may vary from one sample to another and thus complicates the alignment of the spectra. These effects are particularly noticeable for high resolution MRS.

Without knowledge of the physically relevant features, one has to resort to **mathematical feature reduction** methods. In MRS, these techniques are usually based on a particular region of the spectra after Fourier transformation of the preprocessed time domain signals. One might want to select a subset of features from the input features or transform the input data space into a relevant subspace, that is, a subspace defined by a set of variables that, once included in the feature set, improves the predictive performance of the classifier.

To select a subset of features, the literature often considers 3 main types of approaches: filter, wrapper and embedded approaches [20, 104]. The filter methods do not consider the classification learning algorithm to filter the variables and therefore may not find the most useful features, that is, those with the largest prediction ability. They are also less computationally expensive than methods from other approaches. In the wrapper methods, the different subsets of features are tested on the classification algorithm in order to select the best subset. If an exhaustive search is not feasible (too high number of variables), alternative heuristics methods based on backward, forward, or stepwise variable selection are used (other variable selection methods are possible, such as hill climbing [33], best-first search [141], and beam search [20], see [104] for a more extensive list). The wrapper methods are more likely to find the useful features but are also more prone to overfitting [104]. For example, the recursive feature elimination (RFE) method with support vector machines (SVMs) [105] has been used in MRS [162]. In contrast to filter and wrapper approaches, in embedded methods the learning part and the feature selection part can not be separated, the structure of the class of functions under consideration plays a crucial role. For example, Weston *et al.* [307] measure the importance of a feature using a bound that is valid for Support Vector Machines only, thus it is not possible to use this method with, for example, decision trees. Embedded methods perform input selection and model training simultaneously. Probably due to their simplicity and efficiency, filter methods are commonly used in MRS. For example, the Kruskal-Wallis test [115] was used in [165, 171, 172], the Fisher discriminant criterion [84] in [165, 162] and Relief-F [142] in [165].

Another possibility to reduce the feature space is to transform it in order to separate the relevant features from the others which might be due to noise or artefacts, for instance. Several feature extraction methods have been applied successfully in MRS(I): principal component analysis (PCA) [109] in [65, 163, 186, 203], partial least squares (PLS) [186], independent component analysis (ICA) in [250, 186, 134], nonnegative matrix factorization (NMF) in [238], wavelets [4] in [280, 75].

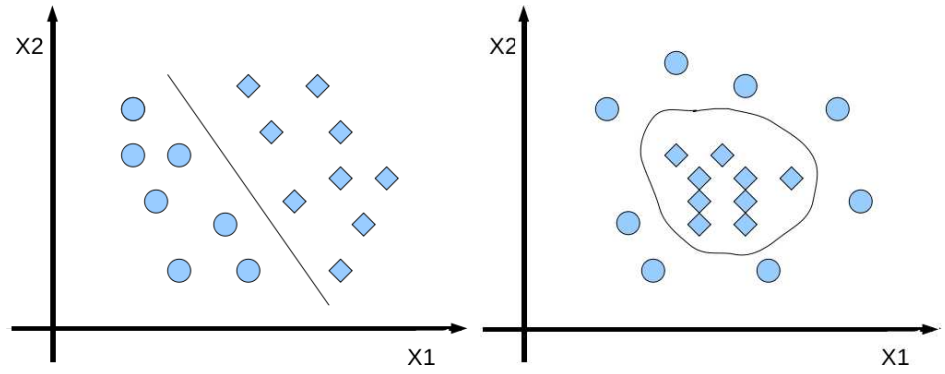
One may also improve classification accuracy by giving weights to the features. These weights can be based on the ranks of feature selection methods or clinical prior knowledge. Note that in MRS(I), the variables are often normalized such that their mean and variance are equal to 0 and 1, respectively. However, taking the original amplitude estimates from quantification or peak integration, without normalization, makes also sense since the largest peaks are less prone to estimation errors due to noise or other artefacts.

Due to the diversity of MRS(I) data and their intrinsic complexity, it is really complicated to assess the superiority of a method over another. Comparisons of feature reduction methods for MRS exist [167, 203, 279], but the results should only be considered for the studied data. Even within the same type of data, conclusions may be difficult to draw. For example, one can wonder whether taking the points of the spectra as features would result in better classification accuracy than using the estimated amplitudes from a quantification method. In [203], Opstad *et al.* conclude that there is an advantage of using the quantitative analysis of LCModel [220] rather than the whole spectra, while in [167], they conclude that the use of the quantification technique AQSES [213] does not improve the results. In [134], Kelm *et al.* found that QUEST performed better than VARPRO and AMARES but not better than the simple PR methods (PCA, ICA, PLS, NMF). What remains sure is that features obtained from quantification are more physically interpretable but are usually also more complicated to extract, especially when the spectra are composed of several overlapping peaks. Since feature reduction methods are often based on the spectra, one might wonder whether it is better to consider the real part or the magnitude of the spectra. It seems that, in several studies [163, 186, 65, 278], the advantage obtained from omitting phase correction, which is necessary when dealing with the real part of the spectra, outweighs the drawback of increasing linewidths and therefore peak overlaps (*i.e.*, magnitude spectra are preferred to real spectra).

4.2.2 Classification methods

A PR process is also defined by its classification method. Classification methods can be completely separated from the feature reduction step – as it is the case with peak integration, peak fitting or feature selection methods based on the filter approach (see above) – or taken into account for selecting the most relevant features when considering wrapper or embedded approaches.

Classification methods are usually categorized in supervised and unsupervised methods (semi-supervised methods are beyond the scope of the thesis). Supervised methods require training and test data sets along with the class labels of the training data, while unsupervised methods cluster data based on a particular similarity measure. Class labels are often known in MRS(I) and supervised methods are therefore more appropriate. Although unsupervised methods have been applied to MRS(I) [118, 282], they are much more used



(a) Linear separation. (b) Nonlinear separation.

Figure 4.2. *Illustration of boundaries from linear (a) and nonlinear (b) classifiers. In Fig. 4.2(b), only nonlinear classifiers can perfectly separate the data between the two classes.*

in MRI [120, 116, 313]. For sake of space, only the supervised methods will be reviewed in this chapter, subdivided in linear and nonlinear methods.

Linear classifiers model the decision boundary as a hyperplane in the space of the explanatory variables. These methods are less computationally expensive but show poor performances in the case of severe non linearity [159]. Several linear methods have been tested on MRS classification: the linear discriminant analysis (LDA) in [65, 165, 163, 278, 217] which models the feature distributions as Gaussians with common covariance matrix, logistic regression (LR) which can be derived from the same probabilistic model by using conditional likelihood ([109], pp.103ff) in [134]. Another problem related to linear methods is that they are often based on covariance matrices having as many rows or columns as the number of features, making their use impossible when dealing with high dimensional data. However, when accompanied by a feature reduction method like PCA, they can be successfully applied [65, 66].

Nonlinear classifiers are more powerful than linear classifiers in the sense that nonlinear decision boundaries can be constructed (see Fig. 4.2). However, the results are usually more difficult to interpret since they behave like black-box methods. Nonlinear methods have been applied in MRS: kernel-based methods such as SVM [300] in [186], Gaussian processes [241] in [134] or least-squares support vector machines (LS-SVM) [274] in [65, 66, 165, 167], the ensemble method “random forests” [22] in [134], artificial neural networks (ANN) [16] in [261, 118, 8], etc.

Similarly to the feature reduction methods, the performances of the classification methods depend on the data and the whole PR process. However, several papers show that nonlinear methods outperform linear methods [134, 167, 165, 66, 65]. Note that most of the aforementioned PR methods are able to deal with binary (two classes) and multiclass classification problems (possibly with some adaptations).

4.3 Tissue segmentation and nosologic images based on MRSI

The interest for MRSI is continuously increasing and several trials to incorporate spatial information have been recently made. Laudadio *et al.* [153] proposed to apply canonical correlation analysis (CCA) to MRSI prostate data as a way to include spatial information when producing nosologic images. An illustration of nosologic image obtained with CCA is given in Fig. 4.3. De Vos *et al.* [63] extended it to brain data using the quantification estimates and MRI data as features, in addition to the whole magnitude spectrum as in [153]. However, this method presents two main drawbacks. First, adjacent voxels with different tissue types (for example, tumor tissue and healthy tissue) may affect the classification performances. Second, the neighborhood is fixed to the direct adjacent voxels so that long-range interactions are not considered, which may have a large impact in the presence of noisy spectra. In [133], Kelm *et al.* suggested to apply conditional random fields to MRSI data to overcome these limitations and claimed that their approach is able to increase the performance of single classifiers by at least 15%. Luts *et al.* [166] have recently proposed a two-step approach: a segmentation step and a classification step where MRSI and MRI data are simultaneously exploited, thereby yielding improved segmentation and classification results. Furthermore, spatial information is included in both steps and class probabilities are also generated. The first step is performed based on the segmentation method presented by Prastawa *et al.* in [216], but with a subject-specific prior for the abnormal tissue based on a LDA classifier rather than based on a contrast-enhanced image. For the second step, multiclass classifiers using kernel logistic regression (KLR) [315], Bayesian least squares support vector machines [294] and CCA were computed. Bayesian LS-SVMs and KLR were used since these kernel-based methods are able to provide class probabilities instead of black or white decisions. CCA was included because it is capable to exploit spatial information.

4.4 Conclusion

Although histopathological analysis of a biopsy remains the gold standard for diagnosis, MRS and MRSI techniques are constantly improving and quantification or pattern recognition methods are being adapted accordingly. A tremendous amount of information is now available from high resolution MR spectra and spatial information can be exploited from MRSI data. Moreover, hospitals acquire data from an increasing number of modalities (MRS, MRSI, MRI, etc.) allowing to combine them to improve the classification performance. Non invasive MRS has the potential to improve the diagnosis without increasing the risk for the patient and constitutes therefore a logical technique to be used prior to surgery. This chapter reviewed briefly the different pattern recognition strategies applied for brain tumor diagnosis using spectroscopic data.

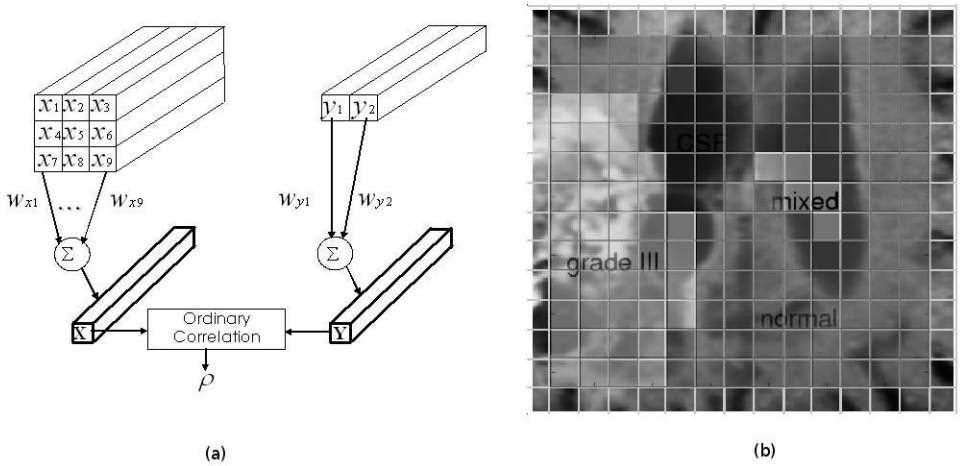


Figure 4.3. *(a) CCA quantifies the relationship between two multivariate vectors X and Y, constructed from the features $x_1, \ldots, x_9$ of the input voxels and the modeled features $y_{1,}y_2$ corresponding to the different tissue types. The voxel is assigned to the tissue which gives the highest canonical correlation coefficient. (b) An example of a nosologic image obtained with CCA. Images taken from [63].*

Chapter 5

The quantification method AQSES

This chapter[1] *describes the performance of the quantification method AQSES with short echo time magnetic resonance spectra. The quantification problem has been described in Chapter 3. Section 5.1 summarizes the main features of AQSES. Section 5.2 describes the experiments: AQSES has been tested on simulated MR spectra with several types of disturbances and on short echo time in vivo proton MR spectra. Moreover, AQSES and QUEST are compared on simulated MRS data. The results are discussed and some conclusions drawn.*

5.1 Introduction

Accurate quantification of metabolites from short echo time *in vivo* magnetic resonance spectroscopy (MRS), such as proton spectra from the human brain, may be a very important aid in the correct noninvasive diagnosis of pathology. This chapter is devoted to the quantification method AQSES, which presents the following characteristics:

- it fits the whole complex signal in the time domain, contrarily to LC-Model, for instance, which fits only the real part of the frequency domain signal;
- it uses a database of metabolite profiles;
- it uses a maximum-phase impulse response filter to remove undesired resonances from specific frequency ranges,

[1] J. Poullet, D.M. Sima, A.W. Simonetti, B. De Neuter, L. Vanhamme, P. Lemmerling, S. Van Huffel, An automated short echo time MR quantification in a open-source software environment: AQSES, NMR Biomed. 20 (2007) 493-504, and
K. Vanderperren, S. Vandeput, J. Poullet, D.M. Sima, S. Van Huffel, Automatic quantification of magnetic resonance spectroscopic signals : Evaluation and comparison of AQSES and QUEST, Proc. of the Belgian day on biomedical engineering - IEEE/EMBS Benelux Chapter Symposium, Brussels, Belgium, Dec. 2006, pp. 251-254.

- it uses a non parametric model based on penalized splines for the baseline, typically requiring less spline functions than smoothing splines, which are used for instance in LC-Model;
- it is based on a variable projection (VARPRO) algorithm for reducing the computation complexity (only the nonlinear parameters are computed in the optimization procedure);
- the classical VARPRO method is modified for imposing constraints on the linear parameters;
- constraints (from prior knowledge) can be imposed on linear parameters (non-negative amplitudes and equal phases) or on the nonlinear parameters via upper and lower bounds or via linear equalities between some variables of the same sort;
- the optimization algorithm is based on the Levenberg-Marquardt algorithm.

AQSES is embedded in java (AQSES GUI) and matlab (SPID) software packages, both available online from www.esat.kuleuven.ac.be/sista/members/biomed/new/[2] with a graphical user interface, under an open source license, which means that the source code is freely available and easy to adapt to specific needs of the user. AQSES GUI and SPID are described in more detail in Appendix A and C.

The goal of this chapter is to discuss the performance of AQSES. In this regard, simulated data, generated from *in vitro* signals, *in vitro* and *in vivo* data have been employed. Five experiments have been designed. The first two ones study the accuracy level that can be reached for the parameter estimation with different databases. The third one studies the influence of nuisance components (water, baseline, noise) on the estimated amplitudes. The fourth and the fifth experiments validate AQSES on *in vitro* and *in vivo* data. An additional experiment also compares AQSES and QUEST on simulated MRS data. Section 5.2 and 5.3 aim at presenting the performances of AQSES through these various experiments on simulated, *in vitro* and *in vivo* MR data. Next, the features of AQSES are discussed in section 5.4 and some conclusions are drawn.

5.2 Simulated examples and *in vivo* quantification

The in vitro database used in this work is described in Appendix A.

Five experiments have been designed to test the robustness and the accuracy of AQSES. The **first** one emphasizes on the accuracy level that can be reached for the parameter estimation. A large amount of simulated signals were created for that purpose. Each simulated signal consisted of a linear combination of 8 metabolite profiles (6 metabolite profiles + 2 simulated lipid profiles) in the basis set, *i.e.*, myo-inositol (Myo), creatine (Cr), phosphocholine (PCh), glutamate (Glu), NAA, lactate (Lac), lipid at 1.3 ppm (Lip1), and lipid at 0.9 ppm (Lip2). These metabolites were chosen since they have been found to be important in the detection of many pathologies. Note that no disturbance components such as baseline, noise or water, were added to the simulated signals. The parameters for amplitude, damping, phase and frequency for each simulated signal were chosen in the following

[2] Accessed: August 1, 2008

way: first, meaningful parameters were estimated from a set of 98 short echo time *in vivo* MRSI spectra acquired from normal brain tissue. Estimates were obtained using AQSES in a controlled way in which results were visually inspected and outliers removed. This was done to mimic a real world situation and to obtain sensible mean values and standard deviations (SD) for all parameters. Then, for the simulated signals, the amplitudes were restricted to the mean $\pm$3*SD (only positive), the damping perturbation was restricted to the mean $\pm$10 Hz. The phases were set variable between -45 and 45 degrees, but were the same for all profiles in one simulated signal. The frequency shifts were restricted to zero $\pm$4.5 Hz. This resulted in a set of data (set 1) with 200 simulated spectra.

For each metabolite k in the simulated signal l, the true amplitudes ($a_{k,l}$) were compared to the estimated ones ($\tilde{a}_{k,l}$) obtained with AQSES by means of a performance measure (PM) defined as:

$$PM_k = 100\sqrt{\frac{\sum_{l=1}^{L}(a_{k,l}-\tilde{a}_{k,l})^2}{\sum_{l=1}^{L}a_{k,l}^2}}, \tag{5.1}$$

where L is the number of simulated signals in each set. A low PM reflects a high performance, and is a percentage measure of the difference between estimated and true amplitudes.

The **second** experiment extends the results of the first one for larger databases, *i.e.*, with more metabolite profiles. We took the same simulated spectra (set 1) as in the first experiment, but three more metabolite profiles were added to the basis set: taurine (Tau), alanine (Ala) and glucose (Glc). We chose these metabolites because they are known to be important metabolites that do not have strong correlation with the metabolites that were already inside the basis set.

The **third** experiment shows the influence of water, baseline and noise on the estimated amplitudes. We considered the same basis set as in the first experiment (using 8 metabolite profiles in AQSES). Five sets of simulated signals were constructed:

set 2 = set 1 with water resonance at 4.7 ppm,

set 3 = set 1 with low white noise (SNR = 25),

set 4 = set 1 with high noise (SNR = 7),

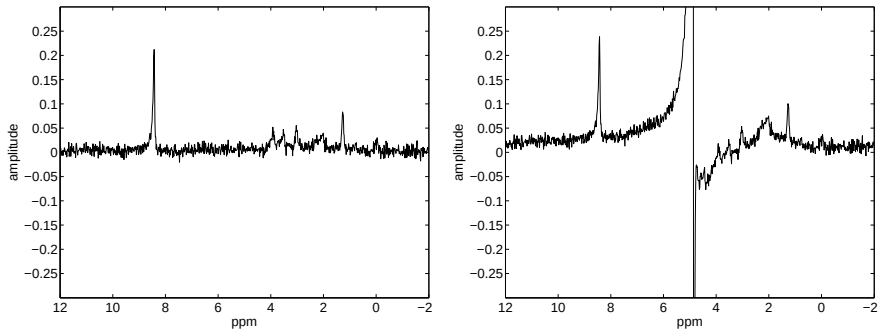
set 5 = set 1 with baseline distortion

set 6 = set 1 with water, baseline and high noise.

The baseline distortion was based on information from Table 1 in [242]; the baseline is the sum of gaussians referred to as lip3, lip4, lip5, mm2, mm3 and mm4 in that work. The water profile has been extracted from an *in vivo* spectrum by means of HLSVD-PRO. The SNR is defined as the ratio of the reference peak height at 8.44 ppm and the standard deviation of the circular[3] white gaussian noise, both in the frequency domain. To determine the

[3]equal variances for real and imaginary part

influence of water, baseline and noise, the PM has been studied. As illustration, we plotted a simulated spectrum from set 4 and from set 6 in Fig. 5.1.



(a) Set 4 (b) Set 6

Figure 5.1. *Simulated spectra from set 4 and set 6. The amplitudes are in arbitrary units.*

In the **fourth** experiment, AQSES was validated using an *in vitro* sample. This test solution contained 9 metabolites of known concentrations: Cr, NAA, Glu, Gln, Myo, PCh, Glycerphosphocholine (GPCh), Tau and Lac. The basis set used in AQSES was: Cr, NAA, Glu, Myo, PCh, Tau and Lac. Glu was selected to fit the combination of Glu and Gln, since Glu and Gln have similar profiles and are highly correlated. Glu will be denoted by Glx in this experiment and in the last experiment to indicate that it fits the combination of Glu and Gln. The combination of PCh and GPCh was fitted similarly with PCh. The true and estimated proportions of metabolites have been compared, the proportion of metabolite k being the ratio of the concentration of metabolite k and the total concentration (all metabolites).

In the **last** experiment, *in vivo* NMR signals from a database containing MRSI spectra from normal tissue (122 spectra selected from data of four volunteers), gliomas of grade II (GII, 90 spectra selected from data of six patients) and Glioblastoma multiforma (GBM, 59 spectra selected from data of five patients) were processed. The goal of this part is to show that AQSES provides results in accordance to the literature. For the specific acquisition procedure and settings, see [249]. The basis set was identical to the one in the first experiment. We also display metabolic images obtained from a patient with a GBM (*I*-1285 from the INTERPRET database [1]) that underwent spectroscopic imaging. The metabolic images have been obtained by processing all spectra of the patient in batch mode by AQSES, using the same basis set as before.

The first three experiments are carried out assuming either no prior knowledge of the phases or that the metabolites are in phase. The last two experiments did not assume any prior knowledge of the metabolite phases.

5.3 Results

5.3.1 Performances of AQSES

Fig. 5.2 shows a boxplot of the distribution of the amplitudes found by AQSES for the *in vivo* spectra of healthy tissue that were used to estimate meaningful values for the simulated signals. For the specific acquisition procedure and settings, see [249] (STEAM ^{1}H-MRSI, 1.5 T, TE = 20 ms, TR = 2000 ms). The means are sensible values with respect to the literature (see, *e.g.*, [284]). The large variances may result from the fact that the spectra of healthy tissue originate from different brain locations, which have an influence on the metabolite concentration as shown in [284].

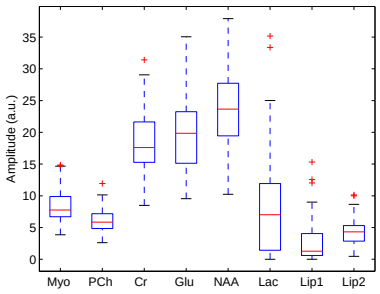


Figure 5.2. *Boxplot showing the quantitated amplitudes of* in vivo *spectra from healthy volunteers.*

The **first** experiment shows that, in 95.5% of the cases, the parameter estimates are almost perfect (*i.e.*, the relative difference between the true and the simulated metabolite amplitudes is under 10^{-6}%). This result holds whether the metabolites are assumed to be in phase or not. Looking at each metabolite separately, the percentages of cases where the relative errors are higher than 1% are quite similar for both assumptions (rows 1 and 3 in Table 5.1). Table 5.1 indicates that Lac is misfit in most of the remaining cases (4% out of 4.5%). In the cases of imperfect parameter estimates, the relative error for NAA never exceeds 1% when we assume equal phases. In 4% out of 4.5% cases, the estimation is corrupted by the value of Lac which overlaps Lip1, resulting in larger amplitude estimation errors. Tables 5.2 and 5.3 report the PM corresponding to each set and to each metabolite, imposing respectively equal phases for all metabolites and letting the phases free. These values are obtained after discarding the signals that do not provide perfect parameter estimates (defined above), *i.e.*, 9 signals out of 200 (same signals in both tables). The first row of these tables shows that a higher degree of accuracy can be reached when equal phases are assumed.

The **second** simulated example shows the results when the number of metabolites in the basis set and in the simulated spectra are not the same. The percentage of almost perfect parameter estimates decreases to 92% when assuming the metabolites in phase, while it decreases to 92.5% when no assumptions about the phases are made. However, imposing equality of phases improves the accuracy of the fit (Tables 5.2 and 5.3, rows 2) when considering the 191 signals that provide perfect parameter estimates in the first

experiment. The goodness of the fit is now complicated by the overlap of metabolites such as Myo, Glc, PCh and Tau. Rows 2 and 4 in Table 5.1 illustrate the loss in accuracy compared to rows 1 and 3; when Glc, Ala and Tau are added to the basis set. The other metabolites, located at other frequency ranges, are less affected by the addition of Tau, Ala and Glc to the basis set. This shows that AQSES is not very sensitive to the choice of the basis set provided its components are not strongly correlated.

Table 5.1. *Percentages of cases (for each metabolite) for which the relative differences between the true and the estimated metabolite amplitudes is smaller than 1% (based on 200 signals for each set). The top (resp. bottom) two rows correspond to the equal phase constraint (resp. no constraints on the phases). The notations are explained in Section 5.2.*

	Myo	PCh	Cr	Glu	NAA	Lac	Lip1	Lip2
exp. 1, Set 1	98.5	99	98.5	98.5	100	96	96.5	97
exp. 2, Set 1	92.5	95	95.5	97	98.5	93.5	94.5	96
exp. 1, Set 1	98.5	97.5	98	98	99.5	96	96	97
exp. 2, Set 1	94	94.5	97.5	95	98.5	93.5	94	95

Table 5.2. *Performance measure (PM) for each metabolite of each simulation set (in percentage, see Equation 5.1 with $L = 191$). Equality of all metabolite phases has been imposed.*

	Myo	PCh	Cr	Glu	NAA	Lac	Lip1	Lip2
exp. 1, Set 1	4.1E-12	1.4E-12	1.9E-12	1.35E-11	1.5E-12	1.81E-11	1.6E-12	1.08E-10
exp. 2, Set 1	1.72	1.21	0.07	0.09	0.01	0.65	0.77	0.19
exp. 3, Set 2	1.24	0.93	0.39	0.67	0.20	6.59	7.91	0.81
exp. 3, Set 3	5.76	4.04	2.87	4.33	2.48	15.18	19.85	6.89
exp. 3, Set 4	8.66	7.07	4.95	6.65	5.67	20.10	29.25	14.74
exp. 3, Set 5	9.51	2.67	1.76	24.39	6.25	10.79	14.01	6.26
exp. 3, Set 6	14.73	8.36	6.44	25.04	9.81	23.53	29.14	17.34

Table 5.3. *Performance measure (PM) for each metabolite of each simulation set (in percentage, see Equation 5.1 with $L = 191$). No prior knowledge has been imposed.*

	Myo	PCh	Cr	Glu	NAA	Lac	Lip1	Lip2
exp. 1, Set 1	6.95E-07	1.92E-07	1.01E-07	6E-07	2.07E-07	8.12E-07	8.51E-07	6.31E-07
exp. 2, Set 1	2.67	3.53	0.44	0.14	0.07	1.34	1.24	0.30
exp. 3, Set 2	1.20	1.40	0.35	0.67	0.46	10.47	6.48	1.26
exp. 3, Set 3	7.37	5.88	4.25	4.27	3.23	19.17	20.01	7.71
exp. 3, Set 4	10.81	9.77	6.22	7.74	5.97	23.00	34.44	15.32
exp. 3, Set 5	10.06	7.68	2.90	29.41	7.97	19.15	14.07	9.76
exp. 3, Set 6	13.45	11.00	7.41	29.71	10.44	24.65	32.44	18.28

The **third** experiment investigates the robustness of AQSES against the addition of disturbance components such as noise, baseline and water resonances. The PM are reported in Tables 5.2 and Tables 5.3 for each simulation set (last four rows).

The extreme values are mainly present in the overlapping peaks, *i.e.*, Lac and Lip1. The maximum-phase filter removes satisfactorily the water component, if we inspect the PM in set 2 in Tables 5.2 and 5.3 (row 3). The PM for different noise levels confirms the stability of AQSES against noise. At low noise values, the PM does not increase dramatically for all metabolites, except for Lac, Lip1 and Lip2. At high noise, the PMs of Lip1 and Lip2 keep increasing strongly, while the PM of Lac is more stable. The fact that these metabolites are estimated with a lower accuracy may be explained by their low magnitude level. They are more embedded in noise than the other ones , or in other words, they have a smaller relative signal-to-noise ratio. The PMs of the 5 main metabolite profiles show stability against noise (columns 1 to 5 in Tables 5.2 and 5.3). The baseline affects each component, but mainly Myo and Glu. Myo and Glu are wider and therefore are more likely to be fitted by the baseline. Cr is less affected by the baseline. The PM of NAA, Cr and PCh remain under 10% in all sets with the assumption of equal phases (Table 5.2) and under 11% without this assumption (Table 5.3). The largest PM value is kept under 30% in Table 5.2 and under 33% in Table 5.3. In most of the cases, a slightly better accuracy is obtained by assuming that the metabolites are in phase.

Since these three experiments involve different models, we have studied the computation time required for each type of model. The results are reported in Table 5.4. For experiment 1, and 3 (sets 2, 3 and 4), we do not consider the baseline in the model and the number of metabolite profiles in the basis set equals 8 (model 1 in Table 5.4). For experiment 2, the baseline is still not included in the model but the number of metabolite profiles in the basis set increases to 11 (model 2). For experiment 3 (sets 5 and 6), the baseline is incorporated in the model which takes into account the contribution of 8 metabolite profiles. The computation times of AQSES using 2 different assumptions have been compared: imposing equal phases for all metabolites or letting the phases free. The values reported in Table 5.4 are the average computation times for one spectrum. AQSES has been run on a Windows XP platform with a Pentium 4 (3 GHz CPU, 1 Gb RAM). The simplest case in terms of computation time is for model 1 when the phases are free with an average quantification time per spectrum of 0.87 s (2'45" for 191 spectra). Assuming equal phases for all metabolites increases the computation time if the baseline is not considered in the model. In the slowest case, *i.e.* the case when the database of metabolites is larger (11 metabolites), the computation time per spectrum is 4.03 s (12'49" for 191 spectra), which remains relatively small.

Table 5.4. *Average computation times (in seconds) per spectrum for each model, imposing equal phases for all metabolites or letting them free.*

Models \ Prior knowledge	Equal phases	Free phases
Model 1: exp. 1, exp. 3 (Sets 2, 3, 4)	1.39	0.87
Model 2: exp. 2	4.03	2.74
Model 3: exp. 3 (Sets 5, 6)	3.29	3.32

For the **fourth** experiment, the true and estimated proportions of the amplitudes of the metabolites in the test sample are reported in Fig. 5.3. The relative errors between the

true and the estimated proportions are relatively small (all $< 26\%$) and especially for the metabolites in higher concentration ($< 8\%$). Note that the estimation of Glx is quite good ($\approx 6\%$) while the individual estimates of Glu and Gln are not as good if we include their corresponding metabolite profile in the database ($\approx 25\%$, data not shown). This is due to the high degree of correlation between these two metabolite profiles. On the contrary, summing up the contributions of Glu and Gln for estimating Glx yields good results (also $\approx 6\%$, data not shown).

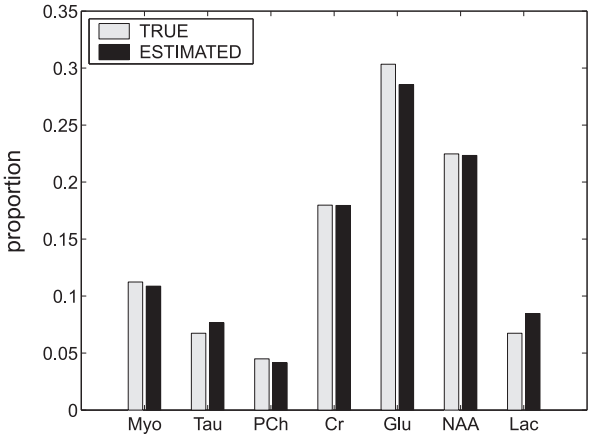


Figure 5.3. In vitro *test sample results.*

For the **fifth** experiment, we show in Fig. 5.4 the averaged estimated amplitudes obtained with AQSES, for 8 metabolites of the three classes normal, grade II and GBM. NAA and Cr decrease with the grade of the tumor, in agreement with [86]. A large difference occurs between the concentration of NAA in normal and glioma tissues. Myo, PCh and Glx exhibit much less variations. We note a small increase in Glx and PCh with the grade of glioma. When ordering comparable metabolites (*i.e.*, without Lip1 and Lip2, see Section 5.2) from the highest to the lowest in concentration, we have

for normal brain: NAA, Glx, Cr, Myo, Lac and PCh;

for GII: Glx, Lac, Cr, NAA, Myo, PCh; and

for GBM: Lac, Glx, PCh, Cr, NAA and Myo.

We note that Lac, Lip1 and Lip2 strongly increase with the grade of the tumor.

Metabolic images such as in Fig. 5.5 can also be displayed. The computation time required by AQSES to provide the quantification results is 2'50" (Windows XP, 1 Gb RAM, 3 GHz CPU). In this example, the affected region is clearly visible on the T2-weighted image (Fig. 5.5a). The tumor region can also be identified from almost all metabolic images (see Fig. 5.5 (d, f, g, h, and i)). The concentrations of NAA and Cr are lower in the tumor

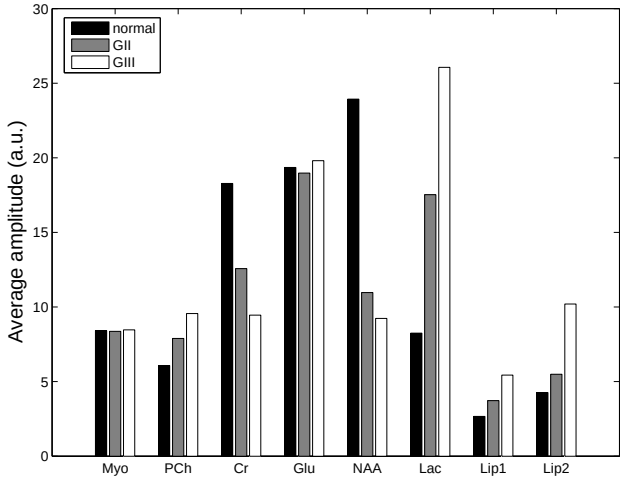


Figure 5.4. *Averaged estimated amplitudes for normal tissues, GII and GBM, in arbitrary units.*

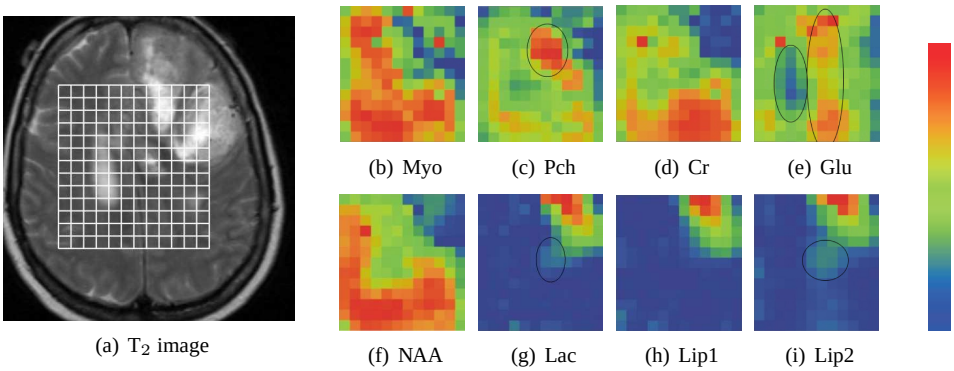
region, while the concentrations of Lac, Lip1 and Lip2 are larger in that region, which agrees with Fig. 5.4 and with the literature (see, *e.g.*, [199] and [80]). Myo decreases in the tumor, but this contrast is less apparent than in the case of NAA or Cr. Also noticeable is the low Glx concentration in the region of the ventricle compared to the central part of the brain (ellipsoid in Fig. 5.5e). An increase of PCh, present in the boundary between the malignant and healthy areas (ellipsoid in Fig. 5.5e), could reflect an increase of membrane synthesis and accelerated cell proliferation (see, *e.g.*, [80]). The ellipsoids in Fig. 5.5(g) and (i) correspond to a region that is slightly higher in intensity in the T2-weighted image. This region has also an increased concentration for Lip2 and Lac. The presence of Lip is thought to correspond to cellular and membrane breakdown corresponding to necrosis [199]. Lac is usually detected only under pathologic conditions, when energy metabolism is affected severely [88]. This shows that pathologic information, which is barely visible on MRI images, can be successfully extracted from metabolic maps.

5.3.2 AQSES versus QUEST

This experiment compares the performances of AQSES and QUEST in the presence of nuisance components (water and baseline). The original simulation set contains 100 signals created similarly as in the previous section with the same 8 metabolites (NAA, Myo, Cr, Pch, Glu, Lac, Lip1, Lip2). Two additional sets were created by adding either a water component or a baseline signal to the original set (same water and baseline signals as in Section 5.3.1). The performance measure is similar to the one in Eq. (5.1).

The results reported in Table 5.5 shows that signals without nuisance components are more accurately estimated in AQSES than in QUEST. In particular, high accuracy levels ($<$0.1% error) are reached in most of the cases with AQSES, while errors larger than 0.1% are generally exhibited by QUEST.

In a second experiment, we compared the effects of the nuisance components on



(a) T_2 image (b) Myo (c) Pch (d) Cr (e) Glu (f) NAA (g) Lac (h) Lip1 (i) Lip2

Figure 5.5. *Metabolic maps of a patient with a glioblastoma. The ellipsoids in (c), (g) and (i) indicate regions where we note a substantial increase of the corresponding metabolites compared to a region with normal tissue (high concentrations in red and low concentrations in blue with a linear scale). This information may particularly be useful since it barely appears on the T2-weighted image. The concentration of Glu is lower in the ventricles (one of the ventricle regions is indicated by the left ellipsoid in (e)). The ellipsoid on the right hand side in (e) encircles the region that lies between the ventricles.*

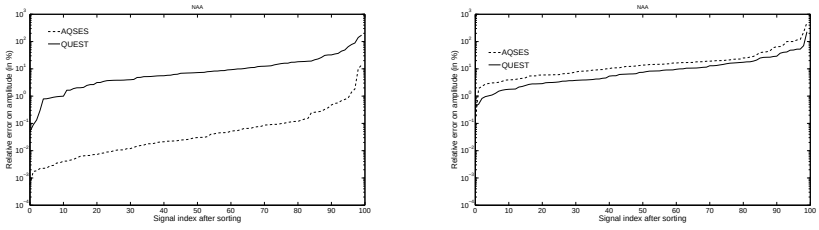
Table 5.5. *Percentages of correctly estimated amplitudes for an error threshold of 0.1% (first 2 rows) and 1% (last two rows). Based on the first simulation set,* e.g.*, signals without nuisance components.*

	NAA	Myo	Cr	Pch	Glu	Lac
AQSES (0.1%)	97%	97%	97%	96%	97%	97%
QUEST (0.1%)	60%	4%	54%	34%	61%	28%
AQSES (1%)	99%	98%	98%	97%	97%	97%
QUEST (1%)	93%	48%	93%	82%	94%	88%

the parameter estimated obtained with AQSES and QUEST. The results are plotted in Fig. 5.6(a) for signals with water and Fig. 5.6(b) for signals with baseline. Signals with a residual water component were better processed in AQSES than in QUEST. This is due to the combination of the intrinsic better accuracy of AQSES when no nuisance components are present and the use of the maximum-phase FIR filter. For signals with baseline, the regularization parameter λ was fixed and may not be optimal for all signals. Fig. 5.6(b) shows larger errors for AQSES, which indicates a better robustness of QUEST when dealing with baseline components. Note that MP-FIR was not used in this last experiment. We shall see in Chapter 6 that MP-FIR plays a role on the baseline as well.

5.4 Discussion

The VARPRO implementation of AQSES, using a modified Levenberg-Marquardt minimization algorithm, is important for fast convergence and reliable numerical computations



(a) Signals with water (b) Signals with baseline

Figure 5.6. *Sorted relative differences between real and estimated amplitudes of NAA for signals with water or baseline component processed by AQSES and QUEST*

and is less affected by local minima, since no starting values are needed for the linear parameters (including the parameters of the baseline). The nonlinear parameters (*e.g.*, frequency shifts or damping corrections) are initialized with zeros, which is the most reasonable choice in the context of short echo time quantification. The classical VARPRO method leaves the linear part of the model completely free such that no constraints can be imposed on the amplitude and phase. But, in theory, the phases of the metabolites are equal. Constraining the phases to be equal implies some modifications of the classical VARPRO implementation as described in section Section 2.3.1. The results show that a high accuracy level can be reached thanks to this algorithm.

Another important aspect is the choice of the basis set in AQSES. The basis set should contain the metabolites actually visible in the spectrum except for those that are too correlated to each other. Indeed, equivalent metabolite profiles can ruin their own individual parameter estimates as we have seen in the experiment 4 when Glu and Gln were both in the database. When the basis set contains more metabolites than actually contained in the spectrum, we showed that the amplitude estimates of the metabolites which were not actually in the signal (*i.e.*, Tau, Ala and Glc), were often close to zero (see experiment 2). These results indicate an added value of the VARPRO method implemented in AQSES over other methods. However, adding more metabolites in the basis set will increase the complexity of the algorithm and consequently the computation time. The results show that the latter could be more than doubled by adding 3 metabolite profiles to the basis set of 8 profiles. Furthermore, the parameter variances will also increase, limiting the accuracy of the algorithm. In case of doubt about the presence of some metabolites, we recommend to add them to the basis set if they do not exhibit profiles too similar to the metabolite profiles already entered in the basis set. Large Cramer-Rao bounds displayed in AQSES GUI or the presence of obvious peaks in the plot of the residue may be an indicator of an incomplete basis set. In this respect, the basis set of 8 metabolite profiles used in this work provides a good compromise although we do not claim that it is the best choice for any type of MRS spectra to be fitted. The protocol of the basis set should be similar to the one used to acquire the spectra to be fitted such that the parameter corrections (α_k, ζ_k) can be assumed as small, reducing the risk of convergence to a local minimum.

One of the underlying goals of a quantification method is to separate the signal from the disturbance components. In this respect, the maximum-phase FIR filter provides sat-

isfactory results. Its high efficiency allows its embedment in the iterative minimization in AQSES, resulting in more accurate parameter estimates. This filter, in addition to filtering out the unwanted components (including the noise) in the frequency region of no interest, removes partially the baseline. This reduces the importance of the regularization parameter, λ, that may influence substantially the results, as shown in the comparisons between AQSES and QUEST. The use of a semi-parametric model reduces the number of steps to obtain the parameter estimates, decreasing their variances and thus increasing the reliability of the results. The baseline remains a crucial issue during fitting due to its large correlation with the other metabolites. Our results show that (compared to the results of data set 1) the errors for all metabolites increase substantially, with a smaller increase for Cr. This seems to be in agreement with the observation of Ratiney *et al.* [226], who noted that the background amplitude was correlated with all metabolite amplitudes except that of Cr. AQSES is robust against noise since the least squares problem that is solved is restricted to a linear combination of corrected metabolite profiles present in the signal; using metabolite profiles instead of individual peaks implies an increased robustness against noise, because correlations between spectral regions that are relatively far apart are taken into account.

5.5 Conclusion

The performances of AQSES have been described in this chapter. AQSES provides more flexibility in exploiting prior knowledge than the classical VARPRO method without sacrifying its advantages in numerical accuracy and computational efficiency. The use of the maximum-phase FIR filter allows more robustness against disturbance components such as water, noise or baseline. AQSES generates fast and accurate results on simulated data and *in vitro* samples. The results of batches of *in vivo* data that contain spectra from healthy, grade II gliomas and glioblastomas are in line with results described in literature. The results of a set of spectroscopic imaging data is in accordance with MR images obtained from the same slice.

Chapter 6

Solvent suppression methods: MP-FIR vs HLSVD-PRO

Accurate and efficient filtering techniques are required to suppress large nuisance components present in short echo time magnetic resonance (MR) spectra. The previous chapter investigates the quantification method AQSES, which employs a maximum-phase finite impulse response filter (MP-FIR) for solvent suppression. In this chapter[1]*, we study in more details MP-FIR and compare it to another widely used method HLSVD-PRO, the Hankel-Lanczos Singular Value Decomposition with Partial ReOrthogonalization. Both filters are validated and compared through extensive simulations. Their properties are discussed. In particular, the capability of MP-FIR for dealing with macromolecular components is emphasized. Although this property does not make a large difference for long echo time MR spectra, it can be important when quantifying short echo time spectra. The theoretical aspects of MP-FIR and AQSES have been discussed in Chapter 2.*

6.1 Introduction

Efficient and accurate quantification of metabolites from short echo time *in vivo* MR spectroscopy (MRS) might be an important aid in the correct noninvasive diagnosis of human brain pathology. Quantification of short echo time MR spectra provides more metabolite information than long echo time spectra, but is hampered by broad baseline signal contributions, resonance line-shape distortions, low signal-to-noise ratios (SNR) and overlapping peaks in the frequency domain (see, *e.g.*, [65]). Therefore, in order to obtain accurate parameter estimates, it is recommended to disentangle the metabolite contributions from the unwanted components. Numerous methods have been developed to address this issue (see Chapter 3). In this study, we focus on two filtering techniques widely used with long echo time MR spectra for solvent suppression: the maximum-phase FIR filter (MP-FIR) [273] and the Hankel-Lanczos Singular Value Decomposition with Partial ReOrthogonalization (HLSVD-PRO) [152]. Since the differences between long echo and short echo time

[1] J. Poullet, D.M. Sima, S. Van Huffel, P. Van Hecke, Frequency-selective quantification of short echo time ^{1}H Magnetic Resonance spectra, J. Magn. Reson. 186(2)(2007) 293-304.

MR spectra are substantial, the appropriateness of these filters for short echo time spectra should be validated. Indeed, to fully understand the behavior of these filters it is imperative to study them in close connection with the type of signals they are applied to. Some characteristics of the filters are more important for short echo time spectra than long echo time spectra. Furthermore, since the final goal is to obtain accurate parameter estimates, a quantification method is needed to validate and compare the filters. AQSES, Automated Quantification of Short Echo time MRS Spectra (see Chapters 2 and 5 or [213] and references therein), has been chosen as quantification method for the reasons described below. The goal of this study is therefore two fold: first, to validate both filtering techniques for short echo time spectra, and second, to show the extra value of MP-FIR over HLSVD-PRO for this type of spectra.

This chapter is organized as follows. First, we discuss briefly the choice of the filtering techniques, MP-FIR and HLSVD-PRO, and the quantification method AQSES. Then, the properties of both filters are described and illustrated on simple examples. The influence of the filters on the estimated parameters is studied through extensive numerical studies. Finally, the advantages of MP-FIR over HLSVD-PRO are pointed out and the combined use of MP-FIR with other quantification methods is discussed.

Why MPFIR and HLSVD-PRO?

Measurement sequences fail to suppress completely the water resonance without affecting the metabolites of interest. Therefore, the so-called water suppressed signals contain a residual water contribution which cannot be depicted by an analytical formulation. Time-domain quantification methods (see, *e.g.*, [213, 297, 230, 226, 78]) cannot be used without first removing the water components, while frequency-domain methods (see, *e.g.*, [175, 190, 111, 267, 89]) can be applied directly to the water suppressed signal, but should consider the water tails as part of the macromolecular baseline. Water suppression methods should not influence the parameter estimates and should have a low computational complexity. We have seen in Section 3.6.2 that they can be categorized in two main groups: on one hand, the convolution-based methods [273, 177, 258, 53, 6, 5, 103] convolve the original signal with the coefficients of a filtering window, and, on the other hand, the methods based on a model function and, in particular, those based on the singular value decomposition of a Hankel matrix [152, 210, 42]. Among the convolution-based methods, we have seen that MP-FIR was the most accurate and efficient method for quantifying long echo time MRS spectra. Among the SVD-based methods, HLSVD-PRO has been shown to outperform the other methods in terms of computational efficiency and numerical reliability. MP-FIR and HLSVD-PRO have been selected since they are the most successful filters for long echo time MR spectra and they are based on two different approaches. Although, the main objective of these filters is to remove the water resonances, we will show that MP-FIR can have a substantial effect on the baseline which can result in better parameter estimates. Nevertheless, MP-FIR will not compete with baseline correction methods but, combined with the latter, might improve the final estimates. In this work, we study three types of nuisance components –noise, baseline and water resonances– and the effect of the filters on these components. The choice of AQSES for validating both filtering techniques can easily be explained since

- AQSES is a time-domain quantification method,

- both filtering techniques can easily be combined with AQSES,
- AQSES has been designed for short echo time MR spectra, in contrast with AMARES [299], for example, which is typically designed for long echo time MR spectra.

6.2 MP-FIR and HLSVD-PRO in quantification methods

The main goal of both filters is to filter out the water component w (see Eq. (2.2)), which has resonance frequencies in a known frequency interval. This interval is disjoint to the frequency region (or interval) of interest where the metabolite resonances are located. Quantification methods based on iterative optimization procedures can reasonably combine filtering methods only if these methods are fast, especially when numerous signals have to be processed (*e.g.* with MRS imaging data). The computational load of SVD-based methods is known to be much larger than the one of simple convolution methods like MP-FIR (see, *e.g.*, [273]). Moreover, the filter coefficients of MP-FIR are computed only once prior to the optimization procedure. The same filter coefficients are then used all along the iterative optimization procedure such that MP-FIR boils down to a simple matrix multiplication, which is considerably faster than calculating the filter coefficients. To be used in the optimization procedure, HLSVD-PRO would require an SVD decomposition of a large matrix at each iteration (see Section 2.2.2 or [152]). A matrix multiplication is much faster than an SVD decomposition, making HLSVD-PRO much less attractive for being used in the iterative optimization procedure.

6.2.1 FIR filter inside AQSES

When using an FIR filter inside AQSES (neglecting the baseline for sake of simplicity), the nonlinear least squares problem becomes:

$$\min_{\alpha_k,\zeta_k} \sum_{n=0}^{N-1} \left| y_{fil}(n) - \sum_{k=1}^{K} \hat{y}_{fil,k}(n) \right|^2 , \tag{6.1}$$

where

$$\hat{y}_{fil,k}(n) = \sum_{m=0}^{M-1} h(m)\alpha_k \zeta_k^{n-m} v_k(n-m). \tag{6.2}$$

The same notations as in Chapter 2 are used. The first $M-1$ points of the filtered metabolite profiles $\hat{y}_{fil,k}$ are discarded to avoid distortion. The idea of the variable projection algorithm (used in AQSES) is to project the linear parameters α_k out of the least squares problem such that only a smaller sized nonlinear least squares problem remains to be solved for the nonlinear variables ζ_k. This problem is solved via an iterative minimization algorithm of the Levenberg-Marquardt type [193] (see Section 2.3.1 for more details).

6.2.2 FIR filter outside AQSES

An FIR filter can also be used as preprocessing method. In that case, the signal is filtered prior to the quantification. The metabolite profiles in the database can also be filtered if they contain nuisance components. The nonlinear least squares problem becomes:

$$\min_{\alpha_k,\zeta_k} \sum_{n=0}^{N-1} \left| y_{fil}(n) - \sum_{k=1}^{K} \alpha_k \zeta_k^n v_{fil,k}(n) \right|^2, \tag{6.3}$$

where

$$v_{fil,k}(n) = \sum_{m=0}^{M-1} h(m) v_k(n-m). \tag{6.4}$$

The first $M-1$ points of the filtered metabolite profiles $v_{fil,k}$ are discarded to avoid distortion.

To understand the effect of the filter, we can compare the filtered signal to the original signal in terms of signal-to-baseline and signal-to-noise ratios. The baseline components are assumed to have large damping values compared to the metabolite peaks. We neglect the fact that y_{fil} is limited to $N-M+1$ points and not N. Each Lorentzian (k,p) is thus multiplied by the complex number $\bar{h}\bar{\zeta}_{k,p}$ as shown in Eq. (2.19). The term $|\bar{h}\bar{\zeta}_{k,p}|$ decreases exponentially (or linearly in a logarithmic scale) with the damping values as illustrated in Fig. 6.1, resulting in an **increased signal-to-baseline ratio**. The broader the passband, the more stable $|\bar{h}\bar{\zeta}_{k,p}|$ with respect to the damping coefficients. The influence of the damping is thus mainly observable for narrow-passband filters. The noise will not be attenuated (or negligibly) by the filter in the region of interest, resulting in a **decreased signal-to-noise ratio**. Choosing the broadest possible passband seems to be reasonable. However, the signal-to-baseline ratio will be higher for narrow-passband filters (see Example 1 below). The choice of the filter region will result in a trade-off between the increase of the signal-to-baseline ratio and the decrease of signal-to-noise ratio. In other words, narrow-passband filters will be preferred for signals with large baseline components, while broad-passband filters will be more indicated for signals with small baseline components like long echo time MR spectra.

Example 1 (referring to Fig. 6.1)
Considering a sampling frequency of 1 kHz, an individual Lorentzian with $d_k = 0.016$ will be attenuated by $\pm$ 0.9 dB ($\approx 10\%$ loss in magnitude) by a narrow-passband filter ([0.25,4.2] ppm), while it will be attenuated by $\pm$ 0.25 dB ($\approx 3\%$ loss in magnitude) by a broad-passband filter ([-3,7] ppm). Note that this Lorentzian would be much more attenuated by a linear-phase filter: 5.6 dB ($\approx 48\%$ loss in magnitude) for [0.25,4.2] and 4.9 dB ($\approx 43\%$ loss in magnitude) for [-3,7]. This shows why a linear-phase filter is not suitable for Lorentzians.

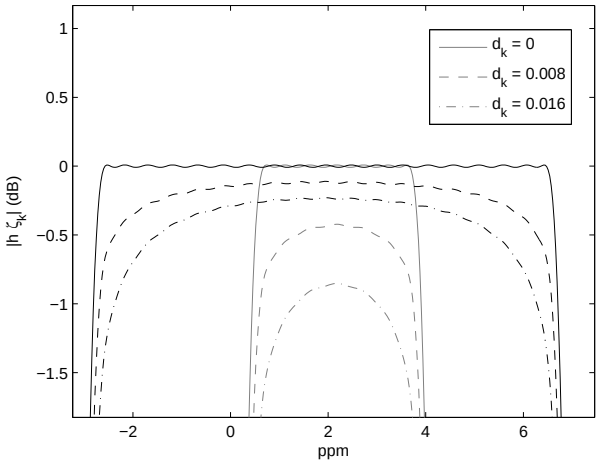


Figure 6.1. *Magnitude of $|\bar{h}\bar{\zeta}_{k,p}|$ as a function of the frequency for different damping coefficients d_k (in kHz*rad) and different filtering regions (in black for the frequency interval [0.25,4.2] ppm and in gray for [-3,7] ppm). The filter order is 70.*

6.2.3 HLSVD-PRO in quantification methods

HLSVD-PRO is a subspace-based method for modeling a sum of exponentially damped sinusoids (Lorentzians), which can be used as a frequency-selective filter. HLSVD-PRO is applied, before entering the iterative quantification procedure, to the MRS signal, as well as to each metabolite profile included in the database. HLSVD-PRO models the original signal and the metabolite profiles such that

$$\begin{aligned}\hat{y}(n) &= \sum_{i=1}^{L_0} \alpha_{0,i}\zeta_{0,i}^n = \sum_{i=1}^{W_0} \alpha_{0,j(i)}\zeta_{0,j(i)}^n + \sum_{i=W_0+1}^{L_0} \alpha_{0,j(i)}\zeta_{0,j(i)}^n \\ \hat{v}_k(n) &= \sum_{i=1}^{L_k} \alpha_{k,i}\zeta_{k,i}^n = \sum_{i=1}^{W_k} \alpha_{k,j(i)}\zeta_{k,j(i)}^n + \sum_{i=W_k+1}^{L_k} \alpha_{k,j(i)}\zeta_{k,j(i)}^n \end{aligned} \tag{6.5}$$

where $j(i)$, $i = 1,\ldots, L_0$ (respectively L_k) is a permutation of $i = 1, \ldots, L_0$ (respectively L_k) such that the indices of Lorentzians with central frequency inside the water resonance region are the first W_0 (respectively W_k) ones. L_0 (respectively L_k) is the model order of HLSVD-PRO applied to the original signal (respectively metabolite profile k), W_0 (respectively W_k) is the number of Lorentzians falling within the water resonance region when applying HLSVD-PRO to the original signal (respectively metabolite profile k). The Lorentzians located in the frequency region of no interest are then subtracted from the

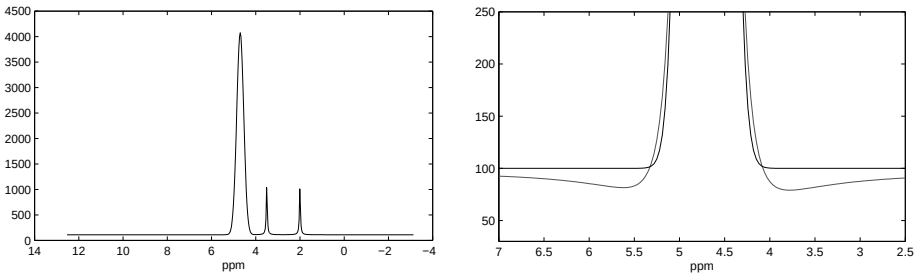
original signal y, as well as from the initial metabolite profiles v_k, $k = 1, \ldots, K$, such that

$$y_{fil}(n) = y(n) - \sum_{i=1}^{W_0} \alpha_{0,j(i)} \zeta_{0,j(i)}^n \ ,$$
$$\hat{y}_{fil}(n) = \sum_{k=1}^{K} \alpha_k \zeta_k^n \left(v_k(n) - \sum_{i=1}^{W_k} \alpha_{k,j(i)} \zeta_{k,j(i)}^n \right), \tag{6.6}$$

where $\hat{y}_{fil}$ denotes the estimate of the filtered MRS signal. The filtered model $\hat{y}_{fil}$ is used to fit the filtered signal y_{fil}.

Besides being relatively slow compared to MP-FIR, the major problem with HLSVD-PRO is that it assumes a Lorentzian model which is optimistic given the random nature of the remaining water resonances. This results in a **decreased signal-to-baseline ratio**, which can be illustrated by Example 2. The **signal-to-noise ratio** is however kept **constant**.

Example 2 (referring to Fig. 6.2)
Suppose a signal containing three peaks, 2 Lorentzians at 2 and 3.5 ppm for the metabolites and 1 Gaussian at 4.7 ppm for the water peak, as plotted in Fig. 6.2(a). We apply HLSVD-PRO on the frequency region [0.25 4] ppm. The model order was set at 4 since at least 2 Lorentzians are used for modeling a Gaussian. In Fig. 6.2(b), we reconstruct the water components that have been removed by the filter. A bump is clearly visible in the transition region between the water and the metabolites. This bump is due to the nature of the model used in HLSVD-PRO. Increasing the model order would help to reduce the water component but would not help to substantially reduce this "bump effect". Consequently, the residual water tails will be seen as baseline components overlapping with the frequency region of interest, resulting in a **decreased signal-to-baseline ratio**.



(a) Real part of the spectrum.

(b) Real part of the water components in the frequency domain (True components in black and estimated ones in gray).

Figure 6.2. *Bump effect illustrated by applying HLSVD-PRO on a signal with a Gaussian water peak.*

To get an idea of the influence of this bump effect on the amplitude estimates, we apply AQSES to the filtered signal. The results are shown in Table 6.1. For comparison, the

results of MP-FIR are also shown. The residual water tail affects the parameter estimates, resulting in a 2.7 % error for the peak at 2 ppm and 6.9 % error for the peak at 3.5 ppm, while the errors are less than 0.5 % when using MP-FIR.

Table 6.1. *Example 2: Amplitude estimates obtained with AQSES in combination with HLSVD-PRO or MP-FIR (last column). The true amplitudes are 10 for each Lorentzian.*

Lorentzian at	True	HLSVD-PRO	MP-FIR
2 ppm	10	10.27	10.04
3.5 ppm	10	10.69	9.96

6.3 Materials and Methods

The properties of the filters are illustrated on simple examples in the previous section. The goal of the following sections is to compare these filters on more complex and more realistic signals. Their robustness is studied with respect to the choice of a variety of nuisance components and filtering regions. An *in vivo* experiment shows the influence of these filters on the sensitivity of the quantification algorithm.

6.3.1 Database and simulated signals

The database used in AQSES is identical to the one used in [213] with 6 metabolites + 2 lipids: Myo-inositol (Myo), Phosphorylcholine (PCh), Creatine (Cr), Glutamate (Glu), N-acetylaspartate (NAA), Lactate (Lac), Lipid at 1.3 ppm (Lip1), Lipid at 0.9 ppm (Lip2). Simulated data were generated to compare the two filtering methods, HLSVD-PRO and MP-FIR. A signal free from nuisance components (except for the reference peaks at 0 and 8.44 ppm which are 3-trimethylsilyl-1-propane-sulfonic acid and formate, respectively) has been chosen from set 1 in [213]. This signal was quantified perfectly (*i.e.*, no error in amplitude estimation) with AQSES. This guarantees that all estimation errors are due to nuisance components. Although AQSES was applied on the unphased signal, we display the phased signal in Fig. 6.3 for a better signal assessment. For sake of clarity and space, only one signal (*i.e.*, one set of parameters a_k, ϕ_k, d_k and f_k) has been analyzed. The true amplitude values are given in Table 6.2.

Table 6.2. *True amplitudes in arbitrary units used to construct the signal in Fig. 6.3.*

NAA	Myo	Cr	Pch	Glu	Lac	Lip1	Lip2
40.60	13.40	27.12	9.64	29.51	16.65	0.21	0.10

Although different signal parameter values will lead to other results, one can expect that the general trends (*i.e.*, limitations and potentials of each filtering technique) are preserved. The nuisance components have been added to this signal to generate 4 different sets of signals as follows:

- set 1 = signal + low noise
- set 2 = signal + low noise + high baseline + water
- set 3 = signal + high noise
- set 4 = signal + high noise + high baseline + water

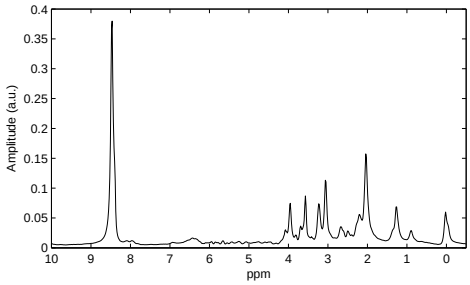


Figure 6.3. *Real part of the phased spectrum chosen from set 1 in [213].*

The baseline distortion was based on information from Table 1 in [242]; the baseline is the sum of Gaussians referred to as lip3, lip4, lip5, mm2, mm3 and mm4 in that work. This baseline b overlaps with the frequency region of the metabolites. The water profile has been extracted from a water-suppressed in vivo spectrum by means of HLSVD-PRO. Low and high noise levels correspond to SNR=300 and SNR=75, respectively. The SNR is defined as the ratio of the reference peak height at 8.44 ppm and the standard deviation of the circular white gaussian noise, both in the frequency domain. Each set contains 256 simulated spectra. As illustration, one signal from set 4 is plotted in Fig. 6.4 (the signal phase is corrected).

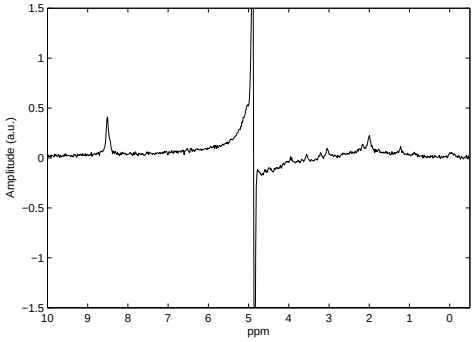


Figure 6.4. *Real part of the phased spectrum from set 4.*

6.3.2 Methodology

In order to test the sensitivity of each method with respect to the frequency bounds of the nuisance region, we defined two filtering regions: [0.25,4.2], [0.25,4.5] in ppm. The frequency region close to the water resonance at 4.7 ppm being more sensitive than the other one, we limited our study to the variations of the bounds for that region.

The effects of the nuisance components are tested with 6 model settings, which differ from each other regarding three options: choice between HLSVD-PRO or MP-FIR, the use of a baseline in the model or not, and the bounds of the region to be filtered. Note that these options can be easily defined in AQSES GUI, the graphical user interface of AQSES [213]. The regularization parameter λ, which controls the degree of smoothness of the baseline, has been defined manually. This parameter is used only when the baseline is included in the model (as a linear combination of spline basis functions). For each set, the best value of λ (*i.e.*, providing the amplitude estimates closest to the true amplitudes) was chosen for each filtering technique, resulting in 2*4=8 values of λ for all sets.

The model settings were defined as follows:

- Model setting 1: Use of the **baseline** in the model and **MP-FIR** filtering in [0.25,**4.2**] ppm
- Model setting 2: Use of the **baseline** in the model and **MP-FIR** filtering in [0.25,**4.5**] ppm
- Model setting 3: **No** use of **baseline** in the model and **MP-FIR** filtering in [0.25,**4.2**] ppm
- Model setting 4: Use of the **baseline** in the model and **HLSVD-PRO** filtering in [0.25,**4.2**] ppm
- Model setting 5: Use of the **baseline** in the model and **HLSVD-PRO** filtering in [0.25,**4.5**] ppm
- Model setting 6: **No** use of **baseline** in the model and **HLSVD-PRO** filtering in [0.25,**4.2**] ppm

Each set defined in Section 6.3.1 was quantified using each model setting. In order to compare the results obtained with the different model settings, we use the relative root mean square error (RRMSE), defined as

$$RRMSE_k = 100\sqrt{\frac{1}{L}\sum_{l=1}^{L}\frac{(a_k - \tilde{a}_{k,l})^2}{a_k^2}}, \tag{6.7}$$

where a_k (respectively $\tilde{a}_{k,l}$) is the true (respectively estimated) amplitude for metabolite profile k, l refers to the lth simulation and L is the total number of simulations within each set, i.e. 256. The model order used in HLSVD-PRO was fixed at 25 as recommended in [29].

***in vivo* experiment**

The performances of MP-FIR and HLSVD-PRO with respect to the regularization parameter λ are tested on an *in vivo* MR proton spectrum of normal brain tissue, acquired on a 1.5 T Philips NT Gyroscan using a PRESS sequence with an echo time of 23 ms, and a PRESS box of 4 x 3 x 3 cm^3. This water-suppressed signal was eddy current corrected using Klose's method [138] (see Fig. 6.5). Note that other methods for eddy current correction such as QUECC [13] could also be used.

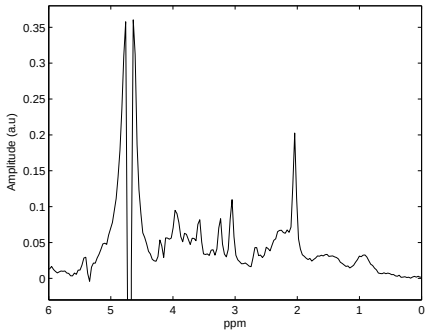
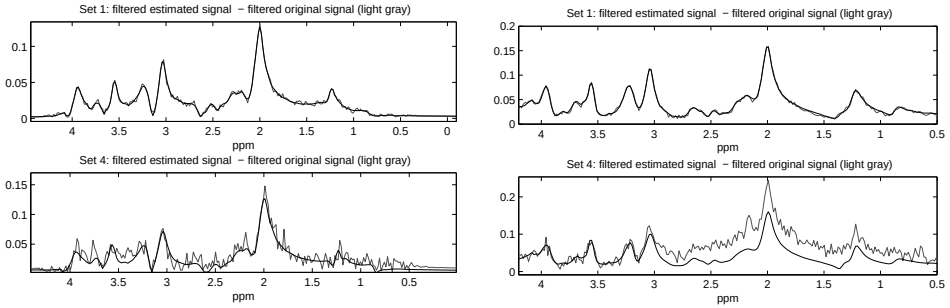


Figure 6.5. *Real part of the* in vivo *spectrum corrected for eddy current effects.*

The database used to fit the signal is identical to the one used for the simulated data. Glu is used to estimate the contribution of glutamate and glutamine and will be denoted Glx, and PCh for the contribution of choline compounds.

6.4 Results

Representative fits of sets 1 and 4, obtained by using model settings 1 and 4, are given as illustration in Fig. 6.6.



(a) Model setting 1 (MP-FIR) (b) Model setting 4 (HLSVD-PRO)

Figure 6.6. *Magnitude of the filtered original spectra vs filtered estimated spectra for sets 1 and 4 using model settings 1 and 4.*

The results are shown in Fig. 6.7. Each subfigure corresponds to one specific set. Model setting 1, where the baseline is modeled and MP-FIR is used, provides the best results with a RRMSE that remains under 50% for all metabolites and all sets. In most of the cases, the RRMSEs are larger when using HLSVD-PRO instead of MP-FIR with some values larger than 100%, especially for lower concentration metabolites such as Lip1 and

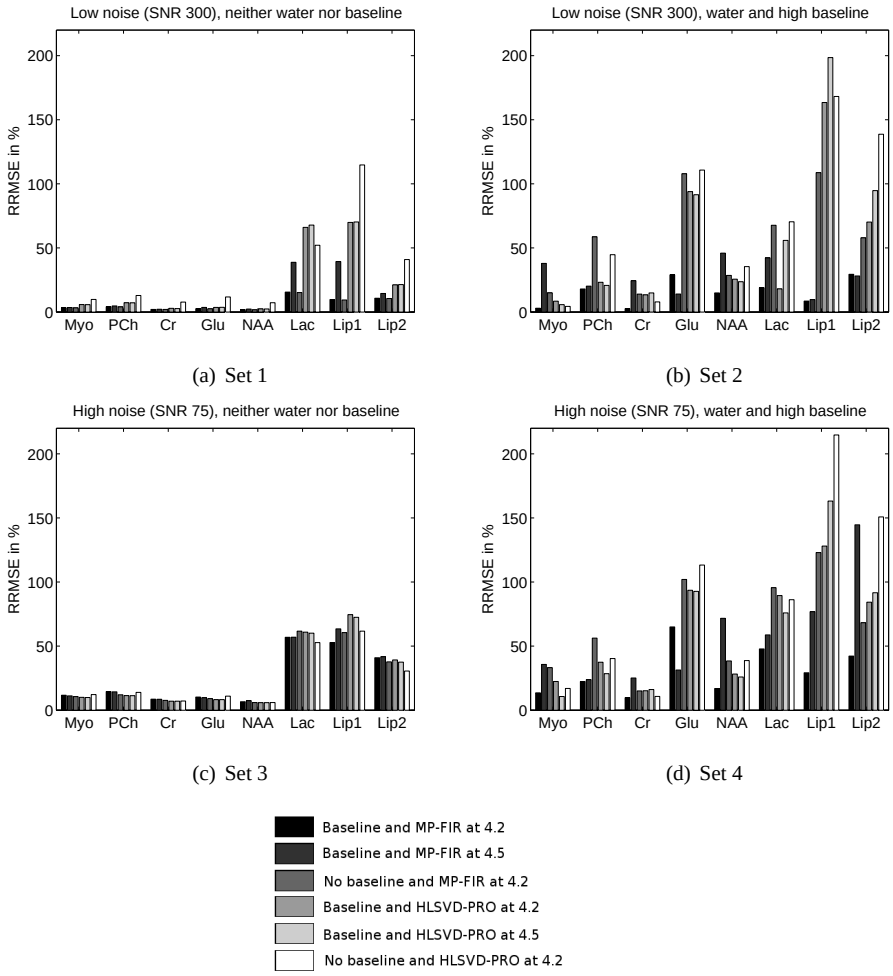
Lip2.

Including the **baseline** into the model is especially interesting when the signal baseline is large even if we observe relatively large errors for set 2 and 4. Cr and Myo are less affected by the addition of the baseline than the other metabolites such as Glu. Cr is known to be less correlated with the baseline [226] and Myo shows up in a frequency range where the baseline is less present (see, *e.g.*, [242]). The profile of Glu is relatively widely spread in the frequency domain. Therefore, in the presence of a strong baseline, Glu tends to fit a part of the baseline resulting in large errors for this metabolite. The differences between HLSVD-PRO and MP-FIR are larger when the signal contains a strong baseline. Indeed, strong differences between HLSVD-PRO and MP-FIR appear in set 1 only for Lac, Lip1 and Lip2, while in sets 2 and 4 with high baseline there are in addition also visible differences between HLSVD-PRO and MP-FIR for Cr, Glu and NAA. Comparing the bottom plots in Fig. 6.6 corresponding to set 4, one can see that a large part of the baseline has been filtered out by MP-FIR while it is still present in the filtered signal (in light gray) when using HLSVD-PRO. The signal-to-baseline ratio is increased as predicted in Section 6.2, resulting in better amplitude estimates. Modeling the baseline seems to be useful when using HLSVD-PRO even if no baseline is added to the signal (see Myo, PCh, Cr, Glu and NAA in Fig. 6.7(a)). This might be due to the difficulty of HLSVD-PRO to model the water peak with pure Lorentzians. Another explanation can be the frequency misalignments between the original signal and the metabolite profiles as described in the discussion section.

The **noise** mainly affects the metabolites of lower concentration such as Lip1 and Lip2. If we only look at set 3 (*i.e.*, signals with high noise and without water nor baseline), all model settings give similar results, thus no model setting seems to be preferable over the others. The RRMSEs of metabolites of larger concentration (NAA, Cr, Glu) turn out to be similar between set 1 and 3 for model setting 6 (error mainly explained by this model setting), but much better for other model settings. When comparing set 2 and 4 (Fig. 6.7(b) and Fig. 6.7(d)), the effect of adding a larger noise level is clearly visible. The tested model settings seem to be robust against noise in the sense that if a small RRMSE is obtained for a certain metabolite in set 1 (respectively set 2), a small RRMSE is also obtained in set 3 for the same metabolite (respectively set 4). For each metabolite, the shapes depicted by the 6 model settings (6 bars) are quite similar for sets 2 and 4, meaning that the effect of the added noise on the RRMSE does not depend on the model setting.

The magnitude of the **water resonance** has a very small impact on the RRMSE for both MP-FIR and HLSVD-PRO. In contrast, the shape of the water resonance has more influence, especially for HLSVD-PRO as described in Section 6.2.3. More important for MP-FIR is the closeness between the region of interest and the water resonance. Regarding the choice of the filtering region, HLSVD-PRO seems to be less sensitive than MP-FIR, which exhibits substantially larger errors when the bound of the filtering region gets closer to the water resonance. This effect is especially noticeable for low-noise signals (compare model settings 1 and 2 in set 1 and 2, Fig. 6.7). Comparable or even better results are obtained with HLSVD-PRO when the filtering region is set to [0.25,4.5] ppm.

The **computation times** needed per spectrum for quantification have been reported in Table 6.3 for model settings 1, 3, 4 and 6. AQSES has been run on a Windows XP platform with a Pentium 4 (3 GHz CPU, 1 Gb RAM). These computation times have been



(a) Set 1 (b) Set 2

(c) Set 3 (d) Set 4

(e) Model settings

Figure 6.7. *Sensitivity of AQSES on the amplitude estimates with respect to the filtering techniques, the nuisance components and the choice of the filtering region.*

averaged out over sets 2 and 4 when modeling the baseline and over sets 1 and 3 when no baseline was modeled. Although modeling the baseline significantly increases the computation time (see [213] for more details), both filtering techniques used as described above are comparable in terms of efficiency.

***in vivo* experiment**

The bounds of the filters are [0.25 4.1] ppm. They are chosen in such a way that the unwanted components outside the frequency range of interest are completely removed by

Table 6.3. *Averaged computation times (in seconds) per spectrum for model setting 1 (MP-FIR and baseline), 3 (MP-FIR and no baseline), 4 (HLSVD-PRO and baseline) and 6 (HLSVD-PRO and no baseline).*

	MP-FIR	HLSVD-PRO
Baseline (sets 2 and 4)	2.13	2.52
No baseline (sets 1 and 3)	0.61	0.72

filtering. The model order of HLSVD-PRO was fixed at 30 to guarantee a complete suppression of the water resonances. The amplitude estimates for the main 5 metabolites are shown in Fig. 6.8 for different **smoothness levels** of the modeled baseline. The results obtained with MP-FIR or HLSVD-PRO are sensitive to these levels of smoothness, lower levels (levels 1 to 3 in Fig. 6.8) providing more variability in the amplitude estimates. Nevertheless, less variability in the results was observed with MP-FIR for higher levels of smoothness. Similar observations were made when estimating the best λ for the simulated spectra (the results are not reported for sake of space). On the contrary, a not sufficiently smooth baseline alters the amplitude estimates when filtering with MP-FIR. In that case, the modeled baseline tends to fit the metabolites widely spread in the frequency domain like Myo and Glx. Note that the amplitude estimates of Cr, PCh and NAA are constant for the different smoothness levels of the baseline.

Relatively large differences appear in the amplitude estimates when comparing the results obtained with MP-FIR and HLSVD-PRO for a specific smoothness level of the modeled baseline. Most often, the frequency correction reaches its maximum fixed value (set at 20 Hz in AQSES) for most of the metabolites when using HLSVD-PRO, suggesting that the metabolites either try to fit the baseline or try to fit other metabolites that are not contained in the database. We also notice larger residue when using HLSVD-PRO. Although conclusions cannot be drawn, one can think that the amplitude obtained with HLSVD-PRO are overestimated. The simulations above confirm this trend to overestimate the metabolite amplitudes when the original signal contains a non-smooth baseline. The results in terms of amplitude ratios are in agreement with the ratios of metabolite concentrations reported by Govindaraju *et al.* (Table 2 in [97]).

6.5 Discussion

SVD-based methods such as HLSVD-PRO are often chosen for removing the water components in MRS spectra. As preprocessing method, they exhibit several advantages: the phase is not distorted, the water resonance seems visually removed, the number of parameters to be chosen by the user is restricted to 2 (the model order and the filtering region). Nevertheless, we showed that, in presence of non-Lorentzian water peaks (see Section 6.2), this algorithm fails to completely remove the residual water tails in the frequency region of interest. The metabolite contributions are normally kept unchanged if there is no misalignment between the metabolite profiles and the original signal. Consequently, the signal-to-baseline ratio (SBR) is decreased. Fortunately, this decrease is usually not dramatic since the residual water tails are often much smaller than the baseline itself. On the contrary,

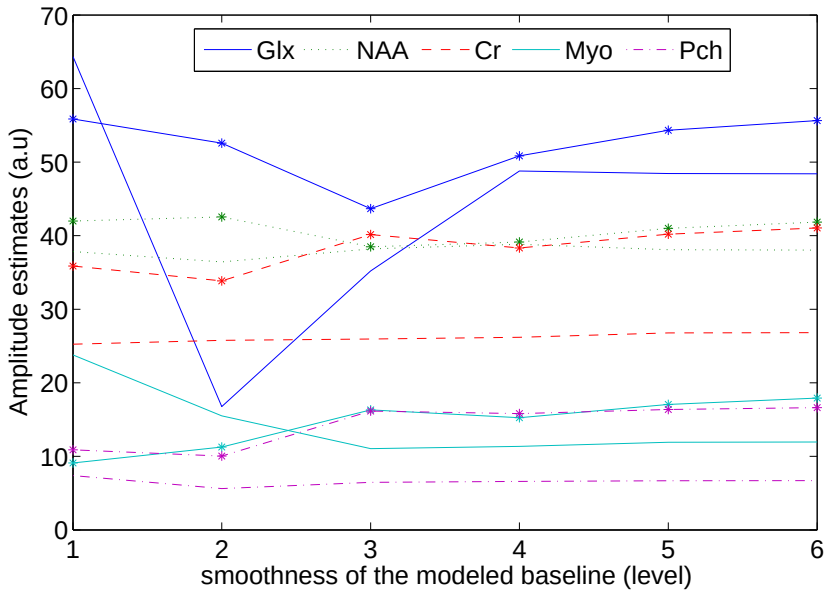


Figure 6.8. in vivo *signal of Fig. 6.5: Amplitude estimates of the 5 main metabolites (Myo, Cr, PCh, Glx and NAA) versus the smoothness of the modeled baseline ('-' for MP-FIR and '-*-' for HLSVD-PRO): level 1 of smoothness means "low smoothness" and level 6 means "high smoothness".*

MP-FIR will increase the signal-to-baseline ratio as described in Section 6.2. The signal-to-noise ratio decreases when using MP-FIR while it is stable in the case of HLSVD-PRO. MP-FIR will not remove the baseline but will reduce it more than it reduces the metabolite contributions. In this sense, MP-FIR can be useful for better disentangling the metabolites from overlapping macromolecules. HLSVD-PRO encounters indeed more difficulties when dealing with signals affected by large baselines (see Section 6.4). MP-FIR also reduces the sensitivity of the regularization parameter λ in AQSES. The results show that the amplitude estimates remain constant over a relatively large range of λ values. We can intuitively think that similar conclusions would be observed for other quantification methods based on a semiparametric model.

The results show that MP-FIR outperforms HLSVD-PRO whatever the nuisance components. A major part of the explanations is due to the increase of signal-to-baseline ratio when using MP-FIR. The fact that HLSVD-PRO is used as a preprocessing step can also generate errors in the amplitude estimation. This will be the case if the metabolite profiles and the original signal are not correctly aligned and if the bounds of the filtering region are too close to the metabolite peaks. Since MP-FIR is applied during quantification at each iteration to the corrected metabolite profiles (see Eq. (2.19)), the transition band of this signal and the metabolite profiles of the basis set will match after a couple of iterations

thereby avoiding border problems. As described above, HLSVD-PRO could be applied after correction of the metabolite profiles, but would result in an inefficient method barely usable when large sets of signals have to be processed. The efficiency depends also on the model order used in HLSVD-PRO. However, we noticed that the choice of the model order was not crucial as long as it remains around 25 and is kept sufficiently high. A similar observation was made by Sundin *et al.* [273] for long echo time MR spectra with a model order of 12 instead of 25. For a typical model order of 25, HLSVD-PRO can encounter technical problems due to shortage of memory when processing very long signals. This is rarely the case for short echo time signals that are usually shorter or equal to 2048 points.

As for long echo time spectra, the choice of the MP-FIR filter order should result from a trade-off between fulfilling the filter requirements (stop band suppression, passband ripple, etc) and preserving most of the useful information from the original signal. For example, a higher filter suppression and therefore a higher filter order is required if some of the nuisance peaks in the stop band have a fast decay [298]. Nevertheless, the filter order should be bounded to a maximum value to keep a good SNR and to avoid numerical problems caused by the computation of polynomial roots and coefficients when transforming the FIR filter into a maximum-phase FIR filter. Numerical problems were encountered in some cases for M larger than 80. We noticed experimentally that a satisfactory transition band and a satisfactory suppression in the stop band are obtained for $M = 60$. A typical stop band suppression of such a filter is -65 dB, which suffices for *in vivo* MR spectra with presaturated water. The experiments show that the filter design algorithm proposed by Vanhamme *et al.* [298] converges in most of the cases to suitable filter parameters for short echo time MR spectra. It optimizes the filter order and the ripple magnitudes in the frequency region of stop band and passband and finds the best corresponding transition bands. The results show that the amplitude estimates can be affected when the cutoff frequency is too close to the water resonances, but good amplitude estimates were obtained in a reasonable range around 4.2 ppm ([4.0 4.3] ppm). In summary, the filter order of MP-FIR should lie between 30 and 80 to ensure a good filtering without facing numerical issues. The region of interest should be kept sufficiently far away from the water resonances (*e.g.*, the frequency region [0.25 4.2] ppm). The baseline should be included in the model in AQSES when a baseline is expected in the original signal. The regularization parameter should be chosen within a range where the amplitude estimates are constant.

As explained before, MP-FIR gives an added value to AQSES compared to an SVD-based method like HLSVD-PRO. First, MP-FIR improves the performance of AQSES when dealing with signals affected by a baseline; and, second, MP-FIR can be used in the optimization procedure without increasing significantly the computation times (simple matrix multiplication).

Increasing the signal-to-baseline ratio improves the initial estimates and thereby reduces the risk of converging to wrong parameter estimates (local minimum). Methods based on the Levenberg-Marquardt least squares minimization method (see, *e.g.*, [213, 78, 312, 220, 225]) are indeed sensitive to the initial parameter estimates. For example, Ratiney *et al.* indicated in [226] that the uncertainty on the final estimates is sensitive to the truncated initial data points which influence directly the initial parameter estimates. Soher *et*

al. studied in [260] four different optimization procedures: the iterative procedures based on Young's method with wavelet or spline baseline characterization, and the single-pass optimization with wavelet or spline baseline function (semi-parametric model). He concluded that the iterative methods were more dependent on having good starting values for the baseline parameters, without dramatic differences in performance regarding the choice of the baseline model (wavelets or splines). This tends to show that the baseline should be included in the model, as confirmed by our results, at least if an initial estimate of the baseline is rather uncertain (*i.e.*, with high risk of wrong initial guess).

Although MP-FIR has been designed for processing time-domain signals, it might be helpful for frequency-domain methods like LCModel [220]. Used as preprocessing method prior to LCModel, it can reduce the contribution of the baseline while suppressing completely the water resonances which might have some contributions in the frequency region of interest. Using LCModel, Seeger *et al.* [242] showed that extending the standard basis set of metabolites by inclusion of parameterized components for macromolecules and lipids can improve the parameter estimates and especially estimates of metabolites such as NAA, Glx or Lac. Our results have shown that those metabolites are indeed sensitive to the baseline. Nevertheless, adding more components (Seeger *et al.* added 5 components to take into account the lipids and the macromolecules) complicates the model, increasing the degrees of freedom and so the risk of converging to a local minimum. MP-FIR might limit this risk since it reduces the contribution of large damping components (like macromolecules and lipids). Furthermore, additional prior knowledge might help in identifying appropriate initial parameter estimates. For example, Hofmann *et al.* [113] showed that the macromolecule baseline is different in composition and concentration between white and gray matter volumes, and depends on the age but not on the gender of the subject. MP-FIR allows to incorporate this prior knowledge in the model.

The fact that MP-FIR can be used in the optimization procedure allows to avoid frequency misalignments between the metabolite profiles and the original signal. Therefore, procedures like QUEST [226] using solvent suppression methods (like HLSVD) prior to quantification will probably require a more stringent alignment of the original signal and the metabolite profiles to avoid that some peaks are (partially) filtered out while they should not (especially for the peaks close to the water resonance). MP-FIR could be used prior to QUEST or inside the iterative procedure in QUEST with the In-Base or the subtract method [225]. The case of the subtract method is detailed in Section 7.3.4 for MP-FIR0, for which the use is similar to MP-FIR.

MP-FIR, already successful for water removal for long echo time MR spectra, might even be more powerful for short echo time MR spectra due to its ability to deal with the baseline, thereby increasing substantially (compared to HLSVD-PRO) the accuracy level of the parameter estimates obtained with AQSES. It can be used within the optimization procedure of most of the time-domain methods based on the Levenberg-Marquardt algorithm (Elster *et al.*'s method [78], AMARES$_W$ [298], VARPRO [292], etc).

6.6 Conclusions

This study shows that HLSVD-PRO and MP-FIR, two filtering techniques used in long echo MRS data quantification, can be successfully applied to short echo time spectra. The potentials and limitations of both techniques have been studied and some recommendations regarding their use have been given. Simulations show that MP-FIR outperforms HLSVD-PRO in terms of accuracy, computational efficiency and robustness against the nuisance components. This is explained by two main reasons: MP-FIR increases the signal-to-baseline ratio while it slightly decreases with HLSVD-PRO, and MP-FIR is used inside the optimization procedure while HLSVD-PRO is used prior to quantification. MP-FIR turns out to be especially powerful for time-domain quantification methods based on a semiparametric model.

Chapter 7

A new FIR filter technique for solvent suppression MRS signals

As we have seen, large water resonances are usually present in MRS signals and time-domain quantification methods require a good suppression of these components in order to obtain accurate parameter estimates. Chapter 6 presented the properties of MP-FIR. In particular, it showed the interest of using MP-FIR when dealing with signals containing baseline components. However, the magnitude response of MP-FIR depends on the widths of the passband or stopband. Distortions on the passband boundaries may happen, generating errors in the parameter estimates. In this chapter[1]*, we propose a new method which optimizes the FIR design for MRS data and thereby reduces the bandwidth effects. It also allows a less important reduction of the signals of interest which decay rapidly in the time domain.*

7.1 Introduction

The water signal intensity is often several orders of magnitude larger than the signal intensities of the metabolites in MRS signals. In order to reduce the range of amplitudes (between the water resonances and the other components), water saturation techniques are used during acquisition (see, *e.g.*, [219, 252, 255]), yielding water-suppressed signals. However, these signals still contain water resonances higher than the metabolite signals. Since the water components are located outside the frequency region of interest, frequency-selective quantification methods are indicated to obtain accurate parameter estimates. Solvent suppression methods have been mainly developed for quantification methods working in the time domain ([52, 152, 273, 298]), where water and metabolite components are not distinguishable. Water-suppressed signals may show various kinds of water shapes due to water saturation and no (or little) prior knowledge can be used to model the water resonances.

In [273], a maximum-phase FIR filter (MP-FIR) has been proposed and has been

[1] J. Poullet, R. Pintelon, S. Van Huffel, A new FIR filter technique for solvent suppression in MRS signals, Internal Report 08-116, ESAT-SISTA, K.U.Leuven (Leuven, Belgium), 2008, accepted for publication to the Journal of Magnetic Resonance.

slightly refined in [298]. It has been shown to be successful for water removal and outperforms most of the existing concurrent methods [52, 214]. However, this filter does not use all the available prior knowledge. Indeed, although little can be said about the shape of the water resonances, the position of the water peak is usually known or can be easily determined in the Fourier transform domain. Therefore the following prior knowledge should be used:

1. the position of the water resonances and other resonances that should be removed (outside the frequency region of interest),
2. the position of the metabolite resonance which is the closest to the water peak in order to determine the transition band

Similarly, the location of any nuisance component (*i.e.*, component in the frequency region of no interest) can be used as prior knowledge. MP-FIR is not explicitly designed for Lorentzian peaks since the filter design constraints are on the unit circle (pure sinusoids). In other words, a sinusoid signal passes through the filter unchanged (if the ripples in the magnitude response are neglected), while the amplitude of a Lorentzian passing through the filter will be reduced proportionally to the damping value of the Lorentzian (see [214] for more details). We propose a new filtering method that uses the above mentioned prior knowledge and reduces the attenuation of the metabolite signal when passing through the filter.

7.2 The proposed filter

As mentioned before, the proposed filter design is based on:

- the fact that we are dealing with Lorentzian signals and not pure sinusoids, and
- prior knowledge of the position of the nuisance peaks.

The general idea of the filter is to place zeros in the z-plane to cancel components of specific frequencies (corresponding to the nuisance components). The z-transform, which allows to transform the domain of the original data (*i.e.*, the time domain for MRS data) into the z-domain (or z-plane), is a well-known concept in signal processing and is defined as

$$X(z) = \sum_{n=0}^{N-1} x(n) z^{-n}. \tag{7.1}$$

where $x(n)$ is a discrete signal in the time domain, $X(z)$ its transform in the z-domain and $z = e^{(-d+j2\pi f)}$. The filtered signal is given by $X_{fil}(z) = H(z)X(z)$ where $H(z)$ is the filter transfer function in the z-domain. Filtering out a component z_0 from the signal is achieved when $H(z_0) = 0$ and z_0 is a root (=a zero) of $H(z)$. The largest nuisance components and their frequencies are automatically determined (see step 3 in the algorithm below) and the zeros are chosen accordingly. The algorithm starts from one pair of zeros corresponding to the largest nuisance component, calculates the filter coefficients, filters the signal and checks whether all the components in the stopband are under the noise level. If this is not the case, it adds a new pair of zeros (=zero and its conjugate), recalculates the

filter coefficients and filters again the signal, and so on until the nuisance components have been sufficiently filtered out. The filter order is increased if a satisfactory attenuation is not reached, and we start back from the first pair of zeros since the position of the zeros may depend on the filter order. Consequently, the initial choice of the filter order by the user is not critical. Zeros are added by pair to insure a flat and nonleaning magnitude response of the filter. A large and wide nuisance peak may need more than one zero to be filtered out and the position of the second zero will be preferably chosen accordingly to the largest remaining nuisance component. This explains the iterative process.

The algorithm is presented in Fig. 7.1 and will be referred to as MP-FIR0 in the rest of the manuscript. The different blocks of the algorithm are described here. The frequencies are normalized in the interval [-0.5,0.5].

Initialization

1. The user defines the passband $PB = [f_{pl}, f_{pu}]$, the transition bandwidth (TBW) in the frequency domain and a starting value for the filter order.

2. An estimate of the noise standard deviation $\tilde{\sigma}$ is calculated as the standard deviation of the complex numbers of the last samples of the signal $y(n)$ divided by $\sqrt{2}$.

3. The frequency f_{NP} of the strongest nuisance peak is automatically determined. The strongest nuisance peak is defined by the peak in the stopband with the highest magnitude, NP_0, in the frequency domain,

$$NP_0 = max \left| \frac{Y(f_l)}{\sqrt{N}} \right|, \tag{7.2}$$

where $f_l \in [f_{sl}, f_{su}]$ (stopband), N is the number of points in the signal, Y is the signal in the frequency domain (spectrum) after Fourier transformation of the time-domain signal:

$$Y(f_l) = \sum_{n=0}^{N-1} y(n) e^{\frac{-2\pi j n l}{N}}. \tag{7.3}$$

Note that the standard deviation of the noise in the frequency domain is given by

$$\tilde{\sigma}_f = \frac{\tilde{\sigma}}{\sqrt{N}}. \tag{7.4}$$

4. A pair of zeros is placed at $e^{(j2\pi f_{NP})}$ and its conjugate in the z-plane.

5. A grid of frequency-damping domain points is generated such that the distance between the newly computed zeros and the points is sufficiently large to avoid any numerical problems (division by zero): the couples

$$(f_l, d) \texttt{ such that } f_l \in [-0.5, 0.5], |f_l - f_r| > 0.001, \tag{7.5}$$

f_r are the frequencies of the zeros, $r = 1, 2$ here (in the initialization step). The points in the interval [-0.5,0.5] are equally spaced (a step of 0.001 is used in the experiments). An initial value for the damping is given in kHz (*e.g.*, $d = 0.008$). This damping value is refined all along the filter design process based on the estimated width of the largest peak

of interest after filtering.

Compute h

6. The transfer function of the filter made from the zeros is calculated at each point of the grid

$$H_1(f_l, d) = \prod_{r=1,...,R} (1 - z_r^{-1}(e^{-d+j2\pi f_l})^{-1}) \tag{7.6}$$

where R is the number of zeros (2 at the first iteration), $z_r = e^{(-d+j2\pi f_r)}$ are the zeros.

7. The target vector is defined as

$$T(f_l) = \begin{cases} e^{-j2\pi f_l D} & if\ f_l \in [f_{pl}, f_{pu}] \\ 0 & else \end{cases} \tag{7.7}$$

where D is the delay. The default value for the delay is $0.7333(M-1)$. This value is based on experiments. Note that this delay is refined at the end of the algorithm (see **Delay tuning**, below).

8. The filter coefficients are calculated following the steps:

- The coefficients of the vector h_2 are computed (more details in the appendix),

$$h_2 = (G^H W G)^{-1} G^H W T_{H_1} \tag{7.8}$$

where $G = \begin{bmatrix} 1 & e^{(d-j2\pi f_1)} & \dots & e^{(d-j2\pi f_1)(M-1)} \\ \vdots & \vdots & \vdots & \vdots \\ 1 & e^{(d-j2\pi f_L)} & \dots & e^{(d-j2\pi f_L)(M-1)} \end{bmatrix}$,

and L is the number of points on the grid. W is a diagonal matrix with $W_{l,l} = H_1^2(f_l, d)$ for $l = 1, ..., L$, and $T_{H_1} = [\frac{T(f_1)}{H_1(f_1,d)} \dots \frac{T(f_L)}{H_1(f_L,d)}]'$. The superscript H indicates the conjugate transpose and the superscript $'$ the transpose.

- The coefficients of h_1 are calculated from its roots (zeros).

- The filter is computed:

$$h = h_1 \otimes h_2, \tag{7.9}$$

where $\otimes$ is the convolution operator, and h_1 is the impulse response of the filter in Eq. (7.6).

- The filter is transformed into a maximum-phase FIR filter (see, *e.g.*, [273] for more details).

Filtering the signal

9. The signal y is filtered

$$y_{fil}(n) = \sum_{m=0}^{M-1} h(m) y(n-m), \tag{7.10}$$

and the $M-1$ first points of the filter are discarded to avoid any distortion (see [214] for more details).

Checking the attenuation of the nuisance components

10. The attenuation of the nuisance components is checked:

- Recording the best attenuation:

$$\begin{cases} if\ NP_i < NP_{best} & NP_{\text{best}} = NP_i,\ h_{\text{best}} = h \\ else & nothing \end{cases} \tag{7.11}$$

  where NP_i is the maximal magnitude of the nuisance components in the spectrum at iteration i, h_{best} are the coefficients of the filter which yields the best attenuation of the nuisance components and NP_{best} is the corresponding maximal magnitude of the nuisance components in the spectrum.

- Checking whether the attenuation is under the noise level:

$$\begin{cases} if\ NP_i < 2.5\tilde{\sigma}_f & \text{go to } \textbf{13.} \end{cases} \tag{7.12}$$

  where the value 2.5 results from the fact that the magnitude of the noise $|N(n)|$ over its standard deviation σ follows a chi distribution ($X = |N(n)|/\sigma \sim \chi_2$). $P(X \leq x) = 95\%$ gives $x = 2.45$ which is rounded to 2.5 in the algorithm.

- Checking whether the attenuation is improved compared to the last iteration:

$$\begin{cases} if\ NP_i < NP_{i-1} & \text{go to } \textbf{11.} \\ else & \text{go to } \textbf{12.} \end{cases} \tag{7.13}$$

where NP_{i-1} is the maximal magnitude of the nuisance components in the spectrum at iterations $i-1$.

Increasing the number of zeros

11. A new pair of zeros is placed at $e^{(j2\pi f_{NP_i})}$ and its conjugate in the z-plane, where f_{NP_i} is the frequency of the strongest nuisance peak in the filtered spectrum Y_{fil}. Go to **6.**.

Increasing the filter order

12. The order of the filter is increased by 10 ($M := M + 10$).

- If the filter length M is larger than a maximum value M_{max}, $h = h_{best}$ and go to **13.**,
- else, keep only the first pair of zeros calculated in the initialization step and go to **6.**.

Delay tuning

13. The goal of the delay tuning is to ensure a flat (nonleaning) magnitude response in the frequency passband. One can use a brute-force search, testing all delay values or start from

an initial delay value and search around it until no flatter magnitude response is found. We propose the following simple search:
a. Initialization: delay step $D_{step} = \min(1 - D_{fact}, D_{fact} - 0)/5$, where the delay factor is the one fixed from the beginning, *e.g.*, $D_{fact} = 0.7333$.
b. The passband is divided into 4 disjoint equal-size intervals. The intervals I_2 and I_3 around the center of the passband are used to calculate the difference:

$$Df_0 = \left| \sum_{f_{l_2}} H(f_{l_2}, d) - \sum_{f_{l_3}} H(f_{l_3}, d) \right| \tag{7.14}$$

where H is the magnitude response of the filter, and f_{l_2} and f_{l_3} are the frequencies in I_2 and I_3.
c. Define 2 new delays around D_{i-1} ($D_0 = 0.7333(M-1)$, for example), the delay at iteration $i-1$: $D_{i_1} = D_{i-1} - D_{step}$ and $D_{i_2} = D_{i-1} + D_{step}$, and recompute H for each delay.
d. Compute Df such as in Eq. (7.14) for each delay (Df_1 and Df_2),

$$Df_{best_i} = \min(Df_1, Df_2, Df_{best_{i-1}}), \tag{7.15}$$

$$\begin{cases} if\ Df_{best_i} = Df_1, & D_i = D_{i_1} \\ \quad if\ D_{i-1} = D_{(i-1)_1}, & D_{step} := D_{step}/1.1,\ else\ D_{step} := D_{step}/2, \\ \quad \text{go to } \textbf{c.} & \\ elseif\ Df_{best_i} = Df_2, & D_i = D_{i_2} \\ \quad if\ D_{i-1} = D_{(i-1)_2}, & D_{step} := D_{step}/1.1,\ else\ D_{step} := D_{step}/2, \\ \quad \text{go to } \textbf{c.} & \\ else & \text{go to END}, \end{cases} \tag{7.16}$$

where $Df_{best_0} = Df_0$, $D_{(i-1)_1}$ and $D_{(i-1)_2}$ are equivalent notations to D_{i_1} and D_{i_2} but at iteration $i-1$ instead of iteration i.

7.3 Experimental results using simulations and real-life examples

In this section the proposed FIR filter-based suppression technique is evaluated to determine the sensitivity of the final parameter estimates with respect to the choice of filter design parameters. The method is compared with the successful MP-FIR method and tests on *in vivo*, *ex vivo* and *in vitro* signals are also performed.

7.3.1 Material

Simulated signals

The simulated signals are constructed as described in Tables 1 and 2 in [273]. The parameters are repeated here in Table 7.1 and Table 7.2 for clarity of exposition.

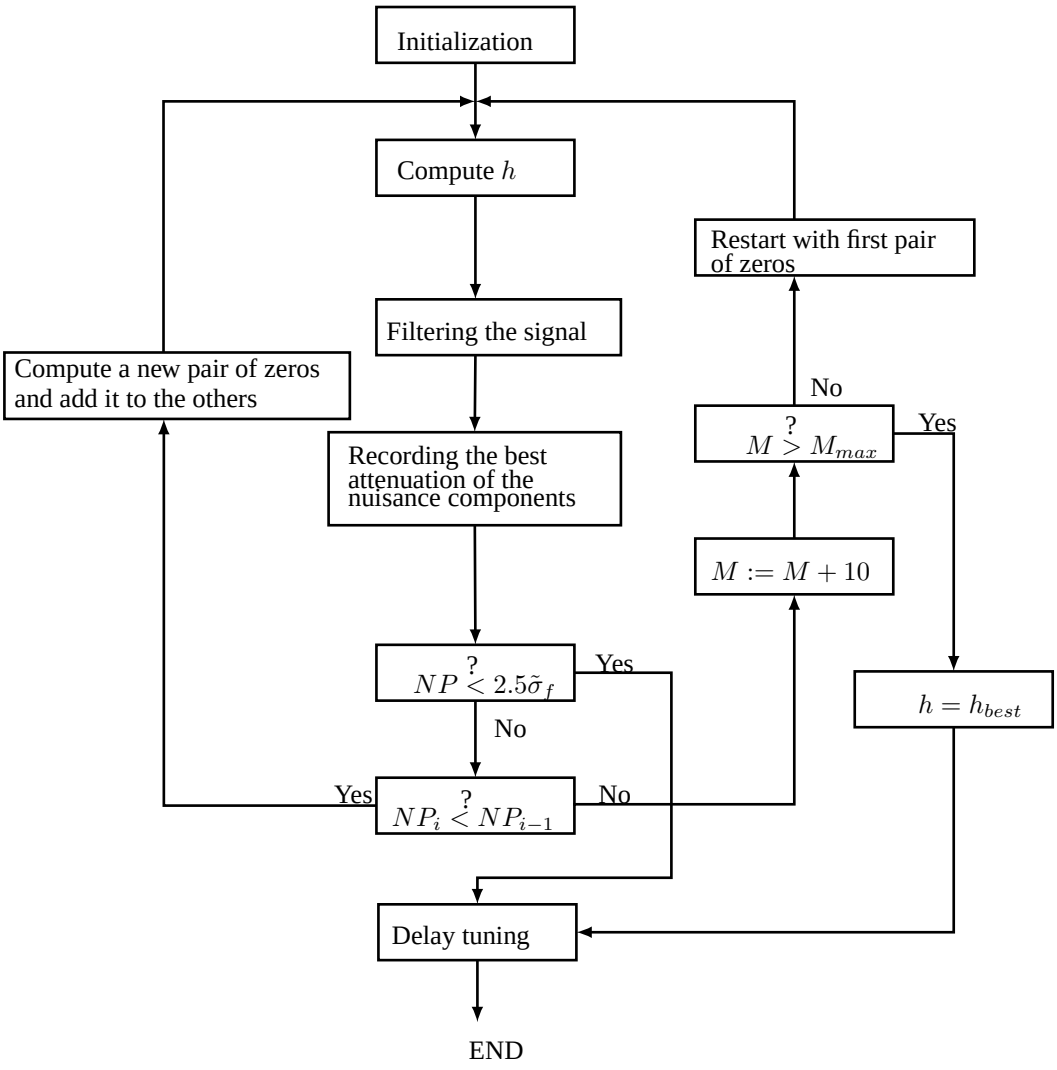


Figure 7.1. *Algorithm of the proposed filter.*

The simulated signals are the sum of the 5 metabolite signals, the nuisance peak (7 components in Table 7.1) and some noise:

$$y(n) = \sum_{k=1}^{5} v_k(n) + w(n) + \varepsilon(n),\ n = 0, \ldots, N-1, \tag{7.17}$$

and

$$v_k(n) = a_{mk} e^{j\phi_{mk}} e^{(-d_{mk}+j2\pi f_{mk})n\Delta t} \tag{7.18}$$

where the values for a_{mk}, ϕ_{mk}, d_{mk} and f_{mk} are in Table 7.2, ε is circular complex dis-

Table 7.1. *Estimated Water Signal Parameters Used in the Reconstruction of the Water Peak*

f_{wk} (Hz)	d_{wk} (Hz)	ϕ_{wk} (deg)	a_{wk} (a.u.)
-8.48	5.1	-90.88	15.01
-5.25	8.28	-45.19	64.74
-2.16	10.51	-2.95	321.25
-0.18	12.45	179.97	1142.3
-0.17	4.24	-170.39	251.92
3.09	6.79	36.77	201.11
6.31	4	81.11	12.3

Table 7.2. *Metabolite Parameters Used in the Simulated Signals*

Peak k	f_{mk} (Hz)	d_{mk} (Hz)	ϕ_{mk} (deg)	a_{mk} (a.u.)
1	61	7	0	20
2	118	7	0	30
3	189	7	0	20
4	231	7	0	20
5	311	7	0	20

tributed white Gaussian noise. The nuisance components in the simulated signals are constructed from Table 7.1:

$$w(n) = \sum_{wk=1}^{7} a_{wk} e^{j\phi_{wk}} e^{(-d_{wk}+j2\pi f_{wk})n\Delta t}. \tag{7.19}$$

No baseline $b(n)$ is added to the simulated signals.

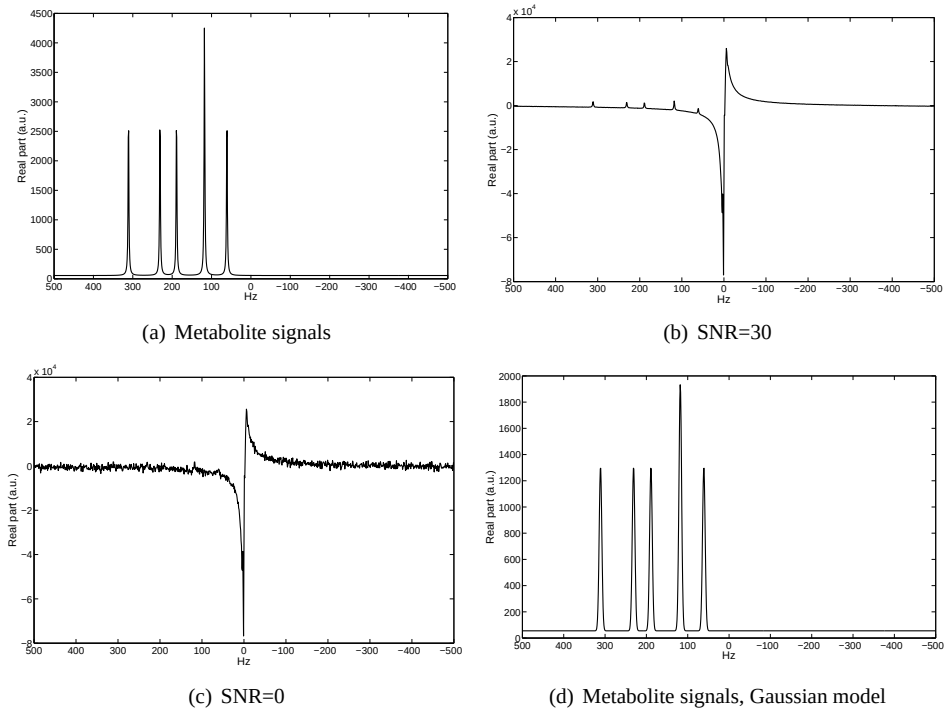
In experiment 4, the value of d_{m2} in Table 7.2 has been replaced by 0.021 kHz (=21 Hz) to study the effect of MPFIR0 on wider peaks, the rest was kept unchanged. The SNR is defined with respect to the largest metabolite peak (peak 2) and is measured in decibels (dB):

$$SNR = 20\log(\frac{a_{m2}}{\sigma}). \tag{7.20}$$

The metabolite profiles in the database used for quantification are constructed from the 5 components in Table 7.2 ($v_k, k = 1, \ldots, 5$), using exactly the same parameter values to reduce the effects of the quantification method on the parameter estimates except for experiment 4 where $f_{m1} = 0.056$ kHz instead of 0.061 kHz.

Examples of simulated spectra are given in Fig. 7.2. Fig. 7.2(d) shows the metabolite signals constructed with a Gaussian model with the same parameter values for a_{mk}, f_{mk} and ϕ_{mk} as in Table 7.2 and $d_{G_k} = 0.0002$ for $k = 1, \ldots, 5$:

$$m_G(n) = \sum_{k=1}^{K} a_{mk} e^{j\phi_{mk}} e^{-d_{G_k}(n\Delta t)^2 + j2\pi f_{mk} n\Delta t},\ n = 0, \ldots, N-1, \tag{7.21}$$



(a) Metabolite signals (b) SNR=30

(c) SNR=0 (d) Metabolite signals, Gaussian model

Figure 7.2. *Examples of simulated signals. (a) Metabolite signals with a Lorentzian model, (b) Simulated signal with SNR=30 (Eq. (7.17)), (c) Simulated signal with SNR=0 (Eq. (7.17)), (d) Metabolite signals with a Gaussian model (Eq. (7.21)).*

In vivo, *ex vivo* and *in vitro* signals

We analyze 4 *in vivo* data chosen randomly from the short echo time INTERPRET[2] database, coming from different centers: Institut de Diagnostic per la Imatge (IDI), Fundacion para la Lucha contra las Enfermedades Neurologicas de la Infancia (FLENI), Uniwersytet Medyczny w Lodzi (MUL). Detailed information about the acquisition parameters for each center are provided in Table 7.3. Quality control criteria have been applied to MR system performance and all data in this study passed a strict validation process [291]. These water-suppressed data were acquired at 1.5 T.

The *ex vivo* high resolution magic angle spinning (HRMAS) signal was acquired with an 1D PRESAT (pulse-and-acquire) pulse sequence at 11.7 T (500 MHz for ^{1}H), at 0-4 °C, and 4,000 Hz spinnning rate using a BRUKER Analytik GmbH spectrometer. The biopsy was extracted from brain tumor tissue (grade II astrocytoma) and frozen at -80 °C until use (TE/TR=31/2000 ms).

[2]http://azizu.uab.es/INTERPRET/ (Accessed: July 9, 2008)

Table 7.3. *Overview of the acquisition parameters for the single voxel MRS data. For each center the manufacturer of the scanner, the sequence, the echo time, the repetition time, the spectral width (SW) and the number of points in the original FID (N) are displayed.*

Center	Manufacturer	Sequence	TE(ms)	TR(ms)	SW(Hz)	N
FLENI	GE	PRESS	30	2000	2500	2048
IDI	Philips	PRESS	30	2000	1000	512
MUL	Siemens	STEAM	20	2000	1000	512

The *in vitro* signal, N-acetyl-aspartate (NAA), was acquired on a 1.5 T Philips spectrometer using a PRESS sequence with an echo time of 23 ms and a repetition time of 6000 ms, and a volume box of $2 \times 2 \times 2$ cm^3.

7.3.2 Description of the experiments

Two experiments have been set up to study the influence of the filter design parameters, which are the initial delay and the transition bandwidth. In two other experiments, MP-FIR (method proposed in [298]) and MP-FIR0 (the proposed filter) are compared. The quantification method AQSES is used for all the experiments. However, the baseline is not considered and therefore not included in the model, the Lorentzian lineshape is assumed. AMARES could have been chosen as well as AQSES for the simulated signals and AQSES is appropriate for long echo time signals as long as the metabolite profiles are properly chosen. AQSES can be used with any FIR filter (see [213]). The following parameters are used for the simulated signals: sampling frequency = 1 kHz, spectrometer frequency = 63.83 MHz. A final experiment shows the effects of MP-FIR0 on *in vivo*, *ex vivo* and *in vitro* signals.

Experiment 1: Influence of the initial delay on the amplitude estimates

MP-FIR0 is used as a preprocessing method with the following filter design parameters:

- the transition bandwidth $TBW = 0.31$ ppm or 0.02 kHz,
- the length of the filter $M = 71$,
- the passband $PB = [5.5, 11]$ ppm or $[51, 402]$ Hz,
- the delays $D = [0.6(M-1), 0.67(M-1), 0.73(M-1), 0.8(M-1), 0.87(M-1)]$

AQSES is used without filtering method and without constraints on the phase.

Experiment 2: Influence of the transition bandwidth on the amplitude estimates

MP-FIR0 is used as a preprocessing method with the following filter design parameters:

- $TBW = [0.01, 0.02, 0.03, 0.04, 0.05]$ kHz,
- $M = 71$,
- $PB = [5.5, 11]$ ppm,
- $D = 0.73(M - 1)$.

AQSES is used without filtering method and without constraints on the phase. The transition bandwidths are illustrated in Fig. 7.3.

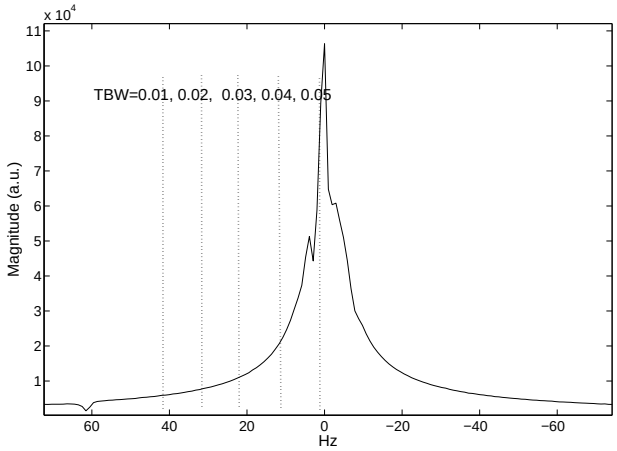


Figure 7.3. *Example of simulated spectrum (SNR = 30) in absolute values. The stopband is delimited by the dotted lines for the different transition bandwidths (TBW=0.01, 0.02, 0.03, 0.04, 0.05).*

Experiment 3: comparison MP-FIR0 vs MP-FIR

In this experiment, MP-FIR0 and MP-FIR are compared. In that respect, 4 simulations have been carried out:

a. MP-FIR0 used as a preprocessing method with the following filter design parameters:

- $TBW = 20$ Hz,
- $M = 71$,
- $PB = [5.5, 11]$ ppm,
- $D = 0.73(M - 1)$.

AQSES is used without filtering method and without constraints on the phase.

b. AQSES is used with MP-FIR0 as filtering method and with constraints on the phase (equal phases). The filter design parameters are identical to the ones in simulation **a**.

c. MP-FIR used as a preprocessing method with the following filter design parameters:

- $ripple = 0.01$,
- $M = 71$,
- $PB = [5.5, 11]$ ppm.

AQSES is used without filtering method and without constraints on the phase.

d. AQSES is used with MP-FIR as filtering method and with constraints on the phase (equal phases). The filter design parameters are identical to the ones in simulation **c**.

Experiment 4: influence of deviations from the database in terms of frequency and damping

Experiment 4 only differs from experiment 3 in the fact that AQSES is always used without constraints on the phase, and that the frequency of the first metabolite in the **database** is 0.056 kHz instead of 0.061 kHz and the damping of the second metabolite in the **signal** is 0.021 kHz instead of 0.007 kHz. The goal of this experiment is to show that more complex problems can be handled with MP-FIR0.

Experiment 5: effects of MP-FIR0 on *in vivo*, *ex vivo* and *in vitro* data

MP-FIR0 is used as a preprocessing method with the following filter design parameters:

- $TBW = [0.02]$ kHz,
- $M = 61$,
- $PB = [0.5, 4]$ ppm,
- $D = 0.73(M - 1)$.

MP-FIR is used as a preprocessing method with the following filter design parameters:

- $ripple = 0.01$,
- $M = 61$,
- $PB = [0.5, 4]$ ppm.

AQSES is not used here.

Comparison criterion

In each experiment on simulated data, the quality of the amplitude estimates is measured with the relative root mean squared error (RRMSE) in percent,

$$RRMSE_k = 100\sqrt{\frac{1}{C}\sum_{c=1}^{C}\frac{(a_k - \tilde{a}_k^c)^2}{a_k^2}},\ k = 1, \ldots, 5 \tag{7.22}$$

where C is the number of simulation runs ($C = 100$ in each experiment) and $\tilde{a}_k^c$ denotes the estimate of a_k obtained in simulation run c. Note that a_k (for $k = 1, \ldots, 5$) is equal to 1 in all the experiments based on simulated data.

7.3.3 Results

The results of **experiment 1** are given in Fig. 7.4. The results are stable for delay factors between 0.6 and 0.73, but too large delay factors make the algorithm unstable in some cases, resulting in higher RRMSEs.

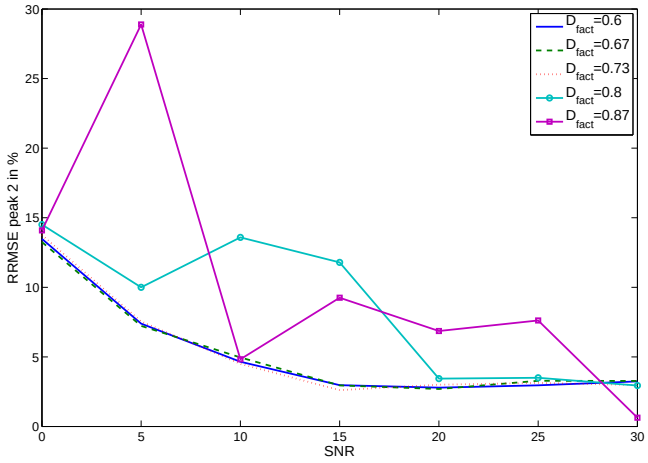


Figure 7.4. *Experiment 1: RRMSE as a function of SNR obtained from 100 simulation runs using different initial delay factors.*

The results of **experiment 2** are given in Fig. 7.5. The algorithm is in general robust with respect to the choice of the transition bandwidth. However, large errors are observed in some simulation runs for TBW=0.01 and SNR=30. This can be explained by too severe filter design constraints since the algorithm aims to attenuate the water peak under the noise level, which is very low, while allowing a too narrow transition band.

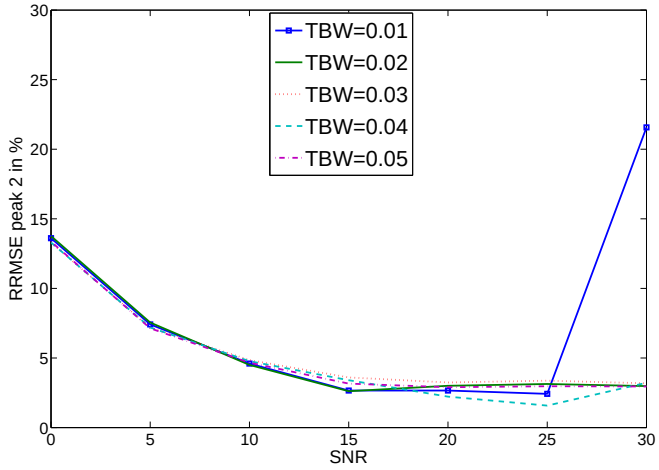
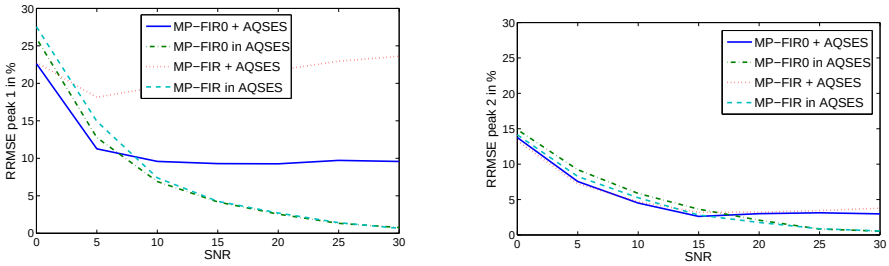


Figure 7.5. *Experiment 2: RRMSE as a function of SNR obtained from 100 simulation runs using different transition bandwidths.*

The results of **experiment 3** are given in Fig. 7.6. It shows in Fig. 7.6(a) that the use of MP-FIR or MP-FIR0 inside AQSES is preferable, at least if the SNR is high. When using MPFIR or MP-FIR0 outside AQSES, peak 1 is attenuated and the RRMSE remains above a certain level since the database profiles remain unchanged. Using MP-FIR0 reduces this attenuation: the RRMSE level reached by MP-FIR0 is twice as small as the one reached by MP-FIR. The attenuation decreases for peaks like peak 2 that are further away from the passband borders. This is illustrated in Fig. 7.7. In Fig. 7.7(c) and Fig. 7.7(d), one can see that MP-FIR0 yields a smaller attenuation than MP-FIR with a flatter magnitude response curve in the passband. A damping of 0.021 has been chosen instead of 0.007 for a better contrast between the magnitude response of MP-FIR and MP-FIR0. The location of the zeros in MP-FIR0 ensures a better suppression of the highest nuisance components as it is illustrated in Fig. 7.7(a) and Fig. 7.7(b). The suppression in the rest of the stopband is better when using MP-FIR. However, there is no peak to be suppressed in the rest of the passband, which illustrates that MP-FIR is not optimal in the sense that it does not take into account the position of the high nuisance peaks, their number being limited.

Fig. 7.8 shows what is the effect of MP-FIR and MP-FIR0 on a Gaussian peak. An example of Gaussian peaks with $d_{G_k} = 0.0002$ are given in Fig. 7.2(d). The passband attenuation is smaller for a Gaussian peak than for a Lorentzian peak.

The results of **experiment 4** are given in Fig. 7.9. Peak 1 (resonance frequency $f_{m1} = 56$ Hz) in the database is located at the border of the passband (passband = [51.06,402.13] in Hz). A better RRMSE is observed when using MP-FIR0 instead of MP-FIR outside AQSES. The differences are less obvious when using MP-FIR or MP-FIR0 inside AQSES.



(a) Peak 1 (b) Peak 2

Figure 7.6. *Experiment 3: RRMSE as a function of SNR obtained from 100 simulation runs using different quantification approaches.*

The ***in vivo*** results of **experiment 5** are given in Fig. 7.10. The magnitude of the signals is plotted to avoid phasing issues due to the use of the filter (see [273] for more details). The different water signals are reduced under the noise level by MP-FIR0.

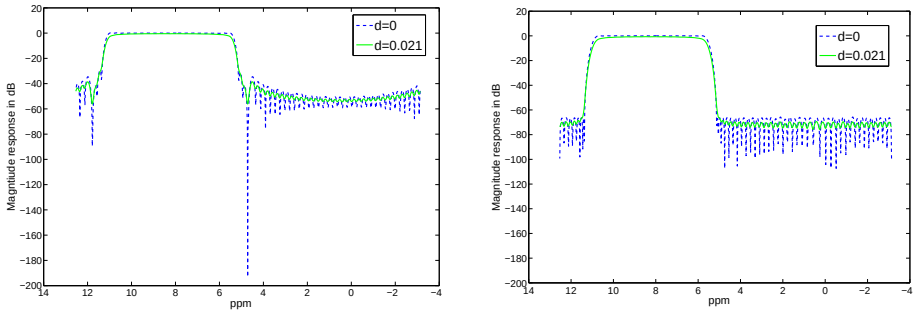
The ***ex vivo*** results are given in Fig. 7.11. The water resonances are perfectly removed. The lipids at 0.9 ppm (comprised in the passband) are more attenuated with MP-FIR than MP-FIR0 as mentioned above for simulated signals. This is also true for large damping components, even if they are not especially close to passband borders (see, *e.g.*, the fatty acids under the lactate doublet at 1.3 ppm).

The ***in vitro*** results are given in Fig. 7.12. Fig. 7.12(a) shows that all the nuisance components (components outside the passband [0.5,4] ppm) are removed. The algorithm automatically places the zeros to remove the largest nuisance components as it is illustrated by the magnitude response of the filter (for $d = 0$) in Fig. 7.12(b).

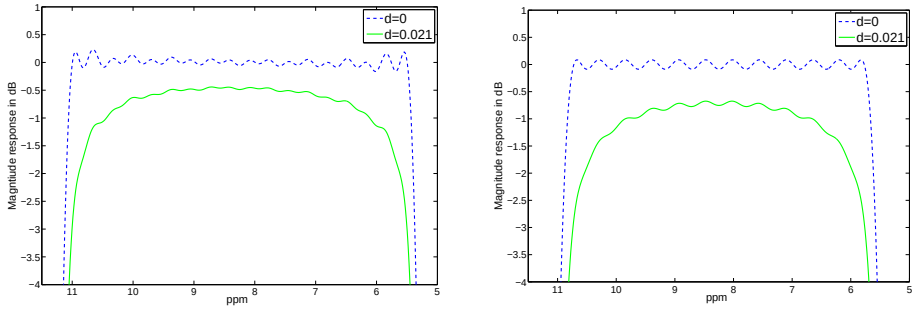
7.3.4 Discussion

The advantages of a method based on a FIR filter compared to a singular value decomposition method such as HLSVD-PRO [152] have been given in [214]. In particular,

- it is fast since it boils down to a simple matrix computation once the filter coefficients are known, and is thereby appropriate in an optimization procedure, whereas HLSVD-PRO requires a singular value decomposition at each iteration of the optimization procedure;
- it is linear and thus can be switched with any other linear operator: in AQSES [213], for example, the filtered signal is fitted with a linear combination of metabolite signals or profiles, and thus, filtering the linear combination of metabolite signals is equal to taking the linear combination of the filtered metabolite signals.



(a) MP-FIR0 (b) MP-FIR



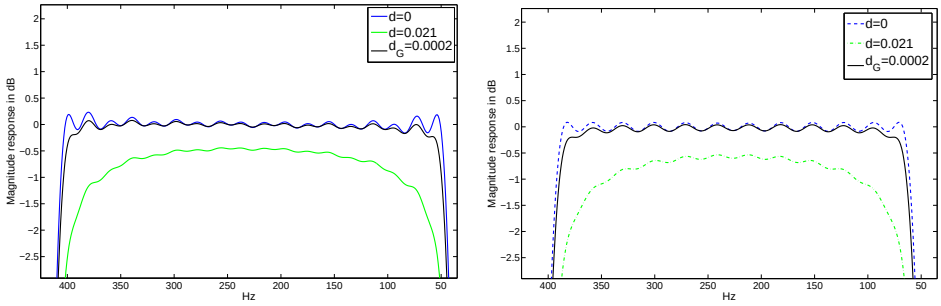
(c) MP-FIR0, zoom in the passband (d) MP-FIR, zoom in the passband

Figure 7.7. *Experiment 3: Examples of magnitude response of MP-FIR0 and MP-FIR in dB for components with different damping values:* $d = 0$ *and* $d = 0.021$.

Moreover, MP-FIR0

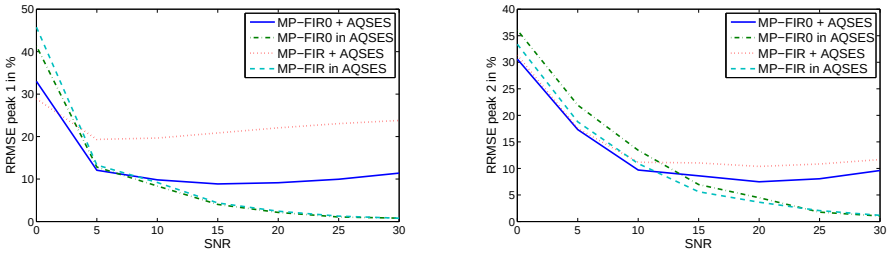
- ensures that the water components and other unwanted components located outside the frequency region of interest are reduced under the noise level; the order of the filter $M - 1$ (*i.e.*, its length minus 1) and the number of iterations are optimized in that perspective;
- uses the information that we deal with nonpure sinusoid peaks in the frequency region of interest, while MP-FIR is designed for sinusoid signals;
- uses the water/unwanted peak positions as prior knowledge;
- is capable of dealing with non Lorentzian water components as shown in the results above.

The constrained least squares design used by Sundin *et al.* for MP-FIR ensures equiripples in both the stopband and passband. However, the amplitudes in the stopband are far from being equal (only one or a few peaks are generally above the noise level) and imposing equal attenuation of all frequency components is usually not optimal. The results show that peaks close to the transition band are more attenuated by MP-FIR than MP-FIR0,



(a) MP-FIR0, zoom in the passband (b) MP-FIR, zoom in the passband

Figure 7.8. *Experiment 3: Examples of magnitude response of MP-FIR0 and MP-FIR in dB for Gaussian (d_G) and Lorentzian (d) components.*



(a) Peak 1 (b) Peak 2

Figure 7.9. *Experiment 4: RRMSE as a function of SNR obtained from 100 simulation runs using different quantification approaches.*

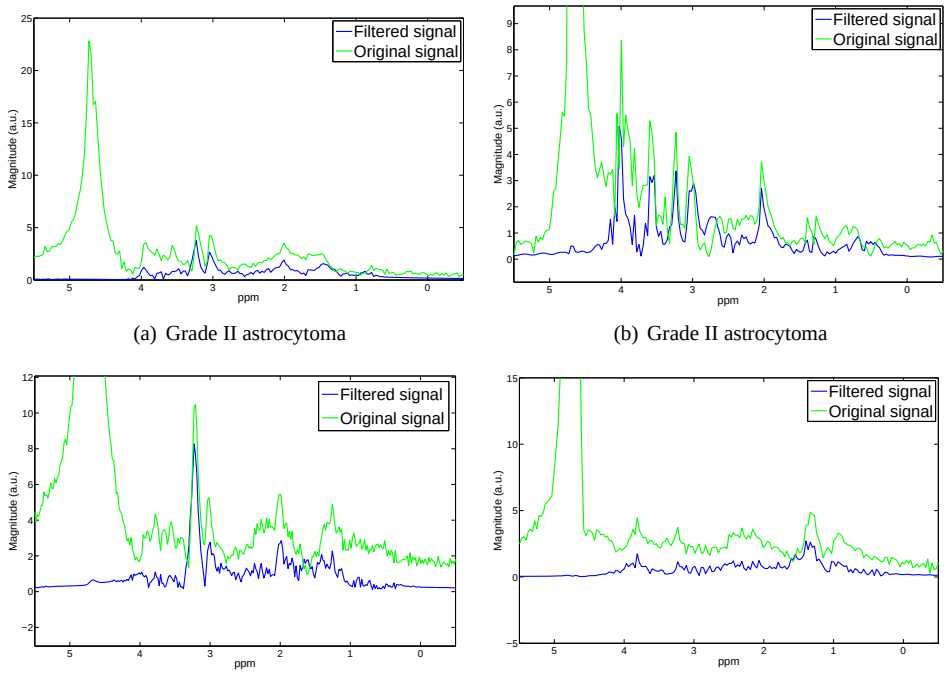
yielding less accurate parameter estimates of these peaks.

Some remarks about the design of MP-FIR0:

- the filter design constraints are imposed outside the unit circle since we assume that the lineshape of a metabolite resonance is closer to a Lorentzian than to a pure sinusoid (*i.e*, an undamped Lorentzian, $d = 0$). The lineshape is also assumed to be similar for all metabolite resonances, and therefore only one value of d is considered when designing the filter. The reason is twofold: it reduces the risk of numerical problems and it decreases the computational load.

- Only one pair of zeros is added at each iteration (see **11.** in the algorithm) to keep the required filter order as low as possible, while still reducing the nuisance components under the noise level. Moreover, one pair of zeros is usually sufficient when there is only one large narrow nuisance component.

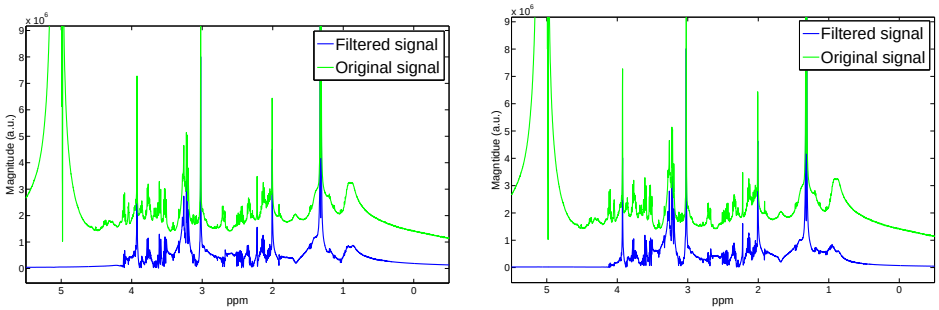
- The zeros of the large nuisance components are chosen on the unit circle since their shapes are usually unknown.



(a) Grade II astrocytoma (b) Grade II astrocytoma

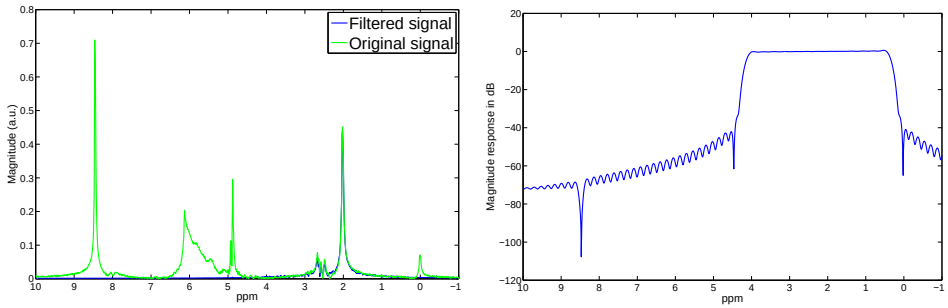
(c) Glioblastoma (d) Meningioma

Figure 7.10. *Experiment 5: Effect of MP-FIR0 on in vivo signals: magnitude spectrum of eddy current corrected signal (top signal) and magnitude spectrum of the same signal after FIR filtering (bottom signal). (a-b) Water-suppressed proton magnitude spectrum from the brain (tumor: Grade II astrocytoma - center: IDI), (c) Water-suppressed proton magnitude spectrum from the brain (tumor: glioblastoma - center: FLENI), (d) Water-suppressed proton magnitude spectrum from the brain (tumor: meningioma - center: MUL)*



(a) MP-FIR0 (b) MP-FIR

Figure 7.11. *Experiment 5: Effect of (a) MP-FIR0 and (b) MP-FIR on an ex vivo signal (tumor: grade II astrocytoma): magnitude spectrum of the signal (top signal) and magnitude spectrum of the same signal after FIR filtering (bottom signal).*



(a) NAA signal (b) Magnitude response of MP-FIR0

Figure 7.12. *Experiment 5: Effect of MP-FIR0 on an in vitro signal (NAA). (a) Magnitude spectrum of the signal (top signal) and magnitude spectrum of the same signal after FIR filtering (bottom signal), (b) magnitude response of the filter in dB. The minima in the magnitude response correspond to the frequencies of the largest nuisance components.*

Similarly to MP-FIR, MP-FIR0 can be used in several quantification methods although we have limited our analysis to the use of AQSES for sake of space. In [298], Vanhamme *et al.* show that MP-FIR can be used inside AMARES. Since the design of the filter is independent from the quantification method (true for MP-FIR and MP-FIR0), it is obvious that MP-FIR0 can also be used inside AMARES. AQSES is based on the variable projection algorithm like VARPRO, therefore MP-FIR0 can similarly be used in VARPRO. The use of MP-FIR0 can also be extended to quantification methods such as QUEST. The original algorithm of QUEST has been detailed in Section 2.3.1. With MP-FIR0, the algorithm would become: (1) truncate the initial points of both the filtered signal and the filtered metabolite profiles, and quantitate with QUEST, (2) estimate the baseline from the metabolite-free and water-free signal by an SVD-based method or AMARES, (3) subtract the parameterized baseline from the raw signal (with nuisance components), and quantitate the metabolites using MP-FIR0 inside QUEST. The number of truncated points in this case is smaller since the baseline is already reduced by the filter as it has been shown in the *in vivo* and *ex vivo* experiments.

7.4 Conclusions

The filter design of the proposed filter exploits more prior knowledge than MP-FIR. The following main advantages have been emphasized:

- a stronger attenuation of the large nuisance components since the choice of the zeros is directly related to the position of these peaks;
- a smaller attenuation of the signals of interest, especially with large damping values at the passband borders.

MP-FIR0 also shows to be successful with different types of signals (simulated, *in vivo*, *in vitro*, *ex vivo*) acquired from different spectrometers (Philips, Siemens, GE, Bruker)

from different centers (IDI, FLENI, etc). MP-FIR0 can be used in several widely used quantification methods.

Chapter 8

Effect of feature extraction on short echo time MR data classification

In Chapter 5, we analyzed the quantification method AQSES. The amplitude estimates can be used as input features in a classifier and, in that sense, AQSES can be considered as a feature extraction method. As explained in Chapter 4, there exist many feature extraction methods that can be used. In this chapter[1]*, we examined the effect of AQSES and other feature extraction methods on the classification of short echo time* ^{1}*H MR data.*

8.1 Introduction

The goal of this study is to compare different pattern recognition methods and more exactly different feature extraction methods for brain tumor diagnosis based on both MRS and MRSI data. The ultimate goal is to implement an automated decision support system (DSS) that would help clinicians in their diagnosis. Currently, no such DSS exists in hospitals and the MR spectral patterns are generally analyzed individually, which is time-consuming and often requires specific spectroscopic expertise. Several pattern recognition (PR) techniques have already been proposed in the literature (see Chapter 4), most of them being automated. In order to be integrated into a DSS, a PR method should be efficient (small execution time) and automated. Some research groups have already made progress in building a DSS. A DSS using single-voxel and multivoxel MR spectra together with magnetic resonance imaging (MRI) has been developed [279] in the European project INTERPRET [2]. As mentioned in Chapter 4, it is difficult to assess that one PR technique is better than the other ones. Conclusions from some of the most relevant papers on the topic have been summarized here:

[1] J. Luts, J. Poullet, J. Garcia-Gomez, A. Heerschap, M. Robles, J.A.K. Suykens, S. Van Huffel, The effect of Feature Extraction for Brain Tumor Classification based on short echo time ^{1}H MR spectra, Magn. Res. Med. 60(2) (2008) 288-298.

[2] http://azizu.uab.es/INTERPRET/ (Accessed: 3 December 2006)

Table 8.1. *Summary of relevant papers. The table contains the type of data, the feature extraction method, the classification method and the conclusions drawn in the corresponding paper. LE = long echo time, SE = short echo time, MC = multicenter, UC = unicenter, TC = tumor classes, WS = whole spectra, PI = peak integration, QM = quantification methods, PR = pattern recognition techniques, GP = gaussian processes, PLS = partial least squares, GPLS = generalized PLS.*

Paper	Data	Features
Lukas *et al.* [163]	LE MRS, MC study with 4 TC	WS, PI, binning
Devos *et al.* [65]	SE MRS, MC study with 4 TC	WS, PI, binning
Simonetti *et al.* [250]	SE MRSI, UC study with 4 TC	PCA, ICA, PI, LCModel
Menze *et al.* [186]	LE MRS, UC study with 4 TC	ICA, PCA, binning, wavelets, QM
Kelm *et al.* [134]	LE MRSI, UC study with 2 TC	ICA, PCA, PLS, VARPRO, AMARES, QUEST
Opstad *et al.* [203]	SE MRS, UC study with 5 TC	WS, LCModel (both reduced by PCA)
Paper	Classification	Conclusion
Lukas *et al.* [163]	LDA, LS-SVM	WS is the best
Devos *et al.* [65]	LDA, LS-SVM	no difference
Simonetti *et al.* [250]	distribution plots	PI is the best
Menze *et al.* [186]	12 methods	PR better than QM
Kelm *et al.* [134]	LR, GPLS, PSR, RF, GP, SVM, 2 kernel methods	PR better than QM
Opstad *et al.* [203]	LDA	LCModel better than WS

From this table, it is indeed complicated to draw firm conclusions. In [186, 134], they conclude that pattern recognition techniques yield better results than quantification methods. Simonetti *et al.* [250] adds that peak integration is better than the quantification method LCModel. No significant difference is expected between peak integration and the use of the whole spectra according to Devos *et al.* [65]. However, Opstad *et al.* [203] have concluded that LCModel increased classifier performance compared to the use of whole spectra. The comparisons are especially difficult to make since the conclusions are based on different types of data and tumor classes. A unique item where all papers seem to agree is that nonlinear classification methods outperform linear ones.

In this chapter we study the effect of some standard feature extraction methods, including quantification approaches, on automated classification techniques for brain tumour diagnosis. Compared to previous studies, two independent data sets, acquired and preprocessed in different ways, containing short echo time multi-center MRS and MRSI signals, are used. Also, various types of tissue specimen are enclosed. Both a kernel and a standard method are used for classification purposes, diverse feature extraction methods are explored.

The following sections are organized as follows. First, Section 8.2 gives an overview of the different data sets, the preprocessing protocols and the methods used for feature extraction. This section concludes with the experimental setup and evaluation. Afterwards the results on the two independent data sets are described in Section 8.3. Finally, the discussion and conclusions are formulated.

8.2 Methods

Compared to [65] and [163], this study explores a wide variety of feature extraction methods and draw its conclusions based on two independent data sets. Also, more tissue classes are included. In the study of Simonetti *et al.* [250] the data set was split only once into a set for training and for testing. By dividing only once in a training and a test set, potentially, high bias is introduced. This study overcomes the problem by splitting the data an extensive number of times. Also, no real statistical analysis was performed in [250]. This aspect is further improved in the present manuscript. Compared with the work of Menze *et al.* [186] and Kelm *et al.* [134], our focus is on short echo time MR signals with much more patients coming from multiple centers. This allows us to further increase the number of tissue classes with respect to the amount in [186] and [134] and formulate conclusions that are possibly less dependent on the MR machine or the acquisition parameters. In the study by Opstad *et al.* only two feature extraction methods were employed. In fact, standard PCA was compared with LCModel based on an LDA classifier. In this way, the authors were not exploiting the power of a method which can truly accept full spectra as input for classification.

For classification, a classical supervised learning method is used, as well as a kernel-based method that handles high dimensional input vectors; both standard LDA and LS-SVMs are applied [274, 275]. It is decided to use a radial basis function kernel for LS-SVMs in the experiments, based on the results of the studies in [66]. For training, testing and (hyper-)parameter estimation KULeuven's LS-SVMlab MATLAB/C Toolbox[3] is used.

[3] http://www.esat.kuleuven.ac.be/sista/lssvmlab/ (Accessed: 2 January 2007)

Table 8.2. *Overview of the acquisition parameters for the single voxel MRS data set. For each center the manufacturer of the scanner, the sequence, the echo time, the repetition time, the spectral width (SW) and the number of points in the original FID (N) are displayed.*

Center	Manufacturer	Sequence	TE(ms)	TR(ms)	SW(Hz)	N
CDP	GE	STEAM	20	1600,2000	2500	2048
SGHMS	GE	STEAM	30	2000,2018,2020	2500	2048
	GE	PRESS	30	2000,2018,2020	2500	2048
FLENI	GE	PRESS	30	2000	2500	2048
IDI	Philips	PRESS	30,31,32	2000	1000	512
UMCN	Siemens	STEAM	20	2000	1000	512
MUL	Siemens	STEAM	20	2000	1000	512

In the following paragraphs, the data and the different feature extraction methods are explained. This study focuses on the standard methods, both pattern recognition and quantification approaches, that are often applied in the field of MRS. As user interaction needs to be minimized, all methods in this analysis are applied in an automated manner. The last paragraph of this section concentrates on the experimental setup and the evaluation procedure.

8.2.1 Data

In the analysis two independent data sets are used. The first data set, as described in [65], contains 205 single voxel proton MR spectra from the short echo time INTERPRET database. This database comprises spectra from 6 contributing centers: Centre Diagnostic Pedralbes (CDP), Fundacion para la Lucha contra las Enfermedades Neurologicas de la Infancia (FLENI), Institut de Diagnostic per la Imatge (IDI), Uniwersytet Medyczny w Lodzi (MUL), St George's Hospital Medical School (SGHMS) and Universitair Medisch Centrum Nijmegen (UMCN). Data were acquired at 1.5T by STEAM or PRESS sequence at an echo time between 20 and 32 ms. Detailed information about the acquisition parameters for each center are provided in Table 8.2. Quality control criteria have been applied to MR system performance and all data in this study passed a strict validation process [291]. Tumour assignment has been done according to the rules of the World Health Organization (WHO). There are four different types of brain tumours included in this data set: glioblastomas, meningiomas, metastasis and grade II astrocytomas. These are the most prevalent types of tumour occurring in the brain. The number of patients for each class are depicted in Table 8.3.

The spectra are preprocessed by frequency alignment and zero order phase correction is performed with Klose's method as in [65, 138]. The residual water peak is filtered using HSVD [12] with 15 singular values over the water region 4.09-5.61 ppm. GE data have been interpolated by piecewise cubic splines in the time domain to match the spectral

Table 8.3. *Number of spectra per center for each class in the MRS database: glioblastomas (1), meningiomas (2), metastasis (3) and grade II astrocytomas (4).*

Center	1	2	3	4
CDP	30	12	5	4
SGHMS	18	12	16	10
FLENI	2	0	0	1
IDI	31	30	17	5
UMCN	2	1	0	1
MUL	4	2	1	1
Total	87	57	39	22

width and number of points of Philips and Siemens data. Water normalization is performed using a corresponding water unsuppressed signal, acquired from the same voxel with equal parameters as the metabolite signal. The amplitude of the water unsuppressed signal is estimated. A Voigt model is used to model the unsuppressed water signal in the time domain, with an additional first order term correcting for eddy currents [179]. HSVD is used to get initial parameter estimates as starting values for a nonlinear least squares algorithm to obtain final parameter estimates. Next, each value in the spectrum is divided by the resulting estimate of the intensity of the water peak. For baseline correction an exponential decreasing apodization function is used [65, 249]. Afterwards the baseline model is substracted from the original signal. Finally, after Fourier transformation, only the points (*i.e.* 138) in the region of interest (0.0-4.17 ppm) are remained. Figure 8.1 depicts the mean magnitude spectra with baseline correction for each class. By using magnitude spectra, phasing problems can be avoided. Also, no and only minor differences have been reported between performances based on magnitude spectra and real spectra in [65, 203].

For the second data set, multivoxel data are selected from the INTERPRET database. MRSI data from 25 patients with a brain tumour and 4 volunteers were acquired at the UMCN. The study was approved by the ethical committee of the UMCN and the rules of the WHO to classify the brain tumours were followed. Data were acquired on a 1.5 T Siemens Vision Scanner with CP-head coil. Both water suppressed and unsuppressed proton MR spectroscopic images were acquired. The MRSI data were acquired using a 2D STEAM sequence with the STEAM box positioned totally in the brain (TR/TE/TM = 2000 or 2500/20/30 ms, slice thickness = 12.5 or 15 mm, FOV = 200 mm, spectral width = 1000Hz and NS = 2). Disturbing signals appearing from the fat tissue surrounding the skull were avoided. The location of the STEAM box was determined using the gadolinium enhanced T1-weighted image showing the largest tumour area. A strict quality control applied, the tumour type is determined by a consensus on a histopathological study. At least two of the three pathologists had to agree about the diagnosis. Voxels, situated in the tumour area, were selected from each patient based on their spectral patterns and the MRI data [250]. An expert in spectroscopy selected voxels for each tissue type only if the considered spectra were found to be typical for that pathology and if they were clearly within the affected brain region. Although this method is subjective, it is chosen because tumours are known to be heterogeneous. Furthermore, no “ground truth” is available in

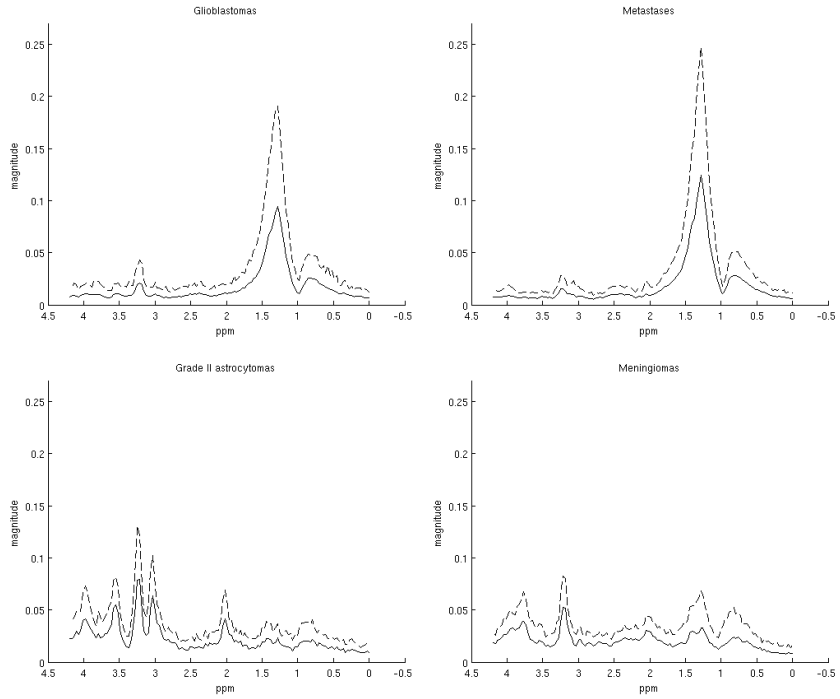


Figure 8.1. *Preprocessed mean magnitude spectra after baseline correction for each tissue type in the MRS data set. The solid lines represent the means, dotted lines depict the means plus the standard deviations.*

tumour diagnosis at the voxel level and often the number of patients is limited. Also, cerebrospinal fluid (CSF) and normal tissue from volunteers and patients were selected. In total, 681 spectra from six classes of pathology are included in the data set: normal brain tissue from volunteers and apparently normal tissue from the contralateral half of the brain of patients, CSF from patients, grade II gliomas, grade III gliomas, meningiomas and glioblastomas. The distribution of the cases over the classes is described in Table 8.4.

The data set is preprocessed as in [249]. Preprocessing includes filtering of k-space data by a Hanning filter of 50 % using the LUISE software package (Siemens, Erlangen, Germany), zero filtering to 32x32, spatial 2D Fourier transformation to obtain time domain signals for each voxel, correction for eddy current effects by a method preventing occasional occurrence of eddy current correction induced artifacts [138, 251], water removal using HLSVD from 4.3 to 5.5 ppm [210], frequency alignment and a simple baseline correction using an exponential filter with a width of 5 ms followed by subtraction of the residual of the original signal. All first order phases are corrected by first manually optimizing the mean spectrum which is calculated from all spectra in the STEAM box of each patient's MRSI data. Next, this correction is applied to each separate signal of the patient's MRSI data. Spectra are normalized using the water signal [284]. Only spectral points (*i.e.* 230) in the region of interest (0.5-4.0 ppm) are remained. In Figure 8.2 the mean magnitude

Table 8.4. *Number of spectra and number of patients for each class in the MRSI database.*

Pathology	Spectra	Patients
Normal tissue	218	8
CSF	100	8
Gliomas grade II	176	10
Gliomas grade III	69	5
Meningiomas	48	3
Glioblastomas	70	7

spectra with baseline correction are shown for each class.

8.2.2 Peak integration

For the multi-center MRS data set, 13 peak integrated values are extracted based on the resonance frequencies reported in [97]. As in [65], the following metabolites are selected: lipids (0.825-0.975 ppm), lipids (1.125-1.275 ppm), lactate (1.235-1.385 ppm), alanine (1.395-1.545 ppm), N-acetylaspartate (1.935-2.085 ppm), glutamate + glutamine (2.270-2.510 ppm), creatine (2.955-3.105 ppm), choline (3.115-3.265 ppm), myo-inositol + taurine (3.195-3.345 ppm), myo-inositol + glycine (3.450-3.680 ppm), taurine + glucose (3.345-3.495 ppm), glutamate + glutamine + alanine (3.665-3.815 ppm) and creatine (3.845-3.995 ppm). For the MRSI data, 10 integrated values are selected as in [66]: lipids (0.835-0.965 ppm), lipids (1.2 ppm) and lactate + alanine (1.265-1.395 ppm), N-acetylaspartate (1.955-2.085 ppm), glutamate + glutamine (2.135-2.265 ppm), creatine (2.955-3.095 ppm), choline (3.135-3.265 ppm), taurine + glucose (3.375-3.505 ppm), myo-inositol + glycine (3.495-3.625 ppm), glutamate + glutamine + alanine (3.685-3.815 ppm) and creatine (3.885-4.015 ppm).

8.2.3 Peak regions - binning

More specifically, 91 variables are selected for the MRS data. For the MRSI data set, 101 features are included based on the peak regions.

8.2.4 Bagging with Fisher criterion, Kruskal-Wallis test and Relief-F

In these three pure filter model approaches, the variables are ranked independently of the classification algorithm [68]. The main advantage of the filter model is the low computational cost, the weakest point is the complete ignorance of the classification algorithm. This analysis uses the Fisher discriminant criterion [84], the Kruskal-Wallis test [115] and Relief-F [229] to rank all the frequency points of the magnitude spectrum in the region of interest. Additionally, to assure more robust results, a bagging analysis is incorporated [21]. For each training set, 50 data sets are generated by bagging. Feature ranking is performed

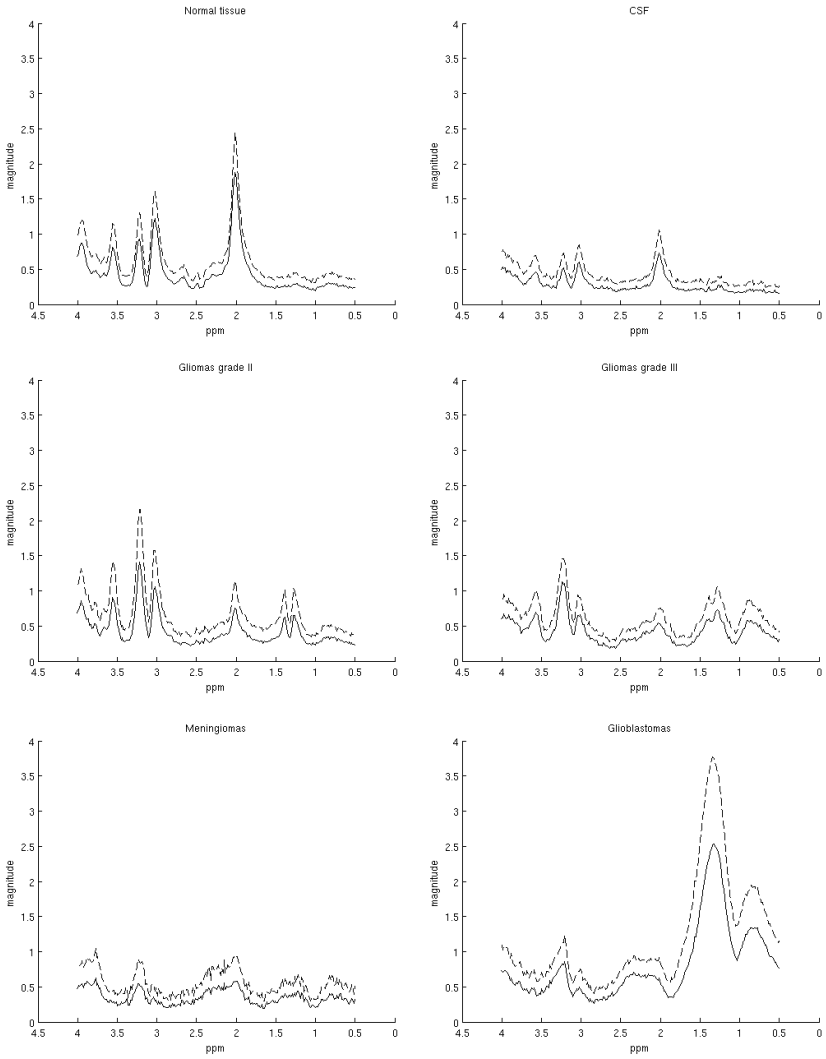


Figure 8.2. *Preprocessed mean magnitude spectra with baseline correction for each class in the MRSI data set. Solid lines represent the means while dotted lines mark the means plus the standard deviations.*

on each of the 50 generated sets, and the most relevant features according to the three ranking criteria and the bagged sets are extracted. To do the comparison in a fair way, the number of spectral points that is selected is equal to the number of variables used for classifying the peak regions as in the previous section.

8.2.5 ICA

As input for the method, the full region of interest of the magnitude spectrum is used. Based on the JADE [31] implementation, 13 independent components are extracted for the single voxel MRS data, while 10 are selected for the MRSI data.

8.2.6 Linear PCA

To have a fair comparison with ICA and peak integrated values, it is decided to choose the first 13 principal components for the MRS data and the first 10 for the MRSI data.

8.2.7 Stepwise selection

Stepwise variable selection is a standard wrapper algorithm from statistics and machine learning to perform feature extraction [201]. Since an exhaustive search is unpractical in case of high dimensional data, a greedy hill climbing approach is applied. The subset of features with the best performance, based on a cross-validation analysis and a measure quantifying the ability to separate [90], is obtained by stepwise adding or deleting features from the model. This method is applied to the full region of interest of the magnitude spectrum. Complementary to the previous approaches, the upper limit of selected variables is 13 for the MRS data. Furthermore, 10 variables are picked out for the MRSI data set.

8.2.8 AQSES

To set up the *in vitro* basis set, 11 separate metabolite solutions are prepared as described in [213]: myo-inositol, taurine, glucose, phosphocholine, creatine, glutamate, N-acetylaspartate, alanine, lactate, lipids (1.3 ppm), lipids (0.9 ppm). The *in vitro* metabolite profiles are acquired at 1.5 T Siemens scanner using a STEAM sequence with an echo time of 20 ms, and a STEAM box of 2 x 2 x 2 cm^3. A maximum-phase FIR filter [273], included in AQSES, is applied to suppress the water resonances. The components outside the frequency interval of 0.25 to 4.2 ppm are filtered out. The regularization parameter (*i.e.*, λ, see Chapter 2) for baseline correction equals 2. No constraints are imposed on the parameters; the amplitudes, damping corrections, phase corrections and frequency shifts are free.

8.2.9 QUEST

The metabolite basis set used in the analysis with QUEST is identical to the one in the analysis with AQSES. Again, all the correction parameters (amplitude, damping, phase and frequency) are free.

8.2.10 Experimental setup and evaluation

The same experimental design and evaluation measure are used on both data sets. For each pair of classes in the individual data sets, the feature extraction methods are compared using stratified random sampling. The data from two specific classes is 100 times randomly split in a stratified way in a set for training and validation (*i.e.* two third of the data), and

one for testing (*i.e.* one third of the data). The training and validation set is used for model selection, the test set is only used to check the performance. As performance measure the area under the ROC curve (AUC) is used. For each pair of classes and each feature extraction method the 100 performance measures on test set are averaged, giving $\overline{\text{AUC}}$. Next, the Friedman test [115] is used on the $\overline{\text{AUC}}$s since the performances for each pair of classes are correlated and can be interpreted as blocks. Additionally, to study the differences between the methods in detail, Tukey's honestly significant difference criterion [112] is used. It corrects for multiple testing and indicates which differences in performance are statistically significant. The paired comparison plot was constructed from Eq. (2.45), where r is the number of combinations of feature selection and classification methods (=12 for MRS data and =14 for MRSI data), $n_T = r * n_b$ is the number of data and n_b the number of pairwise classification problems (=6 for MRS data and =15 for MRSI data), $\bar{Y}_{i.}$ is the mean of the rank of the $\overline{\text{AUC}}$ for the combination i of feature selection and classification methods. The $\overline{\text{AUC}}$s are thus first ranked for each pair classification problem (ranks from 1 to 12 for MRS data and from 1 to 14 for MRSI data).

8.3 Results

In this section the results of the feature extraction methods are summarized for the two data sets. It is decided to compare 14 different combinations of classification algorithm and feature extraction method. The different combinations and their matching label are listed in Table 8.5.

Table 8.5. *The different combinations of feature extraction technique and classification method applied in this study.*

Label	Feature extraction method	Classifier
1	Bagging+Fisher criterion	LS-SVM
2	Bagging+Relief-F	LS-SVM
3	Bagging+Kruskal-Wallis	LS-SVM
4	Full spectra	LS-SVM
5	ICA	LDA
6	ICA	LS-SVM
7	PCA	LDA
8	PCA	LS-SVM
9	Peak regions	LS-SVM
10	Peak integration	LDA
11	Peak intregation	LS-SVM
12	Stepwise selection	LDA
13	AQSES	LS-SVM
14	QUEST	LS-SVM

For each data set a figure is presented with paired comparisons, also, plots of the obtained performances are provided. For the MRS data set the Friedman test resulted in a p-value of 0.0001, indicating that there are significant differences between the methods. Tukey's honestly significant difference criterion for multiple testing results in the paired

comparison plot, depicted in Figure 8.3. This figure gives a global overview of the performance for each method. On the horizontal axis the rank score is indicated. The figure contains a comparison interval for the mean rank of the $\overline{\text{AUC}}$ for each method. The higher the mean rank score, the higher the AUC values for that specific method. Methods perform significantly different if their intervals are disjoint. It is observed that there are some statistical differences between the methods for the MRS data set. By looking at the intervals, some trends can be observed. Relief-F, the Kruskal-Wallis test, the full spectra, ICA, PCA and peak regions obtain good results that are fairly similar. Using PCA in combination with LS-SVMs or the stepwise selection procedure with LDA leads to a significantly decreased performance. In this data set, there is no clear distinction in performance between peak integration or peak regions and the true pattern recognition approaches, but, LDA appears to perform better in combination with ICA and PCA than with peak integrated values. The difference between peak regions and the full spectra, or the Kruskal-Wallis test is rather small. When comparing the classification algorithms, *i.e.* LDA and LS-SVMs, no method outperforms the other. Finally, to illustrate the performances for the different classification problems, the AUCs for the individual feature extraction methods are presented in Figure 8.4.

In the examination of the multivoxel data set, it is decided to include the quantification methods (*i.e.* AQSES and QUEST). An identical statistical analysis is performed and results in the paired comparison plot, depicted in Figure 8.5. According to the Friedman test, a p-value smaller than 0.0001 is obtained. Compared to the previous analysis, stronger differences are detected. Using the full spectra in the region of interest, Relief-F or ICA, all in combination with LS-SVMs, results in the highest AUCs. Though not significantly, using only peak regions decreases the performance. Additionally, 10 peak integrated values with LS-SVMs further decrease the performance. As in the first data set, using LDA and 10 input features, the pattern recognition methods PCA and ICA perform better than peak integrated values. Using LS-SVMs, the automatic pattern recognition approach ICA seems to perform better than peak integrated values. Relief-F tends to perform better than the Fisher criterion and the Kruskal-Wallis test. Both the sophisticated quantification approaches in combination with LS-SVMs have a strong decreased performance compared to the use of the full spectra, ICA or Relief-F. The performance of AQSES and QUEST is not better than peak integration. The smallest AUCs are obtained for the stepwise selection with LDA. Concerning the classifier type, in this data set the LS-SVM method outperforms LDA. To conclude, the AUCs of the various feature extraction methods are compared using boxplots in Figure 8.6.

8.4 Discussion

In this study multiple binary classifiers are used to compare the feature extraction methods. Compared to [65, 134, 163, 186, 203, 250], the results are based on more classification problems and more tissue types are included. In this study, the aim is not to find the best feature extraction method for a specific pairwise problem (*e.g.* grade II glioma versus grade III glioma), since such a study can only produce reliable results when having very extensive databases. The purpose of the present study is to examine the feature extraction techniques over a wide variety of tissue types. As such, the analyses focus on finding the method that

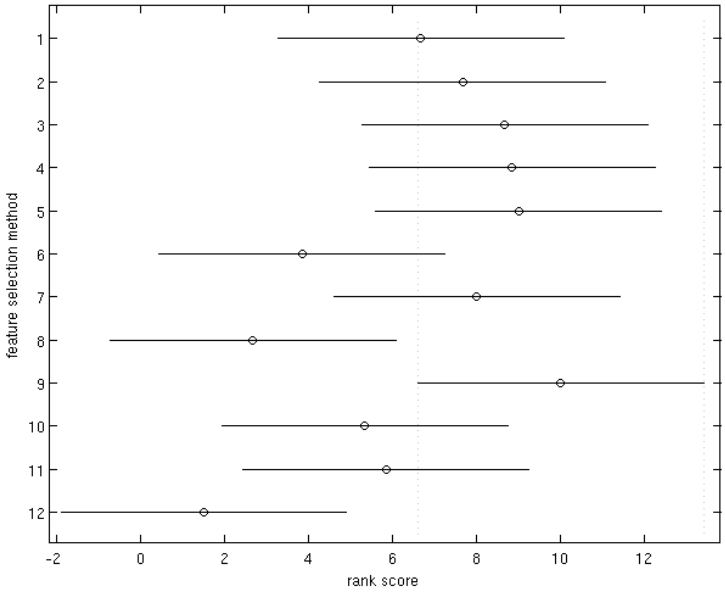


Figure 8.3. *Paired comparison plot for the MRS data set after performing the Friedman test and Tukey's honestly significant difference criterion for multiple testing. The horizontal axis indicates the rank score, where higher rank scores are related to higher AUC values. On the vertical axis the numbers refer to the different combinations of classification algorithm and feature extraction methods as depicted in Table 8.5. Relief-F (2), the Kruskal-Wallis test (3), full spectra (4), ICA (5), PCA (7) and peak regions (9) obtain similar performance scores.*

has the best overall performance. In the statistical analysis, this reflects in averaging the AUCs over the 100 resamplings for a specific classification problem and feature extraction method. Besides, we avoid finding statistical differences purely by artificially increasing the number of samples, used as input for the statistical test.

Since two independent data sets are used in the analysis, results can be verified independently. Also, these data sets are acquired in different ways using various acquisition parameters and coming from different centers. Despite these differences, comparable results are observed for both data sets. The automated pattern recognition techniques ICA, Relief-F and the full spectra in the region of interest result in the highest overall performances. The use of peak regions might slightly decrease the performance, peak integrated values and the stepwise selection procedure further reduce the AUCs. In the multivoxel data set it is clearly observed that Relief-F tends to perform better than the Kruskal-Wallis test or the Fisher criterion. This can be explained by the fact that Relief-F does not assume conditional independence of the features. In [163, 134] it is observed that using full spectra results in the highest performances. This may suggest to avoid feature extraction

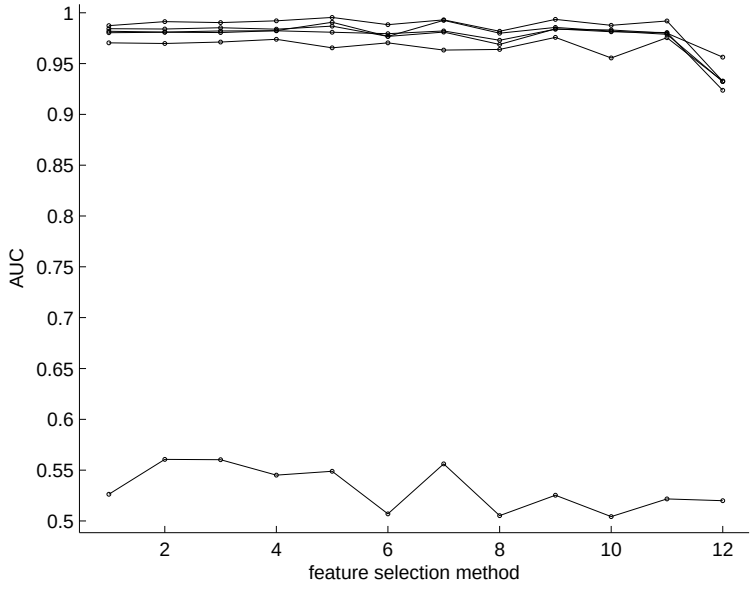


Figure 8.4. *Lineplot of the AUCs for the MRS data where each line represents a specific pairwise classification problem. On the vertical axis the mean AUC values on test set are indicated, on the horizontal axis the numbers refer to the combinations of classification method and feature extraction technique as in Table 8.5. The bottom line corresponds to the classification problem "glioblastoma versus metastasis".*

for kernel-based methods. However, here, we observe an excellent performance for automated pattern recognition approach based on ICA and Relief-F as well. Aditionally, [186] also reports good results for automated pattern recognition approaches. One might argue that still more sophisticated methods [293], which can possibly increase performance for certain classification problems, exist for LS-SVM-based feature extraction. Nevertheless, these algorithms often tend to increase the computation time compared to their gain in accuracy. Certainly in the context of DSSs efficiency is decisive. Compared to its low computational complexity, we experience that a fast automated pattern recognition using ICA or the combination of full spectra with LS-SVMs produces good results.

Concerning the quantification methods, AQSES and QUEST perform worse than the full spectra. The pattern recognition approaches Relief-F and ICA and even peak integration yield higher AUCs. The latter observation is also reported in the study in [250], where LCModel performed worse than peak integration, ICA or PCA. In [186] one reported an increase of 5 to 10 $\%$ in accuracy for automated pattern recognition methods compared to quantification approaches. There, full spectra and pattern recognition methods even performed better than manually supervised quantification. Additionally, in [134] it was observed that QUEST performed worse than using SVMs and full spectra. On the

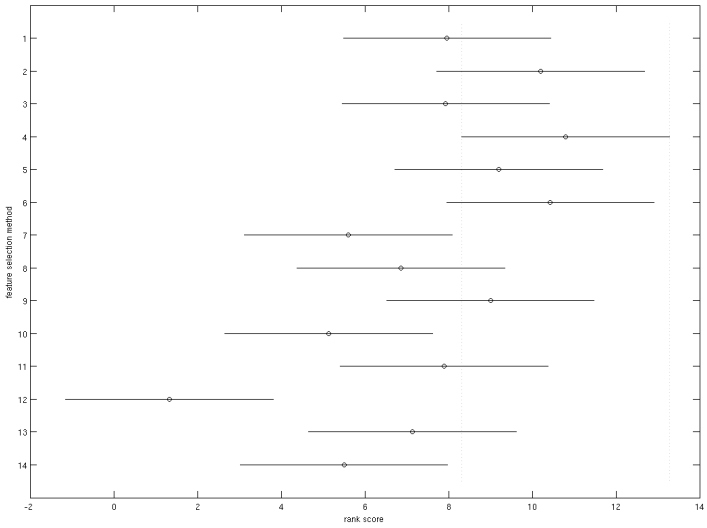


Figure 8.5. *Paired comparison plot for the MRSI data set after performing the Friedman test and Tukey's honestly significant difference criterion for multiple testing. The horizontal axis indicates the rank score, where higher rank scores are related to higher AUC values. On the vertical axis the numbers refer to the different combinations of classification algorithm and feature extraction methods as depicted in Table 8.5. LS-SVMs with full spectra (4), Relief-F (2) and ICA (6) obtain the highest performances.*

contrary, the study in [203] reported an improved performance for LCModel compared to full spectra. However, it seems that the authors were just comparing LCModel with PCA instead of feeding full spectra to the classifier. PCA was needed to use LDA as classification method due to the highly dimensional input feature space when taking the full spectra (each point of the spectrum is considered as an input feature). A more interesting study would have been to compare LCModel and "taking the full spectra", both combined with a nonlinear classification method such as LS-SVM. In this study, it is also observed that AQSES performs slightly better than PCA. Nevertheless, it seems that there are still more complicated methods, which can further increase classifier performance. The problem with the sophisticated quantification methods is that they are in general hard to automate. For AQSES, we fix the parameter controlling the smoothness of the baseline, but this parameter may not be optimal in all cases. In QUEST, where one has to choose the number of points for baseline construction in the subtract method, we were not able to find a fixed value resulting into good AUCs for every pairwise problem. For this reason we decided to use a baseline correction method prior to quantification with QUEST. With this approach, the results of AQSES and QUEST are comparable.

In medical practice, clinicians and technicians lack time to fit each spectrum separately or to try out different parameters influencing the estimation procedure. Besides, it

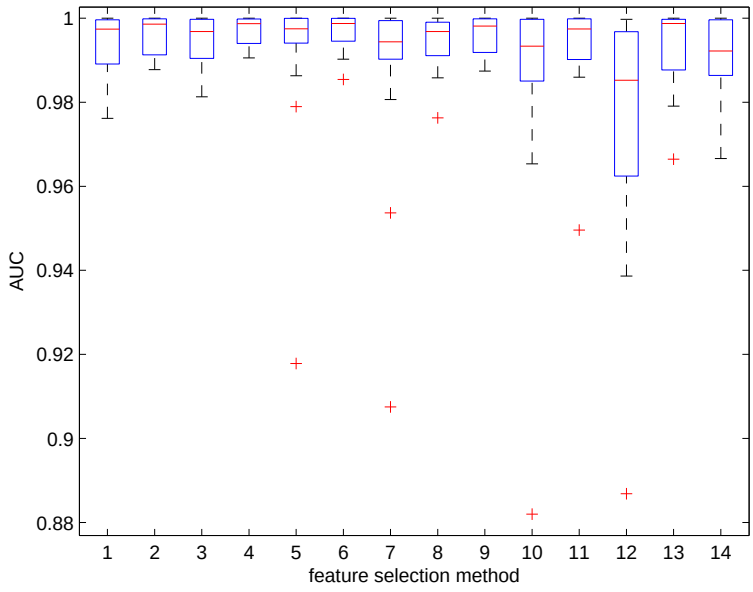


Figure 8.6. *Boxplot for the MRSI data with on the vertical axis the mean AUC values on test set and on the horizontal axis the various combinations of classification method and feature extraction technique as in Table 8.5. It is observed that pattern recognition and in particular the use of LS-SVMs and full spectra (4) results into a good performance and small spread. Quantification methods (13,14) show a degraded performance.*

is not clear how robust these methods are with respect to those parameters. The use of the quantification techniques also requires specific expertise, that is not always available. As a consequence, until now, it seems that quantification methods are not ideally suited for use in automatic DSSs, certainly when comparing their performance with results from automatic pattern recognition approaches. When a blackbox classification method is satisfactory, automated pattern recognition techniques (*e.g.* Relief-F, ICA) or full spectra with LS-SVMs seem more appropriate. In case a biological interpretation of MR spectra is required, quantification approaches are needed since automated pattern recognition approaches may have limited abilities to provide this type of information.

8.5 Conclusions

In order to introduce a DSS in clinical practice, to assess MR spectra of the human brain, automatic procedures are required since user interaction and processing time should be minimized. In this study the focus is on the feature extraction step in the preprocessing protocol of short echo time spectra prior to classification using a DSS. Two independent studies on separate data sets, including single and multivoxel data, are performed and com-

parable results are obtained. Using an automated pattern recognition method, *e.g.* ICA, Relief-F, or full spectra in combination with a regularization technique, handling high dimensional data, produces the highest overall performances. Compared to automated pattern recognition or the use of full spectra, selecting peak regions or using simple peak integration might slightly decrease performance. In addition, sophisticated quantification methods seem hard to automate in a clinical DSS and are often computationally intensive. When only classification is needed, the use of full spectra or an automated pattern recognition technique seems more suitable. Additionally, quantification techniques can provide a biological interpretation if needed. More complicated feature extraction methods from pattern recognition, with higher computational cost, may increase performance, however, simple methods producing good results are frequently preferred in clinical practice. These findings suggest to restrict the feature extraction step in the preprocessing protocol, decreasing execution time of a DSS. This observation may speed up the introduction of DSSs in clinical practice.

Chapter 9

Quantification and classification of HR-MAS signals

The goal of this chapter[1] *is to propose a complete procedure (preprocessing, processing and classification) for diagnosing brain tumors with proton high-resolution magic-angle spinning (^{1}H HR-MAS) data. The different steps of the procedure are detailed and discussed. Feature extraction techniques such as peak integration, including also the automated quantification method AQSES, were combined with linear (LDA) and non-linear (least-squares support vector machine or LS-SVM) classifiers.*

9.1 Introduction

Ex vivo high resolution magic angle spinning (HR-MAS) magnetic resonance (MR) spectroscopy might help for brain tumor diagnosis. Cheng *et al.* [46] demonstrated that proton magnetic resonance spectroscopy (^{1}H MRS) with high-resolution magic-angle spinning (HR-MAS) can preserve tissue histopathology features while producing well-resolved spectra of cellular metabolites. Tugnoli *et al.* [285] and Martinez-Bisbal *et al.* [180] showed that HR-MAS is very helpful for the assignment of the resonances *in vivo* of human meningiomas and glioblastomas and for the validation of the quantification procedure of *in vivo* MR spectra. They concluded that HR-MAS MRS is a complementary method to strongly support *in vivo* MR spectroscopy and increase its clinical potentiality.

In this study, we propose a complete procedure to diagnose brain tumors using HR-MAS data. This procedure contains three main parts: preprocessing, processing and classification of the data. The preprocessing methods are used to clean the spectra from the unwanted underlying components such as the residual water resonances or the macromolecular baseline contributions. They also ensure that the spectra are standardized so that we can compare them. The purpose of the processing techniques is to extract relevant features

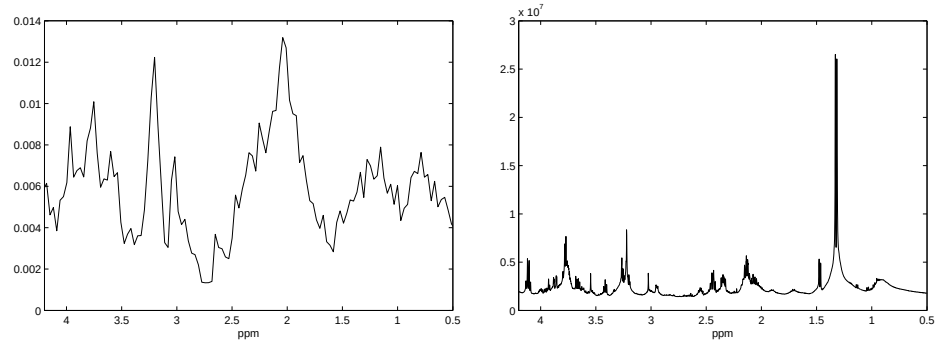
[1] J. Poullet, M.C. Martinez-Bisbal, D. Valverde, D. Monleon, B. Celda, C. Arus, S. Van Huffel, Quantification and classification of high-resolution magic angle spinning data for brain tumor diagnosis, in Proc. of the IEEE 2007 International Conference of the Engineering in Medicine and Biology Society (EMBC 2007), Lyon, Aug. 2007, 5407-5410.

from the filtered spectra, which will then be used as inputs in the binary classifier.

9.2 Materials and methods

Brain tumor biopsies were obtained from 59 patients and stored at -80°C until use. The biopsies were gathered in 4 brain tumor classes: 22 glioblastomas (GBM), 21 grade II and grade III gliomas (GLI), 7 metastasis (MET) and 9 meningiomas (MEN). 1D PRESAT (pulse-and-acquire) data were acquired at 11.7 T (500 MHz for ^{1}H) at 0-4°C and 4,000 Hz spinnning rate using BRUKER Analytik GmbH spectrometers.

By looking at the linewidth and SNR differences between *in vivo* and *ex vivo* spectra (see Fig. 9.1), we may reasonably think that different strategies are required to (pre)process the data. Quantification of HR-MAS spectra is particularly challenging due to the inherent complexity of such spectra (a large amount of peaks that may overlap). However, HR-MAS spectra present much higher signal-to-noise ratios than *in vivo* MR spectra and the macromolecular contribution is not spread over the whole spectrum in the region of interest, but bumps due to fatty acids appear instead in several well-known frequency regions (mainly around 0.9, 1.3 and 2.05 ppm). Furthermore, eddy current effects are negligible in HR-MAS spectra simplifying the preprocessing.



(a) *in vivo* (b) *ex vivo*

Figure 9.1. *Magnitude (arbitrary units)* in vivo *and* ex vivo *spectra in the region of interest from the same meningioma patient.*

The water components were removed by HLSVD-PRO [152]. The filtered 1D "presat" signals were normalized (divided by the L2 norm of the frequency domain signal between 0.25 and 4.2 ppm), aligned with respect to the Alanine doublet at 1.47 ppm, and corrected for the baseline (by subtracting the product of the signal and an apodization function) to obtain the preprocessed signals.

We investigated different processing or feature selection methods: whole spectrum in the region of interest, peak integration and an automated quantification method designed

for short echo time MR spectra (AQSES) (see [213] and references therein).

The whole spectrum in the region of interest
Every point of the magnitude spectra in the region of interest (defined as the frequency interval [0.25 4.2] ppm) is considered as an individual feature.

Peak integration
18 peak integrated values are extracted from each magnitude spectrum in the following intervals in ppm: [1.45 1.47], [1.88 1.94], [1.99 2.03], [2.1 2.14], [2.22 2.32], [2.39 2.49], [3.01 3.05], [3.19 3.21], [3.21 3.23], [3.23 3.25], [3.255 3.275], [3.4 3.44], [3.52 3.56], [3.58 3.64], [3.75 3.79], [3.91 3.95], [4.03 4.07], [4.095 4.155]. This method, largely used in *in vivo* MRS, is less sensitive to the noise and misalignment issues than the previous one.

AQSES
The parameters of interest, *i.e.* the metabolite amplitudes, are the weighting coefficients of a linear combination of 18 simulated metabolite profiles constituting the basis set (see Fig. 9.2): Acetate (Ace), Alanine (Ala), Aspartate (Asp), Choline (Cho), Creatine (Cr), Glucose-α (Glc-α), Glucose-β (Glc-β), Glutamate (Glu), Glutamine (Gln), Glycine (Gly), Glycerophosphocholine (GPCh), Lactate (Lac), myo-Inositol (mI), N-Acetylaspartate (NAA), Phosphocreatine (PCr), Phosphocholine (PCh), Succinate (Succ) and Taurine (Tau). These were quantum mechanically simulated using the method described in [156]. Two methylene resonances were filtered out from PCh and GPCh to reduce the number of overlapping peaks around 3.65 ppm. The phases of the metabolite profiles are imposed to be equal, damping corrections and frequency shifts are free. The main advantage of this method with respect to the previous ones is to allow to disentangle overlapping metabolites. In most of the selected regions, peak integration will integrate the contribution of several metabolites together, loosing thereby information about the individual metabolites.

Two supervised learning methods are used for classification: the classical linear discriminant analysis (**LDA**) and the least-squares support vector machine (**LS-SVM**) [275], a kernel-based method able to handle high dimensional input vectors. For each pair of classes, the feature extraction and classification methods are compared using stratified random sampling. The data obtained after processing the signals are 100 times randomly split in a stratified way in a set for training and validation (*i.e.* 2/3 of the data), and one for testing (*i.e.* 1/3 of the data). Classification accuracy is given for each pair of classes and each procedure.

9.3 Results

A representative fit obtained with AQSES is given as illustration in Fig. 9.3. The preprocessed spectrum (in black) is the result of the preprocessings applied to the signal plotted in Fig. 9.1(b). We observe a good fit in the frequency region between 1 and 3 ppm (Cr peak included) while it presents more residuals from 3 to 4 ppm. The larger residuals around 3.6 ppm are probably due to the low amplitude estimate of mI, which can be explained by the fact that the contribution of mI at 4.05 ppm is almost non-existent in the spectrum. A sim-

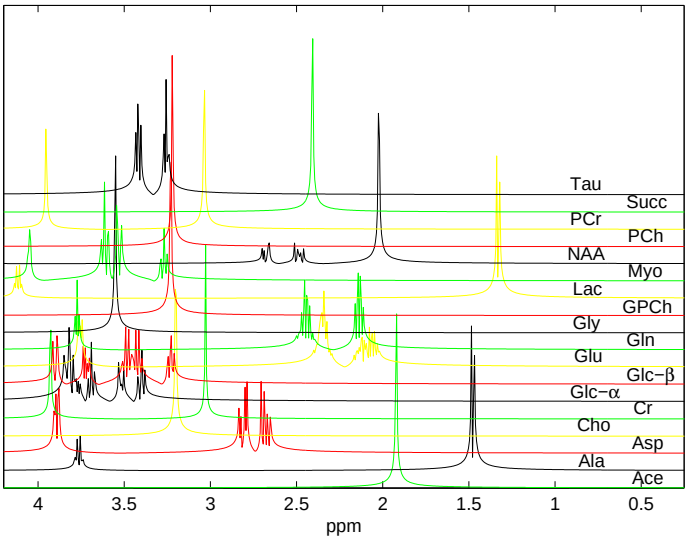


Figure 9.2. *Basis set of metabolite profiles used in AQSES (magnitude spectra).*

ilar observation can be made for Asp around 3.88 ppm. The Asp contribution at 2.8 ppm has probably been removed with the baseline correction due to its overlap with fatty acids. Adding the methylene resonances in the profiles of PCh and GPCh might improve the fit around 3.65 ppm, but this will decrease the quality of the fit around 3.2 ppm (where the largest peaks of PCh and GPCh are located) since the resonances around 3.65 ppm are more largely spread in the frequency domain, and so more reduced by the baseline correction, than the resonances around 3.2 ppm.

The classification results are reported in Table 9.1. Concerning the processing or feature extraction methods, AQSES and the whole spectrum provide generally better results than peak integration and are comparable. LS-SVM seems however to improve the performance of the classifier when compared with the standard linear method LDA.

9.4 Discussion

Although the question of the diagnosis of brain tumors using long echo or short echo time *in vivo* MRS data has been largely studied (see, *e.g.*, [65, 163, 278, 186]), no complete procedure (preprocessing, processing and classification steps) has been proposed for HR-MAS data, even if quantification of brain HRMAS-NMR signals has already been performed [223]. The methods proposed in this work, already used in *in vivo* MRS, have been adapted for HR-MAS data.

Preprocessing HR-MAS is made easier by the almost complete absence of eddy current effects. The large-damping components (fatty acids) are also more localizable (not

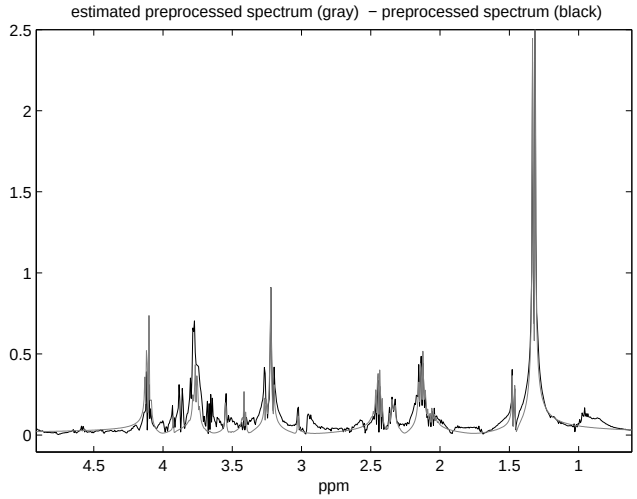


Figure 9.3. *Region of interest of the preprocessed spectrum vs estimated processed spectrum. Spectra are shown in magnitude and the y axis in arbitrary units.*

Table 9.1. *Classification accuracy in percentage for each pair of classes and each procedure.*

Processing	Classifying	GBM vs GLI	GBM vs MET	GBM vs MEN
Whole spectrum	LS-SVM	92.86	94.53	87.38
Peak integration	LDA	85.63	86.79	86.58
Peak integration	LS-SVM	88.37	91.66	91.48
AQSES	LDA	89.67	86.48	87.42
AQSES	LS-SVM	91.95	91.86	90.19
Processing	Classifying	GLI vs MET	GLI vs MEN	MET vs MEN
Whole spectrum	LS-SVM	92.86	94.53	87.38
Peak integration	LDA	84.04	88.53	79.38
Peak integration	LS-SVM	90.86	88.67	85.75
AQSES	LDA	84.75	86.33	88.50
AQSES	LS-SVM	92.93	92.40	89.88

spread over the whole region of interest as in *in vivo* MRS). The baseline correction used in this work to remove these components has two main effects: increasing the signal-to-baseline ratio (SBR) and decreasing the signal-to-noise ratio (SNR). In contrast with *in vivo* MRS, HR-MAS spectra present high SNRs, allowing a larger increase of the SBR and thus a better suppression of the fatty acids.

Although the baseline correction allows to disentangle the metabolites of interest from the lipids (or fatty acids), it also prevents from using the information relative to the lipids. In *in vivo* MRS, the lipids at 0.9 and 1.3 ppm are known to be potential means for separating certain tumor groups (see, *e.g.*, [172]). The baseline modeling of AQSES has not been used since it is not appropriate for HR-MAS data. However, we may reasonably think

that other baseline or lipid modeling might improve the classification accuracy in several classification problems.

Selecting the features (processing step) is more tricky for HR-MAS data than *in vivo* MRS data since the number of available features (number of points) and the number of visible and overlapping resonances are much larger, making methods like peak integration more sensitive to their initial parameters (peak intervals, etc). The interest of using peak integration instead of the whole spectrum is limited by the fact that the disturbing noise and artifacts are rather small in HR-MAS spectra, and averaging out these components will not be as important as in *in vivo* MRS. Magnitude spectra have been chosen to avoid phasing problems, which might result in poor performances of peak integration. The results show that the whole spectrum or AQSES should be preferred to peak integration. This contrasts with *in vivo* MRS where peak integration is often advised compared to other quantification methods like LCModel (see, *e.g.*, [250]).

Better classification accuracies are obtained with the non-linear kernel-based classification method LS-SVM than with LDA. Similar observations were noted in [65] for short echo time *in vivo* MRS. A good separation in general, and especially between GBM and MET, suggests that HR-MAS might be an interesting method as complement of *in vivo* MRS and MR imaging. Better results are generally obtained for GBM vs MET than GBM vs MEN, which contrast with the results in *in vivo* MRS (see, *e.g.*, [65]). This might be due to the strong reduction of lipids at 0.9 and 1.3 ppm by baseline correction, these lipids being not taken into account when using peak integration or AQSES.

Chapter 10

Conclusions and open problems

This last chapter reviews the main conclusions and original contributions of this thesis. More importantly it provides possible leads to improve brain tumor diagnosis.

10.1 General conclusions of the thesis

Although this thesis mainly focuses on quantification, it also studies preprocessing and classification techniques. A short overview of the main conclusions and contributions is given:

- In the first chapter, we focus on the attractive features of MRS for brain tumor diagnosis. Undoubtedly, MRS features may be a precious help in this domain. However, analyzing these data often requires a lot of time and expertise which are often not available in hospitals. Therefore, the developed methods must be automated and as fast as possible to avoid delaying diagnosis. The methods used in this thesis are described in Chapter 2.

- An extensive overview of the quantification methods has been given in Chapter 3. This overview not only outlines the advantages and the limitations of the quantification methods but also emphasizes on the main features, which are important for choosing an appropriate method regarding the data under investigation; among them, the domain of the method (time or frequency), the type of model (Lorentzian, Gaussian or Voigt), the robutsness of the method, the use of the variable projection algorithm. A key word in quantification is "prior knowledge". The more prior knowledge available, the more accurate the parameter estimates. Adding prior knowledge is a way to reduce the complexity of the problem and to increase the accuracy of the estimates. However, only satisfactory assumptions will actually improve the accuracy. MRS data tend to be more and more complicated (large number of overlapping peaks) due to higher electromagnetic field strengths, better instrumentation, etc. Using more prior knowledge becomes a necessity for MR quantification and appropriate methods allowing to incorporate prior knowledge are recommended. Another remark concerns the steps undertaken to obtain the parameter estimates. The number

of steps should be kept as small as possible to prevent error propagation. In any case, the choice of the quantification method depends on the pursued objectives.

- Chapter 4 reviews briefly the pattern recognition methods used in MRS and MRSI. A pattern recognition method combines a feature extraction method and a classification method. For both, the list of possible methods is huge. However, combining feature extraction and classification methods must be done carefully. For example, LDA will not be suitable for high dimensional data, contrarily to methods like LS-SVM, and therefore considering the magnitude of the points from the whole spectrum as input feature for the classifier will not be appropriate. Spectra, if considered as explanatory variables, are highly collinear and the number of these variables is large compared to the number of samples. In that case, standard methods (LDA, k-nearest-neighbors, regression) tend to result in overtrained and unstable classifiers. Little can be said about the best pattern recognition method since this often depends on the type of data (*e.g.*, short echo or long echo time), the tumor type, the location of the tumor, etc. However, several contributions show that the use of nonlinear classification methods are preferable to linear ones.

- Chapter 5 presents a quantification method, AQSES, which has several interesting features: it uses a database of metabolite profiles to incorporate more prior knowledge (especially interesting when metabolite spectra contain more than one peak), it uses an efficient algorithm (based on the variable projection algorithm) and models the baseline simultaneously with the metabolite signals to reduce the risk of error propagation, it also includes water filtering inside the optimization procedure to improve the accuracy of the parameter estimates since exactly the same filtering will be applied to both the signal to be processed and the metabolite profiles. However, the assumptions about the baseline seems to be too limited to obtain a good baseline model and, thus, good parameter estimates. Indeed, the only assumption in AQSES is the smoothness of the baseline in the frequency domain (spectrum). Additional prior knowledge could help to improve the current baseline estimation. We discuss this in Section 10.2.

- The influence of several solvent suppression methods has been investigated in Chapters 6 and 7. This includes the SVD-based technique HLSVD-PRO and the FIR filtering techniques MP-FIR or MP-FIR0. The results showed that FIR filtering techniques were faster and more accurate. Moreover, these methods can easily be incorporated into the optimization procedure contrarily to SVD-based methods. An important feature of MP-FIR and MP-FIR0 is that they increase the signal-to-baseline ratio such that the quantification algorithm is less affected by the baseline. However, this reduction of the baseline might be too severe if one is interested in the macromolecule signals. MP-FIR0 reduces the attenuation of the baseline but increases the attenuation of the nuisance components outside the frequency region of interest, when compared to MP-FIR. MP-FIR0 is recommended for signals without wide baseline overlapping the metabolites of interest in the frequency domain, such as in long echo time or *ex vivo* MRS data, since the components with large damping coefficients (rapidly decaying in the time domain) will be less attenuated. For signals

with wide baseline, *e.g.*, *in vivo* MR signals, the accuracy reached by MP-FIR and MP-FIR0 is similar when they are used inside an iterative optimization process.

- Several feature extraction methods, AQSES included, have been tested on short echo time MR data in Chapter 8. For these data, we confirmed the better behavior of non-linear classification techniques over linear ones. Quantification techniques such as AQSES and QUEST were not the most successful feature extraction methods. This seems to indicate that methods based on mathematical features are more powerful than quantification methods for classification purposes (when used as input features). Moreover, these methods are generally faster than quantification methods. Either the information extracted by quantification methods is not optimal for classification or the studied quantification methods were not accurate enough. The second possibility may be realistic due to the complexity of MR signals, especially when those contain a large baseline, which is the case in short echo time MR data. Prior knowledge may also be insufficient or inappropriate.

- Chapter 9 shows that more complex data, like HR-MAS data, can be handled with methods commonly used with *in vivo* MR data. However, the fitting of such signals becomes more complex and larger residuals are often observable. This chapter also shows the potential of HR-MAS to complete *in vivo* MRS in brain tumor diagnosis.

10.2 Future work and open problems

Further research is necessary in the field of Magnetic Resonance processing. The ultimate goal is to develop an automated decision support system for brain tumor diagnosis. Obviously, some classification problems remain very hard to handle with MRS data (*e.g.*, glioblastoma versus metastasis). In order to improve diagnosis, several ways can be followed: developing new methods, using more prior knowledge, using new data or a combination of data (also called data fusion).

- **Simulated data.** A recurrent criticism in papers about MR quantification is that the simulated signals are too simplistic and do not sufficiently mimic true *in vivo* MR signals. The chosen lineshape is often purely Lorentzian, Gaussian or Voigt without additional artefacts. In order to take the Eddy current (EC), which influences the lineshape, into account, Rabeson *et al.* [221] have recently proposed to use a function of the form

$$y_{EC}(t) = y_0(t)e^{j\Phi_{EC}(t)} \tag{10.1}$$

where $y_{EC}(t)$ is the signal at time t distorted by EC effects, $y_0(t)$ the original signal and $\Phi_{EC}(t)$ the time-dependent phase shift, which is defined by

$$\Phi_{EC}(t) = \sum_{l=1}^{L} a_l e^{-d_l t}, \tag{10.2}$$

where a_l, d_l are real-valued numbers, L is an integer. However, other phenomena can distort the lineshape and not only a phase distortion should be applied to the signal. Space-dependent field distortions should also be created to mimic genuine

signals. In that regard, two possible distortion shapes have been proposed: the triangle shape and the combined Lorentzian-Gaussian shape (one half Lorentzian, the other half Gaussian). Both methods can be followed by some smoothing techniques to avoid discontinuities in the signal. The triangle lineshape has been recently tested by Osorio *et al.* [207].

Many quantification papers do not even take the water peak into consideration, while the water can also be a source of inaccurate parameter estimates. The water peak shape of *in vivo* water-saturated MR signals is unpredictable. Hence it is difficult to simulate such water resonances. However, it is possible to extract the water resonances from *in vivo* (or *ex vivo*) MR signals by executing the following steps: 1) select MRS signals for which a good lineshape correction is possible using one of the classical methods, i.e. ECC [138], QUALITY [58] or QUECC [13] and apply this method on the MRS data, 2) filter the water resonances using an SVD-based method (HLSVD-PRO [152] is advised for its performances in terms of accuracy and efficiency), and 3) reconstruct the denoised water resonances using the resonances estimated by the SVD-based method.

Another major problem when simulating *in vivo* MR signals is how to generate the baseline contributions, which includes baseline distortion and macromolecular signals as mentioned in Chapter 3. Baseline distortion is often achieved by distorting the first points in an FID (see, *e.g.*, [94]) giving rise to a rolling baseline in the frequency domain. The macromolecular signals are more complicated to simulate since they may vary a lot in *in vivo* signals, depending for example on the location of the tumor or on the tumor type. Recent papers [213, 226] generally use Gaussian peaks to simulate the macromolecular signals (see, *e.g.*, [242] for possible parameter values). Generating these signals is also possible by using an inversion-recovery sequence or by measuring macromolecular components *in vitro* (phantom measurement).

Other effects can also be simulated such as a nonideal shimming or a not perfectly centered VOI. These effects can be generated on purpose and extracted by comparing the ideal case with the wrong one.

When classifying *in vivo* signals, normalizing the data becomes necessary except if ratios of metabolite concentrations are considered (for example Cho/Cr, NAA/Cr, etc). In general, normalizing MR data is done either by using the quadratic norm or by using the intensity of water (see Chapter 2). Devos [64] notes that the overall performance of water normalization is worse. When simulating data mimicking *in vivo* MR signals, one should take into account the inter patient variability and intra patient variability (variability due to the tissue type, the tissue location, etc). Otherwise, the normalization effects will not appear in the classification results.

- **Additional prior knowledge for quantification.** In MR quantification, two main problems show up: the lineshape and the baseline as discussed in Chapter 3. Further research in that field should be focussed on how to model them. Recent publications proposed to generate macromolecule profiles from measurement [169, 242, 148, 114, 7, 168, 208] or from theoretical considerations [117] and to add them to the database of metabolites. Although they generally concluded that more accurate parameter estimates could be obtained, this should be further investigated since little is known

about the macromolecule profiles in brain tumor tissue. Although the amplitude of the macromolecule contributions may vary a lot between MR spectra, the macromolecule resonances are located at known frequencies. This characteristic should be exploited in quantification methods of short echo time MR data.

The lineshape of *in vivo* MR signals is also generally difficult to predict and is never purely Lorentzian. In general, lineshape correction methods (see Section 3.6.1) enables to obtain a satisfactory lineshape, *i.e.*, sufficiently close to the Lorentzian lineshape. However, these methods require the acquisition of an additional water signal, which prolongs the acquisition time. To avoid this additional acquisition, one may only acquire the water-unsupressed signal, which becomes competitive thanks to high-resolution analog-to-digital converters (see Section 3.6.2). Processing such signals requires to adapt the methods used for water-suppressed signals. This may also lead to new algorithms. If only water-suppressed signals are available, one can try to estimate the lineshape based on this signal. Osorio *et al.* [207], extending the method presented by Rabeson *et al.* in [221], have recently proposed an iterative method for estimating the lineshape, based on the assumption that each peak in the spectrum follows the same lineshape. In other words, they assume that the lineshape is mainly dominated by the inhomogeneity of the electromagnetic field, not by the relaxation times T_2 of the metabolites. However, the algorithm is not stable at low signal-to-noise ratio and further investigation is necessary.

- **Spatial information.** In 2001, De Edelenyi *et al.* invents the term "nosologic images". Since then, several contributions have considered the spatial information in MRSI data. The common hypothesis is that two adjacent voxels resemble each other in terms of metabolite concentration. Due to the relatively low resolution of MRSI data and the heterogenity of the voxels, this resemblance is limited. As additional information, one can use MRI images to estimate to what extent two adjacent voxels should resemble each other. This depends on the location of the voxels and the tissue type of each voxel. The spatial information can be exploited in MR quantification to prevent the optimization algorithm to converge toward a wrong local mimimum. Kelm [133] proposed to add an additional term in the cost function which insures a certain smoothness in the parameter estimates, with a new regularization factor which finds a trade-off between the squared errors and the smoothness of the parameters. MRI images can help to decide how close should be the parameters of two adjacent voxels. Moreover, a weighting matrix defines to what extent a surrounding voxel influences the voxel under investigation. For example, two adjacent voxels, one with glioblastoma tissue and the other with healthy tissue, should not influence each other in the parameter estimation. Hence, a small weight (since the voxels are never perfectly homogeneous) will be assigned to the surrounding voxel. A quantification method such as AQSES can also be used where the initial values for the damping coefficients and the frequencies are adapted with respect to the values of the surrounding voxels. Spatial information can also be used in classification. Laudadio *et al.* [153] proposed to use CCA based on 3×3 spatial models. Here again, MRI can help to improve the spatial model, giving more weight to the voxels with similar tissue type and similar location. A prior tissue segmentation is also possible to reduce the computation to the voxels in the tumoral and peritumoral region.

This has been done, for instance, by Luts *et al.* [166], who first perform a tissue segmentation and then classify only the voxels located in the (peri)tumoral region. They tested different classification methods, Bayesian least squares support vector machines (LS-SVMs) using pairwise coupling [165], multiclass kernel logistic regression and even CCA, but did not adapt the spatial models used by CCA from the MRI information (segmentation). A particular interest has recently arisen for the differentiation between glioblastoma and metastasis based on the tumor infiltration, glioblastoma being a much more infiltrative tumor. This kind of information is essential since MRI or MRSI fail to differenciate them when based on a voxel-per-voxel approach. Fan *et al.* [80] have also identified some ratios (Cho/Cr, Myo/Cr and Glu-n/Cr should be higher for glioblastoma) that may help to distinguish between glioblastoma and metastasis. Cho/Cr and Glu-n/Cr should also be higher for glioblastoma in the peritumoral region.

- **Fusion of several MR modalities.** As shown in the literature, MRS or MRSI can improve the classification results. But other modalities are now available. First, several MRI modalities such as diffusion- and perfusion-weighted MRI and functional MRI have gained much interest these last years. Second, *ex vivo* techniques such as HR-MAS have also shown their value in brain tumor diagnosis. Furthermore, higher fields are now used (3T, 7T) for *in vivo* experiments, improving both the SNR and the spectral resolution. Next, clinical information (sex, age, etc) is also recognized to be important. Intuitively, extra relevant information (anatomical, clinical or metabolic information) may improve the diagnosis. On the other hand, the fusion of several MR techniques will increase the importance of the feature extraction method, which needs to extract only the relevant parameters. It is recommended then to use methods able to inform about the percentage of contribution of each input feature to the classification.

Appendix A

AQSES GUI

The AQSES framework

To increase the usability, AQSES has been embedded in an application framework which controls the optimization method [62]. In general, an application framework provides a set of abstract classes and interfaces, called hot spots that can be combined to create an application. For AQSES, the framework provides hot spots for plug-ins to read or write, to preprocess, to quantitate, to export and to visualize MRS and MRSI data. The software is developed in Java and is platform independent (*e.g.*, Windows, Linux, OSX and Solaris). The graphical user interface (GUI) of the framework is written using the Swing library. AQSES and the HLSVD-PRO algorithms are implemented in FORTRAN 77. Both methods have been compiled for Windows and Linux and have been made accessible to the Java code, to make sure that the software can run on both platforms. The main optimization part of AQSES is carried out using an extension of the Levenberg-Marquardt algorithm, which accepts linear bounds constraints, in the DN2GB implementation written by David M. Gay [91]. FORTRAN is used since well-tested and optimized numerical libraries (*e.g.*, LAPACK, Blas) exist.

At the moment the AQSES GUI accepts MRS and MRSI data coming from

- Philips (SDAT/SPAR format),
- SIEMENS (RDA format),
- Matlab (The MathWorks, inc., Version 4) and
- text files.

It is easy to add plug-ins to read or write other formats such as DICOM by implementing some of the hot spots. After loading, the data can be visualized in the time or frequency domain and is presented to the user in a 3D graph. It is also possible to work with multiple data sets at the same time, which are stored in projects.

The AQSES GUI offers two types of projects, one called *AQSES database creator* to create personal databases, and another called *MRS* to process the signals. Any metabolite

profile can be loaded in the database. There is no restriction about the acquisition protocol or about the number of metabolite profiles in the database. All preprocessing tools are available in both projects, while the quantification methods are only available in the *MRS* project. The preprocessing methods included at the moment in AQSES GUI are

- Eddy current correction (Klose [138]),
- HLSVD-PRO [152],
- zero filling,
- point truncation, and
- manual phase and frequency correction.

The quantification methods available in the AQSES GUI at the moment are

- AQSES and
- HLSVD-PRO.

AQSES and HLSVD-PRO are the only methods in AQSES GUI whose codes are not open source. AQSES incorporates model functions with three possible lineshapes (Lorentzian, Gaussian and Voigt). Although this is implemented in the FORTRAN code, the user has presently only access via AQSES GUI to the Lorentzian lineshape, since the Gaussian and Voigt lineshapes have not been fully tested yet. The Eddy current correction term discussed in section Section 2.3.1 is also not available yet in AQSES GUI. Therefore, one should use some preprocessing methods (phase correction, Eddy current correction, etc) before applying AQSES. However, these preprocessing techniques might not be recommendable if the basis set of metabolite profiles and the MR spectra were acquired with the same acquisition protocol such that it is reasonable to assume that they have undergone the same pattern of distortions.

The AQSES GUI is template driven, which means that scripts can be built that contain the settings for preprocessing and quantification. Templates can be written from scratch or generated automatically in AQSES GUI when processing the signals. These templates can be saved and used to easily redo experiments or to start processing in batch mode. The GUI is intended to run in two different modes. The *clinical mode* hides most of the complexity by using templates, while the *research mode* provides the user with all features. In the *clinical mode*, the user is restricted to

- load, read, visualize and save data,
- process data **using existing templates**,
- visualize and save results.

The results of the quantification methods are visualized in a separate window and can be exported to a Matlab file.

The database used in Chapter 5

The *in vitro* metabolite profiles in this paper have been acquired on a 1.5 T Philips NT Gyroscan using a PRESS sequence with an echo time of 23 ms, and a PRESS box of $2 \times 2 \times 2\,\mathrm{cm}^3$. To each sample, two reference compounds were added, situated at 0.0 ppm (3-trimethylsilyl-1-propane-sulfonic acid or TSPS) and at 8.44 ppm (formate). One buffer solution of K2HPO4 and KH2PO4 was made including TSPS, formate, phosphate buffer compounds (except for the choline metabolite solutions) and NaOH for pH adjustment (brought to 7.2 pH). The solution was divided in small identical quantities, in which the relevant metabolites were dissolved. All raw FIDs were Eddy current corrected using Klose's method in the "Database Creator" of the AQSES GUI, and the spectra were frequency shifted such that the second reference peak was at 8.44 ppm. All profiles were normalized or scaled with respect to the 8.44 ppm resonance in the sample of creatine, to ensure that absolute comparison between metabolites is possible. This was done as follows. All spectra were first filtered with HLSVD-PRO to keep only the reference peaks at 8.44 ppm. These were fitted using AQSES with the one of the creatine profile. Each metabolite profile was then normalized with respect to the amplitudes obtained in AQSES since the metabolite profiles should have the same reference peak at 8.44 ppm, its concentration being identical for all metabolite solutions. All spectra were finally normalized with respect to the concentration in the sample during the acquisition, the metabolite concentration being different from one metabolite solution to another. Metabolite profiles of lipids at 1.3 ppm and 0.9 ppm have been artificially created from the creatine resonance. Therefore, absolute values of these metabolites cannot be compared with the other metabolites. Their simulation was performed by removing the creatine signal from the spectrum with HLSVD-PRO, followed by addition of a single resonance at 1.3 or 0.9 ppm. Finally, all metabolite profiles have been processed by HLSVD-PRO (from 4.4 ppm to 7.0 ppm) to remove the residual water resonance and some artifacts within that region. As example, the N-acetylaspartate (NAA) profile is plotted in Figure A.1.

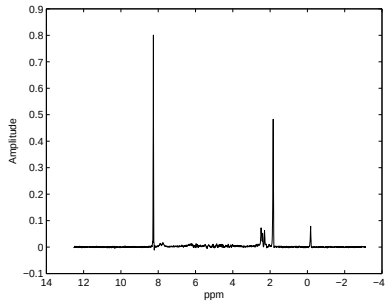


Figure A.1. *NAA profile used in the basis set. The amplitudes are in arbitrary units. At 0.0 ppm and 8.44 ppm, the two reference compounds are visible. They are effectively removed by the FIR filter during quantification.*

At present, two databases are available online from
`www.esat.kuleuven.ac.be/sista/members/biomed/new/`:

Database 1: 16 metabolite profiles acquired on a 1.5 T Philips NT Gyroscan using a PRESS sequence with an echo time of 23 ms, and a PRESS box of $2 \times 2 \times 2\,\mathrm{cm}^3$ + simulated profiles for Lip1 and Lip2.

Database 2: 16 metabolite profiles acquired on a 1.5 T Siemens using a STEAM sequence with an echo time of 20 ms, and a STEAM box of $2 \times 2 \times 2\,\mathrm{cm}^3$ + simulated profiles for Lip1 and Lip2.

A document is also available, which describes the generation and the preprocessing of these databases. Note that AQSES can be combined with any other database, either generated via simulation or by in vitro acquisition. The databases given here are just representative examples.

Appendix B

Least squares cost function in MPFIR0, Eq. (7.8)

We want to minimize the least squares cost function:

$$\min_{H} \sum_{f_l=f_1}^{f_L} \left(H(f_l,d) - T(f_l)\right)^2 \tag{B.1}$$

$$\min_{H_2} \sum_{f_l=f_1}^{f_L} \left(H_1(f_l,d)H_2(f_l,d) - T(f_l)\right)^2 \tag{B.2}$$

$$\min_{H_2} \sum_{f_l=f_1}^{f_L} H_1^2(f_l,d)\left(H_2(f_l,d) - \frac{T(f_l)}{H_1(f_l,d)}\right)^2 \tag{B.3}$$

$$\min_{h_2} \sum_{f_l=f_1}^{f_L} H_1^2(f_l,d)\left(\sum_{m=0}^{M-1} h_2(m)e^{(d-j2\pi f_l)m} - \frac{T(f_l)}{H_1(f_l,d)}\right)^2 \tag{B.4}$$

This yields in matrix notation,

$$G^H W G h_2 = G^H W T_{H_1}, \tag{B.5}$$

and finally gives Eq. (7.8). The inverse of the matrix $G^H W G$ may generate numerical problems depending on the step between two adjacent points of the grid, (f_l, d) and (f_{l+1}, d), $l = 1, \ldots, L-1$. $A = G^H W G$ is an Hermitian matrix, which means that $A^H = A$. Indeed, all the elements $W_{i,i}$ of W are real positive since $H_1(f_l, d)$ is real for all f_l due to the fact that each zero has its conjugate (see step 4 in the algorithm), and the diagonal elements of A are real positive. With a step of 0.001, the experiments showed that A was positive definite (all eigenvalues are positive) and therefore invertible. In that case, the Cholesky decomposition is recommended to solve the least squares problem. In case of very small steps, A becomes ill-conditioned and orthogonalization techniques may be needed. One satisfactory method is the row-oriented modified gram-schmidt method with reorthogonalization proposed by Dax [55]. The condition number of A can be computed in order to select the right method to solve the least squares problem.

Other numerical problems can occur when the distance between the selected zeros z_r and the points of the grid (f_l, d), $l = 1, \ldots, L$ is too small since in that case $H_1(f_l, d)$ will be close to 0 and $\frac{T(f_l)}{H_1(f_l,d)}$ close to ∞. Choosing grid points too far away from the zeros z_r will generate large ripples in the region where no constraints are imposed (between z_r and the grid points).

Appendix C

SPID: Simulation Package based on *In vitro* Databases

The goal of SPID is to provide the user with tools capable to **simulate**, **preprocess**, **process** and **classify** *in vivo* and *ex vivo* MRS signals. These tools are embedded in a matlab graphical user interface (**GUI**). (Pre)processing and classification methods can be automatically run in a row using the matlab command line (**batch mode**). The command line will be preferred when running automatic procedure on large data sets, while the GUI is more appropriate for checking the results of the different steps of the procedure.

Files saved in a .mat format from the JAVA version of AQSES-GUI can be loaded in SPID. Pluging in new tools in SPID is much simpler than in the JAVA version of AQSES (AQSES-GUI) [62] since it is based on a higher programming language level (i.e., Matlab instead of JAVA and FORTRAN). Moreover, SPID contains many more methods than AQSES-GUI and can be used as well for testing new methods as for comparing existing ones. Most of the parameters are fixed in AQSES-GUI while they can be tuned in SPID, making SPID much more flexible.

Download:

SPID v0.1 on http://homes.esat.kuleuven.be/∼biomed/

Readable format:

- .mat format from SPID (see manual)
- .mat format from the JAVA version of AQSES-GUI
- .txt format from jMRUI3.0
- sdat, spar from Philips

Preprocessing methods:

- signal alignment (frequency domain)
- resampling (increase or decrease the resolution)
- truncation of the begin or end points
- eddy current correction with Klose's method
- Lineshape correction with QUALITY method (slightly adapted)
- Water filtering (solvent suppression) with MP-FIR, MP-FIR0 or HLSVD-PRO

- Manual phase correction
- Automatic phase correction based on [44]
- L2-normalization
- ERETIC normalization (using a reference ERETIC signal)
- Baseline correction using an apodization function
- Baseline offset correction
- Rolling baseline correction using an adapted version of Golotvin's method
- Zero filling
- SNR improvement using an apodization function
- Denoising using wavelets
- Denoising using moving average filter

Processing methods:

- Quantification with HLSVD-PRO
- AMARES (linux only)
- AQSES (with the QUEST Subtract method)
- AQSES
- Whole spectrum restricted to the frequency region of interest
- Peak integration
- Peak bucketting or binning
- Fisher Criterion
- Kruskall-Wallis
- Relief-F
- PCA
- Fast-ICA (http://www.cis.hut.fi/projects/ica/fastica/)
- Dimensionality reduction toolbox (http://www.cs.unimaas.nl/l.vandermaaten)
- Scale normalizing

Classification:

- LS-SVM (http://www.esat.kuleuven.ac.be/sista/lssvmlab/
- Kernel Logistic Regression
- LDA
- Multi Layer Perceptron (http://www.ncrg.aston.ac.uk/netlab/)
- Clustering Methods

Requirements:

Run on any platform with version of Matlab 7.0 or higher.

Installation:

No specific installation is required (only matlab files).

Available databases:

DB1: Measured database of metabolite profiles The database is collected at the Philips NT

Gyroscan 1.5 Acquisition method: PRESS Echo time (TE): 23 ms Volume PRESS box: 2x2x2 cm (obtained from SPAR file)
DB2: Simulated database at 11.4T, 600 MHz, step=0.1392, TE=30 ms

User manual:
A user's manual is available in the directory "Readme_doc" under the name "Manual-SPID.pdf". General info about the content of the different directories is available in the txt file "Readme.txt" (in $SPID).

Bibliography

[1] *International network for pattern of tumours using magnetic resonance*.

[2] F. ABILGAARD, H. GESMAR, AND J. LED, *Quantitative analysis of complicated nonideal Fourier transform NMR spectra*, J. Magn. Reson. A, 79 (1988), pp. 78–89.

[3] M. ALA-KORPELA, Y. HILTUNEN, J. JOKISAARI, S. ESKELINEN, K. KIVINIITY, M. J. SAVOLAINEN, AND Y. A. KESÄNIEMI, *A comparative study of ^1H NMR lineshape fitting analyses and biochemical lipid analyses of the lipoprotein fractions VLDL, LDL and HDL, and total human blood plasma.*, NMR Biomed., 6 (1993), pp. 225–233.

[4] A. ALDROUBI AND M. UNSER, *Wavelets in Medicine and Biology*, CRC Press, Boca Raton, FL, 1996.

[5] J. P. ANTOINE, C. CHAUVIN, AND A. CORON, *Wavelets and related time-frequency techniques in magnetic resonance spectroscopy*, NMR Biomed., 14 (2001), pp. 265–70.

[6] J. P. ANTOINE, A. CORON, AND J. M. DEREPPE, *Water peak suppression: time-frequency vs time-scale approach*, J. Magn. Reson., 144 (2000), pp. 189–194.

[7] D. P. AUER, C. GOSSL, T. SCHIRMER, AND M. CZISCH, *Improved analysis of ^1H-MR spectra in the presence of mobile lipids*, Magn. Res. Med., 46 (2001), pp. 615–18.

[8] D. AXELSON, I. J. BAKKEN, I. S. GRIBBESTAD, B. EHRNHOLM, G. NILSEN, AND J. AASLY, *Applications of neural network analyses to in vivo ^1H magnetic resonance spectroscopy of Parkinson disease patients*, J. Magn. Reson. Imaging, 16 (2002), pp. 13–20.

[9] D. BARACHE, J. P. ANTOINE, AND J. M. DEREPPE, *The continuous wavelet transform, an analysis tool for NMR spectroscopy*, J. Magn. Reson., 144 (2000), pp. 189–194.

[10] P. B. BARKER, B. J. SOHER, S. J. BLACKBAND, J. C. CHATHAM, V. P. MATHEWS, AND R. N. BRYAN, *Quantitation of proton NMR spectra of the human brain using tissue water as an internal concentration reference*, NMR Biomed., 6 (1993), pp. 89–94.

[11] H. BARKHUIJSEN, R. DE BEER, W. M. BOVEE, J. H. CREYGHTON, AND D. VAN ORMONDT, *Application of linear prediction and singular value decomposition (LPSVD) to determine NMR frequencies and intensities from the FID*, Magn. Reson. Med., 2 (1985), pp. 86–9.

[12] H. BARKHUIJSEN, R. DE BEER, AND D. VAN ORMONDT, *Improved algorithm for noniterative time-domain model fitting to exponentially damped magnetic resonance signals*, J. Magn. Reson., 73 (1987), pp. 553–57.

[13] R. BARTHA, D. J. DROST, R. S. MENON, AND P. C. WILLIAMSON, *Spectroscopic lineshape correction by QUECC: combined QUALITY deconvolution and eddy current correction*, Magn. Reson. Med., 44 (2000), pp. 641–5.

[14] R. BARTHA, D. J. DROST, AND P. C. WILLIAMSON, *Factors affecting the quantification of short echo in-vivo ^1H MR spectra: prior knowledge, peak elimination, and filtering*, NMR Biomed., 12 (1999), pp. 205–16.

[15] S. J. BARTON, F. A. HOWE, A. M. TOMLINS, S. A. CUDLIP, J. K. NICHOLSON, B. A. BELL, AND J. R. GRIFFITHS, *Comparison of in vivo ^{1}H MRS of human brain tumours with ^{1}H HR-MAS spectroscopy of intact biopsy samples in vitro*, Magn. Reson. Mater. Phys., Biol. Med., 8 (1999), pp. 121–28.

[16] R. BEGG, J. KAMRUZZAMAN, AND R. SARKER, *Neural Networks in Healthcare: potential and challenges*, Idea Group Publishing, 2006.

[17] K. L. BEHAR, D. L. ROTHMAN, D. D. SPENCER, AND O. A. PETROFF, *Analysis of macromolecule resonances in ^{1}H NMR spectra of human brain*, Magn. Reson. Med., 32 (1994), pp. 294–302.

[18] D. BELKIC AND K. BELKIC, *The fast Padé transform in magnetic resonance spectroscopy for potential improvements in early cancer diagnostics*, Phys. Med. Biol., 50 (2005), pp. 4385–408.

[19] C. M. BISHOP, *Pattern Recognition and Machine Learning*, Springer Science+Business, New-York: Wiley, 2006.

[20] A. BLUM AND P. LANGLEY, *Selection of relevant features and examples in machine learning*, Artif. Intell., 97 (1997), pp. 245–271.

[21] L. BREIMAN, *Bagging predictors*, Mach. Learn., 24(2) (1996), pp. 123–140.

[22] ———, *Random forests*, Mach. Learn., 45 (2001), pp. 5–32.

[23] G. L. BRETTHORST, W. HUTTON, J. GARBOW, AND J. H. ACKERMAN, *Exponential parameter estimation (in NMR) using Bayesian probability theory*, Concepts Magn. Reson. Part A, 27A (2005), pp. 55–63.

[24] ———, *Exponential parameter estimation (in NMR) using Bayesian probability theory*, Concepts Magn. Reson. Part A, 27A (2005), pp. 64–72.

[25] J. C. BROOKS, N. ROBERTS, G. J. KEMP, P. A. MARTIN, AND G. H. WHITEHOUSE, *Magnetic resonance imaging-based compartmentation and its application to measuring metabolite concentrations in the frontal lobe*, Magn. Reson. Med., 41 (1999), pp. 883–888.

[26] D. E. BROWN, *Fully automated baseline correction of 1D and 2D NMR spectra using Bernstein polynomials*, J. Magn. Reson. A, 114 (1995), pp. 268–70.

[27] I. M. BURTSCHER, G. SKAGERBERG, B. GEIJER, E. ENGLUND, F. STAHLBERG, AND S. HOLTAS, *Proton MR spectroscopy and preoperative diagnostic accuracy: an evaluation of intracranial mass lesions characterized by stereotactic biopsy findings*, Am. J. Neuroradiol., 21 (2000), pp. 84–93.

[28] S. E. BYRD, T. TOMITA, P. S. PALKA, C. F. DARLING, J. P. NORFRAY, AND J. FAN, *Magnetic resonance spectroscopy (MRS) in the evaluation of pediatric brain tumors, part II: Clinical analysis*, J. Natl. Med. Assoc., 88 (1996), pp. 717–723.

[29] E. CABANES, S. CONFORT GOUNY, Y. LE FUR, G. SIMOND, AND P. J. COZZONE, *Optimization of residual water signal removal by HLSVD on simulated short echo time proton MR spectra of the human brain*, J. Magn. Reson., 150 (2001), pp. 116–25.

[30] D. CALVETTI, L. REICHEL, AND D. SORENSEN, *An Implicitly Restarted Lanczos Method for Large Symmetric eigenvalue problems*, Electron. T. Numer. Ana., 2 (1994), pp. 1–21.

[31] J.-F. CARDOSO AND A. SOULOUMIAC, *Blind beamforming for non gaussian signals*, IEEE Proc. F. Radar and Signal Processing, 140 (1993), pp. 362–370.

[32] M. CASTILLO, J. K. SMITH, AND L. KWOCK, *Correlation of myo-inositol levels and grading of cerebral astrocytomas*, Am. J. Neuroradiol., 21 (2000), pp. 1645–49.

[33] R. CAURANA AND D. FREITAG, *Greedy attribute selection*, in Proceedings of the Eleventh International Conference on Machine Learning, New Brunswick, NJ, 1994, pp. 28–36.

[34] S. CAVASSILA, S. DEVAL, H. C., D. VAN ORMONDT, AND D. GRAVERON-DEMILLY, *The beneficial influence of prior knowledge on the quantitation of in vivo magnetic resonance spectroscopy signals*, Invest. Radiol., 34 (1999), pp. 242–246.

[35] S. CAVASSILA, S. DEVAL, C. HUEGEN, D. VAN ORMONDT, AND D. GRAVERON-DEMILLY, *Cramér-Rao bound expressions for parametric estimation of overlapping peaks: influence of prior knowledge*, J. Magn. Reson., 143 (2000), pp. 311–20.

[36] ———, *Cramér-Rao bounds: an evaluation tool for quantitation*, NMR Biomed., 14 (2001), pp. 278–83.

[37] S. CAVASSILA, B. FENET, A. VAN DEN BOOGAART, C. REMY, A. BRIGUET, AND D. GRAVERON DEMILLY, *ER-Filter: a preprocessing technique for frequency-selective time-domain analysis*, J. Magn. Reson. Anal., 3 (1997), pp. 87–92.

[38] M. CEDERVALL, P. STOICA, AND R. MOSES, *Mode-type algorithm for estimating damped, undamped or explosive modes*, Circ. Syst. Signal Process., 16 (1997), pp. 349–362.

[39] M. C. CHAMBERLAIN AND P. A. KORMANIK, *Practical guidelines for the treatment of malignant gliomas*, West. J. Med., 168 (1998), pp. 114–120.

[40] K. H. CHANG, I. C. SONG, S. H. KIM, M. H. HAN, H. D. KIM, S. O. SEONG, H. W. JUNG, AND M. C. HAN, *In vivo single-voxel proton MR spectroscopy in intracranial cystic masses*, Am. J. Neuroradiol., 19 (1998), pp. 401–405.

[41] H. CHEN, S. VAN HUFFEL, C. DECANNIERE, AND P. VAN HECKE, *A signal enhancement algorithm for time-domain data MR quantification*, J. Magn. Reson. A, 109 (1994), pp. 46–55.

[42] H. CHEN, S. VAN HUFFEL, D. VAN ORMONDT, AND R. DE BEER, *Parameter estimation with prior knowledge of known signal poles for the quantification of NMR spectroscopy data in the time domain*, J. Magn. Reson. A, 119 (1996), pp. 225–34.

[43] H. CHEN, S. VAN HUFFEL, AND J. VANDEWALLE, *Improved methods for exponential parameter estimation in the presence of known poles and noise*, IEEE T. Signal Proces., 45 (1997), pp. 1390–1393.

[44] L. CHEN, Z. WENG, L. GOH, AND M. GARLAND, *An efficient algorithm for automatic phase correction of NMR spectra based on entropy minimization*, J. Magn. Reson., 158 (2002), pp. 164–68.

[45] S. CHEN, T. J. SCHAEWE, R. TEICHMAN, M. I. MILLER, S. NADEL, AND A. GREENE, *Parallel algorithms for maximum-likelihood nuclear magnetic resonance spectroscopy*, J. Magn. Reson. A, 102 (1993), pp. 16–23.

[46] L. L. CHENG, D. C. ANTHONY, A. R. COMITE, P. M. BLACK, A. A. TZIKA, AND R. G. GONZALEZ, *Quantification of microheterogeneity in glioblastoma multiforme with ex vivo high-resolution magic-angle spinning (HRMAS) proton magnetic resonance spectroscopy*, Neuro-oncol., 2 (2000), pp. 87–95.

[47] W. C. W. CHU, K.-W. CHIK, Y.-L. CHAN, D. K. W. YEUNG, D. J. ROEBUCK, R. G. HOWARD, C.-K. LI, AND C. METREWELI, *White matter and cerebral metabolite changes in children undergoing treatment for acute lymphoblastic leukemia: longitudinal study with MR imaging and ^1H MR spectroscopy*, Radiology, 229 (2003), pp. 659–669.

[48] R. A. CHYLLA AND J. L. MARKLEY, *Theory and application of the maximum likelihood principle to NMR parameter estimation of multidimensional NMR data*, J. Biomol. NMR, 5 (1995), pp. 245–258.

[49] D. B. CLAYTON, M. A. ELLIOTT, J. S. LEIGH, AND R. E. LENKINSKI, *^{1}H spectroscopy without solvent suppression: characterization of signal modulations at short echo times*, J. Magn. Reson., 153 (2001), pp. 203–209.

[50] J. C. COBAS, M. A. BERNSTEIN, M. MARTIN-PASTOR, AND P. GARCIA TAHOCES, *A new general-purpose fully automatic baseline-correction procedure for 1D and 2D NMR data*, J. Magn. Reson., 183 (2006), pp. 145–151.

[51] Y. COENRADIE, R. DE BEER, D. VAN ORMONDT, S. CAVASSILA, H. RATINEY, AND D. GRAVERON-DEMILLY, *Background-signal parametrization in in vivo MR spectroscopy*, MAGMA, 15 (2002), p. 369.

[52] A. CORON, L. VANHAMME, J. ANTOINE, P. VAN HECKE, AND S. VAN HUFFEL, *The filtering approach to solvent peak suppression in MRS: a critical review*, J. Magn. Reson., 152 (2001), pp. 26–40.

[53] K. J. CROSS, *Improved digital filtering technique for solvent suppression*, J. Magn. Reson. A, 101 (1993), pp. 220–24.

[54] C. CUDALBU, S. CAVASSILA, H. RABESON, D. VAN ORMONDT, AND D. GRAVERON-DEMILLY, *Influence of measured and simulated basis sets on metabolite concentration estimates*, NMR Biomed., 21(6) (2008), pp. 627–636.

[55] A. DAX, *A modified Gram-Schmidt algorithm with iterative orthogonalization and column pivoting*, Linear Algebra and its Applications, 310 (2000), pp. 25–42.

[56] R. DE BEER AND D. VAN ORMONDT, *NMR basic principles and progress*, vol. 26, Springer, 1992.

[57] C. DE BOOR, *A Practical Guide to Splines*, Applied Mathematical Sciences, New York: Springer, Berlin, 1978.

[58] A. A. DE GRAAF, *QUALITY: quantification improvement by converting lineshapes to the Lorentzian type*, Magn. Reson. Med., 13 (1990), pp. 343–57.

[59] A. A. DE GRAAF AND W. M. BOVÃL'E, *Improved quantification of in vivo ^{1}H NMR spectra by optimization of signal acquisition and processing and by incorporation of prior knowledge into the spectral fitting*, Magn. Reson. Med., 15 (1990), pp. 305–319.

[60] R. A. DE GRAAF AND D. L. ROTHMAN, *In vivo detection and quantification of scalar coupled ^{1}H NMR resonances*, Conc. Magn. Res., 13 (2001), pp. 32–76.

[61] R. A. DE GRAAF, A. VAN KRANENBURG, AND K. NICOLAY, *Off-resonance metabolite magnetization transfer measurements on rat brain in situ*, Magn. Reson. Med., 41 (1999), pp. 1136–1144.

[62] B. DE NEUTER, J. LUTS, L. VANHAMME, P. LEMMERLING, AND S. VAN HUFFEL, *Java-based framework for processing and displaying short-echo-time magnetic resonance spectroscopy signals*, Computer Methods and Programs in Biomedicine, 85 (2007), pp. 129–137.

[63] M. DE VOS, T. LAUDADIO, A. W. SIMONETTI, A. HEERSCHAP, AND S. VAN HUFFEL, *Fast nosologic imaging of the brain*, J. Magn. Reson., 184 (2007), pp. 292–301.

[64] A. DEVOS, *Quantification and classification of magnetic resonance spectroscopy data and applications to brain tumor recognition*, PhD thesis, Katholieke Universiteit Leuven, Leuven, Belgium, 2005.

[65] A. DEVOS, L. LUKAS, J. A. K. SUYKENS, L. VANHAMME, A. R. TATE, F. A. HOWE, C. MAJOS, A. MORENO TORRES, C. VAN DER GRAAF, M. ARUS, AND S. VAN HUFFEL, *Classification of brain tumours using short echo time ^{1}H MR spectra*, J. Magn. Reson., 170 (2004), pp. 164–75.

[66] A. DEVOS, A. SIMONETTI, M. VAN DER GRAAF, L. LUKAS, J. SUYKENS, L. VANHAMME, L. BUYDENS, A. HEERSCHAP, AND S. VAN HUFFEL, *The use of multivariate MR imaging intensities versus metabolic data from MR spectroscopic imaging for brain tumour classification*, J. Magn. Reson., 173 (2005), pp. 218–228.

[67] W. DIETRICH, C. H. RUDEL, AND M. NEUMANN, *Fast and precise automatic baseline correction of one- and two-dimensional NMR spectra*, J. Magn. Reson., 91 (1991), pp. 1–11.

[68] T. DIETTERICH, *Machine learning research: Four current directions*, Artif. Intell. Magazine, 18 (1998), pp. 97–136.

[69] F. DIGENNARO AND D. COWBURN, *Parametric estimation of time-domain NMR signals using simulated annealing*, J. Magn. Reson., 96 (1992), pp. 582–588.

[70] E.-H. DJERMOUNE, M. TOMCZAK, AND P. MUTZENHARDT, *A new adaptive subband decomposition approach for automatic analysis of NMR data*, J. Magn. Reson., 169 (2004), pp. 73–84.

[71] I. DOLOGLOU, S. VAN HUFFEL, AND D. VAN ORMONDT, *Frequency-selective MRS data quantification with frequency prior knowledge*, J. Magn. Reson., 130 (1998), pp. 238–243.

[72] Z. DONG, W. DREHER, AND D. LEIBFRITZ, *Toward quantitative short-echo-time in vivo proton MR spectroscopy without water suppression*, Magn. Reson. Med., 55 (2006), pp. 1441–1446.

[73] F. S. D. EDELENYI, C. RUBIN, F. ESTÈVE, S. GRAND, M. DÉCORPS, V. LEFOURNIER, J. F. L. BAS, AND C. RÉMY, *A new approach for analyzing proton magnetic resonance spectroscopic images of brain tumors: nosologic images*, Nat. Med., 6 (2000), pp. 1287–1289.

[74] P. H. C. EILERS AND B. MARX, *Flexible smoothing with B-splines and penalties*, Stat. Sci., 11 (1997), pp. 89–121.

[75] W. EL-DEREDY, *Pattern recognition approaches in biomedical and clinical magnetic resonance spectroscopy: a review*, NMR Biomed., 10 (1997), pp. 99–124.

[76] M. A. ELLIOTT, G. A. WALTER, A. SWIFT, K. VANDENBORNE, J. C. SCHOTLAND, AND J. S. LEIGH, *Spectral quantitation by principal component analysis using complex singular value decomposition*, Magn. Reson. Med., 41 (1999), pp. 450–455.

[77] C. ELSTER, A. LINK, F. SCHUBERT, F. SEIFERT, M. WALZEL, AND H. RINNEBERG, *Quantitative MRS: comparison of time domain and time domain frequency domain methods using a novel test procedure*, Magn. Reson. Imaging, 18 (2000), pp. 597–606.

[78] C. ELSTER, F. SCHUBERT, A. LINK, M. WALZEL, F. SEIFERT, AND H. RINNEBERG, *Quantitative magnetic resonance spectroscopy: Semi-parametric modeling and determination of uncertainties*, Magn. Reson. Med., 53 (2005), pp. 1288–96.

[79] T. ETHOFER, I. MADER, U. SEEGER, G. HELMS, M. ERB, W. GRODD, A. LUDOLPH, AND U. KLOSE, *Comparison of longitudinal metabolite relaxation times in different regions of the human brain at 1.5 and 3 Tesla*, Magn. Reson. Med., 50 (2003), pp. 1296–1301.

[80] G. FAN, B. SUN, Z. WU, Q. GUO, AND Y. GUO, *In vivo single-voxel proton MR spectroscopy in the differentiation of high-grade gliomas and solitary metastases*, Clin. Radiol., 59 (2004), pp. 77–85.

[81] J. FAVRE, J. M. TAHA, AND K. J. BURCHIEL, *An analysis of the respective risks of hematoma formation in 361 consecutive morphological and functional stereotactic procedures*, Neurosurgery, 50 (2002), pp. 48–56; discussion 56–7.

[82] J. FELBLINGER, R. KREIS, AND C. BOESCH, *Effects of physiologic motion of the human brain upon quantitative ^{1}H-MRS: analysis and correction by retro-gating*, NMR Biomed., 11 (1998), pp. 107–114.

[83] M. FIELD, T. F. WITHAM, J. C. FLICKINGER, D. KONDZIOLKA, AND L. D. LUNSFORD, *Comprehensive assessment of hemorrhage risks and outcomes after stereotactic brain biopsy*, J. Neurosurg., 94 (2001), pp. 545–551.

[84] R. FISHER, *The use of multiple measurements in taxonomic problems*, Ann. Eugenics, 7 (1936), pp. 179–188.

[85] C. L. FLORIAN, N. E. PREECE, K. K. BHAKOO, S. R. WILLIAMS, AND M. NOBLE, *Characteristic metabolic profiles revealed by ^{1}H NMR spectroscopy for three types of human brain and nervous system tumours*, NMR Biomed., 8 (1995), pp. 253–264.

[86] K. N. FOUNTAS, E. Z. KAPSALAKI, S. D. GOTSIS, AND J. Z. KAPSALAKIS, *In vivo proton magnetic resonance spectroscopy of brain tumors*, Stereot. Funct. Neuros., 74 (2000), pp. 83–94.

[87] J. FRAHM, H. BRUHN, M. L. GYNGELL, K. D. MERBOLDT, W. HÄNICKE, AND R. SAUTER, *Localized proton NMR spectroscopy in different regions of the human brain in vivo. relaxation times and concentrations of cerebral metabolites*, Magn. Reson. Med., 11 (1989), pp. 47–63.

[88] S. FURUYA, S. NARUSE, M. IDE, H. MORISHITA, O. KIZU, S. UEDA, AND T. MAEDA, *Evaluation of metabolic heterogeneity in brain tumors using ^{1}H-chemical shift imaging method*, Neurosurgery, 10 (1997), pp. 25–30.

[89] R. E. GABR, R. OUWERKERK, AND P. A. BOTTOMLEY, *Quantifying in vivo MR spectra with circles*, J. Magn. Reson., 179 (2006), pp. 152–163.

[90] U. GARCZAREK, *Classification rules in standardized partition spaces*, PhD thesis, University of Dortmund, 2002.

[91] D. M. GAY, *A trust-region approach to linearly constrained optimization*, Numerical Analysis Proceedings, (1983), pp. 72–105.

[92] S. S. GILL, D. G. THOMAS, N. V. BRUGGEN, D. G. GADIAN, C. J. PEDEN, J. D. BELL, I. J. COX, D. K. MENON, R. A. ILES, AND D. J. BRYANT, *Proton MR spectroscopy of intracranial tumours: in vivo and in vitro studies*, J. Comput. Assist. Tomogr., 14 (1990), pp. 497–504.

[93] P. GILLIES, I. MARSHALL, M. ASPLUND, P. WINKLER, AND J. HIGINBOTHAM, *Quantification of MRS data in the frequency domain using a wavelet filter, an approximated Voigt lineshape model and prior knowledge*, NMR Biomed., 19 (2006), pp. 617–626.

[94] S. GOLOTVIN AND A. WILLIAMS, *Improved baseline recognition and modeling of FT NMR spectra*, J. Magn. Reson., 146 (2000), pp. 122–5.

[95] G. H. GOLUB AND V. PEREYRA, *The differentiation of pseudo-inverses and nonlinear least squares problems whose variables separate*, SIAM J. Numer. Anal., 10 (1973), pp. 413–32.

[96] ———, *Separable nonlinear least squares: the variable projection method and its applications*, Inverse Probl., 19 (2003), pp. 1–26.

[97] V. GOVINDARAJU, K. YOUNG, AND A. A. MAUDSLEY, *Proton NMR chemical shifts and coupling constants for brain metabolites*, NMR Biomed., 13 (2000), pp. 129–53.

[98] G. D. GRAHAM, J. H. HWANG, D. L. ROTHMAN, AND J. W. PRICHARD, *Spectroscopic assessment of alterations in macromolecule and small-molecule metabolites in human brain after stroke*, Stroke, 32 (2001), pp. 2797–2802.

[99] D. GRAVERON-DEMILLY, A. DIOP, A. BRIGUET, AND B. FENET, *Product-operator algebra for strongly coupled spin systems*, J. Magn. Reson. A, 101 (1993), pp. 233–39.

[100] H. GREENBERG, W. CHANDLER, AND H. SANDLER, *Brain Tumours*, Oxford University Press: New York, 1999.

[101] R. T. GREENLEE, T. MURRAY, S. BOLDEN, AND P. A. WINGO, *Cancer statistics, 2000*, CA Cancer J. Clin., 50 (2000), pp. 7–33.

[102] J. GRIVET, *Accurate numerical approximation to the Gauss-Lorentz lineshape*, J. Magn. Reson., 125 (1997), pp. 102–6.

[103] U. L. GÜNTHER, C. LUDWIG, AND H. RÜTERJANS, *WAVEWAT-improved solvent suppression in NMR spectra employing wavelet transforms*, J. Magn. Reson., 156 (2002), pp. 19–25.

[104] I. GUYON, S. GUNN, M. NIKRAVESH, AND L. A. ZADEH, *Feature Extraction: Foundations and Applications (Studies in Fuzziness and Soft Computing)*, Springer, 2006.

[105] I. GUYON, J. WESTON, S. BARNHILL, AND V. VAPNIK, *Gene selection for cancer and classification using support vector machines*, Mach. Learn., 46 (2002), pp. 389–422.

[106] G. HAGBERG, *From magnetic resonance spectroscopy to classification of tumors. A review of pattern recognition methods*, NMR Biomed., 11 (1998), pp. 148–156.

[107] W. A. HALL, *The safety and efficacy of stereotactic biopsy for intracranial lesions*, Cancer, 82 (1998), pp. 1749–1755.

[108] D. L. HARDY AND T. J. NORWOOD, *Spectral editing technique for the in vitro and in vivo detection of taurine*, J Magn Reson, 133 (1998), pp. 70–78.

[109] T. HASTIE, R. TIBSHIRANI, AND J. H. FRIEDMAN, *The Elements of Statistical Learning*, Springer, August 2001.

[110] Y. HILTUNEN, M. ALA-KORPELA, J. JOKISAARI, S. ESKELINEN, K. KIVINIITTY, M. SAVOLAINEN, AND Y. A. KESÄNIEMI, *A lineshape fitting model for ^{1}H NMR spectra of human blood plasma*, Magn. Reson. Med., 21 (1991), pp. 222–232.

[111] Y. HILTUNEN, J. KAARTINEN, J. PULKKINEN, A. M. HAKKINEN, N. LUNDBOM, AND R. A. KAUPPINEN, *Quantification of human brain metabolites from in vivo ^{1}H NMR magnitude spectra using automated artificial neural network analysis*, J. Magn. Reson., 154 (2002), pp. 1–5.

[112] Y. HOCHBERG AND A. TAMHANE, *Multiple comparison procedures*, Wiley, New York, 1987.

[113] L. HOFMANN, J. SLOTBOOM, C. BOESCH, AND R. KREIS, *Characterization of the macromolecule baseline in localized ^{1}H-MR spectra of human brain*, Magn. Reson. Med., 46 (2001), pp. 855–63.

[114] L. HOFMANN, J. SLOTBOOM, B. JUNG, P. MALOCA, C. BOESCH, AND R. KREIS, *Quantitative ^{1}H-magnetic resonance spectroscopy of human brain: Influence of composition and parameterization of the basis set in linear combination model-fitting*, Magn. Reson. Med., 48 (2002), pp. 440–53.

[115] M. HOLLANDER AND D. A. WOLFE, *Nonparametric statistical methods*, New-York: Wiley, 1973.

[116] Z. HOU, W. QIAN, Q. HU, AND W. L. NOWINSKI, *Regularized fuzzy c-means method for brain tissue clustering*, Pattern Recogn. Lett., 28 (2007), pp. 1788–1794.

[117] F. A. HOWE, S. J. BARTON, S. A. CUDLIP, M. STUBBS, D. E. SAUNDERS, M. M. MURPHY, P. WILKINS, K. S. OPSTAD, V. L. DOYLE, M. C. MCLEAN, B. A. BELL, AND J. R. GRIFFITHS, *Metabolic profiles of human brain tumours using quantitative in vivo ^{1}H magnetic resonance spectroscopy*, Magn. Res. Med., 49 (2003), pp. 223–32.

[118] S. L. HOWELLS, R. J. MAXWELL, F. A. HOWE, A. C. PEET, M. STUBBS, L. M. RODRIGUES, S. P. ROBINSON, S. BALUCH, AND J. R. GRIFFITHS, *Pattern recognition of ^{31}P magnetic resonance spectroscopy tumour spectra obtained in vivo*, NMR Biomed., 6 (1993), pp. 237–241.

[119] W. HUANG, G. E. ALEXANDER, L. CHANG, H. U. SHETTY, J. S. KRASUSKI, S. I. RAPOPORT, AND M. B. SCHAPIRO, *Brain metabolite concentration and dementia severity in Alzheimer's disease: a ^{1}H MRS study*, Neurology, 57 (2001), pp. 626–632.

[120] W.-L. HUNG, M.-S. YANG, AND D.-H. CHEN, *Parameter selection for suppressed fuzzy c-means with an application to MRI segmentation*, Pattern Recogn. Lett., 27 (2006), pp. 424–438.

[121] H. IN 'T ZANDT, M. VAN DER GRAAF, AND A. HEERSCHAP, *Common processing of in vivo MR spectra*, NMR Biomed., 14 (2001), pp. 224–232.

[122] H. ISHIMARU AND M. MORIKAWA, *Differenciation between high-grade glioma anf metastasic brain tumor using single-voxel proton MR spectroscopy*, Eur. Radiology, 11 (2001), pp. 1784–91.

[123] T. ISOBE, A. MATSUMURA, I. ANNO, T. YOSHIZAWA, Y. NAGATOMO, Y. ITAI, AND T. NOSE, *Quantification of cerebral metabolites in glioma patients with proton MR spectroscopy using T2 relaxation time correction*, Magn. Reson. Imaging, 20 (2002), pp. 343–349.

[124] P. JANNY, H. CURE, M. MOHR, N. HELDT, F. KWIATKOWSKI, J. J. LEMAIRE, R. PLAGNE, AND R. ROZAN, *Low grade supratentorial astrocytomas. Management and prognostic factors*, Cancer, 73 (1994), pp. 1937–1945.

[125] J. F. A. JANSEN, W. H. BACKES, K. NICOLAY, AND M. E. KOOI, *^{1}H MR spectroscopy of the brain: absolute quantification of metabolites*, Radiology, 240 (2006), pp. 318–332.

[126] M. JOLIOT, B. M. MAZOYER, AND R. H. HUESMAN, *In vivo NMR spectral parameter estimation: a comparison between time and frequency domain methods*, Magn. Reson. Med., 18 (1991), pp. 358–370.

[127] J. KAARTINEN, S. MIERISOVÁ, J. M. OJA, J. P. USENIUS, R. A. KAUPPINEN, AND Y. HILTUNEN, *Automated quantification of human brain metabolites by artificial neural network analysis from in vivo single-voxel ^{1}H NMR spectra*, J. Magn. Reson., 134 (1998), pp. 176–179.

[128] O. KADOTA, K. KOHNO, S. OHUE, Y. KUMON, S. SAKAKI, K. KIKUCHI, AND H. MIKI, *Discrimination of brain abscess and cystic tumor by in vivo proton magnetic resonance spectroscopy*, Neurol. Med. Chir., 41 (2001), pp. 121–126.

[129] K. KAMADA, K. HOUKIN, K. HIDA, H. MATSUZAWA, Y. IWASAKI, H. ABE, AND T. NAKADA, *Localized proton spectroscopy of focal brain pathology in humans: significant effects of edema on spin-spin relaxation time*, Magn. Reson. Med., 31 (1994), pp. 537–540.

[130] M. KANOWSKI, J. KAUFMANN, J. BRAUN, J. BERNARDING, AND C. TEMPELMANN, *Quantitation of simulated short echo time ^{1}H human brain spectra by LCModel and AMARES*, Magn. Reson. Med., 51 (2004), pp. 904–912.

[131] M. N. KASSEM AND R. BARTHA, *Quantitative proton short-echo-time LASER spectroscopy of normal human white matter and hippocampus at 4 Tesla incorporating macromolecule subtraction*, Magn. Reson. Med., 49 (2003), pp. 918–27.

[132] M. R. KAUS, S. K. WARFIELD, A. NABAVI, P. M. BLACK, F. A. JOLESZ, AND R. KIKINIS, *Automated segmentation of MR images of brain tumors*, Radiology, 218 (2001), pp. 586–591.

[133] B. M. KELM, *Evaluation of Vector-Valued Clinical Image Data Using Probabilistic Graphical Models: Quantification and Pattern Recognition*, PhD thesis, Ruprecht-Karls-Universität, Heidelberg, Germany, 2007.

[134] B. M. KELM, B. H. MENZE, C. M. ZECHMANN, K. T. BAUDENDISTEL, AND F. A. HAMPRECHT, *Automated estimation of tumor probability in prostate magnetic resonance spectroscopic imaging: pattern recognition vs quantification*, Magn. Reson. Med., 57 (2007), pp. 150–159.

[135] Y. KINOSHITA, H. KAJIWARA, A. YOKOTA, AND Y. KOGA, *Absolute concentrations of metabolites in human brain tumors using in vitro proton magnetic resonance spectroscopy*, Neurosurgery, 35 (1994), pp. 606–13.

[136] Y. KINOSHITA, H. KAJIWARA, A. YOKOTA, AND Y. KOGA, *Proton magnetic resonance spectroscopy of brain tumors: an in vitro study*, Neurosurgery, 35 (1994), pp. 606–13; discussion 613–4.

[137] Y. KINOSHITA AND A. YOKOTA, *Absolute concentrations of metabolites in human brain tumors using in vitro proton magnetic resonance spectroscopy*, NMR Biomed., 10 (1997), pp. 2–12.

[138] U. KLOSE, *In vivo proton spectroscopy in presence of eddy currents*, Magn. Reson. Med., 14 (1990), pp. 26–30.

[139] J. KNIGHT-SCOTT, *Application of multiple inversion recovery for suppression of macromolecule resonances in short echo time ^1H NMR spectroscopy of human brain*, J. Magn. Reson., 140 (1999), pp. 228–34.

[140] A. KNIJN, R. DE BEER, AND D. VAN ORMONDT, *Frequency-selective quantification in the time domain*, J. Magn. Reson., 97 (1992), pp. 444–50.

[141] R. KOHAVI AND G. H. JOHN, *The wrappers approach. In , Huan Liu & Hiroshi Motoda (Eds.) Feature extraction, construction and selection: A data mining perspective*, 1998.

[142] I. KONONENKO, *Estimating attributes: analysis and extensions of relief*, in Proceedings of the European conference on machine learning on Machine Learning, Springer-Verlag New York, Inc., 1994, pp. 171–182.

[143] R. KREIS, *Quantitative localized ^1H MR spectroscopy for clinical use*, Prog. Magn. Reson. Spectrosc., 31 (1997), pp. 155–195.

[144] ———, *Issues of spectral quality in clinical ^1H-magnetic resonance spectroscopy and a gallery of artifacts*, NMR Biomed., 17 (2004), pp. 361–381.

[145] R. KREIS AND C. BOESCH, *Bad spectra can be better than good spectra*, Toronto, Ontario, Canada, 2003, ISMRM 11th scientific meeting, p. 264.

[146] R. KREIS, T. ERNST, AND B. ROSS, *Absolute quantitation of water and metabolites in the human brain. II. metabolite concentrations*, J. Magn. Reson. B, 102 (1993), pp. 9–19.

[147] R. KREIS, T. ERNST, AND B. D. ROSS, *Development of the human brain: In vivo quantification of metabolite and water content with proton magnetic resonance spectroscopy*, Magn. Reson. Med., 30 (1993), pp. 424–437.

[148] R. KREIS, J. SLOTBOOM, L. HOFMANN, AND C. BOESCH, *Integrated data acquisition and processing to determine metabolite contents, relaxation times, and macromolecule baseline in single examinations of individual subjects*, Magn. Reson. Med., 54 (2005), pp. 761–8.

[149] H. KUGEL, W. HEINDEL, R. I. ERNESTUS, J. BUNKE, R. DU MESNIL, AND G. FRIEDMANN, *Human brain tumors: spectral patterns detected with localized H-1 MR spectroscopy*, Radiology, 183 (1992), pp. 701–709.

[150] Y. KURODA, A. WADA, T. YAMAZAKI, AND K. NAGAYAMA, *Postacquisition data processing method for suppression of the solvent signal*, J. Magn. Reson., 84 (1989), pp. 604–610.

[151] C. LADROUE, F. A. HOWE, J. R. GRIFFITHS, AND A. R. TATE, *Independent component analysis for automated decomposition of in vivo magnetic resonance spectra*, Magn. Reson. Med., 50 (2003), pp. 697–703.

[152] T. LAUDADIO, N. MASTRONARDI, L. VANHAMME, P. VAN HECKE, AND S. VAN HUFFEL, *Improved Lanczos algorithms for blackbox MRS data quantitation*, J. Magn. Reson., 157 (2002), pp. 292–7.

[153] T. LAUDADIO, P. PELS, L. D. LATHAUWER, P. VAN HECKE, AND S. VAN HUFFEL, *Tissue segmentation and classification of MRSI data using canonical correlation analysis*, Magn. Reson. Med., 54 (2005), pp. 1519–1529.

[154] T. LAUDADIO, Y. SELÉN, L. VANHAMME, S. P., P. VAN HECKE, AND S. VAN HUFFEL, *Subspace-based MRS data quantitation of multiplets using prior knowledge*, J. Magn. Reson., 168 (2004), pp. 53–65.

[155] D. LEIBFRITZ AND W. DREHER, *Magnetization transfer MRS*, NMR Biomed., 14 (2001), pp. 65–76.

[156] M. LEVITT, *Spin Dynamics: Basics of Nuclear Magnetic Resonance*, Wiley, 2001.

[157] B. S. Y. LI, H. WANG, AND O. GONEN, *Metabolite ratios to assumed stable creatine level may confound the quantification of proton brain MR spectroscopy*, Magn. Reson. Imaging, 21 (2003), pp. 923–928.

[158] Y.-Y. LIN, P. HODGKINSON, M. ERNST, AND A. PINES, *A novel detection-estimation scheme for noisy NMR signals: Applications to delayed acquisition data*, J. Magn. Reson., 128 (1997), pp. 30–41.

[159] J. C. LINDON, E. HOLMES, AND J. K. NICHOLSON, *Pattern recognition methods and applications in biomedical magnetic resonance*, Prog. Nucl. Mag. Res. Sp., 39 (2001), pp. 1–40.

[160] H. LIU AND H. MOTODA, *Computational Methods of Feature Selection*, Chapman & Hall/Crc Data Mining and Knowledge Discovery Series, 2007.

[161] D. N. LOUIS, H. OHGAKI, O. D. WIESTLER, W. K. CAVENEE, P. C. BURGER, A. JOUVET, B. W. SCHEITHAUER, AND P. KLEIHUES, *The 2007 WHO classification of tumours of the central nervous system*, Acta Neuropathol., 114 (2007), pp. 97–109.

[162] C. LU, A. DEVOS, J. A. K. SUYKENS, C. ARÚS, AND S. VAN HUFFEL, *Bagging linear sparse bayesian learning models for variable selection in cancer diagnosis*, IEEE Trans. Inf. Technol. Biomed., 11 (2007), pp. 338–347.

[163] L. LUKAS, A. DEVOS, J. A. K. SUYKENS, L. VANHAMME, F. A. HOWE, C. MAJOS, A. MORENO TORRES, C. VAN DER GRAAF, A. R. TATE, C. ARÚS, AND S. VAN HUFFEL, *Brain tumor classification based on long echo proton MRS signals*, Artificial Intelligence in Medicine, 31 (2004), pp. 73–89.

[164] D. LUNGA, R. POGNI, AND R. BASOSI, *A simple method for baseline correction in EPR spectroscopy*, J. Magn. Reson. A, 108 (1994), pp. 165–170.

[165] J. LUTS, A. HEERSCHAP, J. A. K. SUYKENS, AND S. VAN HUFFEL, *A combined MRI and MRSI based multiclass system for brain tumour recognition using LS-SVMs with class probabilities and feature selection*, Artif. Intell. Med., 40 (2007), pp. 87–102.

[166] J. LUTS, T. LAUDADIO, A. J. IDEMA, A. W. SIMONETTI, A. HEERSCHAP, D. VANDERMEULEN, J. A. K. SUYKENS, AND S. VAN HUFFEL, *Nosologic imaging of the brain: segmentation and classification using MRI and MRSI*, Accepted for publication in NMR in Biomedicine, (2008).

[167] J. LUTS, J. POULLET, J. M. GARCIA-GOMEZ, A. HEERSCHAP, M. ROBLES, J. A. K. SUYKENS, AND S. VAN HUFFEL, *The effect of feature extraction for brain tumour classification based on short echo time ^{1}H MR spectra*, Magn. Res. Med., 60(2) (2008), pp. 288–298.

[168] M. A. MACRÌ, G. GARREFFA, F. GIOVE, M. GUARDATI, A. AMBROSINI, C. COLONNESE, AND B. MARAVIGLIA, *In vivo quantitative ^{1}H MRS of cerebellum and evaluation of quantitation reproducibility by simulation of different levels of noise and spectral resolution*, Magn. Reson. Imaging, 22 (2004), pp. 1385–1393.

[169] I. MADER, U. SEEGER, J. KARITZKY, M. ERB, F. SCHICK, AND U. KLOSE, *Proton magnetic resonance spectroscopy with metabolite nulling reveals regional differences of macromolecules in normal human brain*, J. Magn. Reson. Imaging, 16 (2002), pp. 538–546.

[170] I. MADER, U. SEEGER, R. WEISSERT, U. KLOSE, T. NAEGELE, A. MELMS, AND W. GRODD, *Proton MR spectroscopy with metabolite-nulling reveals elevated macromolecules in acute multiple sclerosis*, Brain, 124 (2001), pp. 953–961.

[171] C. MAJÓS, J. ALONSO, C. AGUILERA, M. SERRALLONGA, J. PÉREZ-MARTÍN, J. J. ACEBES, C. ARÚS, AND J. GILI, *Proton magnetic resonance spectroscopy (^{1}H MRS) of human brain tumours: assessment of differences between tumour types and its applicability in brain tumour categorization*, Eur. Radiol., 13 (2003), pp. 582–591.

[172] C. MAJÓS, M. MARGARIDA JULIÀ-SAPÉ, J. ALONSO, M. SERRALLONGA, C. AGUILERA, J. J. ACEBES, C. ARÚS, AND J. GILI, *Brain tumor classification by proton MR spectroscopy: comparison of diagnostic accuracy at short and long TE*, AJNR Am. J. Neuroradiol., 25 (2004), pp. 1696–1704.

[173] V. MANDELSHTAM AND H. TAYLOR, *Multidimensional harmonic inversion by filter-diagonalization*, J. Chem. Phys., 108 (1998), pp. 9970–9977.

[174] V. A. MANDELSHTAM, *The multidimensional filter diagonalization method*, J. Magn. Reson., 144 (2000), pp. 343–356.

[175] V. A. MANDELSHTAM, H. S. TAYLOR, AND A. J. SHAKA, *Application of the filter diagonalization method to one- and two-dimensional NMR spectra*, J. Magn. Reson., 133 (1998), pp. 304–312.

[176] D. J. MANTON, M. LOWRY, S. J. BLACKBAND, AND A. HORSMAN, *Determination of proton metabolite concentrations and relaxation parameters in normal human brain and intracranial tumours*, NMR Biomed., 8 (1995), pp. 104–112.

[177] D. MARION, M. IKURA, AND A. BAX, *Improved solvent suppression in one- and two-dimensional NMR spectra by convolution of time-domain data*, J. Magn. Reson., 84 (1989), pp. 425–30.

[178] I. MARSHALL, S. D. BRUCE, J. HIGINBOTHAM, A. MACLULLICH, J. M. WARDLAW, K. J. FERGUSON, AND J. SECKL, *Choice of spectroscopic lineshape model affects metabolite peak areas and area ratios*, Magn. Reson. Med., 44 (2000), pp. 646–649.

[179] I. MARSHALL, J. HIGINBOTHAM, S. BRUCE, AND A. FREISE, *Use of Voigt lineshape for quantification of in vivo ^{1}H spectra*, Magn. Reson. Med., 37 (1997), pp. 651–657.

[180] M. C. MARTINEZ-BISBAL, L. MARTI BONMATI, J. PIQUER, A. REVERT, P. FERRER, J. L. LLÁCER, M. PIOTTO, O. ASSEMAT, AND B. CELDA, *^{1}H and ^{13}C HR-MAS spectroscopy of intact biopsy samples ex vivo and in vivo ^{1}H MRS study of human high grade gliomas*, NMR Biomed., 17 (2004), pp. 191–205.

[181] A. A. MAUDSLEY, *Spectral lineshape determination by self-deconvolution*, J. Magn. Reson. B, 106 (1995), pp. 47–57.

[182] A. A. MAUDSLEY, Z. WU, D. J. MEYERHOFF, AND M. W. WEINER, *Automated processing for proton spectroscopic imaging using water reference deconvolution*, Magn. Reson. Med., 31 (1994), pp. 589–595.

[183] D. Q. MCBRIDE, B. L. MILLER, D. L. NIKAS, S. BUCHTHAL, L. CHANG, F. CHIANG, AND R. A. BOOTH, *Analysis of brain tumors using ^1H magnetic resonance spectroscopy*, Surg. Neurol., 44 (1995), pp. 137–144.

[184] M. A. MCLEAN, R. J. SIMISTER, G. J. BARKER, AND J. S. DUNCAN, *Discrimination between neurochemical and macromolecular signals in human frontal lobes using short echo time proton magnetic resonance spectroscopy*, Faraday Discuss., 126 (2004), pp. 93–102.

[185] M. A. MCLEAN, R. J. SIMISTER, G. J. BARKER, AND J. S. DUNCAN, *Magnetization transfer effect on human brain metabolites and macromolecules*, Magn. Reson. Med., 54 (2005), pp. 1281–1285.

[186] B. H. MENZE, M. P. LICHY, P. BACHERT, B. M. KELM, H.-P. SCHLEMMER, AND F. A. HAMPRECHT, *Optimal classification of long echo time in vivo magnetic resonance spectra in the detection of recurrent brain tumors*, NMR Biomed., 19 (2006), pp. 599–609.

[187] C. METZ, B. HERMAN, AND J.-H. SHEN, *Maximum likelihood estimation of receiver operating characteristic (roc) curves from continuously-distributed data*, Stat. Med., 17 (1998), pp. 1033–1053.

[188] G. J. METZGER, M. PATEL, AND X. HU, *Application of genetic algorithms to spectral quantification*, J. Magn. Reson. B, 110 (1996), pp. 316–320.

[189] R. A. MEYER, M. J. FISHER, S. J. NELSON, AND T. R. BROWN, *Evaluation of manual methods for integration of in vivo phosphorus NMR spectra*, NMR Biomed., 1 (1988), pp. 131–135.

[190] S. MIERISOVÁ AND M. ALA-KORPELA, *MR spectroscopy quantitation: a review of frequency domain methods*, NMR Biomed., 14 (2001), pp. 247–259.

[191] M. I. MILLER, T. J. SCHAEWE, C. S. BOSCH, AND J. J. ACKERMAN, *Model-based maximum-likelihood estimation for phase- and frequency-encoded magnetic-resonance-imaging data*, J. Magn. Reson. B, 107 (1995), pp. 210–221.

[192] V. MLYNÁRIK, S. GRUBER, Z. STARCUK, Z. STARCUK, AND E. MOSER, *Very short echo time proton MR spectroscopy of human brain with a standard transmit/receive surface coil*, Magn. Reson. Med., 44 (2000), pp. 964–967.

[193] J. J. MORÉ, *The Levenberg-Marquardt algorithm: Implementation and theory*, Numerical Analysis: Proceedings of the Biennial Conference held at Dundee, June 28-July 1, 1977 (Lecture Notes in Mathematics #630), (1978), pp. 104–16.

[194] G. MORRIS, *Compensation of instrumental imperfections by deconvolution using an internal reference signal*, J. Magn. Reson., 80 (1988), pp. 547–552.

[195] D. MOSKAU, *Application of real time digital filters in NMR spectroscopy*, Concepts Magn. Reson., 15 (2002), pp. 164–176.

[196] M. MURPHY, A. LOOSEMORE, A. G. CLIFTON, F. A. HOWE, A. R. TATE, S. A. CUDLIP, P. R. WILKINS, J. R. GRIFFITHS, AND B. A. BELL, *The contribution of proton magnetic resonance spectroscopy (^{1}HMRS) to clinical brain tumour diagnosis*, Br. J. Neurosurg., 16 (2002), pp. 329–334.

[197] P. A. NARAYANA, D. JOHNSTON, AND D. P. FLAMIG, *In vivo proton magnetic resonance spectroscopy studies of human brain*, Magn. Reson. Imaging, 9 (1991), pp. 303–308.

[198] W. G. NEGENDANK, R. SAUTER, T. R. BROWN, J. L. EVELHOCH, A. FALINI, E. D. GOTSIS, A. HEERSCHAP, K. KAMADA, B. C. LEE, M. M. MENGEOT, E. MOSER, K. A. PADAVIC-SHALLER, J. A. SANDERS, T. A. SPRAGGINS, A. E. STILLMAN, B. TERWEY, T. J. VOGL, K. WICKLOW, AND R. A. ZIMMERMAN, *Proton magnetic resonance spectroscopy in patients with glial tumors: a multicenter study*, J. Neurosurg., 84 (1996), pp. 449–458.

[199] S. J. NELSON, *Magnetic resonance spectroscopic imaging*, IEEE Eng. Med. Biol., (2004), pp. 30–39.

[200] S. J. NELSON, D. B. VIGNERON, AND W. P. DILLON, *Serial evaluation of patients with brain tumors using volume MRI and 3D ^1H MRSI*, NMR Biomed., 12 (1999), pp. 123–138.

[201] J. NETER, M. H. KUTNER, C. J. NACHTSHEIM, AND W. WASSERMAN, *Applied Linear Statistical Models (Fourth Edition)*, New York: WCB McGraw-Hill, 1996.

[202] N. OBUCHOWSKI AND M. LIEBER, *Confidence intervals for receiver operating characteristic area in studies with small samples*, Academic Radiol., 5 (1998), pp. 561–571.

[203] K. S. OPSTAD, C. LADROUE, B. A. BELL, J. R. GRIFFITHS, AND F. A. HOWE, *Linear discriminant analysis of brain tumour ^1H MR spectra: a comparison of classification using whole spectra versus metabolite quantification*, NMR Biomed., 20 (2007), pp. 763–770.

[204] R. ORDIDGE AND I. CRESSHULL, *The correction of transient B_0 field shifts following the application of pulsed gradients by phase correction in the time domain*, J. Magn. Reson., 69 (1986), pp. 151–155.

[205] A. M. OROS-PEUSQUENS, M. LAURILA, AND N. J. SHAH, *Magnetic field dependence of the distribution of NMR relaxation times in the living human brain*, MAGMA, 21 (2008), pp. 131–147.

[206] M. OSBORNE, *Numerical methods for non-linear optimization*, Academic Press, London, 1972.

[207] M. OSORIO, D. SIMA, J. POULLET, D. VAN ORMONDT, AND S. VAN HUFFEL, *Improvement of lineshape estimation for MRS signals*, in IEEE International workshop on Imaging Systems and Techniques, Chania, Crete, 2008, pp. 326–329.

[208] J. PFEUFFER, I. TKAC, S. W. PROVENCHER, AND R. GRUETTER, *Toward an in vivo neurochemical profile: Quantification of 18 metabolites in short-echo-time ^1H NMR spectra of the rat brain*, J. Magn. Reson., 141 (1999), pp. 104–20.

[209] J. PIEPMEIER, S. CHRISTOPHER, D. SPENCER, T. BYRNE, J. KIM, J. P. KNISEL, J. LACY, L. TSUKERMAN, AND R. MAKUCH, *Variations in the natural history and survival of patients with supratentorial low-grade astrocytomas*, Neurosurgery, 38 (1996), pp. 872–8; discussion 878–9.

[210] W. W. F. PIJNAPPEL, A. VAN DEN BOOGAART, R. DE BEER, AND D. VAN ORMONDT, *SVD-based quantification of magnetic resonance signals*, J. Magn. Reson., 97 (1992), pp. 122–34.

[211] H. POPTANI, R. K. GUPTA, V. K. JAIN, R. ROY, AND R. PANDEY, *Cystic intracranial mass lesions: possible role of in vivo MR spectroscopy in its differential diagnosis*, Magn. Reson. Imaging, 13 (1995), pp. 1019–1029.

[212] J. POULLET, M. C. MARTINEZ-BISBAL, D. VALVERDE, D. MONLEON, B. CELDA, C. ARÚS, AND S. V. HUFFEL, *Quantification and classification of high-resolution magic angle spinning data for brain tumor diagnosis*, Conf. Proc. IEEE Eng. Med. Biol. Soc., 2007 (2007), pp. 5407–5410.

[213] J. POULLET, D. M. SIMA, A. W. SIMONETTI, B. DE NEUTER, L. VANHAMME, P. LEMMERLING, AND S. VAN HUFFEL, *An automated quantitation of short echo time MRS spectra in an open source software environment: AQSES*, NMR Biomed., 20 (2007), pp. 493–504.

[214] J. POULLET, D. M. SIMA, S. VAN HUFFEL, AND P. VAN HECKE, *Frequency-selective quantitation of short-echo time ^1H magnetic resonance spectra*, J. Magn. Reson., 186 (2007), pp. 293–304.

[215] P. J. POUWELS AND J. FRAHM, *Regional metabolite concentrations in human brain as determined by quantitative localized proton MRS*, Magn. Reson. Med., 39 (1998), pp. 53–60.

[216] M. PRASTAWA, E. BULLITT, S. HO, AND G. GERIG, *A brain tumor segmentation framework based on outlier detection*, Med. Image Anal., 8 (2004), pp. 275–283.

[217] M. C. PREUL, Z. CARAMANOS, D. L. COLLINS, J. G. VILLEMURE, R. LEBLANC, A. OLIVIER, R. POKRUPA, AND D. L. ARNOLD, *Accurate, noninvasive diagnosis of human brain tumors by using proton magnetic resonance spectroscopy*, Nat. Med., 2 (1996), pp. 323–325.

[218] M. C. PREUL, Z. CARAMANOS, R. LEBLANC, J. G. VILLEMURE, AND D. L. ARNOLD, *Using pattern analysis of in vivo proton mrsi data to improve the diagnosis and surgical management of patients with brain tumors*, NMR Biomed., 11 (1998), pp. 192–200.

[219] E. PROST, P. SIZUN, M. PIOTTO, AND J. M. NUZILLARD, *A simple scheme for the design of solvent-suppression pulses*, J. Magn. Reson., 159 (2002), pp. 76–81.

[220] S. W. PROVENCHER, *Estimation of metabolite concentrations from localized in vivo proton NMR spectra*, Magn. Reson. Med., 30 (1993), pp. 672–79.

[221] H. RABESON, E. CAPOBIANCO, R. DE BEER, D. VAN ORMONDT, AND D. GRAVERON-DEMILLY, *Correction for B_0-inhomogeneity and Eddy Current effects without using a reference line*, in GRAMM, 2008.

[222] H. RABESON, F. FAUVELLE, H. RATINEY, C. CUDALBU, S. CAVASSILA, D. VAN ORMONDT, AND D. GRAVERON-DEMILLY, *Quantitation with QUEST of ER-filtered HRMAS-NMR signals*, in Proc. ProRISC, IEEE Benelux, Veldhoven, The Netherlands, November 2006, pp. 171–175.

[223] H. RABESON, F. FAUVELLE, G. TESTYLIER, A. FOQUIN, P. CARPENTIER, F. DORANDEU, D. VAN ORMONDT, AND D. GRAVERON-DEMILLY, *Quantitation with QUEST of brain HRMAS-NMR signals: Application to metabolic disorders in experimental epileptic seizures*, Magn. Reson. Med., 59 (2008), pp. 1266–1273.

[224] B. RAO, *Relationship between matrix pencil and state space based harmonic retrieval methods*, IEEE Trans. Acc. Sp. Sig. Proc., 38 (1990), pp. 177–179.

[225] H. RATINEY, Y. COENRADIE, S. CAVASSILA, D. VAN ORMONDT, AND D. GRAVERON-DEMILLY, *Time-domain quantitation of ^1H short echo-time signals: background accommodation*, MAGMA, 16 (2004), pp. 284–96.

[226] H. RATINEY, M. SDIKA, Y. COENRADIE, S. CAVASSILA, D. VAN ORMONDT, AND D. GRAVERON-DEMILLY, *Time-domain semi-parametric estimation based on a metabolite basis set*, NMR Biomed., 18 (2005), pp. 1–13.

[227] G. REYNOLDS, M. WILSON, A. PEET, AND T. N. ARVANITIS, *An algorithm for the automated quantitation of metabolites in in vitro NMR signals*, Magn. Reson. Med., 56 (2006), pp. 1211–1219.

[228] M. RIJPKEMA, J. SCHUURING, Y. VAN DER MEULEN, M. VAN DER GRAAF, H. BERNSEN, R. BOERMAN, A. VAN DER KOGEL, AND A. HEERSCHAP, *Characterization of oligodendrogliomas using short echo time ^1H MR spectroscopic imaging*, NMR Biomed., 16(1) (2003), pp. 12–18.

[229] M. ROBNIK-ŠIKONJA AND I. KONONENKO, *Theoretical and empirical analysis of ReliefF and RReliefF*, Mach. Learn., 53 (2003), pp. 23–69.

[230] R. ROMANO, A. MOTTA, S. CAMASSA, C. PAGANO, M. T. SANTINI, AND P. L. INDOVINA, *A new time-domain frequency-selective quantification algorithm*, J. Magn. Reson., 155 (2002), pp. 226–35.

[231] A. J. ROSS AND P. S. SACHDEV, *Magnetic resonance spectroscopy in cognitive research*, Brain Res. Rev., 44 (2004), pp. 83–102.

[232] B. ROSS AND T. MICHAELIS, *Clinical applications of magnetic resonance spectroscopy*, Magn. Reson. Q., 10 (1994), pp. 191–247.

[233] R. ROY AND T. KAILATH, *ESPRIT-estimation of signal parameters via rotational invariance techniques*, IEEE Trans. Acc. Sp. Sig. Proc., 37 (1989), pp. 984–995.

[234] J. L. RUIZ-PEÑA, P. PIÑERO, G. SELLERS, J. ARGENTE, A. CASADO, J. FORONDA, A. UCLÉS, AND G. IZQUIERDO, *Magnetic resonance spectroscopy of normal appearing white matter in early relapsing-remitting multiple sclerosis: correlations between disability and spectroscopy*, BMC Neurol., 4 (2004), p. 8.

[235] D. R. RUTGERS, P. B. KINGSLEY, AND J. VAN DER GROND, *Saturation-corrected t_1 and t_2 relaxation times of choline, creatine and N-acetyl aspartate in human cerebral white matter at 1.5 T*, NMR Biomed., 16 (2003), pp. 286–288.

[236] S. S. MIERISOVA, A. VAN DEN BOOGAART, I. TKÁC, P. V. HECKE, L. VANHAMME, AND T. LIPTAJ, *New approach for quantitation of short echo time in vivo ^1H MR spectra of brain using AMARES*, NMR Biomed., 11 (1998), pp. 32–39.

[237] N. SAEED, *Magnetic resonance image segmentation using pattern recognition, and applied to image registration and quantitation*, NMR Biomed., 11 (1998), pp. 157–167.

[238] P. SAJDA, P. SAJDA, S. DU, T. BROWN, R. STOYANOVA, D. SHUNGU, X. MAO, AND L. PARRA, *Nonnegative matrix factorization for rapid recovery of constituent spectra in magnetic resonance chemical shift imaging of the brain*, IEEE Trans. Med. Imag., 23 (2004), pp. 1453–1465.

[239] N. SANDGREN, Y. SELEN, P. STOICA, AND J. LI, *Parametric methods for frequency-selective MR spectroscopy - A review*, J. Magn. Reson., 168 (2004), pp. 259–72.

[240] T. SCHIRMER AND D. P. AUER, *On the reliability of quantitative clinical magnetic resonance spectroscopy of the human brain*, NMR Biomed., 13 (2000), pp. 28–36.

[241] B. SCHÖLKOPF AND A. J. SMOLA, *Learning with Kernels: Support Vector Machines, Regularization, Optimization, and Beyond (Adaptive Computation and Machine Learning)*, The MIT Press, December 2001.

[242] U. SEEGER AND U. KLOSE, *Parameterized evaluation of macromolecules and lipids in proton MR spectroscopy of brain diseases*, Magn. Reson. Med., 49 (2003), pp. 19–28.

[243] I. W. SELESNICK, M. LANG, AND C. S. BURRUS, *Constrained least square design of fir filters without specified transition bands*, IEEE T. Signal Proces., 44 (1996), pp. 1879–92.

[244] H. SERRAI, L. SENHADJI, D. B. CLAYTON, C. ZUO, AND R. E. LENKINSKI, *Water modeled signal removal and data quantification in localized MR spectroscopy using a time-scale postacquistion method*, J. Magn. Reson., 149 (2001), pp. 45–51.

[245] H. SERRAI, L. SENHADJI, J. D. DE CERTAINES, AND J. L. COATRIEUX, *Time-domain quanification of amplitude, chemical shift, apparent relaxation time T2, and phase by wavelet-transform analysis. Application to biomedical magnetic resonance spectroscopy*, J. Magn. Reson., 124 (1997), pp. 20–34.

[246] D. M. SIMA AND S. VAN HUFFEL, *Regularized semiparametric model identification with application to NMR signal quantification with unknown macromolecular baseline*, J. Roy. Stat. Soc. B, 68 (2006), pp. 383–409.

[247] ———, *Separable nonlinear least squares fitting with linear bound constraints and its application in magnetic resonance spectroscopy data quantification*, J. Comput. Appl. Math., 203(1) (2006), pp. 264–278.

[248] H. SIMON, *The lanczos algorithm with partial reorthogonalization*, Math. Comp., 42 (1984), pp. 115–142.

[249] A. W. SIMONETTI, W. MELSEN, M. VAN DER GRAAF, G. POSTMA, A. HEERSCHAP, AND L. M. C. BUYDENS, *A chemometric approach for brain tumor classsification using magnetic resonance imaging and spectroscopy*, Anal. Chem., 75(20) (2003), pp. 5352–5361.

[250] A. W. SIMONETTI, W. J. MELSSEN, F. S. DE EDELENYI, J. J. A. VAN ASTEN, A. HEERSCHAP, AND L. M. C. BUYDENS, *Combination of feature-reduced MR spectroscopic and MR imaging data for improved brain tumor classification*, NMR Biomed., 18 (2005), pp. 34–43.

[251] A. W. SIMONETTI, W. J. MELSSEN, M. VAN DER GRAAF, A. HEERSCHAP, AND L. M. C. BUYDENS, *Automated correction of unwanted phase jumps in reference signals which corrupt MRSI spectra after eddy current correction*, J. Magn. Reson., 159 (2002), pp. 151–157.

[252] A. J. SIMPSON AND S. A. BROWN, *Purge NMR: effective and easy solvent suppression*, J. Magn. Reson., 175 (2005), pp. 340–6.

[253] J. SLOTBOOM, C. BOESCH, AND R. KREIS, *Versatile frequency domain fitting using time domain models and prior knowledge*, Magn. Reson. Med., 39 (1998), pp. 899–911.

[254] J. SLOTBOOM, A. NIRKKO, AND D. VAN ORMONDT, *A comparison of time domain and frequency domain all rank selection order statistics filtering (ARSOS) of single voxel ^{1}H MRS-signals*, Berlin, May 2007, Joint ISMRM and ESMRMB Meeting.

[255] M. A. SMITH, J. GILLEN, M. T. MCMAHON, P. B. BARKER, AND X. GOLAY, *Simultaneous water and lipid suppression for in vivo brain spectroscopy in humans*, Magn. Reson. Med., 54 (2005), pp. 691–6.

[256] S. A. SMITH, T. O. LEVANTE, B. H. MEIER, AND R. R. ERNST, *Computer simulations in magnetic resonance. An object-oriented programming approach*, J. Magn. Reson. A, 106 (1994), pp. 75–105.

[257] G. SOBERING, M. KIENLIN, C. MOONEN, P. ZIJL, AND A. BIZZI, *Post-acquisition reduction of water signals in proton spectroscopic imaging of the brain*, vol. 1, San Francisco, 1991, ISMRM, 10th Annual Meeting, p. 771.

[258] P. SODANO AND M. DELEPIERRE, *Binomial frequency response to non-binomial pulse sequences for efficient water suppression*, J. Biomol. NMR, 3 (1993), pp. 471–7.

[259] B. J. SOHER, K. YOUNG, V. GOVINDARAJU, AND A. A. MAUDSLEY, *Automated spectral analysis III: application to in vivo proton MR spectroscopy and spectroscopic imaging*, Magn. Reson. Med., 40 (1998), pp. 822–31.

[260] B. J. SOHER, K. YOUNG, AND A. A. MAUDSLEY, *Representation of strong baseline contributions in ^{1}H MR spectra*, Magn. Reson. Med., 45 (2001), pp. 966–72.

[261] R. L. SOMORJAI, B. DOLENKO, A. K. NIKULIN, N. PIZZI, G. SCARTH, P. ZHILKIN, W. HALLIDAY, D. FEWER, N. HILL, I. ROSS, M. WEST, I. C. SMITH, S. M. DONNELLY, A. C. KUESEL, AND K. M. BRIÈRE, *Classification of ^{1}H MR spectra of human brain neoplasms: the influence of preprocessing and computerized consensus diagnosis on classification accuracy*, J. Magn. Reson. Imaging, 6 (1996), pp. 437–444.

[262] J. C. SPALL AND J. P. GARNER, *Parameter identification of state-space models with nuisance parameters*, IEEE T. Aero. Elec. Sys., 26 (1990), pp. 992–98.

[263] J. A. STANLEY AND J. W. PETTEGREW, *Postprocessing method to segregate and quantify the broad components underlying the phosphodiester spectral region of in vivo ^{31}P brain spectra*, Magn. Reson. Med., 45 (2001), pp. 390–396.

[264] J. M. STAR-LACK, E. ADALSTEINSSON, G. E. GOLD, D. M. IKEDA, AND D. M. SPIELMAN, *Motion correction and lipid suppression for ^{1}H magnetic resonance spectroscopy*, Magn. Reson. Med., 43 (2000), pp. 325–330.

[265] D. STEPHENSON AND G. BINSCH, *Automated analysis of high-resolution NMR spectra. II. illustrative applications of the computer program DAVINS*, J. Magn. Reson., 37 (1980), pp. 409–30.

[266] P. STOICA AND R. MOSES, *Introduction to spectral analysis*, Prentice Hall, 1997.

[267] P. STOICA, N. SANDGREN, Y. SELEN, L. VANHAMME, AND S. VAN HUFFEL, *Frequency-domain method based on the singular value decomposition for frequency-selective NMR spectroscopy*, J. Magn. Reson., 165 (2003), pp. 80–8.

[268] P. STOICA, P. STOICA, Y. SELEN, N. SANDGREN, AND S. VAN HUFFEL, *Using prior knowledge in SVD-based parameter estimation for magnetic resonance spectroscopy-the ATP example*, IEEE Trans. Biom. Engin., 51 (2004), pp. 1568–1578.

[269] P. STOICA AND T. SUNDIN, *Nonparametric NMR spectroscopy*, J. Magn. Reson., 152 (2001), pp. 57–69.

[270] R. STOYANOVA AND T. R. BROWN, *NMR spectral quantitation by principal component analysis*, NMR Biomed., 14 (2001), pp. 271–277.

[271] R. STOYANOVA AND T. R. BROWN, *NMR spectral quantitation by principal component analysis. III. a generalized procedure for determination of lineshape variations*, J. Magn. Reson., 154 (2002), pp. 163–75.

[272] R. STOYANOVA, A. KUESEL, AND T. BROWN, *Application of principal-component analysis for spectral quantitation*, J. Magn. Reson., 115 (1995), pp. 265–269.

[273] T. SUNDIN, L. VANHAMME, P. VAN HECKE, I. DOLOGLOU, AND S. VAN HUFFEL, *Accurate quantification of ^{1}H spectra: From finite impulse response filter design for solvent suppression to parameter estimation*, J. Magn. Reson., 139 (1999), pp. 189–204.

[274] J. A. K. SUYKENS, T. VAN GESTEL, J. DE BRABANTER, B. DE MOOR, AND J. VANDEWALLE, *Least squares support vector machines*, World Scientific, 2002.

[275] J. A. K. SUYKENS AND J. VANDEWALLE, *Least squares support vector machine classifiers*, Neural Processing Letters, 9(3) (1999), pp. 293–300.

[276] C. TANG, *An analysis of baseline distortion and offset in NMR spectra*, J. Magn. Reson. A, 109 (1994), pp. 232–240.

[277] J. TANG AND J. NORRIS, *LP-ZOOM, a linear prediction method for local spectral analysis of NMR signals*, J. Magn. Reson., 79 (1988), pp. 190–96.

[278] A. R. TATE, C. MAJÓS, A. MORENO, F. A. HOWE, J. R. GRIFFITHS, AND C. ARÚS, *Automated classification of short echo time in in vivo ^{1}H brain tumor spectra: a multicenter study*, Magn. Reson. Med., 49 (2003), pp. 29–36.

[279] A. R. TATE, J. UNDERWOOD, D. M. ACOSTA, M. JULIÀ-SAPÉ, C. MAJÓS, A. MORENO-TORRES, F. A. HOWE, M. VAN DER GRAAF, V. LEFOURNIER, M. M. MURPHY, A. LOOSEMORE, C. LADROUE, P. WESSELING, J. L. BOSSON, M. E. CABANAS, A. W. SIMONETTI, W. GAJEWICZ, J. CALVAR, A. CAPDEVILA, P. R. WILKINS, B. A. BELL, C. RÉMY, A. HEERSCHAP, D. WATSON, J. R. GRIFFITHS, AND C. ARÚS, *Development of a decision support system for diagnosis and grading of brain tumours using in vivo magnetic resonance single voxel spectra*, NMR Biomed., 19 (2006), pp. 411–434.

[280] A. R. TATE, D. WATSON, S. EGLEN, T. N. ARVANITIS, E. L. THOMAS, AND J. D. BELL, *Automated feature extraction for the classification of human in vivo ^{13}C NMR spectra using statistical pattern recognition and wavelets*, Magn. Reson. Med., 35 (1996), pp. 834–840.

[281] R. D. TIEN, P. H. LAI, J. S. SMITH, AND F. LAZEYRAS, *Single-voxel proton brain spectroscopy exam (PROBE/SV) in patients with primary brain tumors*, Am. J. Roentgenol., 167 (1996), pp. 201–209.

[282] P. TIWARI, A. MADABHUSHI, AND M. ROSEN, *A hierarchical unsupervised spectral clustering scheme for detection of prostate cancer from magnetic resonance spectroscopy (MRS)*, Med. Image Comput. Comput. Assist. Interv. Int. Conf. Med. Image Comput. Comput. Assist. Interv., 10 (2007), pp. 278–286.

[283] M. TOMCZAK AND E.-H. DJERMOUNE, *A subband ARMA modeling approach to high-resolution NMR spectroscopy*, J. Magn. Reson., 158 (2002), pp. 86–89.

[284] Z. TONG, T. YAMAKI, K. HARADA, AND K. HOUKIN, *In vivo quantification of the metabolites in normal brain and brain tumors by proton MR spectroscopy using water as an internal standard*, Magn. Reson. Imaging, 22 (2004), pp. 735–742.

[285] V. TUGNOLI, L. SCHENETTI, A. MUCCI, F. PARENTI, R. CAGNOLI, V. RIGHI, A. TRINCHERO, L. NOCETTI, C. TORACI, L. MAVILLA, G. TRENTINI, E. ZUNARELLI, AND M. R. TOSI, *Ex vivo HR-MAS MRS of human meningiomas: a comparison with in vivo ^{1}H MR spectra*, Int. J. Mol. Med., 18 (2006), pp. 859–869.

[286] V. TUGNOLI, M. R. TOSI, G. BARBARELLA, R. RICCI, M. LEONARDI, F. CALBUCCI, AND A. BERTOLUZZA, *Magnetic resonance spectroscopy study of low grade extra and intracerebral human neoplasms*, Oncol. Rep., 5 (1998), pp. 1199–1203.

[287] A. TZIKA, L. L. CHENG, L. GOUMNEROVA, J. R. MADSEN, D. ZURAKOWSKI, L. G. ASTRAKAS, M. K. ZARIFI, R. M. SCOTT, D. C. ANTHONY, R. G. GONZALEZ, AND P. M. BLACK, *Biochemical characterization of pediatric brain tumors by using in vivo and ex vivo magnetic resonance spectroscopy*, J. Neurosurg., 96 (2002), pp. 1023–31.

[288] J. P. USENIUS, S. TUOHIMETS'A, P. VAINIO, M. ALA-KORPELA, Y. HILTUNEN, AND R. A. KAUPPINEN, *Automated classification of human brain tumours by neural network analysis using in vivo ^{1}H magnetic resonance spectroscopic metabolite phenotypes*, Neuroreport, 7 (1996), pp. 1597–1600.

[289] A. VAN DEN BOOGAART, *Quantitative data analysis of in vivo MRS data sets*, Magn. Reson. Chem., 35 (1997), pp. 146–152.

[290] A. VAN DEN BOOGAART, F. A. HOWE, L. M. RODRIGUES, M. STUBBS, AND J. R. GRIFFITHS, *In vivo ^{31}P MRS: absolute concentrations, signal-to-noise and prior knowledge*, NMR Biomed., 8 (1995), pp. 87–93.

[291] M. VAN DER GRAAF, M. JULIÀ-SAPÉ, F. A. HOWE, A. ZIEGLER, C. MAJÓS, A. MORENO-TORRES, M. RIJPKEMA, D. ACOSTA, K. S. OPSTAD, Y. M. VAN DER MEULEN, C. ARÚS, AND A. HEERSCHAP, *MRS quality assessment in a multicentre study on MRS-based classification of brain tumours*, NMR Biomed., 21 (2008), pp. 148–158.

[292] J. W. VAN DER VEEN, R. DE BEER, P. R. LUYTEN, AND D. VAN ORMONDT, *Accurate quantification of in vivo ^{31}P NMR signals using the variable projection method and prior knowledge*, Magn. Reson. Med., 6 (1988), pp. 92–8.

[293] T. VAN GESTEL, J. A. K. SUYKENS, B. DE MOOR, AND J. VANDEWALLE, *Automatic relevance determination for least squares support vector machine classifiers*, in European Symposium on Artificial Neural Networks, D-facto publications, Evere, 2001, pp. 13–18.

[294] V. VAN GESTEL, J. SUYKENS, G. LANCKRIET, A. LAMBRECHTS, B. DE MOOR, AND J. VANDEWALLE, *Bayesian framework for least-squares support vector machine classifiers, gaussian processes, and kernel fisher discriminant analysis*, Neural Comput., 14 (2002), pp. 1115–1147.

[295] S. VAN HUFFEL, H. CHEN, C. DECANNIERE, AND P. VAN HECKE, *Algorithm for time-domain NMR data fitting based on total least squares*, J. Magn. Reson. A, 110 (1994), pp. 228–237.

[296] L. VANHAMME, R. D. FIERRO, S. VAN HUFFEL, AND R. DE BEER, *Fast removal of residual water in proton spectra*, J. Magn. Reson., 132 (1998), pp. 197–203.

[297] L. VANHAMME, T. SUNDIN, P. VAN HECKE, AND S. VAN HUFFEL, *MR spectroscopy quantitation: a review of time-domain methods*, NMR Biomed., 14 (2001), pp. 233–46.

[298] L. VANHAMME, T. SUNDIN, P. VAN HECKE, S. VAN HUFFEL, AND R. PINTELON, *Frequency-selective quantification of biomedical magnetic resonance spectroscopy data*, J. Magn. Reson., 143 (2000), pp. 1–16.

[299] L. VANHAMME, A. VAN DEN BOOGAART, AND S. VAN HUFFEL, *Improved method for accurate and efficient quantification of MRS data with use of prior knowledge*, J. Magn. Reson., 129 (1997), pp. 35–43.

[300] V. VAPNIK, *The nature of statistical learning theory*, Springer, New York, 1995.

[301] ———, *Statistical learning theory*, Wiley, 1998.

[302] P. VERMATHEN, K. D. LAXER, N. SCHUFF, G. B. MATSON, AND M. W. WEINER, *Evidence of neuronal injury outside the medial temporal lobe in temporal lobe epilepsy: N-acetylaspartate concentration reductions detected with multisection proton MR spectroscopic imaging–initial experience*, Radiology, 226 (2003), pp. 195–202.

[303] Y. WANG AND S. J. LI, *Differentiation of metabolic concentrations between gray matter and white matter of human brain by in vivo ^{1}H magnetic resonance spectroscopy*, Magn. Reson. Med., 39 (1998), pp. 28–33.

[304] P. G. WEBB, N. SAILASUTA, S. J. KOHLER, T. RAIDY, R. A. MOATS, AND R. E. HURD, *Automated single-voxel proton MRS: technical development and multisite verification*, Magn. Reson. Med., 31 (1994), pp. 365–373.

[305] O. M. WEBER, C. O. DUC, D. MEIER, AND P. BOESIGER, *Heuristic optimization algorithms applied to the quantification of spectroscopic data*, Magn. Reson. Med., 39 (1998), pp. 723–730.

[306] N. WESTERGAARD, U. SONNEWALD, AND A. SCHOUSBOE, *Metabolic trafficking between neurons and astrocytes: the glutamate/glutamine cycle revisited*, Dev. Neurosci., 17 (1995), pp. 203–211.

[307] J. WESTON, S. MUKHERJEE, O. CHAPELLE, M. PONTIL, T. POGGIO, AND V. VAPNIK, *Feature Selection for SVMs*, vol. 12, Cambridge. MIT Press, MA, USA, 2000.

[308] J. WESTON AND C. WATKINS, *Multi-class support vector machines*, Brussels, 1999, ESANN'99, D-Facto publications.

[309] D. C. WILLIAMSON, H. HAWESA, N. A. THACKER, AND S. R. WILLIAMS, *Robust quantification of short echo time ^{1}H magnetic resonance spectra using the Padé approximant*, Magn. Reson. Med., 55 (2006), pp. 762–71.

[310] H. WITJES, W. J. MELSSEN, H. J. IN 'T ZANDT, M. VAN DER GRAAF, A. HEERSCHAP, AND L. M. BUYDENS, *Automatic correction for phase shifts, frequency shifts, and lineshape distortions across a series of single resonance lines in large spectral data sets*, J. Magn. Reson., 144 (2000), pp. 35–44.

[311] K. YOUNG, V. GOVINDARAJU, B. J. SOHER, AND A. A. MAUDSLEY, *Automated spectral analysis I: formation of a priori information by spectral simulation*, Magn. Reson. Med., 40 (1998), pp. 812–815.

[312] K. YOUNG, B. J. SOHER, AND A. A. MAUDSLEY, *Automated spectral analysis II: application of wavelet shrinkage for characterization of non-parameterized signals*, Magn. Reson. Med., 40 (1998), pp. 816–21.

[313] D.-Q. ZHANG AND S.-C. CHEN, *A novel kernelized fuzzy c-means algorithm with application in medical image segmentation*, Artif. Intell. Med., 32 (2004), pp. 37–50.

[314] G. ZHU, W. Y. CHOY, AND B. C. SANCTUARY, *Spectral parameter estimation by an iterative quadratic maximum likelihood method*, J. Magn. Reson., 135 (1998), pp. 37–43.

[315] J. ZHU AND T. HASTIE, *Kernel logistic regression and the import vector machine*, J. Comput. Graph. Stat., 14(1) (2005), pp. 185–205.

[316] X. P. ZHU, K. YOUNG, A. EBEL, B. J. SOHER, L. KAISER, G. MATSON, W. M. WEINER, AND N. SCHUFF, *Robust analysis of short echo time ^{1}H MRSI of human brain*, Magn. Reson. Med., 55 (2006), pp. 706–711.

[317] K. ZOU, W. J. HALL, AND D. SHAPIRO, *Smooth non-parametric receiver operating characteristic (ROC) curves for continuous diagnostic tests*, Stat. Med., 16 (1997), pp. 2143–2156.

Publication list

Papers in international journals

1. J. Poullet, D.M. Sima, A.W. Simonetti, B. De Neuter, L. Vanhamme, P. Lemmerling, S. Van Huffel, An automated short echo time MR quantification in a open-source software environment: AQSES, NMR Biomed. 20 (2007) 493-504.

2. J. Poullet, D.M. Sima, S. Van Huffel, P. Van Hecke, Frequency-selective quantitation of short echo time ^{1}H Magnetic Resonance spectra, J. Magn. Reson. 186(2)(2007) 293-304.

3. J. Luts, J. Poullet, J. Garcia-Gomez, A. Heerschap, M. Robles, J.A.K. Suykens, S. Van Huffel, The effect of Feature Extraction for Brain Tumor Classification based on short echo time ^{1}H MR spectra, Magn. Res. Med. 60(2) (2008) 288-298.

4. J. Poullet, D.M. Sima, S. Van Huffel, MRS signal quantitation: a review of time- and frequency-domain methods, J. Magn. Reson. 195(2) (2008) 134-144.

5. J. Poullet, R. Pintelon, S. Van Huffel, A new FIR filter technique for solvent suppression in MRS signals, Internal Report 08-116, ESAT-SISTA, K.U.Leuven (Leuven, Belgium), 2008, accepted for publication in the Journal of Magnetic Resonance.

Papers in proceedings of (inter)national conferences

6. J. Poullet, D.M. Sima, S. Van Huffel, Frequency-selective quantification of short-echo time Magnetic Resonance spectra, Proc. of the IEEE 2006 International Conference of the Engineering in Medicine and Biology Society (EMBC 2006), New-York, Aug.-Sep. 2006, 6351-6355.

7. J. Poullet, M.C. Martinez-Bisbal, D. Valverde, D. Monleon, B. Celda, C. Arus, S. Van Huffel, Quantification and classification of high-resolution magic angle spinning data for brain tumor diagnosis, Proc. of the IEEE 2007 International Conference of the Engineering in Medicine and Biology Society (EMBC 2007), Lyon, Aug. 2007, 5407-5410.

8. K. Vanderperren, S. Vandeput, J. Poullet, D.M. Sima, S. Van Huffel, Automatic quantification of magnetic resonance spectroscopic signals : Evaluation and comparison of AQSES and QUEST, in Proc. of the Belgian day on biomedical engineering -

IEEE/EMBS Benelux Chapter Symposium, Brussels, Belgium, Dec. 2006, pp. 251-254.

9. V. Van Belle, J. Poullet, D. Monleon, B. Celda, M. Martinez-Bisbal, S. Van Huffel, Classification of brain tumors by means of high resolution magic angle spinning spectra, in Proc. of the Belgian Day on Biomedical Engineering IEEE/EMBS Benelux Chapter Symposium, Brussels, Belgium, Dec. 2006, pp. 199-202.

10. A. Croitor Sava, T. Laudadio, J. Poullet, D. Monleon, M.C. Martinez-Bisbal, B. Celda, S. Van Huffel, Data Fusion of HR-MAS and in-vivo Information with Application in Brain Tumor Recognition, Proc. of the European Symposium on Biomedical Engineering (ESMBE 2008), Chania, Greece, Jun. 2008.

11. M.I. Osorio, D.M. Sima, J. Poullet, D. Van Ormondt, S. Van Huffel, Improvement of lineshape estimation for MRS signals, IEEE International workshop on Imaging Systems and Techniques, Chania, Greece, Sept. 2008, 326-329.

12. M.I. Osorio, D.M. Sima, J. Poullet, D. Van Ormondt, S. Van Huffel, Iterative improvement of lineshape estimation, Proc. of the 4th European Congress of the International Federation for Medical and Biomedical Engineering (MBEC 2008), Antwerp, Belgium, Nov. 2008.

13. A. Croitor Sava, T. Laudadio, J. Poullet, D. Monleon, M.C. Martinez-Bisbal, B. Celda, S. Van Huffel, Combining HR-MAS and in vivo MRI and MRSI information for robust brain tumor recognition, Proc. of the 4th European Congress of the International Federation for Medical and Biomedical Engineering (MBEC 2008), Antwerp, Belgium, Nov. 2008.

Abstracts for (inter)national conferences

14. J. Poullet, D.M. Sima, B. De Neuter, L. Vanhamme, P. Lemmerling, A. Simonetti, P. Van Hecke, S. Van Huffel, Accurate and automated time-domain quantitation of short-echo-time spectra. (Oral presentation at ESMRMB Congress, Basel, Switzerland, September 2005)

15. J. Poullet, D. M. Sima, S. Van Huffel AQSES GUI a free open-source software package for accurate quantification of short-echo time NMR spectra; National Day of Biomedical Engineering, October 2005 in Brussels.

16. J. Poullet, D. M. Sima, S. Van Huffel, An automated quantification solution of short echo time MR spectra in an open source software environment: AQSES (Oral presentation at ESMRMB Congress, Warsaw, Poland, September 2006).

17. J. Poullet, M. Wilson, C. Martinez-Bisbal, D. Monleon, B. Celda, A. Peet and S. Van Huffel, Quantitation and Classification of HR-MAS Brain Biopsy Tissue Spectra (Electronic poster presentation at ISMRM-ESMRMB Congress, Berlin, Germany, May 2007).

18. J. Poullet, D. Monleon, M. Martinez-Bisbal, B. Celda, and S. Van Huffel, Automating brain tumour classification using high resolution magic angle spinning data, (Electronic poster presentation at ISMRM Congress, Toronto, Canada, May 2008).

Internal reports (including submitted papers)

19. J. Poullet, D.M. Sima, S. Van Huffel, Metabolite quantification in MRS and pattern recognition, Internal Report 08-84, ESAT-SISTA, K.U.Leuven (Leuven, Belgium), 2008, submitted for publication to the Encyclopedia of Magnetic Resonance.

20. J. Poullet, D.M. Sima, M.I. Osorio, S. Van Huffel, FAST report: short-echo time MRS quantitation, Internal Report 08-127, ESAT-SISTA, K.U.Leuven (Leuven, Belgium), 2008.

Curriculum vitae

Jean-Baptiste Poullet was born on January 23, 1981, in Namur. He received the degree of electrical engineering, option telecommunications, from the Catholic University of Louvain-la-Neuve, Belgium, in 2003. He received the master degree of statistics in June 2004 from the Katholieke Universiteit Leuven, Belgium, and started in October of the same year as a researcher at the Department of Electrical Engineering (ESAT) of the K.U. Leuven.